Fully Selective Pb(II) Templated Heterotrimeric Redox and Hydrolytic Metalloenzymes
by

Audrey Elizabeth Tolbert

A dissertation submitted in partial fulfillment
of the requirements for the degree of
Doctor of Philosophy
(Chemistry)
in the University of Michigan
2021

Doctoral Committee:

Professor Vincent L. Pecoraro, Chair
Professor Nicolai Lehnert
Professor James E. Penner-Hahn
Professor Clotilde Policar, École Normale Supérieure
Professor Yang Zhang

Audrey Elizabeth Tolbert

atolb@umich.edu

ORCID iD: 0000-0003-0936-8568

To my parents

Acknowledgements

There are many people without whom I would not have made it to this point. First, my deepest thanks to my advisor, Vince Pecoraro. Vince has supported and encouraged me throughout this process, but especially in the past year while attempting to finish a thesis during a pandemic. Throughout my time in his lab, I have learned myriad techniques and how to think critically about the work that I am doing. I've learned how to engage deeply with my projects and to contribute to the work of others in the group. Without his expert guidance, I would not be the scientist or person that I am today.

I also want to express my gratitude to my other committee members, Dr. Nicolai Lehner, Dr. Jim Penner-Hahn, and Dr. Yang Zhang for their critical review of my work over the years. They have brought perspective necessary for deeper interpretation of my work as well as encouragement to think about my work within the broader scientific community. I also need to express my gratitude for Dr. Clotilde Policar, not just for serving on my committee, but also for hosting me in her laboratory for a year. This experience and her mentorship pushed me and my work far past where I thought I would ever be. To her and to the Chateaubriand Fellowship I am eternally grateful. And of course, my thanks to all my collaborators for their discussions, scientific contributions, and critiques of this work: Dr. Rajeev Prabhakar, Dr. Amy Barrios, Dr. Cédric Tard, Dr. Nicolai Lehnert, Dr. Jim Penner-Hahn, Dr. Aniruddha Deb, Dr. Jennifer Meagher, and Dr. Jeanne Stuckey.

And of course, to all the lab members, past and current, who have been there every day, offering advice and encouragement along the way: Cathy, Leela, Adrian, Jake, Tu, April, Bernadette, Shuri, Elvin, and Winston and the members of the Policar group: Antoine, Koudedja, Manon, Martha, Menglan, Amandine, Gabrielle, Nicolas, Lucas, Elodie, and Anne-Sophie. You all have made my time in the lab an unforgettable experience. This list would not be complete without Karl and Tyler, who mentored me, laughed with me, listened to me complain, and answered an unimaginable amount of questions, even after they moved on to new positions. I never would have made it here if not for them.

Lastly, I need to acknowledge the role my family has played in getting me to this point. Despite having no idea what I'm working on, they have been so encouraging. Hours of phone calls, especially in the past year, have brought me distraction, clarity, and the constant reminder that I can do hard things. I can never fully express my gratitude for this.

Table of Contents

List of Tables

List of Figures

List of Abbreviations

2SCC: Two stranded coiled coil

3SCC: Three stranded coiled coil

4SCC: Four stranded coiled coil

BCS: Bathocuproinedisulfonic acid

CA: Carbonic anhydrase

CC: Coiled coil

CD: Circular dichroism

CHES: N-Cyclohexyl-2-aminoethanesulfonic acid

DIEA: N,N-Diisopropylethylamine

EPR: Electron paramagnetic resonance

ESI-MS: Electrospray ionization mass spectrometry

EXAFS: Extended X-ray absorption fine structure

GuHCl: Guanidinium hydrochloride

HBTU: (2-(1H-benzotriazol-1-yl)-1,1,3,3-tetramethyluronium hexafluorophosphate

HEPES: N-2-hydroxyethylpiperazine-N-ethanesulfonic acid

HOBt: Hydroxybenzotriazole

HPLC: High pressure liquid chromatography

ICP-MS: Ion coupled plasma mass spectrometry

MALDI-TOF MS: Matrix assisted laser desorption ionization-time of flight mass spectrometry

MBHA: methylbenzhydrylamine

NiR: Nitrite reductase

NMR: Nuclear magnetic resonance

QM/MM: Quantum mechanics/molecular mechanics

SOD: Superoxide dismutase

XANES: X-ray absorption near edge spectroscopy

XAS: X-ray absorption spectroscopy

XO: Xanthine oxidase

XTT: Sodium 2,3-bis-(2-methoxy-4-nitro-5-sulfophenyl)-2*H*-tetrazolium-5-carboxanilide

Zi: Zincon (2-carboxy-2’-hydroxy-5’-(sulfoformazyl)benzene)

Abstract

The design and characterization of the first fully selective, self-assembling, asymmetric *de novo* designed three stranded coiled coils and their use to induce non-3-fold symmetric transition metal coordination for hydrolytic and redox catalysis is presented. This work was done in a peptide scaffold of the sequence Ac-G-(L**a**K**b**A**c**L**d**E**e**E**f**K**g**)$_5$-G-NH$_2$ where subscripts indicate position in the heptad. Leu residues are substituted with metal binding residues to both induce asymmetry at one site and perform transition metal catalysis at a second, distant site. Full selectivity for both A_2B- and AB_2-type heterotrimers was achieved using a **d**-site Cys, Pb(II), and an adjacent layer (toward the C terminus) of reduced steric bulk with mixed Leu and Ala residues. This work presents a significant improvement over a reported scaffold using **a**-site Cys residues that was only selective for A_2B-type (2 Ala) heterotrimers. To maintain stability, these scaffolds are limited to 3 Leu substitutions per strand. These **d**-site scaffolds allow for both X_1His_3 and X_2His_3 transition metal sites, expanding the scope of asymmetry that can be explored.

The selectivity of heterotrimers with **d**-site Cys was determined via ^{207}Pb NMR. Homotrimeric peptides had a single resonance at 5762 ppm (3 Ala) and 5789 ppm (3 Leu) and heterotrimeric mixtures had a single resonance at 5875 ppm (2 Ala, 1 Leu) and 5803 ppm (1 Ala, 2 Leu). Crystallographic comparison of the homotrimers found that the hydrogen bonding network present in the Ala_3 homotrimer was significantly different for **a**- and **d**-site Cys residues, where solvent was able to hydrogen bond two **a**-site Cys residues at 3.0 and 3.4 Å while only one solvent molecule could hydrogen bond a **d**-site Cys at 3.4 Å. The energetic differences between hydrogen bonding and leucine packing in the adjacent layer yields the observed selectivity between **a-** and **d**-site Cys heterotrimers.

A distant His_3 site can be incorporated into the scaffold and can coordinate a transition metal without perturbing the Pb(II)Cys_3 site, or the heterotrimer stoichiometry, as determined by ^{207}Pb NMR. As such, this work utilized **a**-site His residues with adjacent Glu to investigate Zn(II) hydrolysis as found in carbonic anhydrase. A potential hydrogen bonding residue with a long

side chain assessed whether the Zn(II)His_3OH coordination environment previously characterized was maintained, while also affording a second sphere hydrogen bond as found in the native system. Co(II) spectroscopy determined that an asymmetric 5-coordinate environment was generated with 1 or 2 Glu residues while a symmetric 6-coordinate environment was observed for 1 or 3 Glu. Ultimately, Zn(II) coordinated Glu_1His_3 (k_{cat}/K_M=11.4 $M^{-1}s^{-1}$), Glu_2His_3 (22 $M^{-1}s^{-1}$), and Glu_3His_3 (18.7 $M^{-1}s^{-1}$) did not improve upon the most efficient His_3 model (23.3 $M^{-1}s^{-1}$), likely because the Glu residue was instead able to hydrogen bond directly to a His residue, precluding Zn(II)$His_3(H_2O)$ coordination.

Redox catalysis, modelling Cu-only superoxide dismutase, was found at pH 7.5 with a variety of His_3, His_4, and mixed Carboxy/His binding environments. This work describes the best peptidic models of this system. The **d**-site His_3 (k_{McF}=4.5x10^7 $M^{-1}s^{-1}$) was ~7.5x faster than **a**-site His_3 (6.7x10^6 $M^{-1}s^{-1}$) despite having a less ideal reduction potential (695 vs 541 mV vs NHE, respectively). The fastest construct contained 2 His and 1 Asp in the **d**-site and 1 His in the **a**-site (k_{McF}= 6.2x10^7 $M^{-1}s^{-1}$). These experiments could only be completed by using these new asymmetric heterotrimers.

Chapter 1 Introduction

De novo design vs redesign

Protein design has been a tool of biochemists and bioinorganic chemists for decades to study the relationship between protein structure and function. Over the course of several billion years, evolution has produced proteins that can perform myriad reactions with high efficiency and selectivity. Protein chemists have aimed to understand the properties of enzymes that allow for such robust function in several ways: *de novo* protein design, protein redesign, and synthetic small molecule models. *De novo* design, the focus of this work, is the creation of a new peptide or protein "from scratch" in which the linear array of amino acids may be inspired by native sequences but is not itself a native protein. Protein redesign instead modifies existing proteins, exploiting well defined and stable scaffolds, to induce novel functions. Synthetic small molecules aim to recapitulate the active site of native systems in a non-protein environment. This allows chemists to replicate activity, but does not provide as much insight into the native enzyme.

Both protein redesign and *de novo* design require an intimate knowledge of DNA sequencing, genome mapping, selective amino acid mutations, and protein purification. Recent advances in solid phase peptide synthesis have removed several of these barriers, allowing for facile synthesis of simple peptide sequences with relatively straightforward purification methods. Computational power has advanced rapidly, allowing for the explosion of protein redesign work via directed evolution. This has introduced non-natural functionalities to robust enzymes, but has yet to characterize how structural changes have affected catalysis. If one aims to understand the intricacies of enzymes, one must be able to build an enzyme, not simply modify an existing structure. Dr Frances Arnold, a 2018 Nobel Laurate in Chemistry, has even said of her directed evolution method that "We could not explain how mutations…enhanced activity in high concentrations of organic solvent, much less plan them in a rational approach to engineering an enzyme with this new capability. But we had a *process* that gave the right result."[1] *De novo* designed constructs allow for an intimate investigation into the relationship between structure

and function via the stepwise incorporation of amino acid residues. In the Pecoraro lab, we investigate the "how" and "why" of enzymatic evolution in a stepwise, rational manner. Our work has focused on *de novo* design to determine the factors that lead to diffusion limited rates of metalloenzymes that are essential for human health.

Need for asymmetry

Nature is inherently asymmetric, with proteins exhibiting asymmetry at both the micro and macro levels. A major challenge for *de novo* design has been how to appropriately incorporate this asymmetry into a peptide scaffold. There are also many aspects of asymmetry that one must consider: the asymmetry of the protein itself in tertiary and quaternary structures, the asymmetry of individual amino acids, and the asymmetry in coordination environment of enzyme cofactors. As this work is focused only on metalloenzyme active sites, macro level tertiary and quaternary asymmetry in native systems will not be considered. Asymmetry at the micro level, that of amino acids and their coordination environments, is within the scope of this project. One could consider asymmetry to exist solely due to the incorporation of L-amino acids and the chiral environment created by this well controlled stereochemistry. How metal coordination is affected by the stereochemistry of amino acid residues has been explored before, including significant work on heavy metal incorporation by both D- and L- residues in the Pecoraro lab.[2-5] The work described herein, however, focuses specifically on a metal cofactor and its coordinating atoms. As such, asymmetry in this work is defined as the incorporation of different protein ligand types (imidazole, thiol, carboxylate,…) within the primary and secondary metal coordination spheres. Both first and second coordination sphere asymmetry exist within native systems. Asymmetry in the primary coordination sphere means simply that no symmetry operators (other than the identity operator) can be applied when one considers only the atoms directly coordinated to the metal. Symmetry of the second coordination sphere is defined in relation to the primary coordination sphere. A fully symmetric second coordination sphere occurs when the same symmetry operator can be applied to the primary and secondary coordination spheres. If not, or if the primary coordination sphere is asymmetric, the second coordination sphere is asymmetric. One can think of this as building a binding environment from the metal out, rather than imposing a binding environment from the protein inward. To understand what asymmetry means in the context described above, one can consider two enzyme

systems: human carbonic anhydrase II (CA) and copper only superoxide dismutase (Cu-only SOD).

Carbonic anhydrase is a zinc metalloenzyme that catalyzes the hydrolysis of carbon dioxide to carbonate (Figure 1-1).[6] The active site of CA contains a zinc bound to three histidine residues and a solvent molecule in pseudotetrahedral geometry (Figure 1-2).[7-8] The histidines are coordinated with two epsilon and one delta nitrogen. As all three protein ligands are histidine residues, however, this site will be treated as three-fold symmetric in this work. One can investigate the effect of epsilon vs delta nitrogen coordination, as was done for copper nitrite reductase,[9] but these studies are not discussed herein. The nuance of this asymmetry is discussed further in Chapter 6 as an expansion of asymmetric studies in *de novo* systems.

The trigonal symmetry of the His residues in the first coordination sphere is rather straightforward to model and has been achieved by several groups, including the Pecoraro lab, in both peptide and small molecule models.[10-14] The more challenging step is to incorporate second sphere asymmetry. The Zn(II)-coordinated solvent molecule is further coordinated by a single threonine reside, T199 in human CAII, that is essential for mediating the pKa of the active site.[7, 15-17] As only one hydrogen bonding residue is present in a site that is three-fold symmetric in the first coordination sphere, this site is asymmetric in the second coordination sphere. This particular interaction is of note because, in the native enzyme, the loss of this hydrogen bonding interaction via a Thr to Ala mutation resulted in an increase of the pKa from 6.8 to 8.5 and ~100 fold loss in catalytic efficiency.[16-17] The role of T199 is discussed further in Chapter 4. How to best model this interaction has been of interest to the Pecoraro lab for some time now and is addressed, in part, by this work.

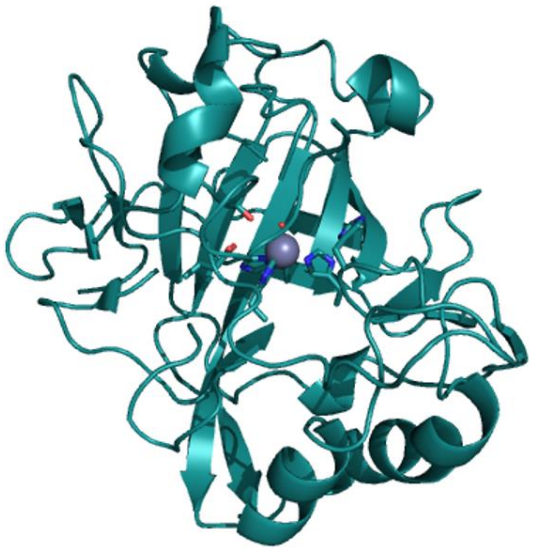

Figure 1-1 Human Carbonic Anhydrase II with Zn(II) shown as a grey sphere (PDB 2CBA)

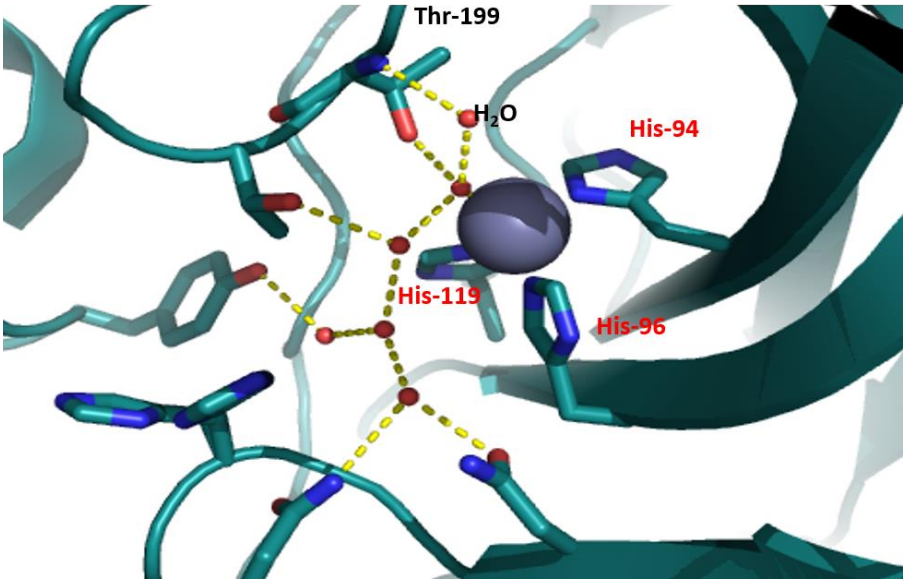

Figure 1-2 Close up of the active site of CAII. H94, H96, and H119 directly coordinate the Zn(II) (grey sphere). T199 hydrogen bonds to a water molecule that is coordinated to the Zn ion (PDB 2CBA)

First coordination sphere asymmetry has been a bigger challenge for the Pecoraro group as one cannot start with a symmetric model as was done with CA. This work describes the best model of Cu-only SOD (Figure 1-3), which has an asymmetric Cu(II) environment in the first coordination sphere.[18] Superoxide dismutases remove superoxide (O_2^-) by both oxidizing it to molecular oxygen (O_2) and reducing it to peroxide (H_2O_2) at diffusion limited rates by cycling through reduced and oxidized metal species.[19-24] The most recently discovered class of this enzyme, Cu-only SOD, cycles between Cu(I) bound to three histidine residues, in an

environment like that of CA, and Cu(II) bound to four histidine residues (Figure 1-4). This fourth histidine residue disrupts the three-fold symmetry found in the Cu(I) state, resulting in an asymmetric primary coordination sphere. This work aimed to incorporated first sphere asymmetry to investigate this enzyme.

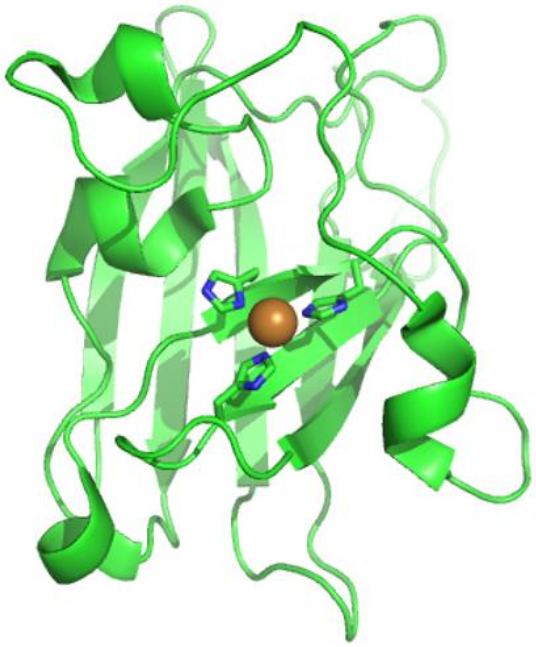

Figure 1-3 Cu-only SOD in the Cu(I) bound form with copper shown as an orange sphere (PDB 4N3T)

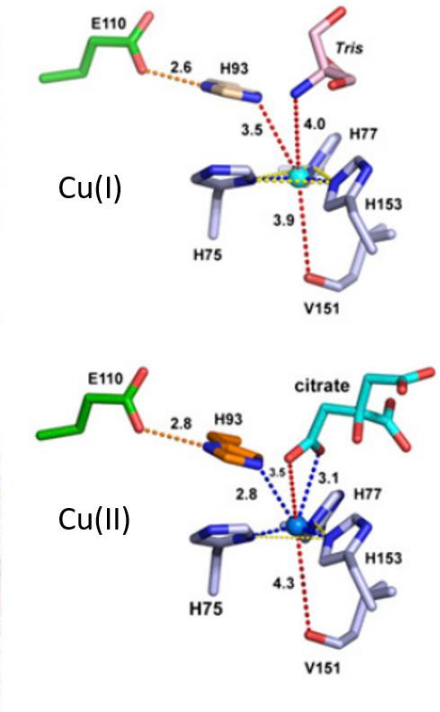

Figure 1-4 The Cu(I) (top) and Cu(II) (bottom) bound active site of Cu-only SOD (PDB 4N3T).[18]

A further challenge presented by Cu-only SOD is the change in coordination number throughout the catalytic cycle. Zn(II) remains four-coordinate throughout the catalytic cycle of CA, but Cu(I) and Cu(II) have different preferred geometries and coordination numbers. Cu(I) generally prefers to be linear two-coordinate or trigonal three coordinate. Cu(II), however, is more commonly four or five coordinate.[25]

De novo scaffold

De novo protein design has utilized the coiled coil (CC) motif based on first principles learned from the ubiquity of this motif.[26-30] To generate a coiled coil, all that is required is a seven residue "heptad" repeat of amino acids with appropriate placement of hydrophobic and hydrophilic residues.[31] The positions of the heptad are designated by the letters a through g. Hydrophobic residues are placed in the first (**a**) and fourth (**d**) position, forming one face of the alpha helix (Figure 1-5).[30, 32] In solution, a hydrophobic collapse occurs to form a coiled coil. The number of helices that comprise the CC is determined by the hydrophobic residues used and the presence of exterior salt bridging. The most commonly utilized native hydrophobes are leucine, isoleucine, and valine. Selective placement of these residues in either the **a** or **d** positions dictates CC assembly into two stranded coiled coils (2SCCs), three stranded coiled

coils (3SCCs), or four stranded coiled coils (4SCCs). Two stranded coiled coils can result from Ile or Val in the **a** position and Leu in a **d** position.[33-34] Additionally, 2SCCs can be formed via negative design through the removal of exterior salt bridging interactions (Figure 1-7, top). 4SCCs are generated with bulkier hydrophobes, including phenylalanine, or if leucine is placed in the **a** position and isoleucine in the **d** position.[34] Any other combination of leucine, isoleucine, or valine tends to result in 3SCCs.

The Pecoraro lab has previously had great success in the *de novo* design of three-fold symmetric enzymes using a 3SCC. The heptad repeat used to generate these 3SCCs is LKALEEK, with hydrophobic leucine residues at positions **a** and **d**. The scaffolds discussed in this work have either four heptad repeats, forming the TRI scaffold, or five heptad repeats, forming the Grand (GR) scaffold. In solution, the heptads fold into an alpha helix with the **a** and **d** residues (Leu) forming one face of the helix (Figure 1-5). These leucine residues hydrophobically pack to form the core of a coiled coil (Figure 1-6). The 3SCC is further stabilized by salt bridging interactions of glutamate (**e**) and lysine (**g**) residues on adjacent strands. The N-terminus is capped with an acetyl glycine and the C-terminus with an amidated glycine to prevent fraying and aid in neutralizing the helical dipole (

Table 1-1). A tryptophan residue in the first **a** position is used for spectroscopic determination of protein concentration. This residue does not interfere with metal binding.

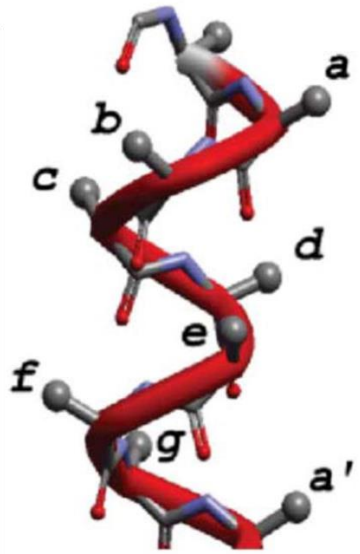

Figure 1-5 One heptad of an alpha helix[35]

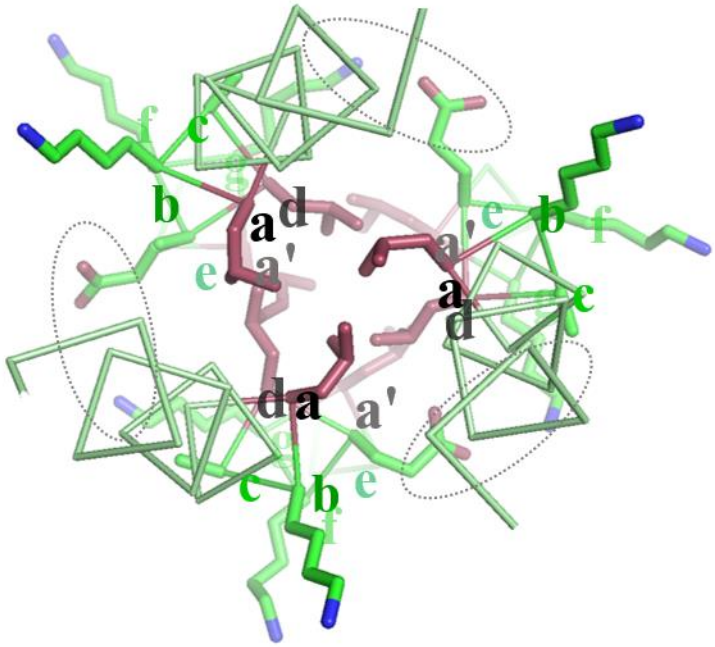

*Figure 1-6 Top down view of a 3SCC with **a** and **d** residues in red and salt bridging interactions in dotted ovals*

The type of coiled-coil formed is pH dependent. In strongly acidic conditions, two stranded coiled coils are formed and 3SCCs are formed in basic and mildly acidic solutions with a pKa of 5.5 for 2SCC to 3SCC conversions (Figure 1-7). This conversion is dependent on the deprotonation of Glu residues in the **e** position. When deprotonated, they are able to form salt bridges with Lys residues in the **g** position of an adjacent strand. The angles of this salt bridge are such that a 3SCC is preferred when leucines are used as the hydrophobe.

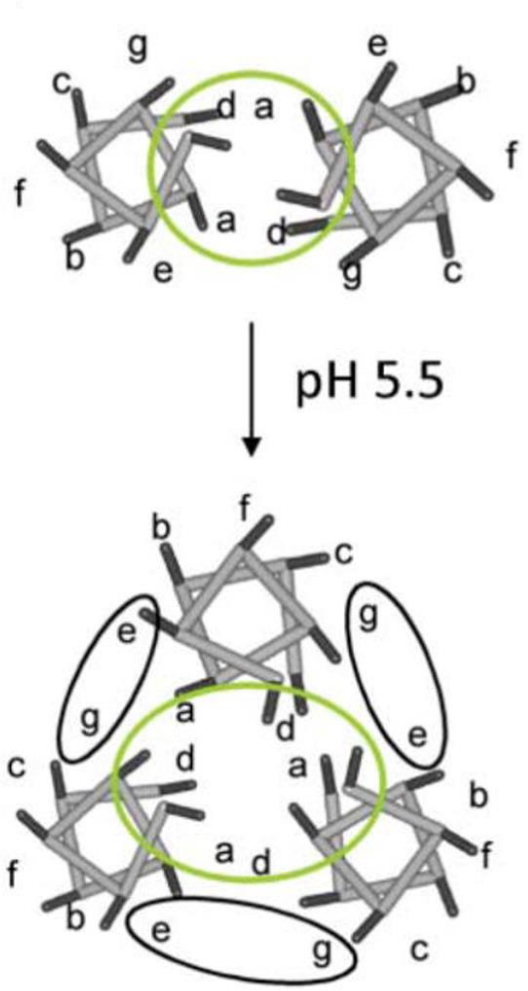

Figure 1-7 pH dependent conversion of 2SCC to 3SCC with the hydrophobic core in a green circle and salt bridging interactions in black ovals

For crystallographic studies, attempts to obtain single crystals of the TRI 3SCC has not been successful because it does not pack well in three dimensions. Thus, the CoilSer (CS) scaffold is used. This scaffold maintains the heptad repeat with **a** and **d** leucine residues, but the hydrophilic residues differ. The most notable difference is a single histidine residue in the **f** position of the C-terminal heptad. This histidine is solvent exposed and, in the presence of

Zn(II), packs three dimensionally with equivalent His residues of other coiled coils. These exterior interactions were shown to have no effect on the core of the helix .[36] CS is not used for metal binding assays because of this exterior metal binding residue, which often makes it difficult to understand spectroscopic or catalytic features of metal sites in catalytic centers.

Crystal structures of CS show that the 3SCC is able to associate in either a parallel or antiparallel orientation.[37] The parallel orientation is when all the N-termini and C-termini are aligned, while in the antiparallel orientation one strand is flipped so two N-termini and one C-terminus are aligned. With all core Leu residues there is no energetic preference for either alignment and it is thought that an antiparallel orientation, as seen in an earlier CS structure, was the result of canceling helical dipoles. No steric or ionic constraints are placed on the core of the coiled coil that would require either parallel or antiparallel orientation. This presents an avenue for asymmetric trimer formation that must be controlled to achieve full selectivity of a single heterotrimeric species. When a related peptide, coil V_aL_d was crystalized, it formed parallel 3SCCs because of the alternating alanine and leucine layers that formed energetic better matches when valine or leucine were always in the same layer, which could only be achieved in a parallel orientation.[38] This suggested, and was then verified, that peptides with one or two substitutions could exclusively form parallel assemblies (e.g., $(CS\ L16C)_3$). Further studies have shown the relative stabilities of core residues as they relate to hydrophobic packing. It has been shown that layers containing all Ala residues are less stable than those containing bulkier hydrophobes such as Val, Ile, or Leu, even though Ala is known to be a helix inducing residue.[39] As Ala is a small hydrophobe in comparison to the others considered in CC core formation, it is insufficient to fully exclude solvent from this environment. Larger side chains are necessary to provide the steric constraints necessary to create a well packed hydrophobic core.

*Table 1-1 List of peptide sequences referenced in this chapter with Trp for concentration determination in **bold green** and mutations at metal binding sites in **bold red***

Peptide name	Abbreviation	Sequence
Coil Ser		Ac E WEALEKK LAALESK LQALEKK LEALEHG NH_2
TRI		Ac G LKALEEK LKALEEK LKALEEK LKALEEK G NH_2
Grand (GR)		Ac G LKALEEK LKALEEK LKALEEK LKALEEK LKALEEK G NH_2
TRI L2WL16C	Cys^a	Ac G **W**KALEEK LKALEEK **C**KALEEK LKALEEK G NH_2
TRI L2WL12C	Cys^d	Ac G **W**KALEEK LKA**C**EEK LKALEEK LKALEEK G NH_2
TRI L2WL19C	$19Cys^d$	Ac G **W**KALEEK LKALEEK LKA**C**EEK LKALEEK G NH_2
TRI L9CL23H		Ac G **W**KALEEK **C**KALEEK LKALEEK **H**KALEEK G NH_2
GR L2WL16C	Cys^a	Ac G **W**KALEEK LKALEEK **C**KALEEK LKALEEK LKALEEK G NH_2
GR L2WL12AL16C	Ala^dCys^a	Ac G **W**KALEEK LKA**A**EEK **C**KALEEK LKALEEK LKALEEK G NH_2
α_3D		MGSWAEFKQRLAAIKTRLQALGG SEAELAAFEKEIAAFESELQAYKGKGNPE VEALRKEAAAIRDELQAYRVNGSGA
α_3D H3		MGSWAEFKQRLAAIKTR**H**QALGG SEAE**H**AAFEKEIAAFESELQAYKGKGNPE VEALRKEAAAIRDE**H**QAYRVNGSGA
GRα_3D		MGSWAEFKQRLAAIKTRLAAIKSRLDALGGS-EAELAAFEKEIAAFESEIAAFESELQAYKGKG-NPEVEALRKEAAAIRDEAAAIRDELQAYRLNGSGA
GRα_3D H3		MGSWAEFKQRLAAIKTRLAAIKSR**H**DALGGS-EAELAA**H**EKEIAAFESEIAAFESELQAYKGKG-NPEVEALRKEAAAIRDEAAAIRDE**H**QAYRLNGSGA
GRα_3D H4		MGSWAEFKQRLAAIKTRLAAIKSR**H**DALGGS-EAE**H**AA**H**EKEIAAFESEIAAFESELQAYKGKG-NPEVEALRKEAAAIRDEAAAIRDE**H**QAYRLNGSGA
GRα_3D H3D		MGSWAEFKQRLAAIKTRLAAIKSR**H**DALGGS-EAE**D**AA**H**EKEIAAFESEIAAFESELQAYKGKG-NPEVEALRKEAAAIRDEAAAIRDE**H**QAYRLNGSGA
GRα_3D H2DH		MGSWAEFKQRLAAIKTRLAAIKSR**H**DALGGS-EAE**H**AA**D**EKEIAAFESEIAAFESELQAYKGKG-NPEVEALRKEAAAIRDEAAAIRDE**H**QAYRLNGSGA

Cys_3 sites for heavy metal binding

For the study of native metal binding sites, one can easily substitute a leucine residue in the **a** or **d** position for a metal binding residue (Cys, His, Glu, Asp, …). This generates an interior trigonal binding site (Figure 1-8). Work in the Pecoraro group began with investigations of a Cys_3 layer for the coordination of heavy metals and metalloids such as Hg(II), Pb(II), Cd(II), Bi(III), and As(III).[3-4, 37, 40-58] The position of this site is noted by the native residue, the position number in the sequence, and the mutated residue, thus a Leu to Cys mutation at the 16^{th} position in the TRI scaffold is written as TRI L16C. An additional nomenclature is used throughout this work to refer only to the type and heptad position of metal binding residues. TRI L16C has a Cys

in an **a** position, referred to as Cys^{a}. The trimer of Cys^{a} peptide strands is noted as Cys_3^{a}. A full list of sequences is found in table (

Table 1-1).

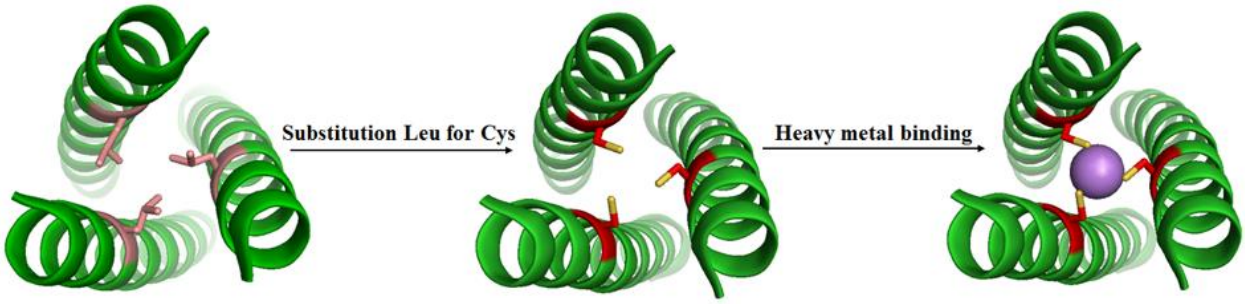

Figure 1-8 A schematic representation of a leucine to cystine mutation followed by Pb(II) binding. All figures generated from PDB 5KB0

The introduction of this metal binding site also solves a puzzle unique to self-assembling alpha helices. As stated above, a core containing entirely Leu residues can fold into either a parallel or antiparallel 3SCC. The parallel configuration leads to distinct layers of **a** or **d** residues, while the antiparallel configuration gives mixed **a** and **d** layers (Figure 1-9). The antiparallel orientation is preferred in the absence of a metal binding site or in the presence of an apo metal binding site. [37, 59] This apo Cys site, when placed equidistant of the N- and C-termini, does not require parallel orientation for the Cys layers to align.[37] There is, however, a significant destabilization of the CC over the non-substituted parent peptide due to the loss in hydrophobic packing.[37, 60] With the addition of a metal ion, however, parallel coiled coils are strongly favored. This is due to alignment necessary to both hydrophobically pack the Leu residues and generate a plane of metal binding residues with favorable salt bridging interactions.[36] The positive design of the **e** and **g** residue interactions prove to be essential in enforcing the parallel strand orientation to sufficiently destabilize a skewed plane generated by three Cys[a] residues across adjacent layers in an antiparallel CC. The addition of a metal also mitigates some loss of stability that is conferred by the introduction of negatively charged residues to the hydrophobic core of the coiled coil.[36-37] While an antiparallel orientation presents an interesting means to acquiring asymmetry, one must be able to selectively control the orientation of strands for this avenue to be useful, requiring a redesign of the salt bridging interactions to stabilize the antiparallel orientation over the parallel orientation.

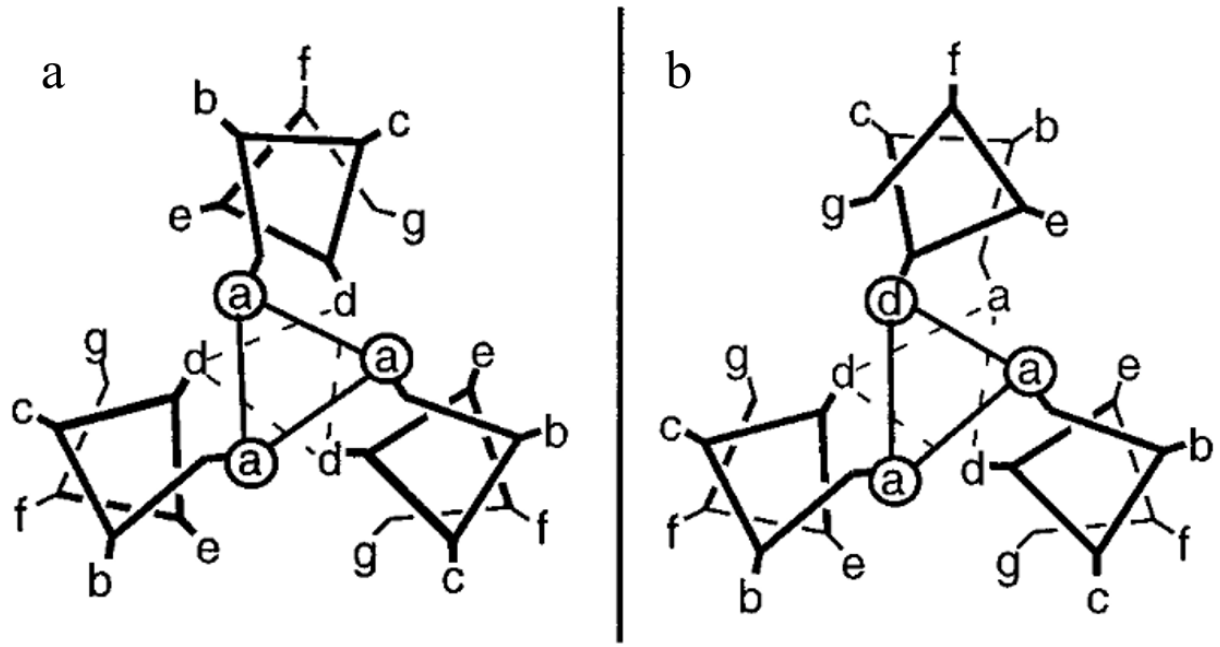

Figure 1-9 Arrangement of the helical core with (a) parallel or (b) antiparallel 3SCCs[36]

Work in the Pecoraro lab began with a study of heavy metal binding to Cys_3 sites. An understanding of how a variety of metals and metalloids interact with this binding environment is necessary to identify a key factor in heterotrimer formation. This Cys_3 site can be either preorganized or predisposed for thiophilic metal binding. A preorganized site is one in which minimal reorientation of the Cys sidechains in the apo structure is necessary for the metal to bind, as is the case for Pb(II) or As(III). A predisposed site, however, contains the residues necessary for metal binding in an appropriate layer, but significant reorientation is required for the metal to bind, such as for Hg(II) or Zn(II).[56] Additionally, there are thiophilic metals with such diversity of binding geometries that preorganization and predisposition cannot be applied, as a strict binding geometry is not enforced. This is observed for Cd(II).[3-4] When one considers metal binding to these sites, we must consider both the geometric preferences of the metal and the energetics of the protein necessary to generate the necessary environment.

The first metal considered by the Pecoraro group was divalent mercury, which binds to Cys_3^a in a 1:1 ratio under stoichiometric conditions. With higher concentrations of mercury, the more common linear two-coordinate mercury is observed.[37] Structural analysis of this site found that the mercury is bound in a trigonal plane (Figure 1-10).[56] This site is predisposed for Hg(II) binding, meaning it requires significant rearrangement of the Cys side chains from the apo form

to accommodate the mercury ion. In the apo structure, the cysteine residues are oriented with the sulfur atoms pointed directly towards the helical core with a S-S distance of 3.3 Å (Figure 1-11). In the Hg(II) structure, however, a top down view highlights the drastic rearrangement necessary for mercury binding (Figure 1-12). The S-S distance is increased to 4.1 Å with a S-Hg distance of 2.9 Å.

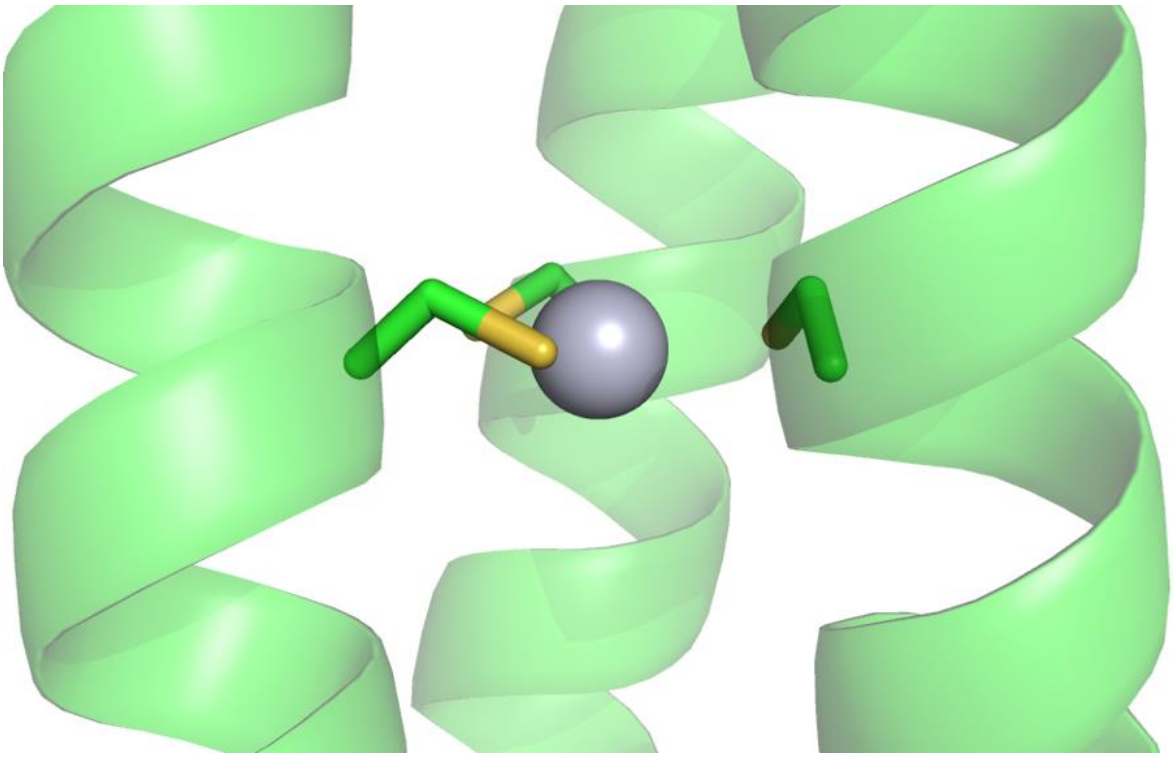

Figure 1-10 Side view of Hg(II) (grey sphere) bound to a Cys_3^a site (PDB 5KB1) with Hg-S distances of 2.9 Å and S-S distances of 5.1 Å.

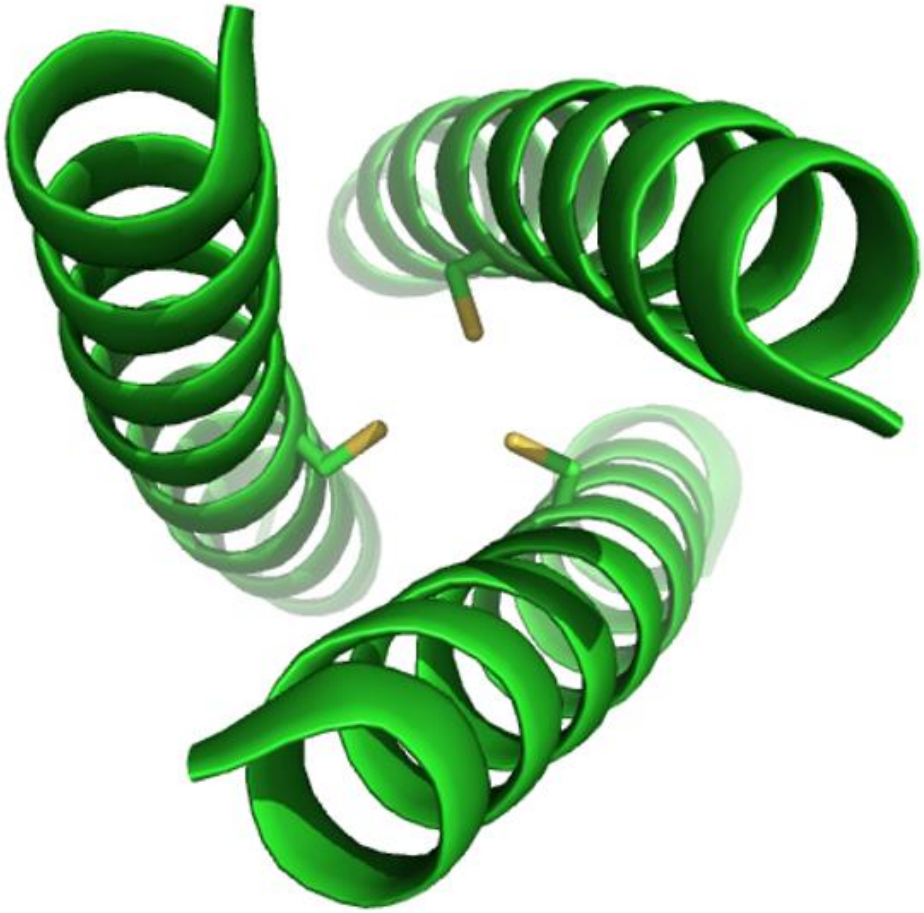

Figure 1-11 Top down view of an apo Cys_3^a site (PDB 5K92).

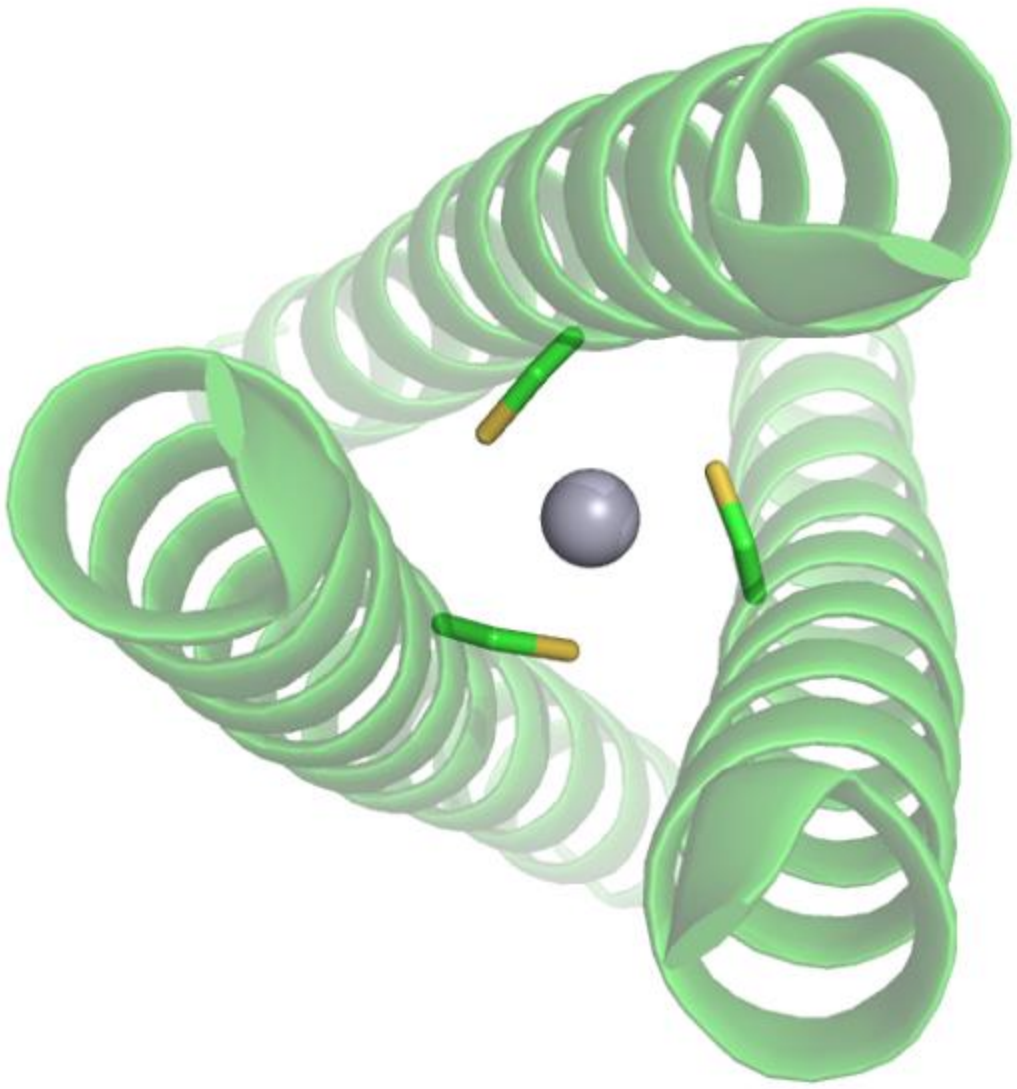

Figure 1-12 Top down view of Hg(II) (grey sphere) bound to Cys_3^a (PDB 5KB1) with Hg-S distances of 2.9 Å and S-S distances of 5.1 Å.

Given the size of this ion, one can imagine that a larger binding site may aid in metal binding. In addition to the Cys^a site, one must also consider the Cys^d site (TRI L12C). While both **a** and **d** sites are interior positions, they are not equivalent. Two residues separate an **a** residue from the next **d** residue and three residues separate a **d** residue from the following **a** residue. This uneven spacing results in a different sidechain angle relative to the center of the coiled coil (Figure 1-6). The apo structure of Cys_3^d is not symmetric as with Cys_3^a (Figure 1-13). In this structure there are S-S distances of 4.6 Å, 4.6 Å, and 3.4 Å. Studies of Hg(II) binding to this site found that, while a 3SCC is formed, there is no evidence for trigonal Hg(II)-S_3. Even

with 1:1 ratio of Hg(II) to trimer, only a linear Hg(II)-S_2 species was observed.[36] Thus, in the case of Hg(II) binding, the Cys^d site is unorganized for the formation of trigonal mercury. These studies highlight the differences in **a** and **d** sites, proving that, though they are both interior, they are not equivalent. These differences will be exploited throughout this work and are described in more detail below as it relates to Pb(II) binding.

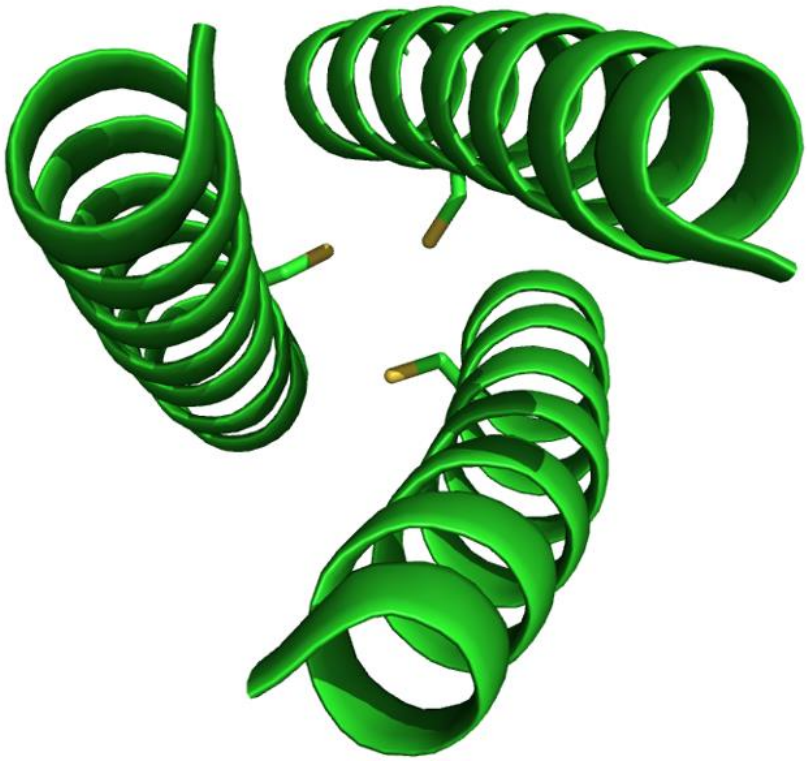

Figure 1-13 Apo Cys_3^d structure (Unpublished)

An alternate way to generate a larger Hg(II) binding site was then explored using the Cys^a site. The substitution of a bulky leucine hydrophobe layer with a layer of alanine residues generates a larger cavity in the core of the 3SCC. The peptide TRI L12AL16C (Ala^dCys^a) was utilized for this purpose (N.B. In this work, peptides with multiple leucine substitutions are abbreviated by listing the substitutions in order from the N- to the C- terminus). This peptide replaces the native leucines directly above (N-terminal to) the Cys^a with alanine residues. As with Cys_3^a, Hg(II) bound in a trigonal planar geometry but with the additional space generated by the alanine substation filled by solvent (Figure 1-14). As seen from a top down view (Figure 1-15), a single water molecule at the center of the helical core is able to hydrogen bond to the

Cys residues at a distance of 3.56 Å but is too far to directly coordinate with the Hg(II) at 2.8 Å (Figure 1-15). This highlights an important characteristic for the formation of the heterotrimer,

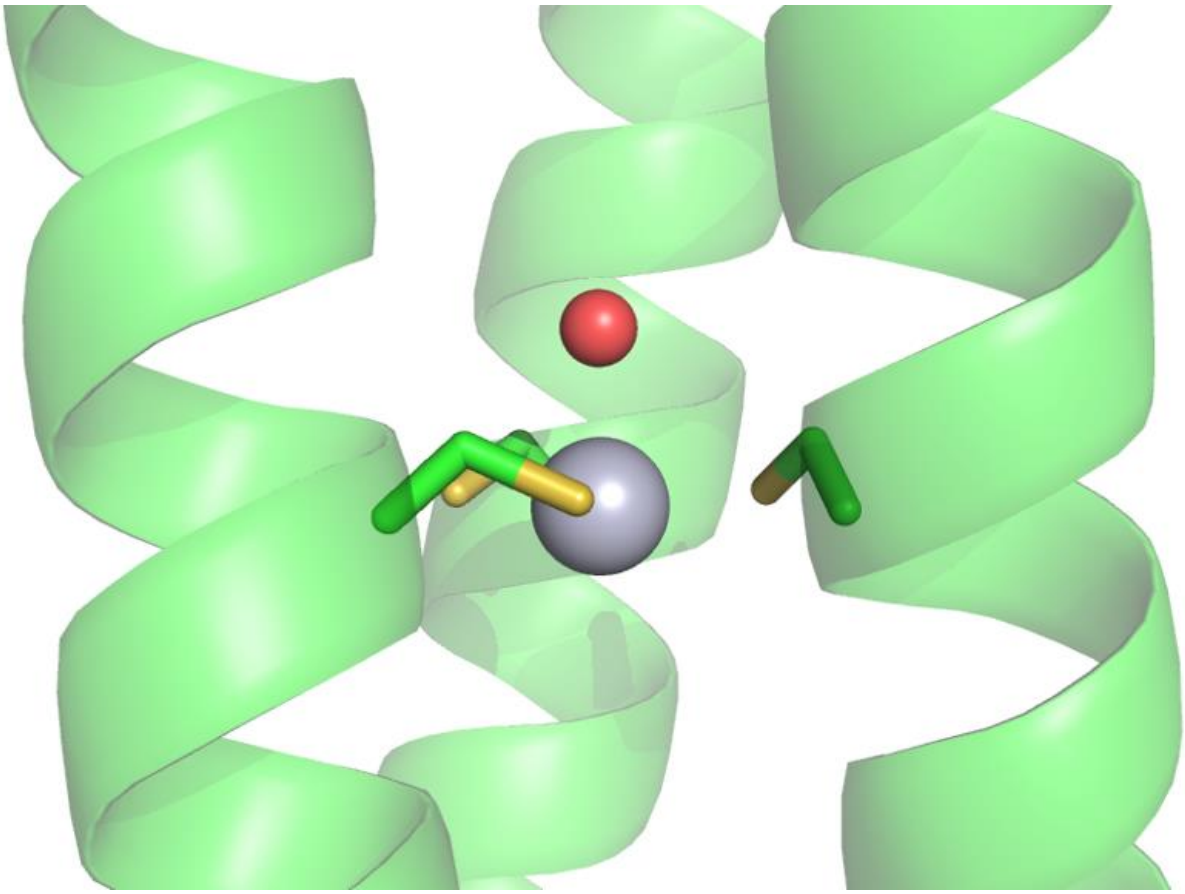

Figure 1-14 Side view of Hg(II) bound to $Ala_3^dCys_3^a$ with a coordinated solvent molecule at 2.8 Å shown in red (PDB 6EGO)

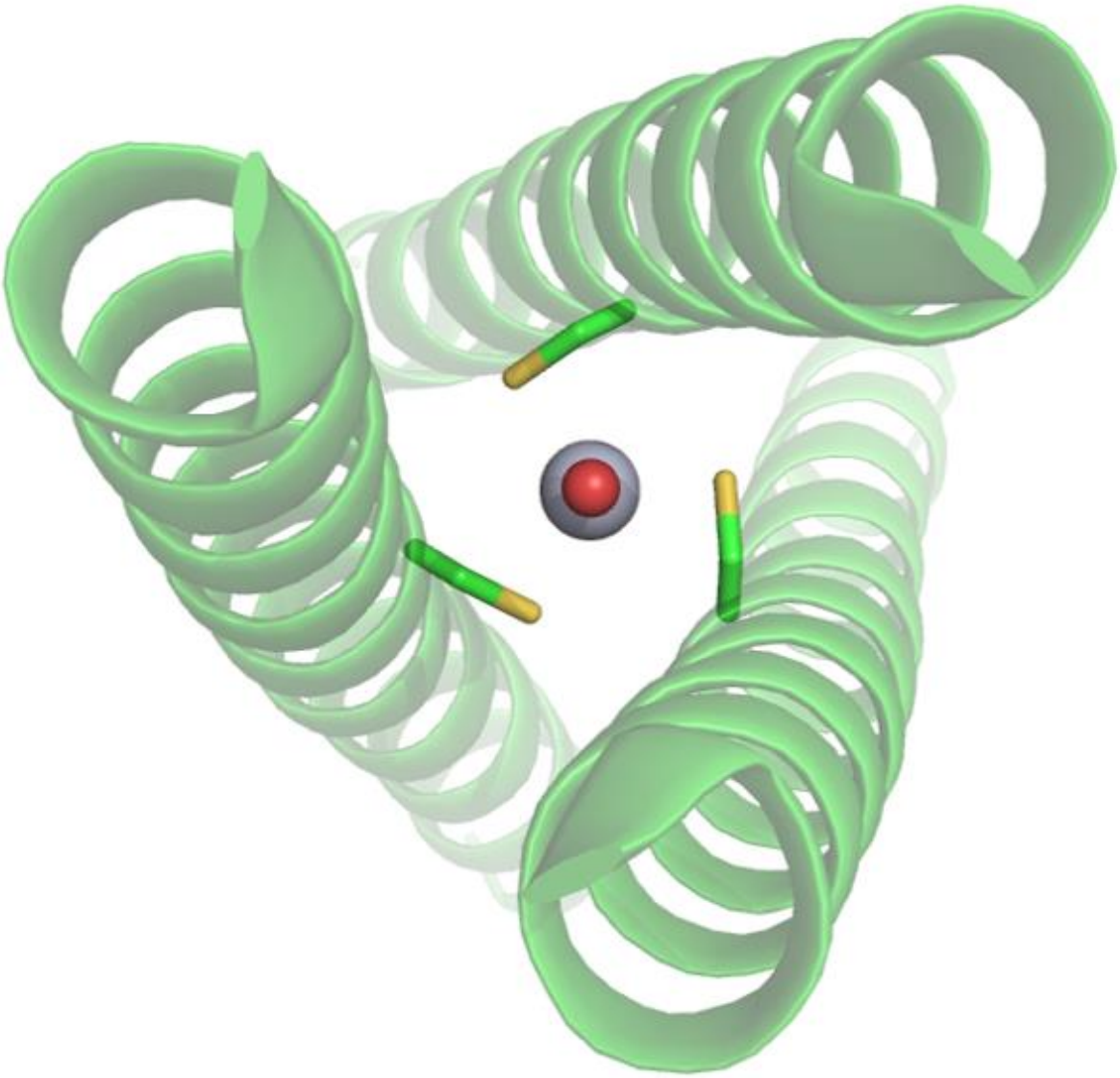

Figure 1-15 Top down view of Hg(II) bound to $Ala_3^dCys_3^a$ with coordinated water at 2.8 Å shown in red

In the same Cys^a site, Cd(II) binds quite differently. Cd(II) is more promiscuous in its binding geometry. Extensive spectroscopic and crystallographic characterization of this site have found that cadmium can bind in three, four, or five coordinate structures. $Cd(II)Cys_3^a$ contains both Cd-S_3 and Cd-S_3O species.[3-4] To selectively form the three coordinate species, additional steric constraints were required to exclude water. By substituting Cys with penicillamine, a non-natural amino acid in which the hydrogens of Cys-Cβ are replaced with methyl groups, water was excluded from the helical core.[35] Alternatively, the four coordinate species could be formed selectively with the same Ala^dCys^a peptide that allowed for solvent access with Hg(II). Unlike with Hg(II), however, the water was directly coordinated to the Cd(II), resulting in

pseudotetrahedral geometry. Increasing the space around this site further increased the Cd(II) coordination number. Space below (C-terminal to) the Cys^a layer was generated by substituting the L-leucine, whose sidechain is angled towards the N-terminus, with D-leucine, whose side chain is angled towards the C-terminus, away from the cysteine site.[3] Here, a five-coordinated trigonal bipyramid is observed. Thus, studies with Cd(II) and Hg(II) have demonstrated that decreased steric restraints adjacent to the Cys^a site allows for solvent access, but that the way solvent interacts is dependent upon the bound metal.

Now let us consider a metal that is preorganized to bind in the Cys^a site, Pb(II). The same 1:1 metal/trimer stoichiometry is achieved as with Hg(II) and Cd(II), but with a different binding geometry; Pb(II) binds in a trigonal pyramid(Figure 1-16). The three coordinate species of both mercury and cadmium are trigonal planes, with the metal ion bisected by the sulfur plane. In a trigonal pyramid, however, the center of the metal ion is not in line with the sulfur plane. When the center of the metal ion is on the same side of the sulfur plane as the Cys-Cβ, it is bound in the endo conformation. Conversely, when the metal and beta-carbon are on opposite sides of the sulfur plane the metal is bound in the exo conformation. More commonly, Pb(II) binds in the exo configuration, but Pb(II) is bound in the endo conformation to Cys_3^a. In the endo configuration, the lone pair electrons of Pb(II) are oriented above (N-terminal to) the Cys_3^a site. The space occupied by this lone pair is the same space that allows for $Cd(II)S_3O$ coordination, precluding water coordination to lead in this environment. Even the replacement of Pb(II) with As(III), a much smaller ion with trigonal pyramidal coordination, does not allow room for solvent access within the core of the 3SCC.[56] Crystallographic analysis by Dr. Leela Ruckthong showed that, unlike Hg(II), the Cys^a site is preorganized for lead binding, meaning no significant rearrangement of the Cys side chains is necessary for the metal to bind. This is more noticeable from a top-down view (Figure 1-17). The S-S distance of 3.4 Å found in the apo structure (Figure 1-11) is maintained at 3.4 Å with a Pb(II)-S distance of 2.5 Å. Thus Pb(II) is preorganized to bind to Cys^a sites in a well-controlled $Pb\text{-}S_3$ environment. These key differences in Cys^a metal binding geometry and solvent accessibility between Hg(II), Cd(II), and Pb(II) prove to be vital to heterotrimer formation.

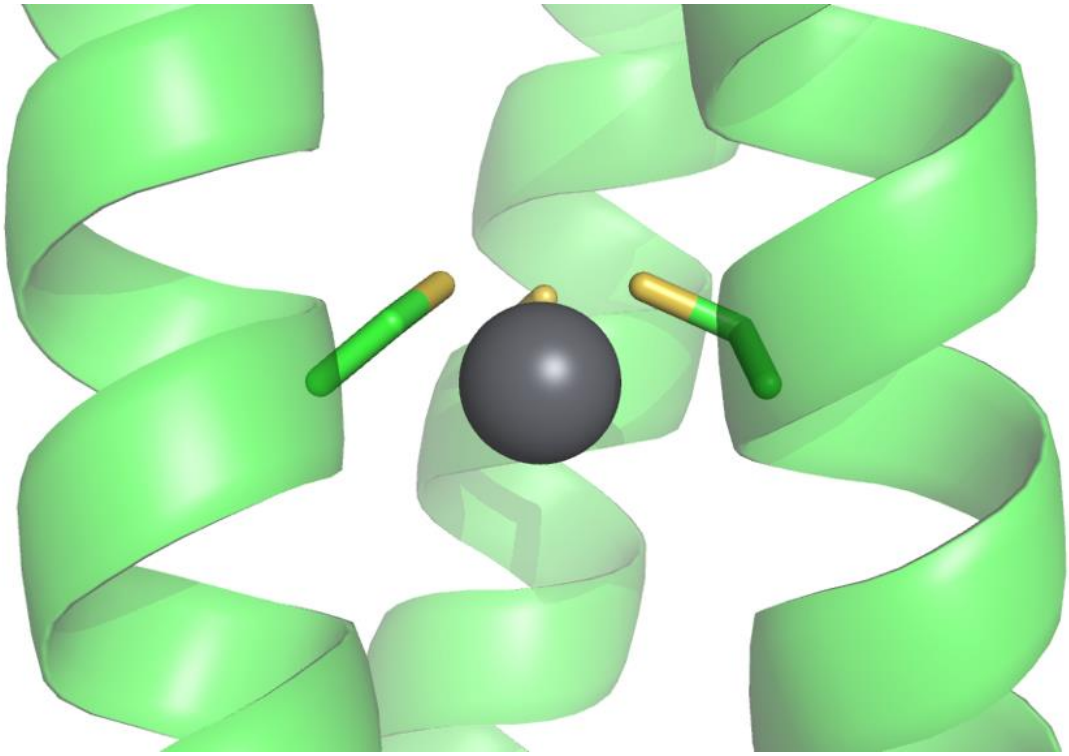

Figure 1-16 Side view of Pb(II) bound to Cys_3^a. The endo configuration is clearly seen with the Pb(II) and Cys-Cβ on the same side of the sulfur plane (PDB 5KB0)

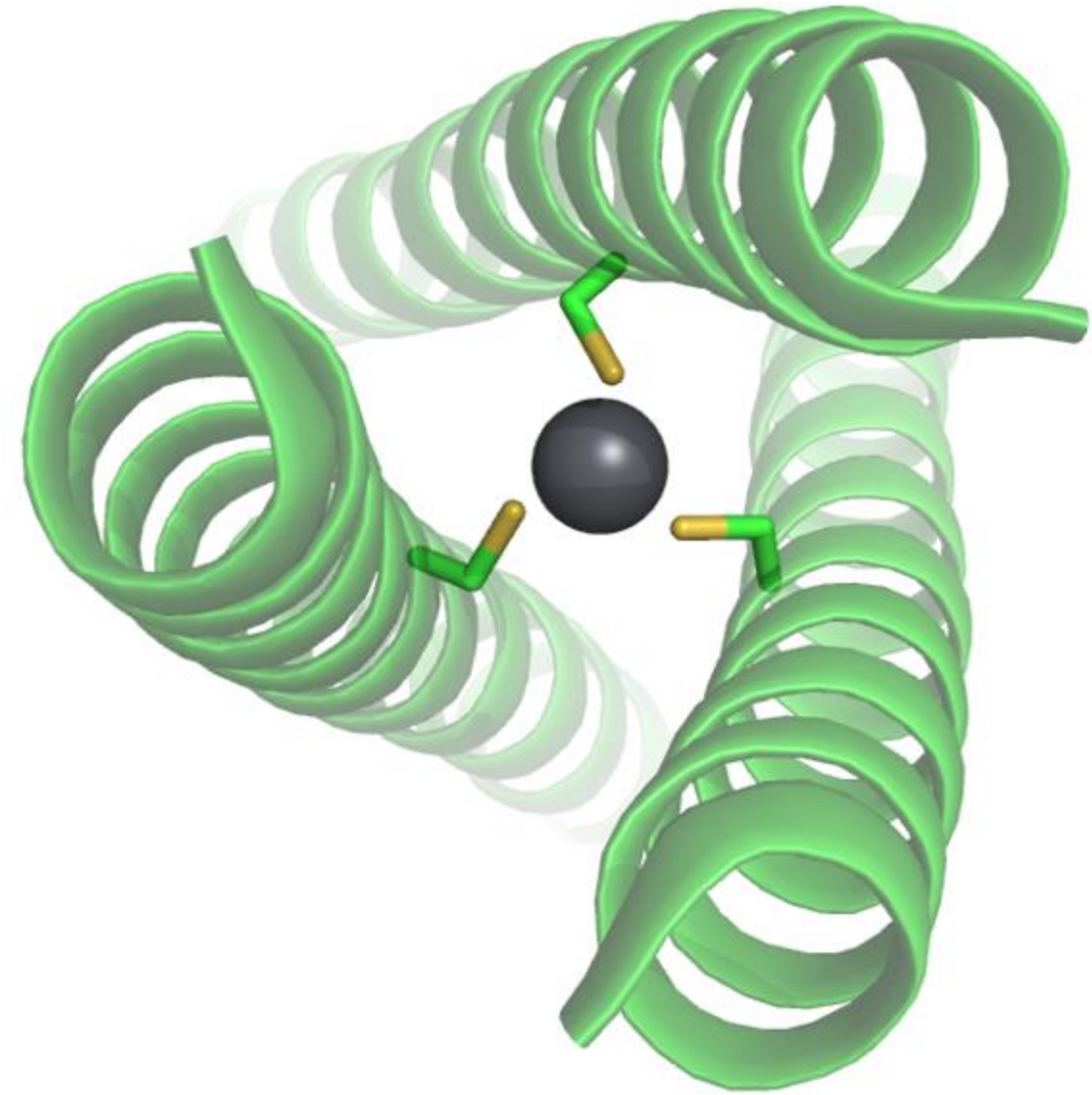

Figure 1-17 Top down view of Pb(II) bound Cys_3^a (PDB 5KB0)

Pb(II) also binds differently than Hg(II) and Cd(II) to in the Ala^dCys^a peptide. Prior to obtaining this crystal structure, it was hypothesized that the reduced steric bulk above the Cys_3^a site would allow for lead to re-orient to bind in the exo conformation. This hypothesis was justified because generating more space opposite the sulfur plane to the Cys-Cβ should decrease the energetic barrier for Pb(II) to bind in the exo conformation. Instead, the Pb(II) remains in the endo conformation and the area of reduced steric bulk allows for solvent access (Figure 1-18). This is consistent with what was found for Hg(II) and Cd(II), but again the orientation is different. Instead of a single solvent molecule in the center of the coiled-coil as is seen with Hg(II) and Cd(II), three water molecules are able to hydrogen bond to the Cys-S. Unlike with

Cd(II), Pb(II) is unlikely to increase in coordination number to allow for direct coordination to the metal ion. The lone pair electrons also prevent water coordination at the core of the 3SCC. The water molecules are instead located close to the interface between two helices and are hydrogen bonding distance to the sulfur atoms of both strands, at 3.0 and 3.4 Å (Figure 1-19). This hydrogen bonding network generated by the reduced steric bulk of the Leu to Ala mutation is thought to mitigate the loss of stability from the removal of a layer of hydrophobes. In the absence of Pb(II), a loss of stability of ~ 5 kJ/mol is seen in the GR peptide.[61] Analyses of sulfur hydrogen bond strength in proteins have shown that each hydrogen bonding interaction can have a bond energy of up to 30 kJ/mol depending on the angle of interaction and the hydrogen environment.[62] While it is difficult to say the exact energy of this hydrogen bond, it is possible for the $Ala^{d}Cys^{a}$ structure to be just as stable, or more stable than, the Cys^{a} structure in the presence of Pb(II).

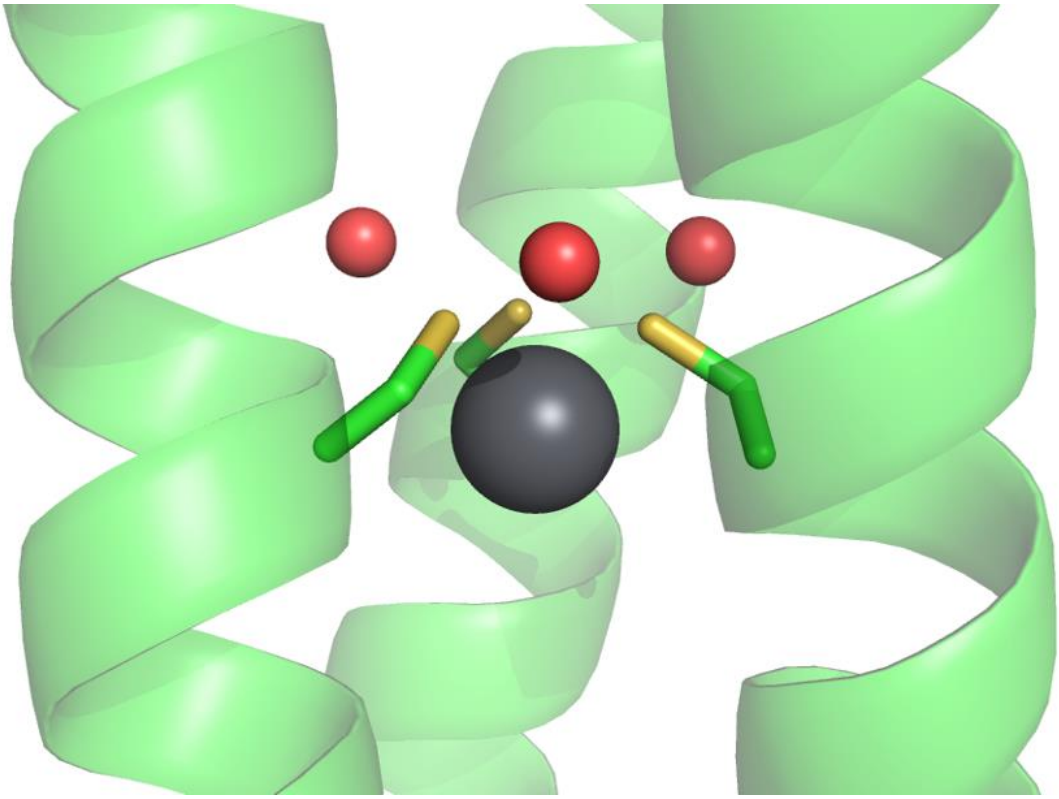

Figure 1-18 Side view of Pb(II) bound $Ala_3{}^{d}Cys_3{}^{a}$ with coordinated water molecules in red (PDB 6EGF)

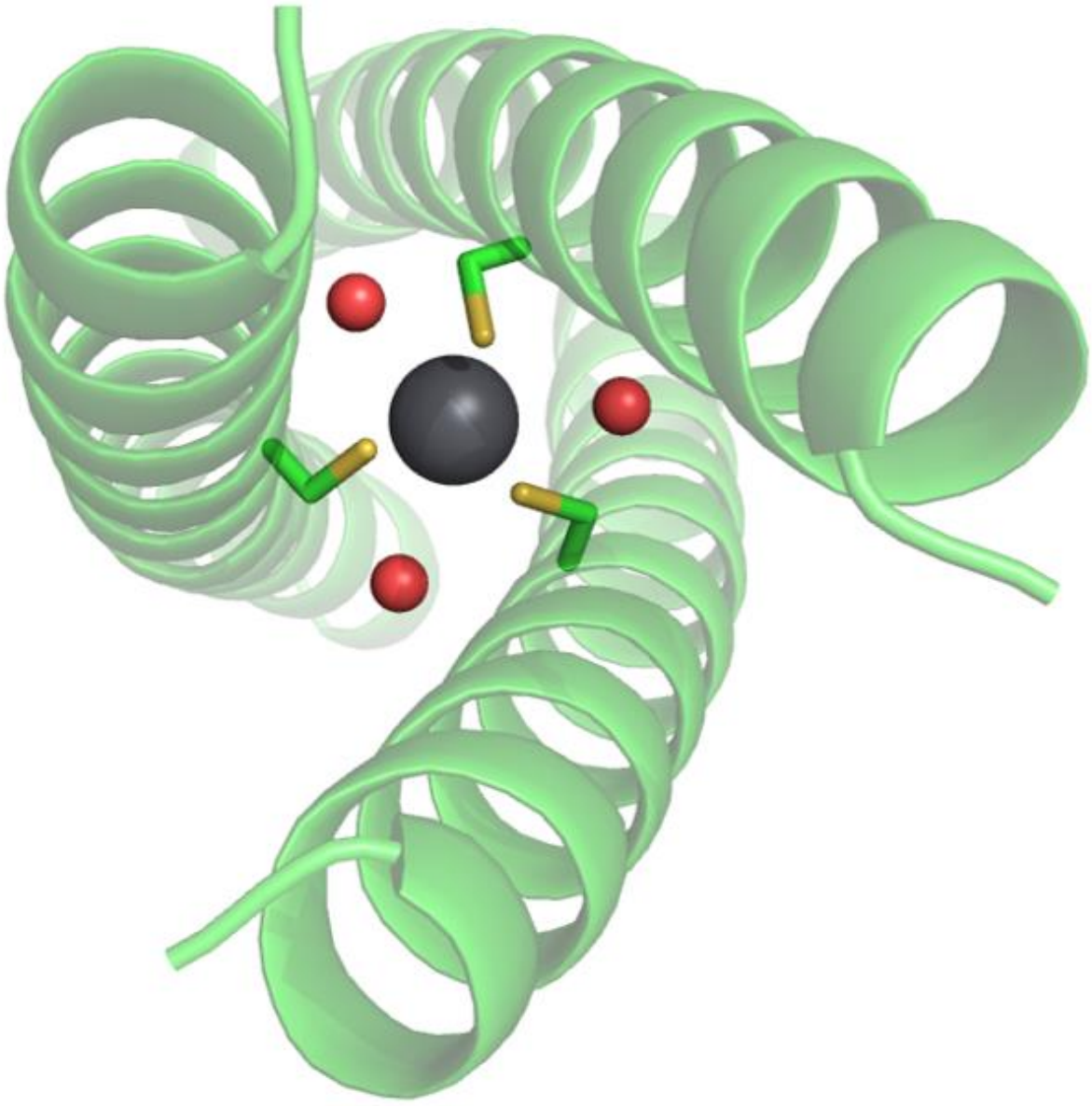

Figure 1-19 Top down view of Pb(II) bound $Ala_3^dCys_3^a$ (PDB 6EGF)

Pb(II) also behaves differently in Cys^d than Hg(II) does. Pb(II) still binds in a 1:1 ratio with a 2.6 Å Pb(II)-S distance, as in the Cys^a site. The difference in apo structure of Cys_3^a and Cys_3^d, however, means the **d** layer is predisposed, but not preorganized, for Pb(II) binding. The sulfurs have to reorient such that S-S distances are 2.6 Å, 3.3 Å, and 3.6 Å, rather than the preorganized distance of 3.4 Å in Cys^a (Figure 1-20 and Figure 1-21). The endo configuration is, however, maintained despite the larger apo binding site. Because the angle of the **d** site Cys is different than the **a** site Cys, the Pb(II) is located above (N-terminal to) the sulfur plane, as are

the Cys beta carbon atoms. Pb(II) remains trigonal pyramidal despite these changes, which was not observed for Hg(II).

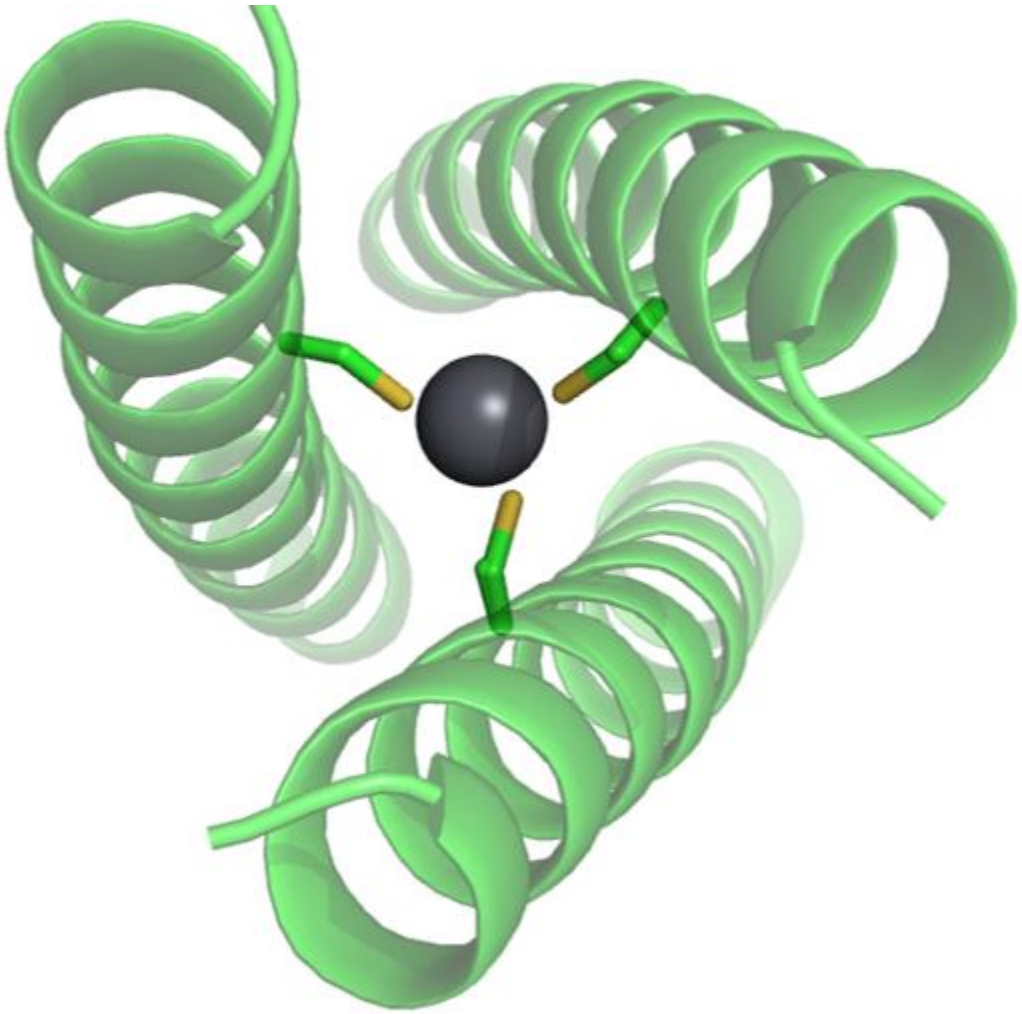

Figure 1-20 Top down view of Pb(II) bound Cys_3^d (Unpublished structure of CS L12C)

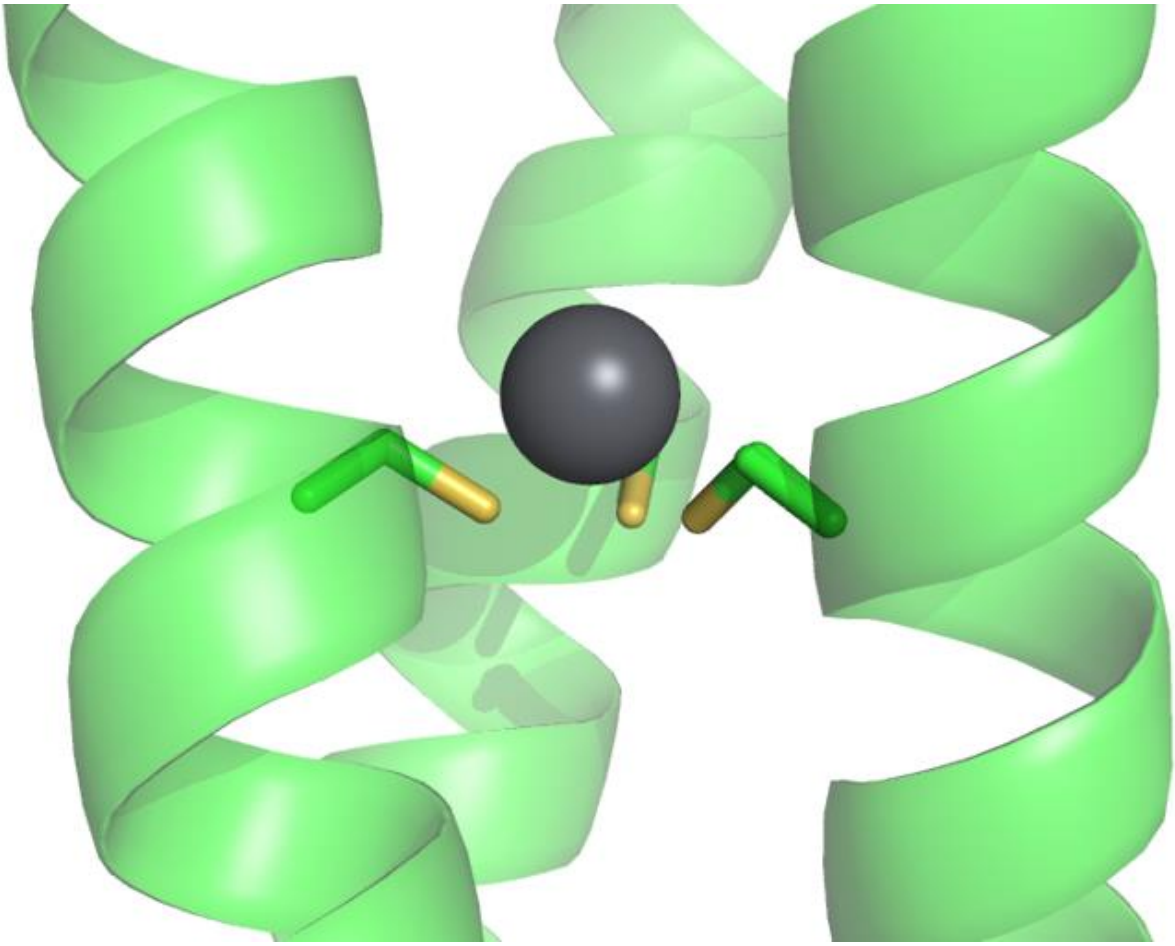

Figure 1-21 Side view of Pb(II) bound to Cys_3^d (unpublished structure of CS L12C)

These differences in protein structure of **a** and **d** layers result in a different Pb(II) affinity to the Cys_3^d and to the Cys_3^a site. ^{207}Pb NMR analysis was used to determine the relative affinity of Pb(II) for Cys_3^a and Cys_3^d. The lead nucleus is extremely sensitive, with a chemical shift range of ~16000 ppm. Dr. Kosh Neupane determined the chemical shift range of Pb(II)-S_3 species within this range and found that Pb(II) bound to **d** site Cys residues have a chemical shift that is several hundred ppm downfield of Pb(II) bound to **a** site Cys residues.[54, 63] It was found by both ^{207}Pb NMR and NOESY experiments that Pb(II) binds tighter to Cys_3^d than to Cys_3^a. Dr. Debbie Touw performed these experiments with a peptide containing both a Cys_3^a site (L9C) and a Cys_3^d site (L19C) and increasing amount of Pb(II) (Figure 1-22). With 0.25 equivalents of Pb(II) per Cys_3, Pb(II)Cys_3^d begins to form and is fully formed at 0.75 equivalents of Pb(II). Pb(II) bound Cys_3^a, however, does not begin to form until 0.5 equivalents of Pb(II) and requires a full equivalent of Pb(II) to be fully formed.[64] As both species are partially formed with intermediate amounts of Pb(II), there is competition between these sites for the metal ion, but the

formation of Pb(II)Cys_3^d occurs with sub-stoichiometric amounts of Pb(II) indicating tighter binding. Additionally, Pb(II) binds tighter to $Ala_3^dCys_3^a$ than to Cys_3^a as determined by Dr. Giuseppe Zampella. Dr. Zampella titrated Pb(II) into a solution containing equivalent amounts of Cys_3^a (CS L9C) and $Ala_3^dCys_3^a$ (TRI L12AL16C) and observed a major peak corresponding to $Ala_3^dCys_3^a$ with 0.5 equivalents of Pb(II) per Cys_3 site.[58] The differences in Cys^d and Cys^a structure and Pb(II) affinity are explored in Chapter 2 as it relates to heterotrimer formation.

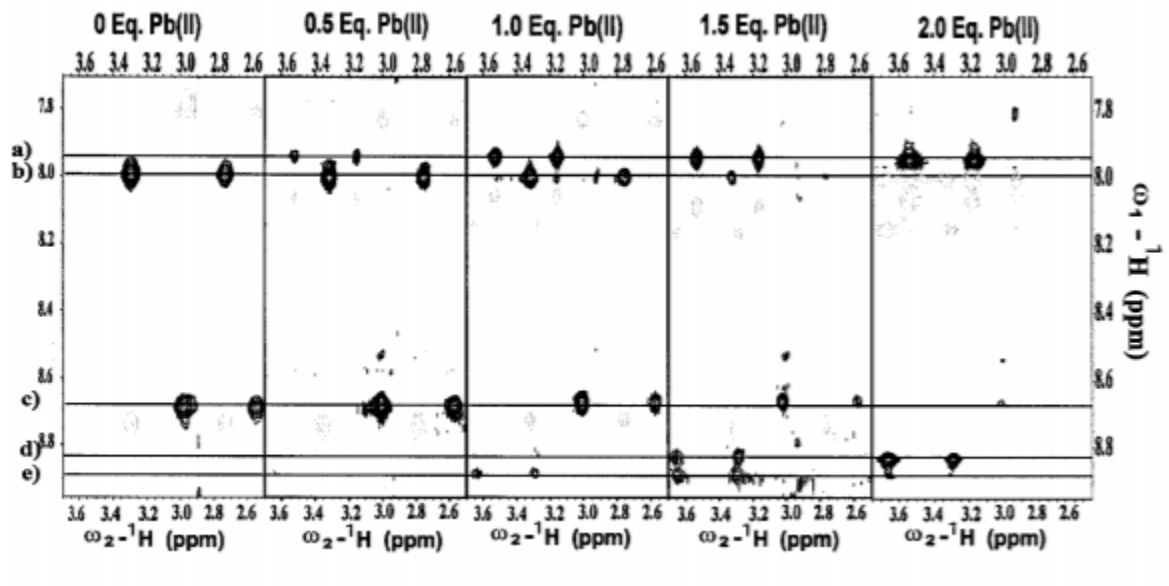

Figure 1-22 2D NMR of Pb(II) binding to Cys_3^a and Cys_3^d sites. Peaks on line (a) correspond to Pb(II)Cys_3^d, (b) apo Cys_3^d, (c) apo Cys_3^a, and (d) and (e) Pb(II)Cys_3^a.[64]

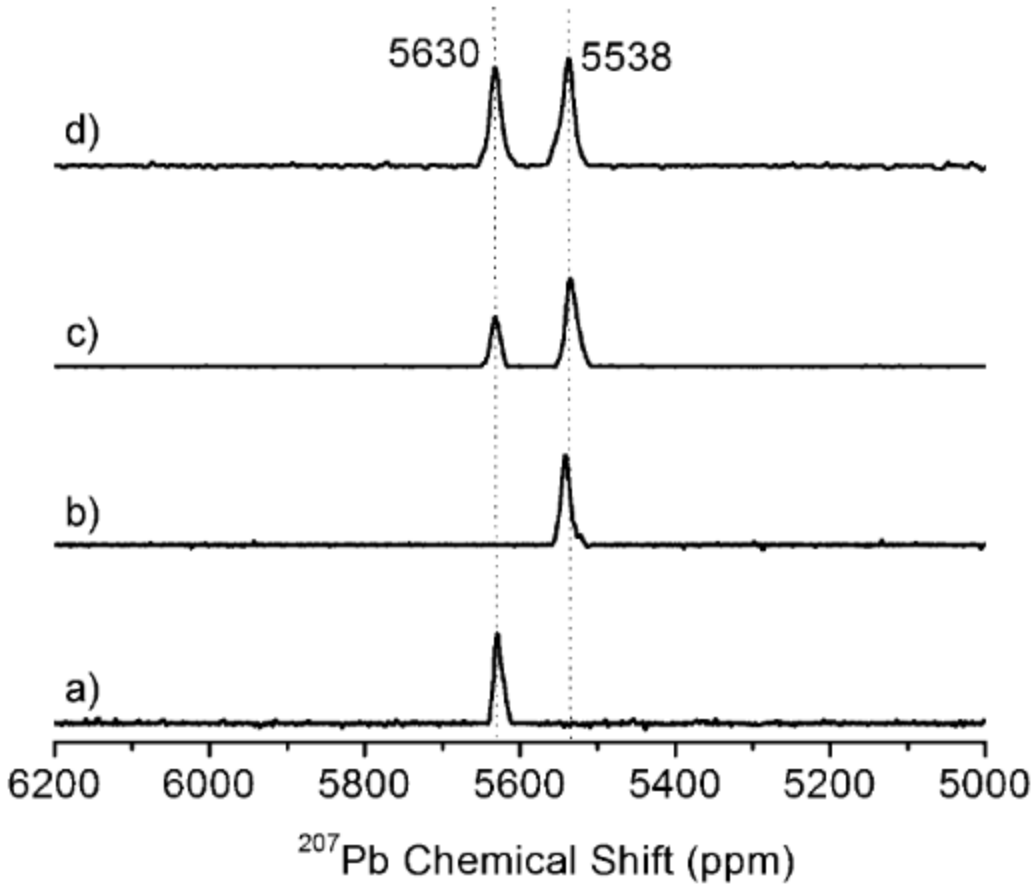

Figure 1-23 ^{207}Pb NMR of (a) Cys_3^a with 1 equivalent of Pb(II) per binding site, (b) $Ala_3^dCys_3^a$ with 1 equivalent of Pb(II), (c) Cys_3^a and $Ala_3^dCys_3^a$ with 0.5 equivalents of Pb(II) and (d) Cys_3^a and $Ala_3^dCys_3^a$ with 1 equivalent of Pb(II).[58]

TRI scaffold metallocatalysts

To understand where the field of protein design and catalysis must go, one must first understand where it is currently. The Pecoraro lab has made *de novo* constructs capable of binding copper and zinc for catalysis as well as cobalt as a spectroscopic probe. Of greatest interest to this work is the Zn CA work done by Dr. Melissa Zastrow. In addition to an a site Cys_3 for Hg(II) binding, she introduced an a site His_3 for transition metal binding, generating the peptide TRI L9CL23H (Figure 1-24). The Hg(II)Cys_3^a and Zn(II)His_3^a were not found to interact with one another and to bind specifically to the desired site. This alone was a significant feat in protein design. Previously, we had been able to incorporate multiple binding sites for the same metal within a single scaffold,[42, 47, 65] but this design allowed for two different metals to bind to unique sites within the same scaffold. The Hg(II) site was used to maintain stability of the trimer even with the inclusion of the bulky histidine residues and does not possess catalytic activity.

The Zn(II) site was used to investigate transition metal catalysis. Thus, one can have both a heavy metal and a transition metal selectively bound to the same scaffold.

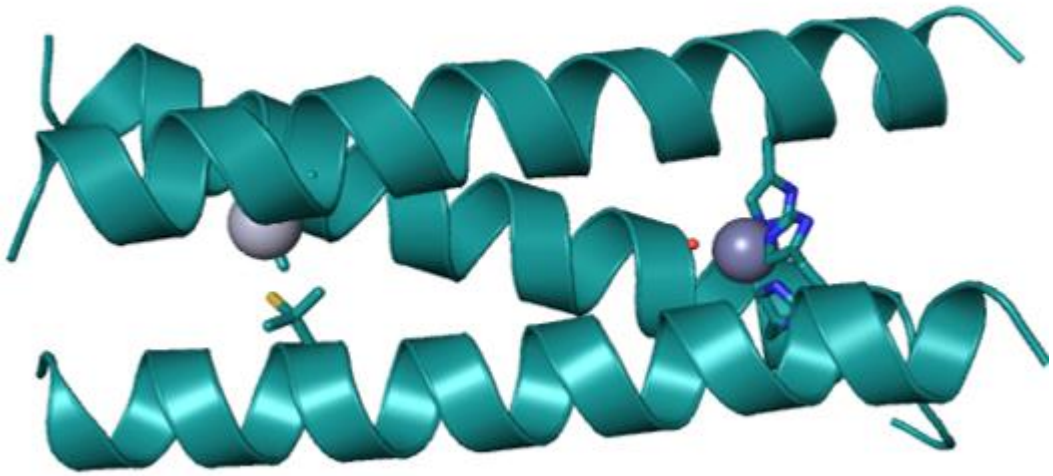

Figure 1-24 Dual metal peptide with Hg(II) bound to a tris-thiolate site and Zn(II) bound to a tris-histidine site (PDB 3PBJ)

X-ray crystallography showed that Zn(II) binds to the His_3 site as a pseudotetrahedron with a coordinated exogenous solvent molecule. This model is very similar to the first coordination sphere of CAII (Figure 1-25). The only notable difference between these two Zn environments is the particular nitrogen of the His residue that is coordinating the metal. In the native enzyme, one delta and two epsilon nitrogen are coordinated. In this *de novo* system, however, the crystal structure was three-fold symmetric with only epsilon nitrogen coordination. Epsilon vs delta nitrogen coordination can be controlled via non-natural methyl-histidine residues. The Pecoraro group has successfully done as much for copper catalyzed nitrite reductase activity.[9] But, as outlined previously, this level of asymmetry is not considered in the present work. It does present an interesting avenue for future research.

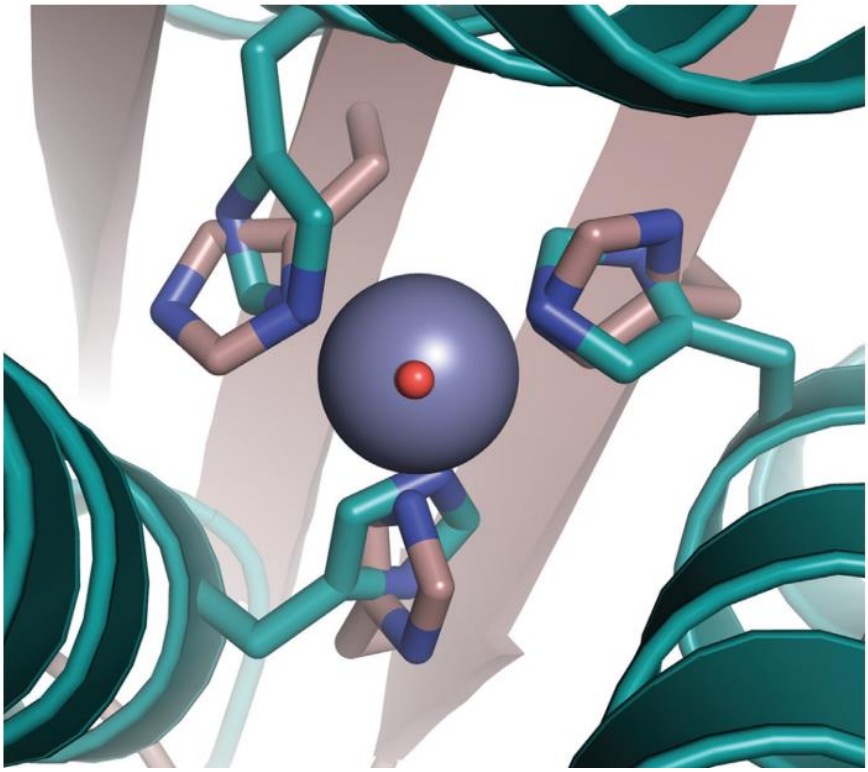

Figure 1-25 Overlay of CAII in tan (PDB 2CBA) and Dr. Zastrow's TRI model (PDB 3PBJ) in green. Note the different nitrogen coordination in the upper left.[66]

Kinetic analysis of this system was performed on both the native CO_2 hydration assay as well as a facile colorimetric ester hydrolysis assay, a secondary function of the native enzyme. This system was found to be the most efficient model of CAII and was optimized for aqueous media, unlike most small molecule CA models. At pH 9.5, where the reaction was most efficient, Dr. Zastrow's model has a k_{cat}/K_M of 23.3±0.3 $M^{-1}s^{-1}$ while the native enzyme has a k_{cat}/K_M of 2320 $M^{-1}s^{-1}$ at pH 9.0. A difference of two orders of magnitude leaves a lot of room for improvement. More notably, CO_2 hydration at pH 9.5 has a catalytic efficiency of $1.8\pm0.3x10^5$ $M^{-1}s^{-1}$ and is only ~400 fold slower than the native enzyme.[66-67] The pK_a of this active site is 8.8, which is 2 pH units more basic than the native enzyme. The kinetics of this His_3 motif were also dependent upon its location within the trimer. It was found that moving the His_3 site to different **a** positions within the trimer affected k_{cat} or K_M, but maintained the overall catalytic efficiency described above.[67] The ability to move this site within the trimer, therefore, is necessary to fine-tune different kinetic parameters. This work explores the ability to shift the heterotrimer nucleation site to a different heptad to allow for shifting of the histidine site.

The great success of this system, as well as the wealth of knowledge regarding the native enzyme, provides a clear path for improvement. As described above, the mutation of a second coordination sphere Thr residue in the native enzyme to a non-hydrogen bonding Ala residue increased the pK_a of the active site by about 2 pH units and decreased the efficiency by a factor of ~100. We hypothesize that an asymmetric scaffold capable of providing a similar second coordination sphere ill result in a more acidic pK_a and an increased efficiency of this enzyme, particularly at lower pH values.

It is essential that this hydrogen bonding residue remains in the second coordination sphere rather than the primary coordination sphere. Studies with native CA in which this Thr residue was mutated to Asp, Glu, or Cys resulted in displacement of the solvent molecule and direct amino acid coordination to the Zn(II).[68-70] A more detailed discussion of these sites follows in chapter 4, where Zn(II) catalysis is discussed. Creating such an asymmetric outer coordination sphere is one of the main motivations for this thesis work.

In addition to Zn(II) hydrolytic chemistry, the Pecoraro group has made significant advancements in the field of copper redox chemistry through studies of copper nitrite reductase (NiR). NiR catalyzes the conversion of NO_2^- to NO and water via a copper catalyzed redox reaction.[71] The active site contains both a Type 1 copper center for electron transfer and a Type two copper center for catalysis (Figure 1-26).[72-73] The Type 2 center coordinates Cu(I/II) with three histidine residues, an ideal system to model in a 3SCC.

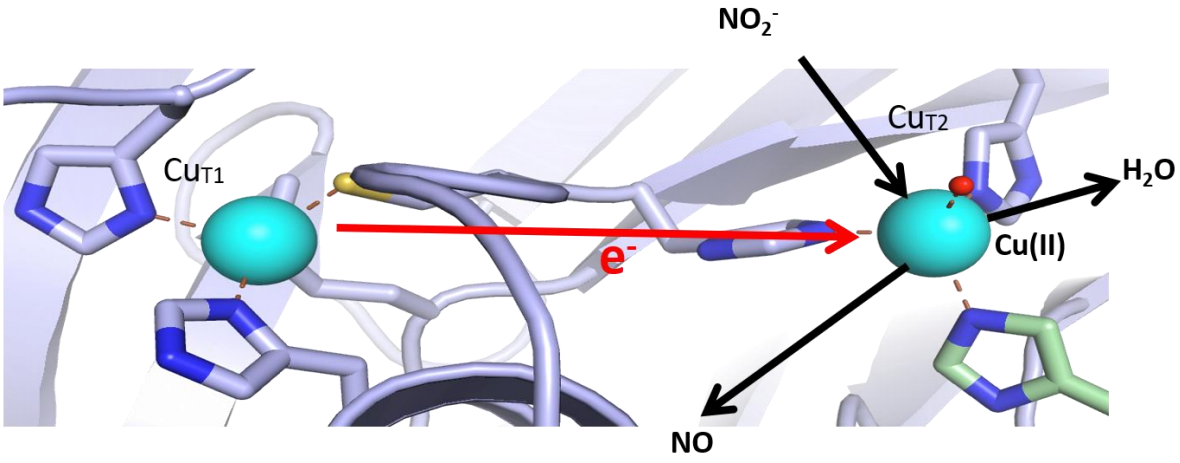

Figure 1-26 Active site of CuNiR with both the Type 1 electron transfer center and the Type 2 redox center (PDB: 2DY2)

Dr. Fangting Yu began work with this system using the same His_3 scaffold as with Dr. Zastrow's CA work, but lacking the Cys binding site. This binding site was excluded because

Cu(I) has a high affinity for sulfur and, as stability was not significantly decreased in the absence of this site, the possibility for Cu(I) promiscuity was eliminated. What Dr. Yu found was that activity of this site was improved by a factor of 75 via reducing the steric bulk in the **d** layer adjacent to the His_3^a site (Figure 1-27, green). There was a minimal difference in the first order rate if the steric bulk was reduced by substituting an adjacent leucine for an alanine or an aspartate. The aspartate was introduced to model a hydrogen bonding interaction, but instead the three aspartate residues interacted with each other rather than the copper binding site.[74] The most significant effects, however, were observed when the His residues were forced to coordinate with either three delta or three epsilon nitrogens. With methylated epsilon nitrogens, meaning only delta nitrogens can coordinate copper, the rate increased by only 2.3x. The opposite nitrogen coordination resulted in a 300-fold increase in activity. An additional ~2.5 fold increase was found with both reduced steric bulk and delta nitrogen methylation.[9] This work is mentioned to highlight three key points: (i) redox chemistry has been successfully investigated in the TRI scaffold, (ii) the coordinated nitrogen plays a significant role in catalysis, and (iii) three-fold symmetric mutations of charged residues do not accurately model asymmetric hydrogen bonding environments. While Cu NiR activity will not be discussed in this work, copper redox chemistry will be using analogues of Cu-only SOD. Thus, what was learned by studying the CuNiR system is applicable to the copper work described in Chapter 5.

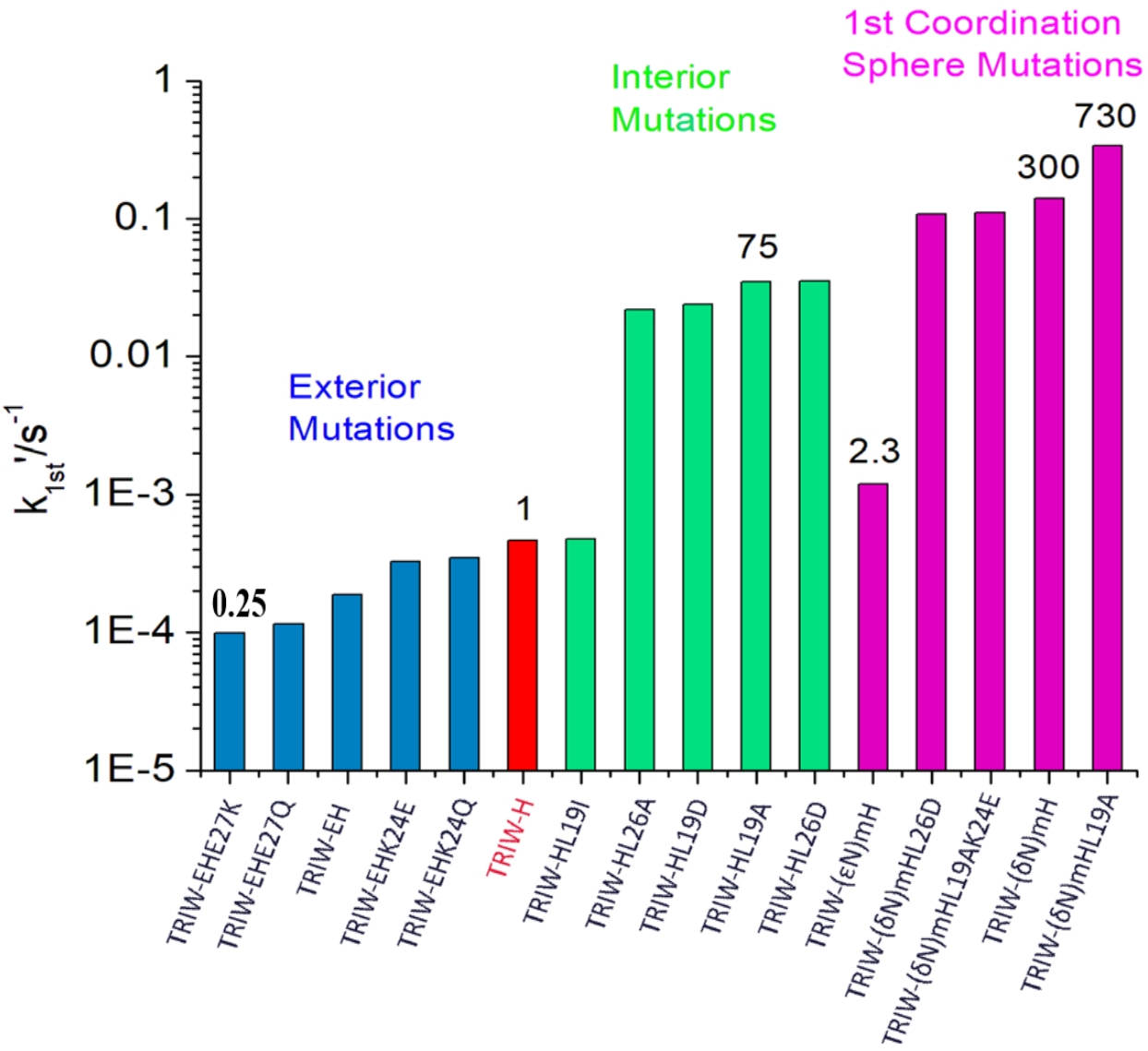

Figure 1-27 First order rates of TRI NiR models with exterior mutations in blue, interior mutations in green, and first coordination sphere mutations in pink. Figure courtesy of Dr. Karl Koebke.

***De novo* asymmetry**

Several groups, including the Pecoraro lab, have previously made asymmetric *de novo* peptide scaffolds to varying degrees of success for the study of metalloenzyme active sites. The most straightforward way to accomplish this is with a single peptide that is able to fold into a helical bundle. Research groups have utilized helical bundles from two stranded to six stranded.[27-28, 30, 32, 75-80] Through a collaboration with the DeGrado group, the Pecoraro group was

able to design a version of the three helix bundle (3HB) protein α_3D that contains metal binding residues.[41] This construct relies on a similar heptad pattern as the TRI family, though the hydrophobe arrangement is less strict. Interior resides include Leu, Ile, and Phe residues instead of all Leu residues. Unlike with self-assembling coiled-coil structures, the hydrophobic residue used and its placement in **a** or **d** positions does not determine the number of strands in the bundle. Instead, three heptad repeat regions are separated by a flexible "loop" region, allowing the peptide chain to bend so the heptad repeat regions can self-associate (Figure 1-28). This manner of folding is inherently asymmetric because one strand is antiparallel to the other two.

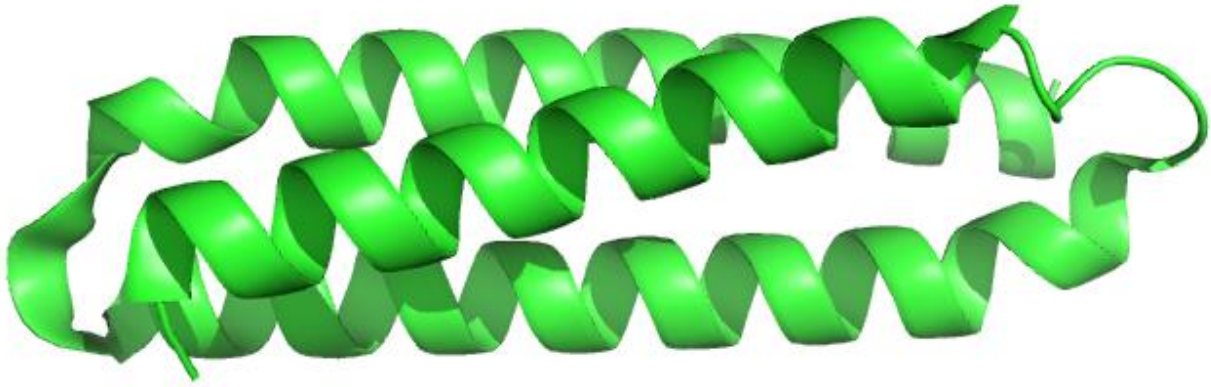

Figure 1-28 Crystal structure of GRα_3D (PDB 6DS9)

The asymmetry of an antiparallel strand is due both to the angle of each interior sidechain and the packing of the core. Unlike in a parallel system, **a** and **d** layers of an antiparallel trimer do not align perfectly. Two residues separate an **a** residue from the following **d** residue, while three residues separate that **d** residue from the following **a** residue. The uneven spacing means that the antiparallel strand must align a **d** residue with **a** residues and an **a** residue with **d** residues to match the hydrophobe spacing of the two parallel strands. Additionally, the angle at which interior residues are oriented within the core of the 3HB is controlled by the orientation of the strand.

As with the TRI system, one can mutate an interior hydrophobic residue to a metal binding residue. This work began with studies of hydrophobe to Cys mutations for the coordination of heavy metals. Solution state NMR structures of this apo peptide showed that no loss of stability was incurred through the inclusion of these residues.[41-42] The benefit of this system is that because this system is self-contained and does not require any supramolecular interactions to fold appropriately, the incorporation of metal binding residues can be done

asymmetrically. This allows for a layer of side chain asymmetry in addition to the inherent antiparallel asymmetry of the system. A previous postdoctoral researcher in the Pecoraro lab, Dr. Virginia Cangelosi, investigated CA in α_3D. With only a His_3 model, Dr. Cangelosi found that this system does not perform as well as TRI L9CL23H. The pK_a of this system is even more basic, at 9.4 and the catalytic efficiency of CO_2 hydration is $3.8\pm0.5x10^4$ $M^{-1}s^{-1}$, an order of magnitude lower than Dr. Zastrow's system.[10] With the ease of incorporating asymmetric amino acid substitutions in this system, Dr. Cangelosi added serine and threonine residues meant to model the interaction of T199. These mutations were incorporated at several different positions in the 3HB, but no placement resulted in increased catalytic efficiency over the His_3 model. Despite these shortcomings, this work does function well as a first generation model for more complicated systems.

Cu NiR activity was also explored in α_3D by Dr. Alison Tebo and Dr. Karl Koebke. Dr. Tebo investigated the same His_3 binding site that Dr. Cangelosi used for CA studies and found that the first order rate increased by a factor of ~6 by shifting the site from TRI to α_3D.[81] Dr. Koebke expanded upon this work by elongating the scaffold from α_3D to GRα_3D and investigating second coordination sphere asymmetry via Asp and His hydrogen bonding residues (Figure 1-29). In the native enzyme, mutations of these residues can result in loss of activity of up to three orders of magnitude.[82] To this end, three constructs were designed, two with an additional Asp residue either axial to the His_3 plane or as an equatorial residue with an axial His and one with four histidine residues.

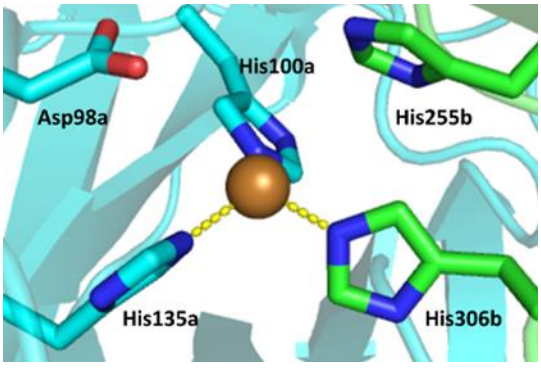

Figure 1-29 Catalytic site of NiR with subunit a in blue and subunit b in green (PDB: 2PPC)

These systems provided an interesting look into what effects asymmetric mutations can have. By increasing the length of the scaffold, activity increased ~3-fold because the increased stability of the overall scaffold led to minor changes in the His_3 environment. The coordination

number of Cu(I) decreased from a mix of 2 and 3 coordinate to mostly 2 coordinate. All of the intended second sphere mutations, however, resulted in decreased activity. The addition of an Asp below the His_3 plane resulted in a 17-fold loss in activity over the His_3 site (Figure 1-30, left). If the Asp residue is placed in the same layer as two His residues with the third His in the axial position the rate increases by an order of magnitude. The repositioning of the His_3 plane likely shifts Cu(I) coordination closer to the helical interface, allowing for better substrate access. The construct with four histidine residues behaved similarly to the model with an axial Asp residue. This system shows that asymmetric incorporation of amino acids in de novo systems does affect activity, though not always in the intended way. The repositioning of the Asp residue also highlights the importance of amino acid positioning on catalysis, an effect that is also observed in the models of Cu-only SOD discussed in Chapter 5.

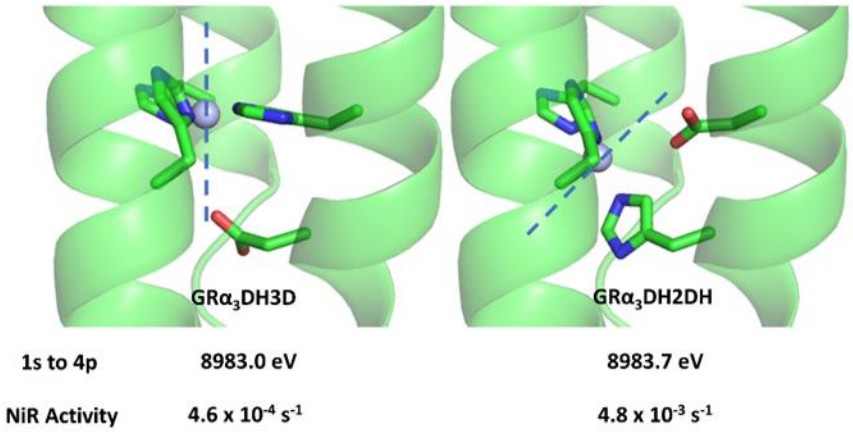

Figure 1-30 Pymol active site models of GRα_3D H3D (left) and GRα_3D H2DH (right) with the Cu(I) z-axis shown as a dashed line (Based on the structure of GRα_3D PDB: 6DS9). Figure courtesy of Dr. Karl Koebke.

Another α_3D model relevant to this work is that of a Cu-only SOD mimic. In collaboration with Dr. Clotilde Policar's group, four different possible ligand environments were investigated in the GRα_3D scaffold. Much of this work was performed by Dr. Emilie Mathieu as part of her doctoral thesis, but Cu affinity values and thermal denaturation experiments were performed by me. As this represents a small fraction of the characterization of this system, this experimental work is not discussed in following chapters. As with Dr. Cangelosi's model, a His_3 system was investigated, annotated H_3, which was meant to model the Cu(I) binding environment of the native enzyme (Figure 1-4). A four His (H_4) model was also characterized as a model of the Cu(II) binding environment. Two additional systems of three histidines and one

aspartate were also studied (Figure 1-31). These serve to study both the effect of a charged residue in the active site as well as to determine if Cu catalysis can occur in a site more similar to the native Fe/Mn SOD than Cu-only SOD. One system, H_3D, maintains the histidine plane of H_3 and has an additional axial aspartate residue. Alternately, H_2DH has a plane of 2 His and 1 Asp residue with an axial His residue, which best models the Fe/Mn active site (Figure 1-32).[83]

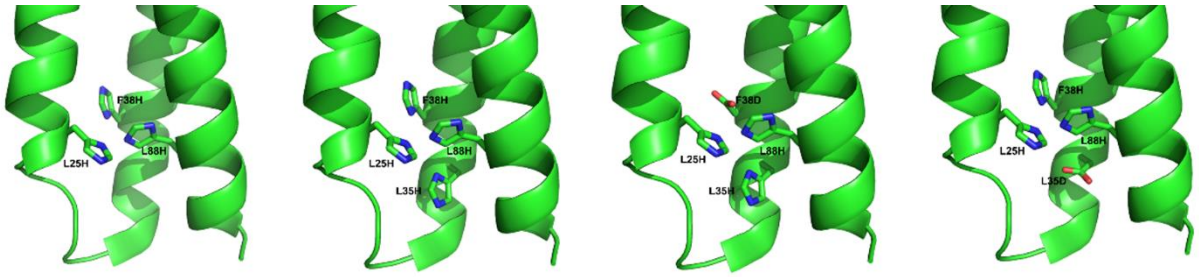

Figure 1-31 Pymol models of H_3, H_4, H_2DH, and H_3D based on the structure of GRα_3D (PDB 6DS9)

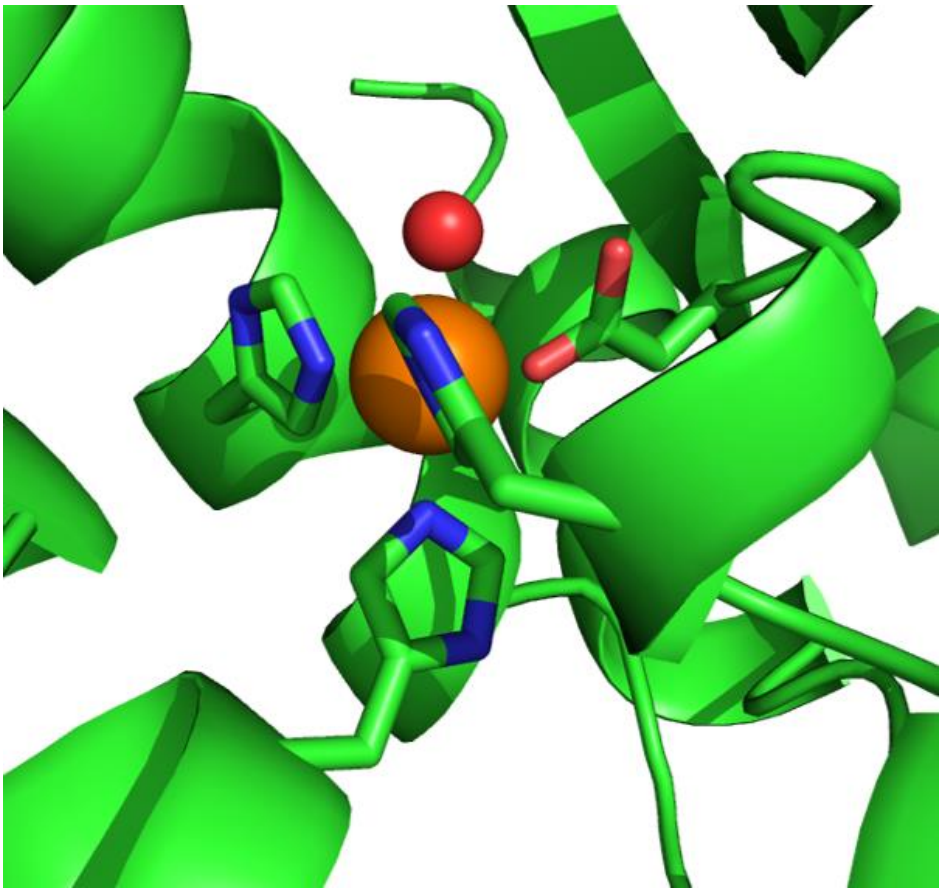

Figure 1-32 Active site of MnSOD with manganese in orange and water in red (PDB: 1VEW)

These metallopeptides were found to be the best models of Cu-only superoxide dismutation as measured by the Fridovich assay. This assay is a competition reaction between

the enzyme and a reporter compound, so all rates are determined only for this system and are reported as k_{McF} values. A more complete description of this assay follows in Chapter 5 where asymmetric 3SCCs are examined for SOD activity. There is no statistical difference between H_3, H_3D, and H_2DH which have k_{McF} values of ~$3x10^6$ $M^{-1}s^{-1}$. Of all spectroscopies performed, there was no notable trend observed in copper affinity, redox potential, or coordination environment for the four constructs (Table 1-2).[84-85] One can hypothesize, however, that based on the results of CA studies, simply putting these sites in GR instead of GRα_3D could result in a significant increase in activity. Thus, a selective, asymmetric, self-assembling, parallel trimer is necessary.

Table 1-2 Apparent standard potentials at pH 7.5, affinity constants and SOD activity of Cu(II)-protein complexes

	$E_{1/2}$ [a] (mV *vs.* NHE)	Cu(II) K_d (10^{-10} M)	Cu(I) K_d (10^{-16} M)	IC_{50} (μM)	k_{McF} (10^6 $M^{-1}s^{-1}$)
GRα_3D H_3	550 ± 10	5.00 ± 0.17	1.22 ± 0.04	2.9 ± 0.6	3.0 ± 0.6
GRα_3D H_4	463 ± 10	5.7 ± 0.3	41 ± 2	8.0 ± 1.7	1.1 ± 0.2
GRα_3D H_2DH	420 ± 10	1.4 ± 0.4	54 ± 15	3.5 ± 1.1	2.6 ± 0.8
GRα_3D H_3D	470 ± 10	1.6 ± 0.2	8.8 ± 1.1	3.3 ± 0.3	2.6 ± 0.2

The other main approach to achieving asymmetry has been through modification of the hydrophobic core via steric matching of hydrophobic residues or ionic interaction of core residues within self-assembling coiled-coil systems.[86-92] Most notably, Dr. Alan Kennan of Colorado State University successfully generated A_2B and ABC heterotrimers via steric matching. His group found that steric matching of a bulky amino acid with two small residues resulted in an A_2B type heterotrimer. In this case, a non-natural residue, cyclohexylalanine, in an **a** position is paired with two alanine residues. The stability of the A_2B heterotrimer is greater than that of the alanine homotrimer, but comparable to the stability of a control peptide containing cyclopropylalanine. To increase the stability of the heterotrimer, multiple **a** layers throughout the trimer were utilized for steric matching. This resulted in stable A_2B and ABC heterotrimers, depending on the strands on which the cyclohexylalanine were located (Figure

1-33).[90] This work was a significant advancement in the field of *de novo* design, but the use of the full coiled-coil core prohibits its use as a scaffold for metal binding site incorporation.

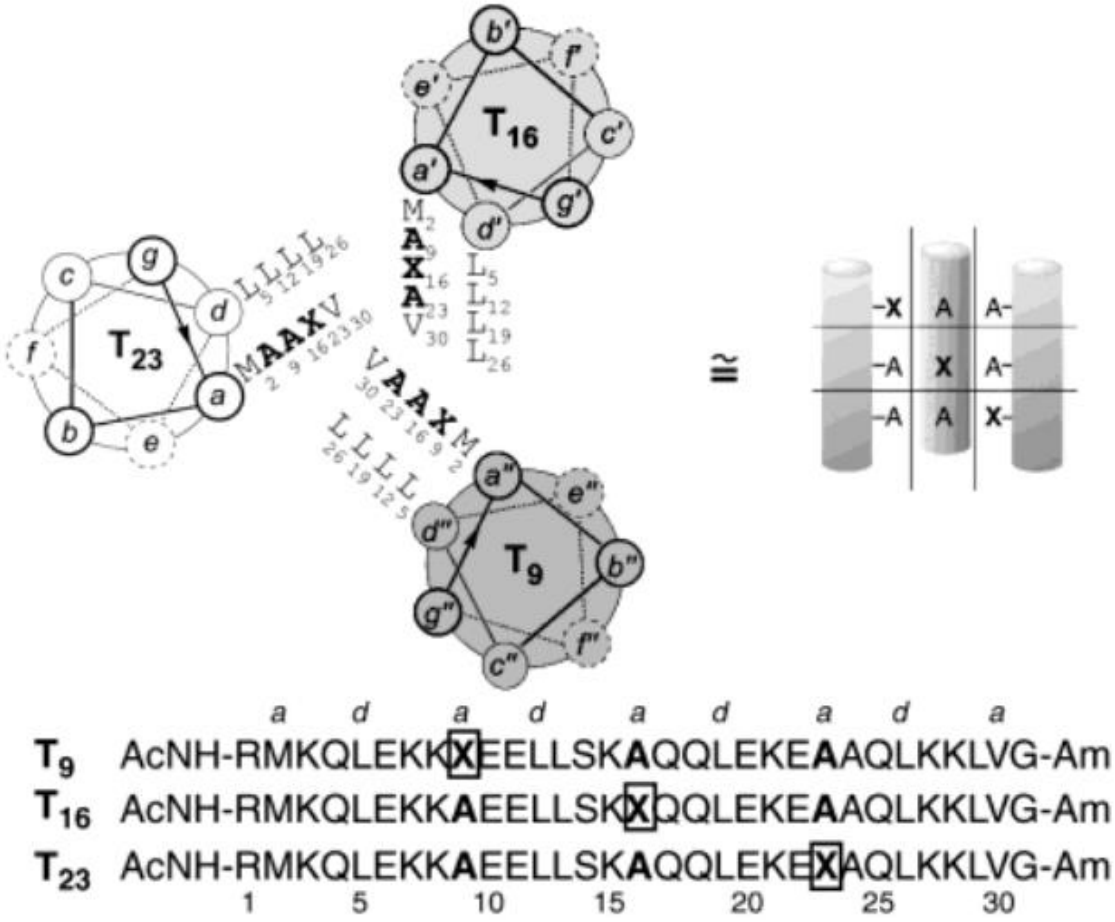

Figure 1-33 Helical wheel diagram of the ABC heterotrimer with peptide sequences[90]

Asymmetric TRI scaffold

Using a similar approach as Dr. Kennan, Dr. Cathy Mocny characterized a heterotrimer using the GR peptide, which is one heptad longer than TRI. The steric matching used in these heterotrimers, however, was designed to optimize Pb(II) binding stability to a Cys_3 site. While attempting to determine the relative affinity for Pb(II) to Cys_3^a vs $Ala_3^dCys_3^a$ by ^{207}Pb NMR, Dr. Kosh Neupane found that sub-stoichiometric amounts of Pb(II) gave rise to species with chemical shifts intermediate of the homotrimer positions. He hypothesized that this mixed steric matching resulted in heterotrimeric species. Using GR L16C, the GR analog of TRI L16C, Dr. Mocny introduced a layer of mixed steric bulk in the **d** position directly above the Cys site. The GR scaffold was used for increased stability but will still be referred to as Cys^a or Ala^dCys^a in this work. It was hypothesized that the layer of reduced steric bulk allowed for a repositioning of

Pb(II) to a more stable conformation. A crystal structure of Pb(II) bound Cys_3^a showed that Pb(II) bound in the endo conformation with the Pb(II) sitting C-terminally of the Cys_3 site. Prior to obtaining the crystal structure of the $Ala_3^dCys_3^a$ peptide, it was hypothesized that Pb(II) was in this less favorable position because the endo conformation was too sterically hindered. By opening space in the layer directly above the Cys_3 layer, the Pb(II) could have space to bind N-terminally of the Cys_3 layer. Rather than using the synthetically expensive cyclohexylalanine as Dr. Kennan had done, Dr. Mocny utilized the native Leu as the bulky residue and Ala as the less bulky residue. Interestingly, later crystallographic studies of the alanine containing peptide showed that this steric matching did not occur as hypothesized. Rather than reorienting to bind in the exo conformation, the Pb(II) remains endo and three water molecules are able to hydrogen bond to the Cys-S in the space created by the smaller alanine residues (Figure 1-19).

Via ^{207}Pb NMR, it was found that Pb(II) bound $Ala_3^dCys_3^a$ and Cys_3^a have chemical shifts ~75 ppm apart. A stoichiometric mixture of two alanine containing strands (Ala^dCys^a) and one leucine strand (Cys^a) formed a species, $Ala_2^dCys_3^a$, with a unique chemical shift. The reverse heterotrimer, containing two leucine strands and one alanine strand, $Ala_1^dCys_3^a$, had a major peak corresponding to a unique heterotrimer and a minor peak corresponding to the alternate heterotrimer (Figure 1-34). As the peaks for the heterotrimeric species were spaced stepwise between the two homotrimeric signals, an experiment was performed to determine if this was simply due to coalescence of homotrimeric signals. A 5:1 mixture of Ala^dCys^a and Cys^a with 2 equivalents of Pb(II) was investigated as this would either result in two peaks, one for $Ala_2^dCys_3^a$ and one for $Ala_3^dCys_3^a$, or a single resonance halfway between those two possible peaks. Two peaks at the expected chemical shift were observed, proving that heterotrimers do exist as unique species in solution. Dr. Mocny additionally found that this phenomenon was unperturbed by the addition of a distant transition metal site and was consistent between pH 7.5 and 9.5. A more complete analysis of these heterotrimers follows in Chapter 2.

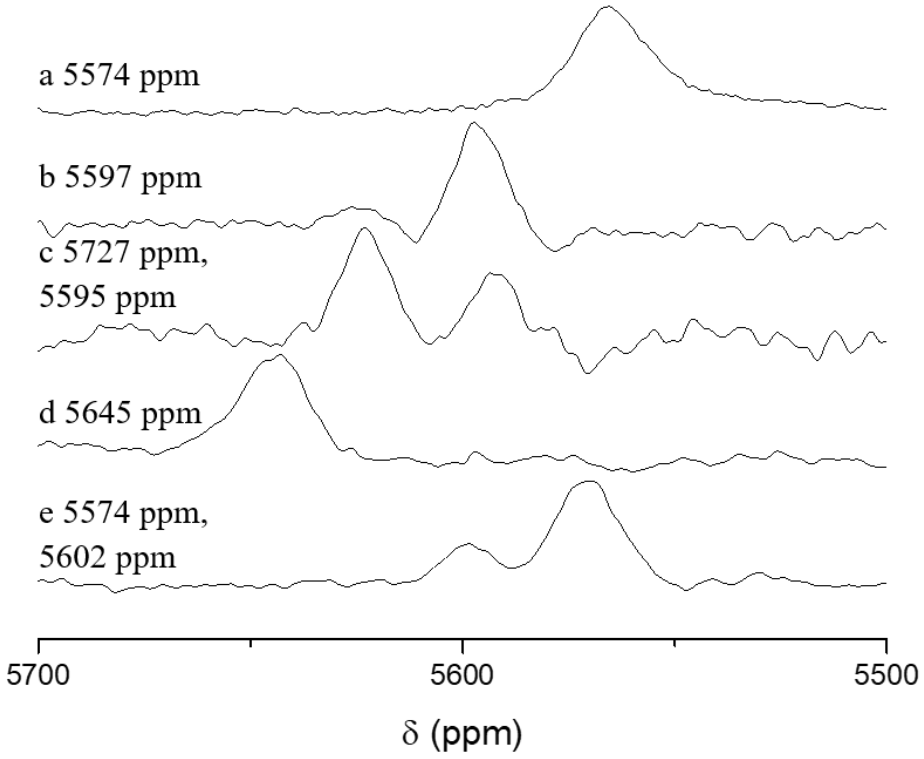

Figure 1-34 ^{207}Pb NMR of (a) Ala$_3^d$Cys$_3^a$, (b) Ala$_2^d$Cys$_3^a$, (c) Ala$_1^d$Cys$_3^a$, (d)Cys$_3^a$, and (e) 5:1 ratio of Ala^{d}Cys^a and Cys^a with 2 eq. of Pb(II) at pH 7.5 with 3.5-5 mM trimer for a-d and 6 mM trimer for e

The key conclusion of these studies is that selective and stoichiometric metal chelated heterotrimer formation is possible, but only with A_2B type systems, not the reverse AB_2. This work aimed to improve upon the groundbreaking results of Drs. Neupane and Mocny by creating a similar system that is able to selectively form both A_2B and AB_2 type heterotrimers. While this may seem like a small distinction, one must consider that the goal was not simply to make asymmetric trimers, but to make asymmetric transition metal binding sites elsewhere in the scaffold. The stability of the GR construct drops with each Leu mutation, with a significant drop in stability with four or more substitutions. To generate the heterotrimer, one strand must contain the single Leu to Cys substitution, allowing for two more possible substitutions. The other strand, however, must contain both the Cys and Ala substitutions, limiting this strand to only one further substitution. The system described above requires two Ala^{d}Cys^a strands, which can only have one transition metal binding residue. Thus, this system is limited to an X_1His_3 transition metal site, not an X_2His_3 site, where X is any residue. The ability to selectively generate both

scaffolds will allow for a wider range of asymmetry to be investigated in transition metal binding sites.

This work will first describe how both systems (A_2B and AB_2) can be achieved using an altered Pb(II) coordination environment afforded by Cys^d sites. The differences in heterotrimer formation in Cys^a and Cys^d sites is described using both experimental and computational analyses. The ability to transfer these Pb(II) binding sites to other heptads within the 3SCC is also investigated for both **a** and **d** layers. Chapter 2 will also show how a distant His_3 site can be incorporated into the scaffold without perturbing the Pb(II) environment. This scaffold remains fully selective in the presence of a bound transition metal and over a range of neutral to basic pH.

Spectroscopic characterization of Co(II), Zn(II), and Cu(I/II) in this transition metal site follows in Chapter 3. This work demonstrates that asymmetry at the Pb(II) site induces asymmetry at the transition metal site via the incorporation of 1-3 Glu residues in addition to three histidines. This chapter will also describe spectroscopic differences in copper binding to His_3^a, His_3^d, and mixed layer His_3 sites which were found to have very different catalytic properties. This chapter will provide a thorough analysis of how metal binding environments are influenced by the asymmetric incorporation of metal binding residues.

The spectroscopic characterization will be followed by catalytic studies of Zn(II) CA and Cu-only SOD in asymmetric sites. These chapters will discuss how catalysis is affected by asymmetric transition metal binding sites. First coordination sphere asymmetry proves to have significant effects on SOD activity, as will be discussed in Chapter 5. The result of including an intended second coordination sphere residue is also explored Zn(II) activity as a model of CA in Chapter 4. This work concludes with a discussion of the differences of copper and zinc activity as well as how asymmetry can be used in this scaffold to expand the scope of this work.

References

1. 2020, N. M. A. Frances H. Arnold – Nobel Lecture.

2. Ruckthong, L. Crystallographic comparison of tris-thiolate sites in designed proteins to control metal geometries. University of Michigan, Ann Arbor, MI, 2016.

3. Ruckthong, L.; Peacock, A. F. A.; Pascoe, C. E.; Hemmingsen, L.; Stuckey, J. A.; Pecoraro, V. L., d -Cysteine Ligands Control Metal Geometries within De Novo Designed Three-Stranded Coiled Coils. **2017**, 8232-8243.

4. Ruckthong, L.; Deb, A.; Hemmingsen, L.; Penner-Hahn, J. E.; Pecoraro, V. L., Incorporation of second coordination sphere d-amino acids alters Cd(II) geometries in designed thiolate-rich proteins. *JBIC J. Biol. Inorg. Chem.* **2018,** *23* (1), 123-135.

5. Liang, Q.; Eason, P. D.; Long, E. C., Metallopeptide—DNA Interactions: Site-Selectivity Based on Amino Acid Composition and Chirality. *J. Am. Chem. Soc.* **1995,** *117*, 9625-9631.

6. Maren, T. H., Carbonic Anhydrase: Chemistry, Physiology, and Inhibition. *Physiol. Rev.* **1967,** *47*, 597-781.

7. Krebs, J. F.; Ippolito, J. A.; Christianson, D. W.; Fierke, C. A., Structural and Functional Importance of a Conserved Hydrogen Bond Network in Human Carbonic Anhydrase II. *The Journal of Biological Chemistry* **1993,** *268* (36), 27458-27466.

8. Lindskog, S., Structure and Mechanism of Carbonic Anhydrase. *Pharmacol. Ther.* **1997,** *74* (1), 1-20.

9. Koebke, K. J.; Yu, F.; Van Stappen, C.; Pinter, T. B. J.; Deb, A.; Penner-Hahn, J. E.; Pecoraro, V. L., Methylated Histidines Alter Tautomeric Preferences that Influence the Rates of Cu Nitrite Reductase Catalysis in Designed Peptides. *J. Am. Chem. Soc.* **2019,** *141* (19), 7765-7775.

10. Cangelosi, V. M.; Deb, A.; Penner-Hahn, J. E.; Pecoraro, V. L., A de novo designed metalloenzyme for the hydration of CO2. *Angewandte Chemie - International Edition* **2014,** *53* (30), 7900-7903.

11. Zastrow, M. L.; Pecoraro, V. L., Designing hydrolytic zinc metalloenzymes. *Biochemistry* **2014,** *53* (6), 957-78.

12. Nath, I.; Chakraborty, J.; Verpoort, F., Metal organic frameworks mimicking natural enzymes: a structural and functional analogy. *Chem. Soc. Rev.* **2016,** *45* (15), 4127-70.

13. Kunz, Peter C.; Reiß, Guido J.; Frank, W.; Kläui, W., A Novel Water-Soluble Tripodal Imidazolyl Ligand as a Model for the Tris(histidine) Motif of Zinc Enzymes: Nickel, Cobalt and Zinc Complexes and a Comparison with Metal Binding in Carbonic Anhydrase. *Eur. J. Inorg. Chem.* **2003,** *2003* (21), 3945-3951.

14. Brown, R. S.; Curtis, N. J.; Huguet, J., Tris(4,5-diisopropylimidazol-2-yl)phosphine:Zinc(2+). A Catalytically Active Model for Carbonic Anhydrase. *J. Am. Chem. Soc.* **1981,** *103,* 6953-6959.

15. Kiefer, L. L.; Paterno, S. A.; Fierke, C. A., Hydrogen Bond Network in the Metal Binding Site of Carbonic Anhydrase Enhances Zinc Affinity and Catalytic Efficiency. *J. Am. Chem. Soc.* **1995,** *117* (26), 6831-6837.

16. Liang, Z.; Xue, Y.; Behravan, G.; Jonsson, B.-H.; Lindskog, S., Importance of the conserved active-site residues Try7, Glu106 and Thr199 for the catalytic function of human carbonic anhydrase II. *Eur. J. Biochem.* **1993,** *211* (3), 821-827.

17. Xue, Y.; Liljas, A.; Jonsson, B.; Lindskog, S., Structural analysis of the zinc hydroxide-Thr-199-Glu-106 hydrogen-bond network in human carbonic anhydrase II. *Proteins* **1993,** *17* (1), 93-106.

18. Gleason, J. E.; Galaleldeen, A.; Peterson, R. L.; Taylor, A. B.; Holloway, S. P.; Waninger-Saroni, J.; Cormack, B. P.; Cabelli, D. E.; Hart, P. J.; Culotta, V. C., Candida albicans SOD5 represents the prototype of an unprecedented class of Cu-only superoxide dismutases required for pathogen defense. *Proc. Natl. Acad. Sci. U. S. A.* **2014,** *111* (16), 5866-5871.

19. McCord, J. M.; Fridovich, I., Superoxide Dismutase: An enzymatic function for erythrocuprein (hemocuprein). *J. Biol. Chem.* **1969,** *244,* 6049-6055.

20. Sheng, Y.; Abreu, I. A.; Cabelli, D. E.; Maroney, M. J.; Miller, A. F.; Teixeira, M.; Valentine, J. S., Superoxide dismutases and superoxide reductases. *Chem. Rev.* **2014,** *114* (7), 3854-3918.

21. Miller, A. F., Superoxide dismutases: active sites that save, but a protein that kills. *Curr. Opin. Chem. Biol.* **2004,** *8* (2), 162-8.

22. Miller, A.-F., Superoxide dismutases: Ancient enzymes and new insights. *FEBS Lett.* **2012,** *586* (5), 585-595.

23. Abreu, I. A.; Cabelli, D. E., Superoxide dismutases—a review of the metal-associated mechanistic variations. *Biochim. Biophys. Acta* **2010,** *1804,* 263–274.

24. Zelko, I. N.; Mariani, T. J.; Folz, R. J., Superoxide dismutase multigene family: A comparison of the CuZn-SOD (SOD1), Mn-SOD (SOD2), and EC-SOD (SOD3) gene structures, evolution, and expression. *Free Radical Biol. Med.* **2002,** *33* (3), 337-349.

25. Koebke, K. J.; Pecoraro, V. L., Development of de Novo Copper Nitrite Reductases: Where We Are and Where We Need To Go. *ACS Catal* **2018,** *8* (9), 8046-8057.

26. Apostolovic, B.; Danial, M.; Klok, H. A., Coiled coils: attractive protein folding motifs for the fabrication of self-assembled, responsive and bioactive materials. *Chem. Soc. Rev.* **2010,** *39* (9), 3541-75.

27. Bryson, J. W.; Betz, S. F.; Lu, H. S.; Suich, D. J.; Zhou, H. X.; O'Neil, K. T.; DeGrado, W. F., Protein Design: A Hierarchic Approach. *Science* **1995,** *270* (5238), 935-941.

28. Degrado, W. F.; Summa, C. M.; Pavone, V.; Nastri, F.; Lombardi, A., De Novo Design and Structural Characterization of Proteins and Metalloproteins. *Annu. Rev. Biochem.* **1999**, 779-819.

29. Gruber, M.; Lupas, A. N., Historical review: Another 50th anniversary - New periodicities in coiled coils. *Trends Biochem. Sci.* **2003,** *28* (12), 679-685.

30. Lupas, A. N.; Bassler, J., Coiled Coils – A Model System for the 21st Century. *Trends Biochem. Sci.* **2017,** *42* (2), 130-140.

31. Woolfson, D. N., Coiled-Coil Design: Updated and Upgraded. *Subcell. Biochem.* **2017,** *82*, 35-61.

32. Lupas, A. N.; Bassler, J.; Dunin-horkawicz, S., The Structure and Topology of Alpha-Helical Coiled Coils.

33. Gonzalez, L. J.; Brown, R. A.; Richardson, D.; Alber, T., Crystal structures of a single coiled-coil peptide in two oligomeric states reveal the basis for structural polymorphism. *Nat. Struct. Biol.* **1996,** *3* (12), 1002-1010.

34. Harbury, P. B.; Zhang, T.; Kim, P. S.; Alber, T., A Switch Between Two-, Three-, and Four-Stranded Coiled Coils in GCN4 Leucine Zipper Mutants. *Science* **1993,** *262* (5138), 1401-1407.

35. Peacock, A. F. A.; Iranzo, O.; Pecoraro, V. L., Harnessing natures ability to control metal ion coordination geometry using de novo designed peptides. *Dalton Trans.* **2009,** *9226* (13), 2271-80.

36. Dieckmann, G. R.; McRorie, D. K.; Lear, J. D.; Sharp, K. A.; DeGrado, W. F.; Pecoraro, V. L., The role of protonation and metal chelation preferences in defining the properties of mercury-binding coiled coils. *J. Mol. Biol.* **1998,** *280* (5), 897-912.

37. Dieckmann, G. R.; MoRorie, D. K.; Tierney, D. L.; Utschig, L. M.; Singer, C. P.; O'Halloran, T. V.; Penner-Hahn, J. E.; DeGrado, W. F.; Pecoraro, V. L., De novo design of mercury-binding two- and three-helical bundles. *J. Am. Chem. Soc.* **1997,** *119* (26), 6195-6196.

38. Ogihara, N. L.; Weiss, M. S.; DeGrado, W. F.; Eisenberg, D., The crystal structure of the designed trimeric coiled coil coil-Va Ld: Implications for engineering crystals and supramolecular assemblies. *Protein Sci.* **1997,** *6*, 80-88.

39. Tripet, B.; Wagschal, K.; Lavigne, P.; Mant, C. T.; Hodges, R. S., Effects of side-chain characteristics on stability and oligomerization state of a de novo-designed model coiled-coil: 20 amino acid substitutions in position "d". *J. Mol. Biol.* **2000,** *300* (2), 377-402.

40. Chakraborty, S.; Iranzo, O.; Zuiderweg, E. R. P.; Pecoraro, V. L., Experimental and theoretical evaluation of multisite cadmium(II) exchange in designed three-stranded coiled-coil peptides. *J. Am. Chem. Soc.* **2012,** *134* (14), 6191-6203.

41. Chakraborty, S.; Kravitz, J. Y.; Thulstrup, P. W.; Hemmingsen, L.; DeGrado, W. F.; Pecoraro, V. L., Design of a three-helix bundle capable of binding heavy metals in a triscysteine environment. *Angew. Chem. Int. Ed.* **2011,** *50* (9), 2049-53.

42. Chakraborty, S.; Touw, D. S.; Peacock, A. F. a.; Stuckey, J.; Pecoraro, V. L., Structural comparisons of apo- and metalated three-stranded coiled coils clarify metal binding determinants in thiolate containing designed peptides. *J. Am. Chem. Soc.* **2010,** *132* (38), 13240-50.

43. Farrer, B. T.; Harris, N. P.; Balchus, K. E.; Pecoraro, V. L., Thermodynamic model for the stabilization of trigonal thiolato mercury(II) in designed three-stranded coiled coils. *Biochemistry* **2001,** *40* (48), 14696-14705.

44. Farrer, B. T.; McClure, C. P.; Penner-Hahn, J. E.; Pecoraro, V. L., Arsenic(III) - Cysteine interactions stabilize three-helix bundles in aqueous solution. *Inorg. Chem.* **2000,** *39* (24), 5422-5423.

45. Farrer, B. T.; Pecoraro, V. L., Hg(II) binding to a weakly associated coiled coil nucleates an encoded metalloprotein fold: A kinetic analysis. *Proceedings of the National Academy of Sciences* **2003,** *100* (7), 3760-3765.

46. Ghosh, D.; Lee, K.-H.; Demeler, B.; Pecoraro, V. L., Linear free-energy analysis of mercury(II) and cadmium(II) binding to three-stranded coiled coils. *Biochemistry* **2005,** *44*, 10732-10740.

47. Iranzo, O.; Cabello, C.; Pecoraro, V. L., Heterochromia in designed metallopeptides: geometry-selective binding of CdII in a de novo peptide. *Angew. Chem. Int. Ed. Engl.* **2007,** *46* (35), 6688-91.

48. Iranzo, O.; Jakusch, T.; Lee, K.-H.; Hemmingsen, L.; Pecoraro, V. L., The correlation of 113Cd NMR and 111mCd PAC spectroscopies provides a powerful approach for the characterization of the structure of Cd(II)-substituted Zn(II) proteins. *Chemistry (Weinheim an der Bergstrasse, Germany)* **2009,** *15* (15), 3761-72.

49. Iranzo, O.; Thulstrup, P. W.; Ryu, S.-B.; Hemmingsen, L.; Pecoraro, V. L., The application of (199)Hg NMR and (199m)Hg perturbed angular correlation (PAC) spectroscopy to define the biological chemistry of Hg(II): a case study with designed two- and three-stranded coiled coils. *Chemistry (Weinheim an der Bergstrasse, Germany)* **2007,** *13* (33), 9178-9190.

50. Łuczkowski, M.; Stachura, M.; Schirf, V.; Demeler, B.; Hemmingsen, L.; Pecoraro, V. L., Design of thiolate rich metal binding sites within a peptidic framework. *Inorg. Chem.* **2008,** *47* (23), 10875-88.

51. Matzapetakis, M. De novo design of heavy metal binding proteins. University of Michigan, 2004.

52. Matzapetakis, M.; Farrer, B. T.; Weng, T. C.; Hemmingsen, L.; Penner-Hahn, J. E.; Pecoraro, V. L., Comparison of the binding of cadmium(II), mercury(II) and arsenic(III) to the de novo designed peptides TRI L12C and TRI L16C. *J. Am. Chem. Soc.* **2002,** *124* (27), 8042-8054.

53. Matzapetakis, M.; Ghosh, D.; Weng, T.-C.; Penner-Hahn, J. E.; Pecoraro, V. L., Peptidic models for the binding of Pb(II), Bi(III) and Cd(II) to mononuclear thiolate binding sites. *Journal of biological inorganic chemistry : JBIC : a publication of the Society of Biological Inorganic Chemistry* **2006,** *11* (7), 876-90.

54. Neupane, K. P.; Pecoraro, V. L., Probing a homoleptic PbS3 coordination environment in a designed peptide using 207Pb NMR spectroscopy: Implications for understanding the molecular basis of lead toxicity. *Angewandte Chemie - International Edition* **2010,** *49* (44), 8177-8180.

55. Peacock, A. F. A.; Stuckey, J. A.; Pecoraro, V. L., Switching the chirality of the metal environment alters the coordination mode in designed peptides. *Angew. Chem. Int. Ed.* **2009,** *48* (40), 7371-4.

56. Ruckthong, L.; Zastrow, M. L.; Stuckey, J. A.; Pecoraro, V. L., A Crystallographic Examination of Predisposition versus Preorganization in de Novo Designed Metalloproteins. *J. Am. Chem. Soc.* **2016,** *138* (36).

57. Tebo, A. G.; Hemmingsen, L.; Pecoraro, V. L., Variable primary coordination environments of Cd(II) binding to three helix bundles provide a pathway for rapid metal exchange. *Metallomics* **2015,** *7* (12), 1555-61.

58. Zampella, G.; Neupane, K. P.; De Gioia, L.; Pecoraro, V. L., The importance of stereochemically active lone pairs for influencing Pb(II) and As(III) protein binding. *Chemistry* **2012,** *18* (7), 2040-50.

59. Lovejoy, B.; Choe, S.; Cascio, D.; McRorie, D. K.; DeGrado, W. F.; Eisenberg, D., Crystal Structure of a Synthetic Triple-Stranded Alpha-Helical Bundle. *Science* **1993,** *259* (1288-1293).

60. Boice, J. A.; Dieckmann, G. R.; DeGrado, W. F.; Fairman, R., Thermodynamic analysis of a designed three-stranded coiled coil. *Biochemistry* **1996,** *35* (46), 14480-14485.

61. Mocny, C. S. Ph.D. Dissertation, Examining the metal selectivity of thiol rich de novo designed peptides as a strategy to make asymmetric alpha- helical protein assemblies. 2016.

62. Mundlapati, V. R.; Ghosh, S.; Bhattacherjee, A.; Tiwari, P.; Biswal, H. S., Critical Assessment of the Strength of Hydrogen Bonds between the Sulfur Atom of Methionine/Cysteine and Backbone Amides in Proteins. *J Phys Chem Lett* **2015,** *6* (8), 1385-9.

63. Neupane, K. P.; Pecoraro, V. L., Pb-207 NMR spectroscopy reveals that Pb(II) coordinates with glutathione (GSH) and tris cysteine zinc finger proteins in a PbS3 coordination environment. *J. Inorg. Biochem.* **2011,** *105* (8), 1030-4.

64. Touw, D. S. Structural and spectroscopic studies of heavy metal binding to de novo designed coiled coil peptides. University of Michigan, United States, 2007.

65. Touw, D. S. Structural and spectroscopic studies of heavy metal binding to de novo designed coiled-coil peptides. University of Michigan, Ann Arbor, Michigan, 2007.

66. Zastrow, M. L.; Peacock, A. F.; Stuckey, J. A.; Pecoraro, V. L., Hydrolytic catalysis and structural stabilization in a designed metalloprotein. *Nat. Chem.* **2011,** *4* (2), 118-23.

67. Zastrow, M. L.; Pecoraro, V. L., Influence of active site location on catalytic activity in de novo-designed zinc metalloenzymes. *J. Am. Chem. Soc.* **2013,** *135* (15), 5895-903.

68. Kiefer, L. L.; Krebs, J. F.; Paterno, S. A.; Fierke, C. A., Engineering a Cysteine Ligand into the Zinc Binding Site of Human Carbonic Anhydrase II. *Biochemistry* **1993,** *32*, 9896-9900.

69. Ippolito, J. A.; Baird, T. T.; McGee, S. A.; Christianson, D. W.; Fierke, C. A., Structure-assisted redesign of a protein-zinc-binding site with femtomolar affinity. *Proceedings of the National Academy of Sciences* **1995,** *92*, 5017-5021.

70. Christianson, D. W.; Fierke, C. A., Carbonic Anhydrase: Evolution of the Zinc Binding Site by Nature and by Design. *Acc. Chem. Res.* **1996,** *29*, 331-339.

71. Li, Y.; Hodak, M.; Bernholc, J., Enzymatic mechanism of copper-containing nitrite reductase. *Biochemistry* **2015,** *54* (5), 1233-42.

72. Murphy, M. E. P.; Turley, S.; Adman, E. T., Structure of Nitrite Bound to Copper-containing Nitrite Reductase from Alcaligenes faecalis : MECHANISTIC IMPLICATIONS. *The Journal of Biological Chemistry* **1997,** *272* (45), 28455-28460.

73. Kukimoto, M.; Nishiyama, M.; Horinouchi, S.; Beppu, T.; Murphy, M. E. P.; Turley, S.; Adman, E. T., X-ray Structure and Site-Directed Mutagenesis of a Nitrite Reductase from Alcaligenes faecalis S-6: Roles of Two Copper Atoms in Nitrite Reduction. *Biochemistry* **1994,** *33* (17), 5246-5252.

74. Koebke, K. J.; Yu, F.; Salerno, E.; Van Stappen, C.; Tebo, A. G.; Penner-Hahn, J. E.; Pecoraro, V. L., Modifying the Steric Properties in the Second Coordination Sphere of Designed Peptides Leads to Enhancement of Nitrite Reductase Activity. *Angew. Chem. Int. Ed. Engl.* **2018**.

75. Betz, S. F.; Bryson, J. W.; Passador, M. C.; Brown, R. J.; O'Neil, K. T.; DeGrado, W. F., Expression of de novo Designed alpha-Helical Bundles. *Acta Chem. Scand.* **1996,** *50* (8), 688-696.

76. Bryson, J. W.; Desjarlais, J. R.; Handel, T. M.; Degrado, W. F., From coiled coils to small globular proteins: Design of a native-like three-helix bundle. *Protein science : a publication of the Protein Society* **1998,** *7* (6), 1404-1414.

77. Fletcher, J. M.; Boyle, A. L.; Bruning, M.; Bartlett, S. J.; Vincent, T. L.; Zaccai, N. R.; Armstrong, C. T.; Bromley, E. H. C.; Booth, P. J.; Brady, R. L.; Thomson, A. R.; Woolfson, D.

N., A basis set of de novo coiled-Coil peptide oligomers for rational protein design and synthetic biology. *ACS Synthetic Biology* **2012,** *1* (6), 240-250.

78. Lupas, a. N.; Gruber, M., The structure of a-helical coiled coils. *Adv. Protein. Chem.* **2005,** *70* (04), 37-78.

79. Smith, B. A.; Hecht, M. H., Novel proteins: from fold to function. *Curr. Opin. Chem. Biol.* **2011,** *15* (3), 421-6.

80. Zaccai, N. R.; Chi, B.; Thomson, A. R.; Boyle, A. L.; Bartlett, G. J.; Bruning, M.; Linden, N.; Sessions, R. B.; Booth, P. J.; Brady, R. L.; Woolfson, D. N., A de novo peptide hexamer with a mutable channel. *Nat. Chem. Biol.* **2011,** *7* (12), 935-41.

81. Tebo, A. G. De Novo designed metallopeptides to investigate metal ion homeostasis, electron transfer, and redox catalysis. 2015.

82. Boulanger, M. J.; Kukimoto, M.; Nishiyama, M.; Horinouchi, S.; Murphy, M. E., Catalytic roles for two water bridged residues (Asp-98 and His-255) in the active site of copper-containing nitrite reductase. *J. Biol. Chem.* **2000,** *275* (31), 23957-64.

83. Kerfeld, C. A.; Yoshida, S.; Tran, K. T.; Yeates, T. O.; Cascio, D.; Bottin, H.; Berthomieu, C.; Sugiura, M.; Boussac, A., The 1.6 Å resolution structure of Fe-superoxide dismutase from the thermophilic cyanobacterium Thermosynechococcus elongatus. *J. Biol. Inorg. Chem.* **2003,** *8* (7), 707-714.

84. Mathieu, E. Anti-oxidant MnII-complexes: design and study in a cellular model of inflammatory diseases. Investigation of subcellular location. 2017.

85. Mathieu, E.; Tolbert, A. E.; Koebke, K. J.; Tard, C.; Iranzo, O.; Penner-Hahn, J.; Policar, C.; Pecoraro, V. L., Rational De Novo Design of a Cu-Metalloenzyme for Superoxide Dismutation. *Chem.--Eur. J.* **2019,** *26*, 249-258.

86. Diss, M. L.; Kennan, A. J., Heterotrimeric coiled coils with core residue urea side chains. *J. Org. Chem.* **2008,** *73* (24), 9752-5.

87. Kiyokawa, T.; Kanaori, K.; Tajima, K.; Kawaguchi, M.; Mizuno, T.; Oku, J.; Tanaka, T., Selective formation of AAB- and ABC-type heterotrimeric alpha-helical coiled coils. *Chemistry* **2004,** *10* (14), 3548-54.

88. Lombardi, A.; Bryson, J. W.; DeGrado, W. F., De Novo Design of Heterotrimeric Coiled Coils. *Peptide Science* **1996,** *40* (5), 495-504.

89. Lumb, K. J.; Kim, P. S., A Buried Polar Interaction Imparts Structural Uniqueness in a Designed Heterodimeric Coiled Coil. *Biochemistry* **1995,** *34* (27), 8642-8648.

90. Schnarr, N. A.; Kennan, A. J., Peptide Tic-Tac-Toe: Heterotrimeric Coiled-Coil Specificity from Steric Matching of Multiple Hydrophobic Side Chains. *J. Am. Chem. Soc.* **2001,** *124*, 9779-9783.

91. Schnarr, N. A.; Kennan, A. J., Coiled-Coil Formation Governed by Unnatural Hydrophobic Core Side Chains. *J. Am. Chem. Soc.* **2001,** *123*, 11081-11082.

92. Schnarr, N. A.; Kennan, A. J., Strand Orientation by Steric Matching: A Designed Antiparallel Coiled-Coil Trimer. *J. Am. Chem. Soc.* **2004,** *126* (44), 14447-14451.

Chapter 2 Generation of Fully Selective, Asymmetric, Self-Assembling Heterotrimeric Peptides

Introduction

The elucidation of the relationship between protein structure and function is typically approached in one of two ways: *de novo* protein design or protein redesign. *De novo* design utilizes simple, non-native scaffolds to build peptides from the ground up. Protein redesign instead uses native proteins as the starting point from which modifications are introduced. Both techniques afford advantages to the study of the structure-function relationship, but this work will focus solely on *de novo* design. The Pecoraro lab has utilized a *de novo* designed three stranded coiled-coil peptide scaffold to study heavy metal toxicity and essential metal catalytic activity.

One such study is that of Zn(II) Carbonic Anhydrase (CA), an enzyme that converts CO_2 to HCO_3^- at diffusion limited rates.[1] The active site consists of a Zn(II) bound to three His residues and an exogenous solvent molecule that is further hydrogen bonded to a Thr residue (Figure 2-1).[2] Dr. Melissa Zastrow successfully modeled the primary coordination sphere of the Zn(II), resulting in the fastest aqueous model of CA to date.[3-4] This model, however, was limited by the three-fold symmetry inherent to the 3SCC scaffold and could not model the second coordination sphere hydrogen bonding network within the native enzyme. To address this asymmetry a new *de novo* scaffold is necessary.

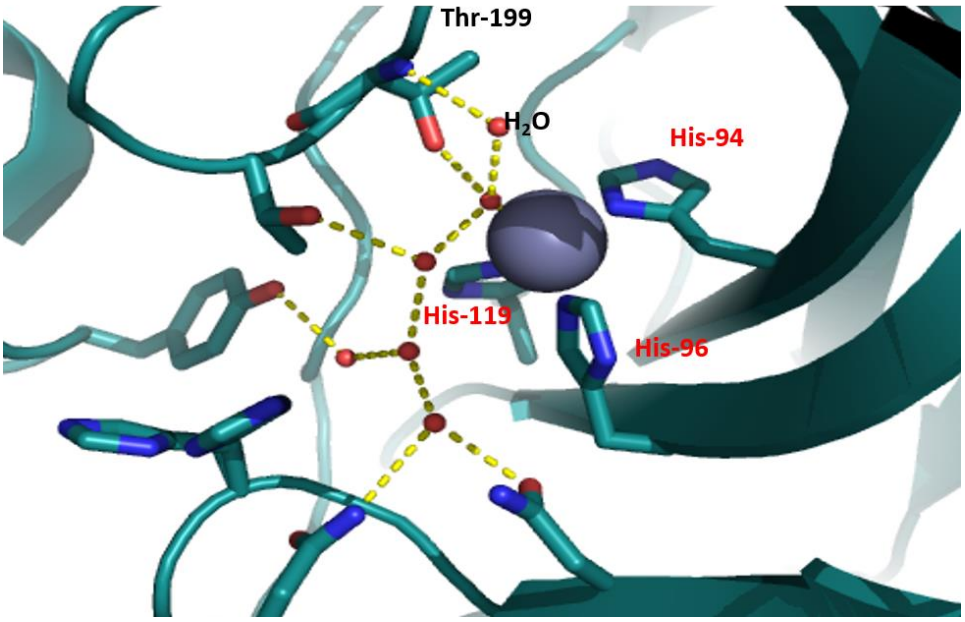

Figure 2-1 CA active site with second coordination sphere hydrogen bonding interactions of T199 (PDB 2CBA).

Dr. Catherine Mocny developed and characterized a self-assembling asymmetric scaffold utilizing Pb(II), a Cys_3 binding site, and an adjacent layer of reduced steric bulk to allow for solvent interactions. This was the first example of a self-assembling asymmetric peptide that utilized only natural amino acids and a single heptad rather than the full hydrophobic core, which was a significant advancement of the field of protein design. This design, however, could only achieve full selectivity with an A_2B-type trimer and not with the corresponding AB_2-type, limiting the asymmetry that can be introduced at a distant site. The stability of these peptides is greatly affected by the number of core leucine substitutions, with a significant drop in stability observed with four substitutions in the GR length scaffold. One could imagine simply increasing the length of the peptide to incorporate more substitutions while maintaining stability. As will be described later in this work, increasing the length of the peptide may increase the pH at which the 2SCC to 3SCC transition occurs. As the pH of this transition increases, the range of reactions one is able to study decreases. Additionally, one advantage of this system over other attempts to make heteromeric peptides is the cost effectiveness. This is achieved both by using only natural amino acids and by utilizing the shortest possible sequence necessary to achieve asymmetry and incorporate a transition metal binding site. Thus, my work focuses on only the GR scaffold. To maintain stability in the GR length peptide, therefore, each strand can contain no more than three metal binding residues in place of core leucines. To form the heterotrimer, one strand requires

only the Leu to Cys substitution, allowing for two metal binding residues to be included at a distant site. The other strand, however, requires both a Cys and Ala mutation, so only a single mutation can be incorporated at a distant metal binding site. The construct characterized by Dr. Mocny only achieves full selectivity with the $Ala_2^dCys_3^a$ heterotrimer. Thus, the transition metal site is limited to X_1His_3 sites to investigate enzymes such as CA, SOD, or NiR.[5] My works aimed to improve upon this limitation by modifying this scaffold to form both A_2B and AB_2 type heterotrimers selectively to allow for both X_1His_3 and X_2His_3 transition metal binding sites.

To understand how full selectivity could be achieved, one must understand the mechanism for which any asymmetry is induced in these systems. The scaffold described by Dr. Mocny required two different peptide strands in a 2:1 ratio to form the asymmetric 3SCC. The first peptide sequence incorporated a Cys residue in the first position ("**a**" site) of the third heptad (Cys^a, Table 2-1). In the Pb(II)-bound homotrimer, Cys_3^a, the side chains of the Cys residue are pointed directly toward the center of the trimer with 3.4 Å between each sulfur atom (Figure 2-2). The Pb(II) binds in an endo conformation, meaning the Pb(II) is positioned on the same side of the S_3 plane as the Cys-C_β (Figure 2-3).

*Table 2-1 List of peptide sequences with mutations from the parent sequence in **bold red***

Peptide	Full sequence
GR	Ac-G WKALEEK LKALEEK LKALEEK LKALEEK LKALEEK G-NH_2
Cys^a	Ac-G WKALEEK LKALEEK **C**KALEEK LKALEEK LKALEEK G-NH_2
Ala^dCys^a	Ac-G WKALEEK LKA**A**EEK **C**KALEEK LKALEEK LKALEEK G-NH_2
Cys^d	Ac-G WKALEEK LKA**C**EEK LKALEEK LKALEEK LKALEEK G-NH_2
Cys^dAla^a	Ac-G WKALEEK LKA**C**EEK **A**KALEEK LKALEEK LKALEEK G-NH_2
$23Cys^a$	Ac-G WKALEEK LKALEEK LKALEEK **C**KALEEK LKALEEK G-NH_2
Ala^d23Cys^a	Ac-G WKALEEK LKALEEK LKA**A**EEK **C**KALEEK LKALEEK G-NH_2
$19Cys^d$	Ac-G WKALEEK LKALEEK LKA**C**EEK LKALEEK LKALEEK G-NH_2
$19Cys^dAla^a$	Ac-G WKALEEK LKALEEK LKA**C**EEK **A**KALEEK LKALEEK G-NH_2
$30Cys^a$	Ac-G WKALEEK LKALEEK LKALEEK LKALEEK **C**KALEEK G-NH_2
Baby L9C	Ac-G WKALEEK **C**KALEEK LKALEEK G-NH_2

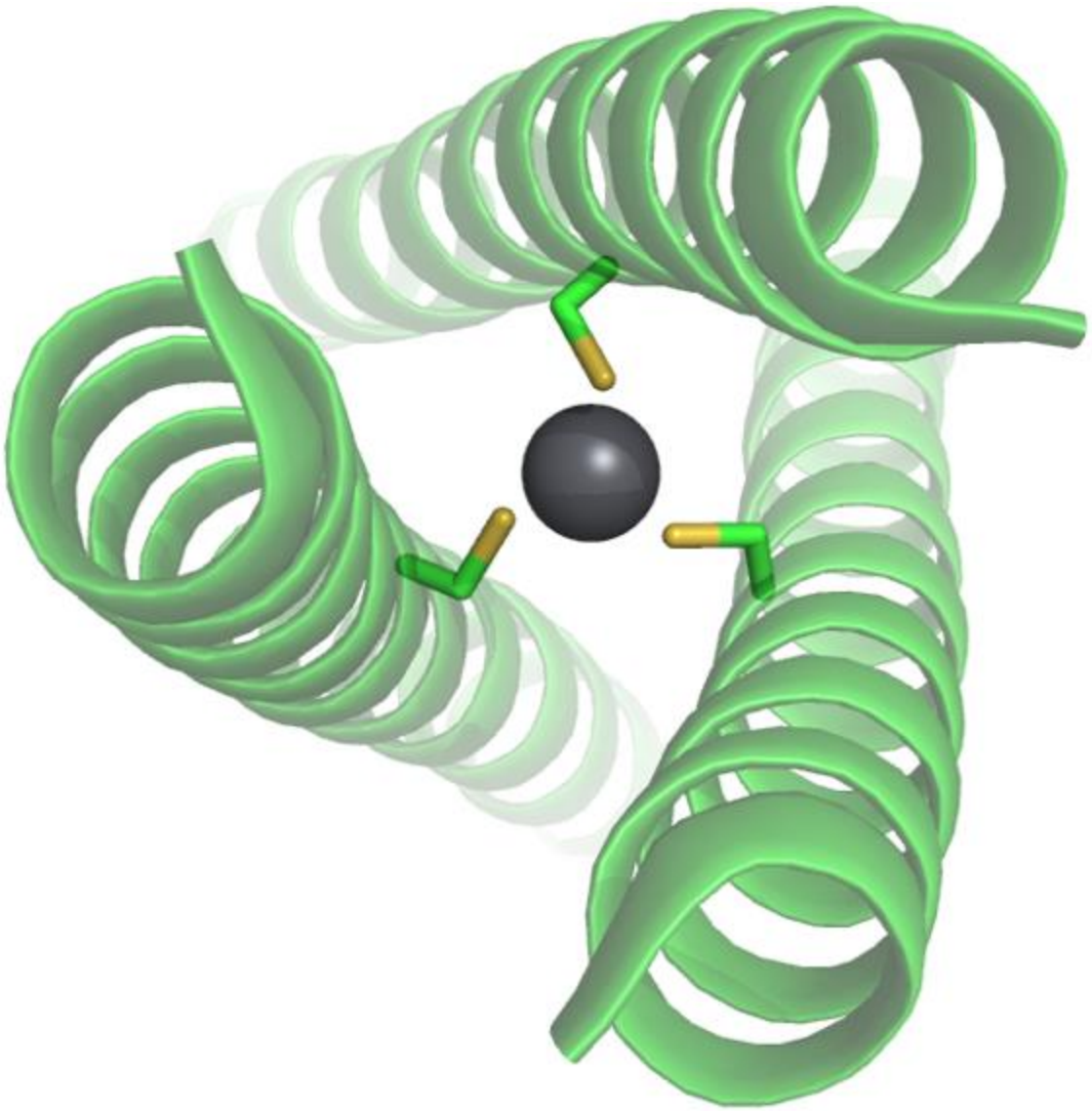

Figure 2-2 Top down view of Cys_3^a with Pb(II) shown as a grey sphere (PDB 5KB0).

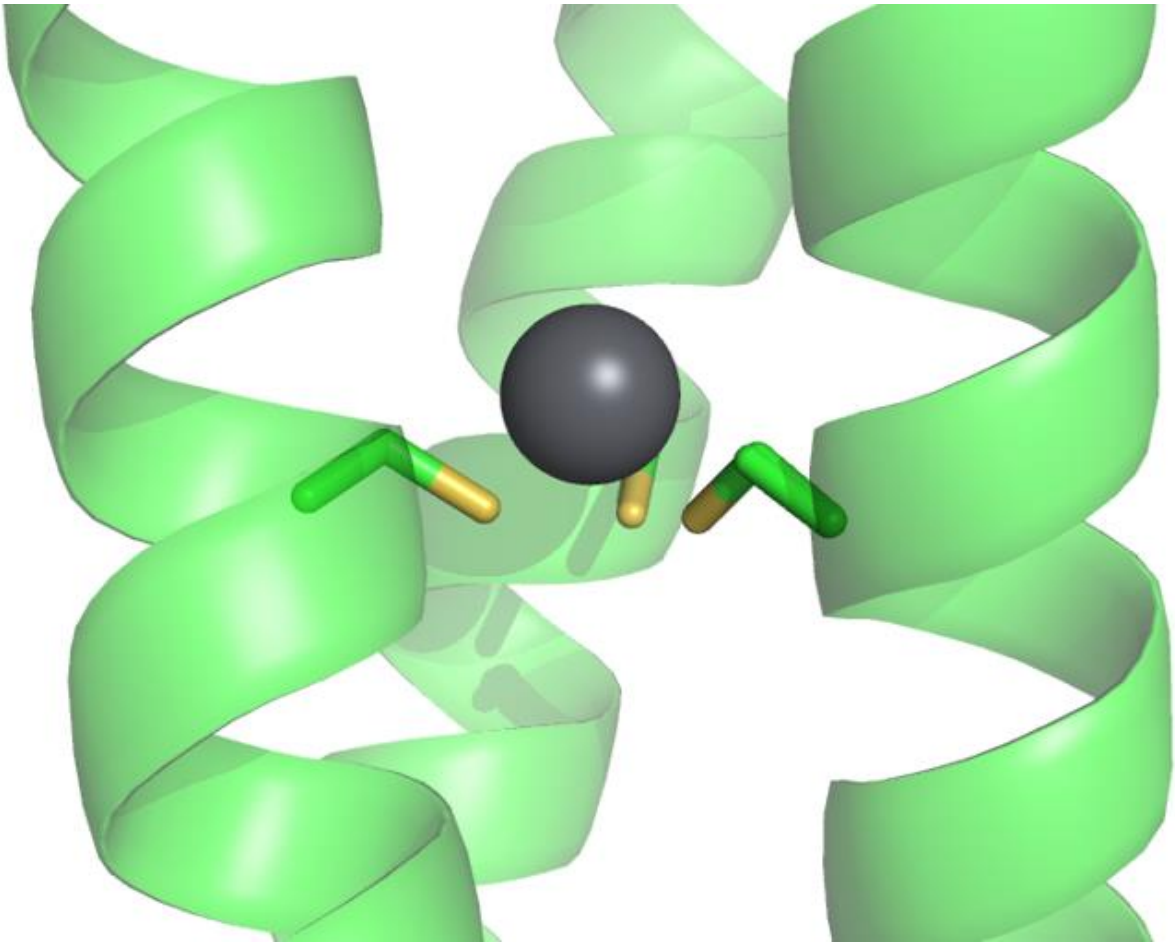

Figure 2-3 Side view of Pb(II) bound Cys_3^a with Pb(II) in grey and sulfur in yellow (PDB 5KB0)

It was previously hypothesized that the introduction of a less sterically hindered layer above the Cys_3^a site would allow the Pb(II) to bind in the more preferred exo conformation.[6-8] Thus, an alanine was introduced in the **d**-site directly above Cys^a, Ala^dCys^a. (N.B. peptide sequences are noted by the Leu substitutions from N to C terminus with subscripts denoting the number of each residue in the 3SCC and superscripts denoting **a** or **d** layers.) In this peptide, it was proposed that Pb(II) bound N-terminally of Cys_3^a in the exo conformation. To determine the relative affinities of Pb(II) for Cys_3^a and $Ala_3^dCys_3^a$ in the TRI scaffold, Dr. Kosh Neupane performed ^{207}Pb NMR experiments and found that, rather than two distinct peaks corresponding to single resonances for each homotrimer, intermediate peaks were observed. Dr. Mocny expanded upon this Pb(II) binding hypothesis by examining steric matching to produce heterotrimers. Dr. Kennan had previously produced heterotrimers using alanine and cyclohexylalanine throughout the core of the coiled-coil.[9] Could alanine and leucine behave similarly but require only two core layers and utilize natural amino acids?

The combination of Cys^a and Ala^dCys^a strands in the presence of Pb(II) resulted in unique spectra as observed by ^{207}Pb NMR (Figure 2-4). The homotrimeric constructs, Cys_3^a and $Ala_3^dCys_3^a$, are separated by 75 ppm, with the heterotrimeric constructs at 25 ppm intervals between the two. Unfortunately, the $Ala_1^dCys_3^a$ construct is not fully selective, a major peak is observed for the heterotrimeric construct with a minor peak from the $Ala_2^dCys_3^a$ construct. To demonstrate further that the intermediate heterotrimeric peaks were not the result of coalescence of homotrimeric signals a 5:1 mixture of Cys^a and Ala^dCys^a with 2 equivalents of Pb(II) was examined. Two resonances that correspond to the Cys_3^a and $Ala_1^dCys_3^a$ spectra were observed rather than a single peak 1/6 of the way between the homotrimeric signals. This behavior was consistent between pH 7.4 and 9.4 (Figure 2-5).

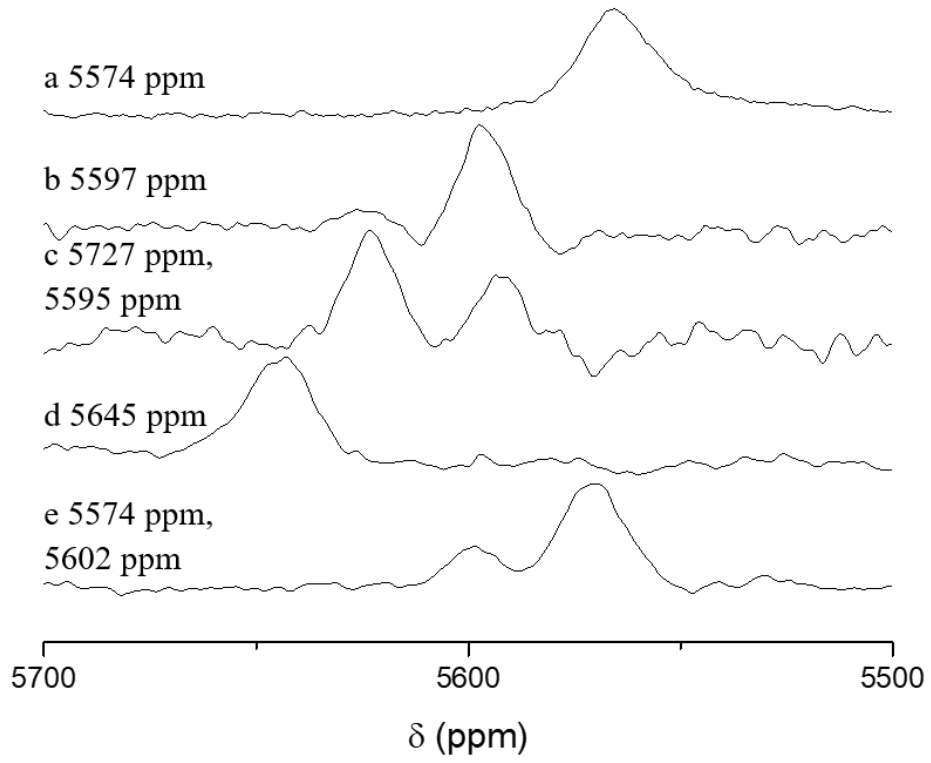

Figure 2-4 ^{207}Pb NMR of (a) $Ala_3^dCys_3^a$, (b) $Ala_2^dCys_3^a$, (c) $Ala_1^dCys_3^a$, (d) Cys_3^a, and (e) a 5:1 mixture of Cys^a and Ala^dCys^a with 2 equivalents of Pb(II) all at pH 7.4

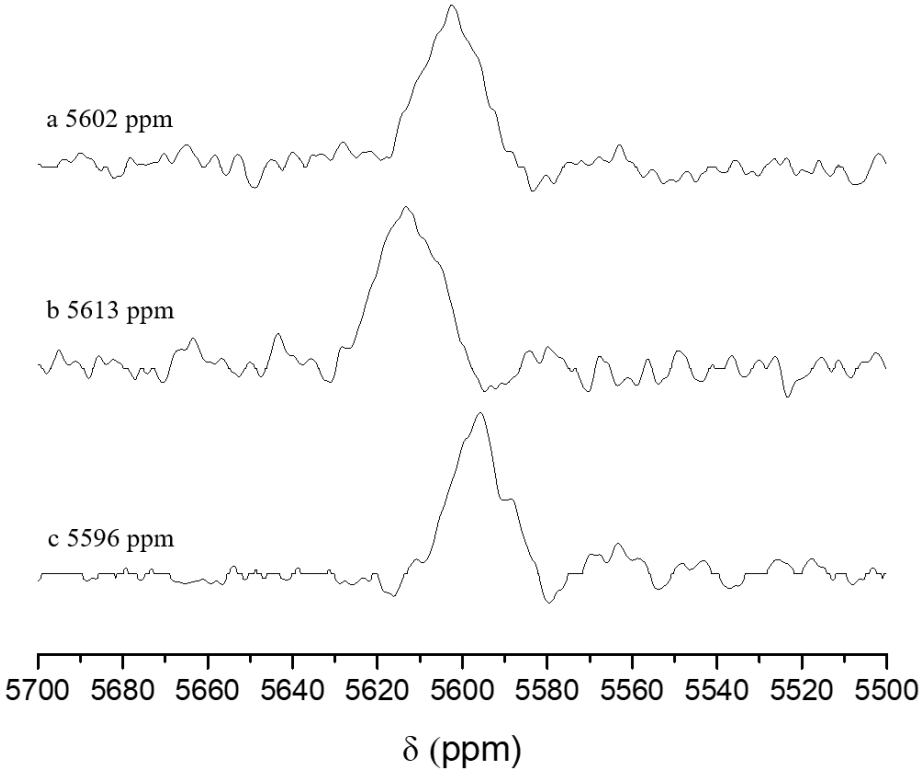

Figure 2-5 ^{207}Pb NMR of $Ala_2{}^dCys_3{}^a$ at (a) pH 9.4, (b) pH 8.4, and (c) pH 7.4

It was confirmed that these heterotrimeric peaks were of unique species rather than the coalescence of homotrimeric peaks by determination of the Pb(II) binding pK_a with heterotrimeric mixtures having more acidic pK_a's than calculated ratios of homotrimeric peaks (Table 2-2).[5, 10] These experiments, individually and considered together, demonstrate that it is possible to generate asymmetric self-assembling trimers with only Pb(II), $Cys_3{}^a$, and an adjacent mixed Ala/Leu layer.

Table 2-2 pK_a values for Pb(II)-S_3 complexation of Cys^a peptides

Peptide	pK_a
$Cys_3{}^a$	11.65 ± 0.03
$Ala_1{}^dCys_3{}^a$	10.93 ± 0.11
$Ala_2{}^dCys_3{}^a$	10.55 ± 0.07
$Ala_3{}^dCys_3{}^a$	10.88 ± 0.03

X-ray crystallography was able to determine the mode in which Pb(II) binds in $Ala_3{}^dCys_3{}^a$. Rather than the hypothesized rearrangement of Pb(II) binding, the metal remains in

the endo conformation and the space generated by the Ala substitution generated space for solvent to enter the hydrophobic cavity (Figure 2-6). With solvent within the coiled coil scaffold, these water molecules could interact either with the metal or the ligand sulfur atoms. The Cys residues maintain their conformation as in Cys_3^a, but three additional water molecules are present at the interface between two helices, allowing for interactions with two sulfur atoms, one at 3.0 Å and one at 3.4 Å (Figure 2-7). So, though some stability afforded by hydrophobic packing of Leu in the trimer is lost, this hydrogen bonding network provides stability through a different method. Thus, Dr. Mocny hypothesized that heterotrimer formation was, in fact, directed by the solvent interactions with the most stable trimer maximizing the stability of both leucine hydrophobic packing and space generated by the shorter alanine sidechain allowing for solvent hydrogen bonding. This stability was further investigated via QM/MM analysis as discussed below.

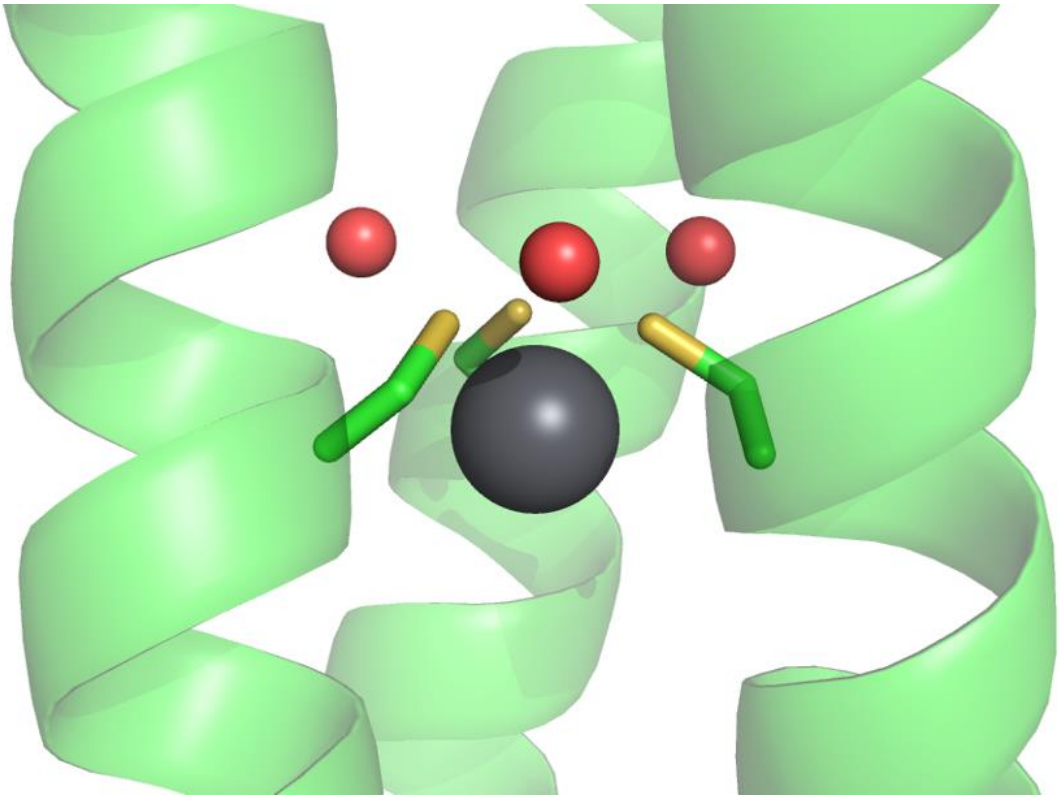

Figure 2-6 Side view of Pb(II) bound $Ala_3^dCys_3^a$ with Pb(II) in grey, water in red, and sulfur in yellow (PDB 6EGP).

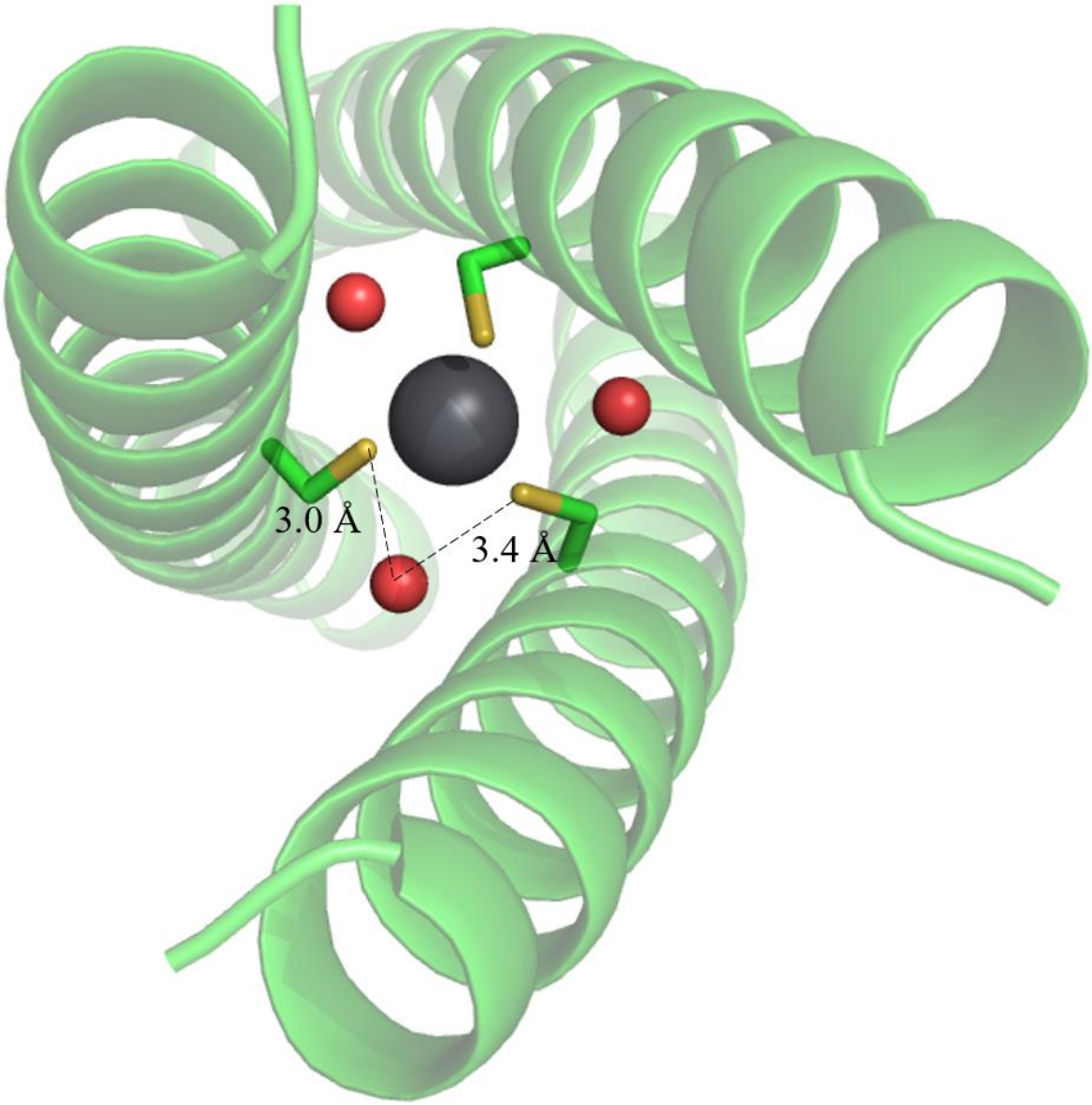

Figure 2-7 Top down view of $Ala_3{}^dCys_3{}^a$ (PDB 6EGP) with Pb(II) in grey and water in red with water-S distances shown as a dashed line.

In this chapter I escribe a method to form fully selective heterotrimeric constructs using alternate Cys_3 positions and characterize Pb(II) mediated heterotrimeric scaffolding throughout the GR peptide sequence. As described in chapter 1, the Pecoraro group has previously characterized apo and Pb(II) bound $Cys_3{}^a$ and $Cys_3{}^d$ sites. Initially, one would believe that $Cys_3{}^a$ is a better site for Pb(II) studies as it is preorganized for lead binding, meaning no significant rearrangement of Cys rotamers is required for Pb(II) to bind.[11] The $Cys_3{}^d$ site is only predisposed

for lead binding, with the requisite amino acids present but significant rearrangement necessary for Pb(II) to bind. Pb(II), however, has such a strong preference for trigonal pyramidal Pb-S_3 environments that this proves to be an insufficient barrier. In fact, Pb(II) was found to bind tighter to Cys_3^d than to Cys_3^a.[12] We hypothesized that by moving the Cys layer to a **d** site, Cys^d these changes in rotamer position and metal affinity could have a profound effect on heterotrimer formation. I aim to generate a site that can form selectively the 1 Ala: 2 Leu heterotrimer, which cannot form selectively with Cys^a sites and, ideally, also selectively form the 2 Ala: 1 Leu heterotrimer. This chapter will then describe how both Cys^a and Cys^d sites in alternate heptads bind Pb(II) and behave as potential heterotrimer nucleation sites. This aspect of my work was not aimed at generating new heterotrimers, but at the ability to change the location of the transition metal center. Dr. Zastrow found that kinetic parameters for pNPA hydrolysis using Zn CA mimics were affected by the positioning of the His_3 layer,[4] so an asymmetric system in which the His_3 site can be repositioned allows for maximal investigation of these parameters. This work describes the successful repositioning of this site to an alternate interior heptad and the unsuccessful repositioning at a C-terminal **a** site.

To this end, the GR L12C, a Cys^d peptide, was chosen as the new heterotrimer nucleation site. This position was chosen as it is an interior layer that is at least one heptad removed from both the Trp in position 2 and the His site in position 30 which proved to be successful for Cys^a (Figure 2-8). The alanine layer was incorporated in an analogous position to Ala^dCys^a based on the positioning of Pb(II) relative to the Cys-S plane. In Cys_3^d, Pb(II) remains in the endo conformation, but the different Cys orientation instead positions the Pb(II) on the N-terminal side of this layer, rather than on the C-terminal side as in Cys_3^a (Figure 2-9). Thus, I investigated Cys^dAla^a to generate a similar sterically open site opposite the Pb(II). I also investigated if this scaffolding technique could be applied to alternate heptad locations within the 3SCC because previous studies using homotrimeric Carbonic Anhydrase mimics demonstrated that K_M and V_{max} values differed depending on whether the catalytic Zn site was at the N vs C-terminal position of the protein. Thus, heterotrimers with varying catalytic sites, potentially having different activities might be realized. The goal of this project is to create a diverse library of asymmetric scaffolds in which A_2B and AB_2 trimers form selectively at multiple locations within the peptide trimer.

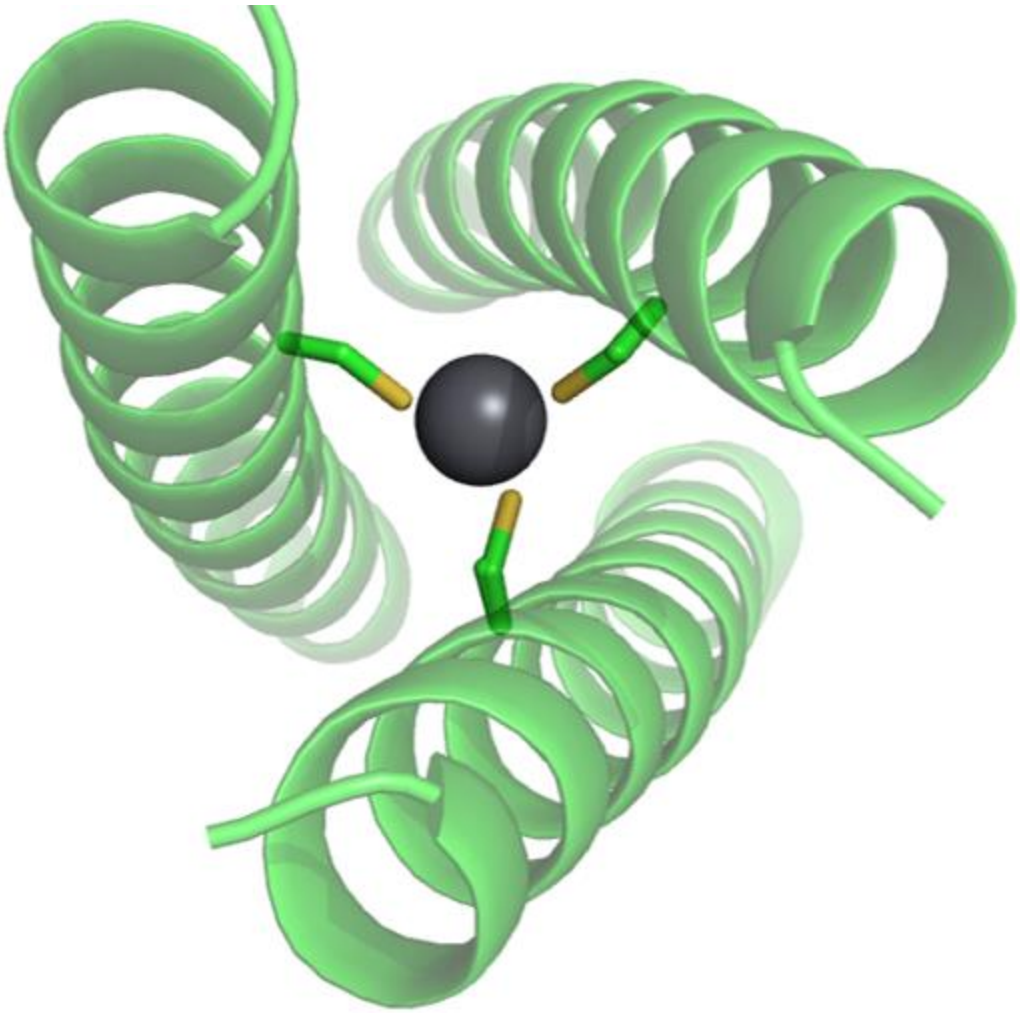

Figure 2-8 Top down view of Pb(II) bound Cys_3^d with lead in grey and sulfur in yellow

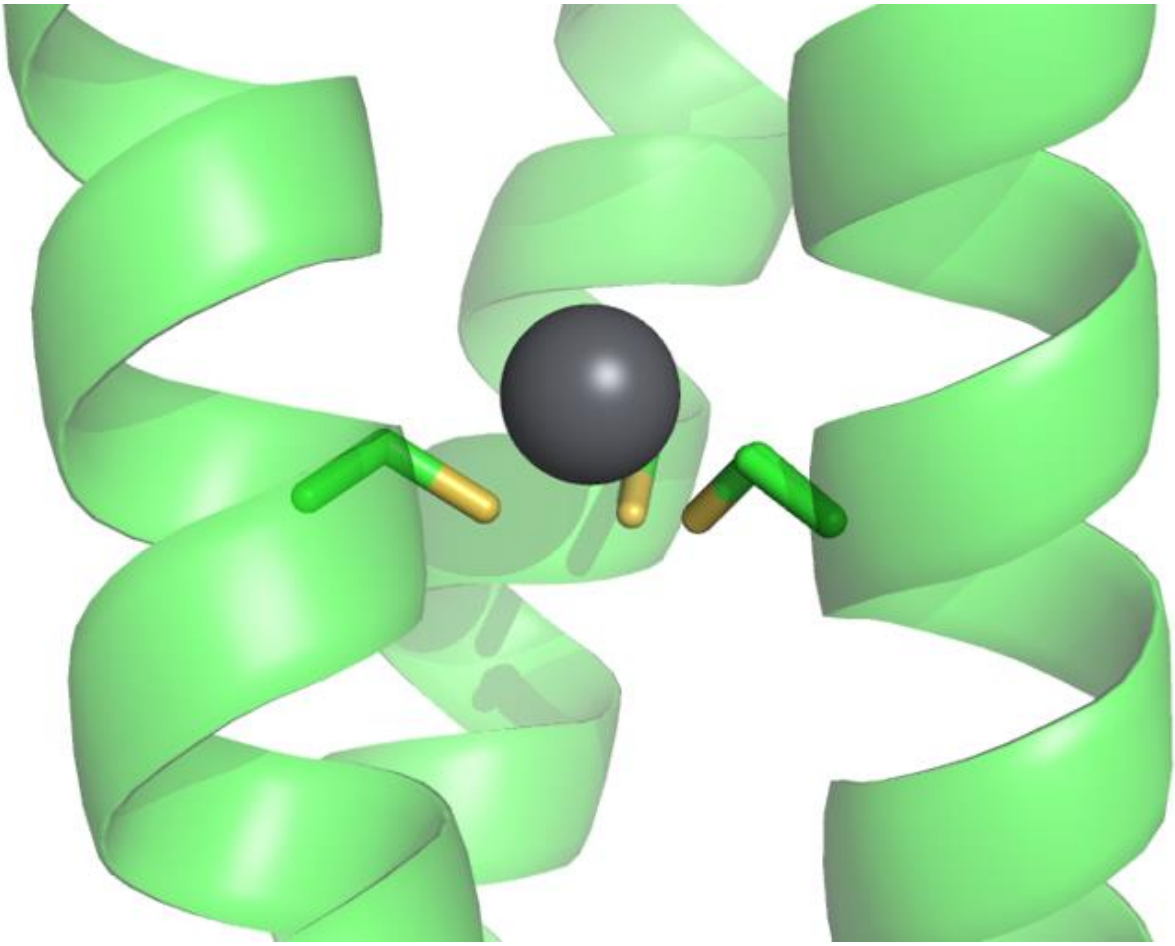

Figure 2-9 Side view of Cys_3^d with Pb(II) in grey and sulfur in yellow

Methods

Protein synthesis and purification

Peptides were synthesized on a Biotage Initiator+ Alstra peptide synthesizer using Fmoc-rink amide-methylbenzhydrylamine (MBHA) resin. Standard deprotection and coupling protocols with HOBt/HBTU/DIEA were used.[13] Peptides were cleaved from the resin using trifluoroacetic acid, thioanisole, ethanedithiol, and anisole (90:5:3:2) for four hours, precipitated with cold ether, and redissolved in double distilled water. The crude peptide was then lyophilized to dryness. The peptide was purified using a Waters 600 HPLC with a reverse phase C-18 column. A linear gradient from 70% A (0.1% trifluoroacetic acid in double distilled water) 30% B (0.1 % trifluoroacetic acid, 10% double distilled water, 90% acetonitrile) to 20% A/80% B was utilized at a flow rate of 20 mL/min over 35 minutes. ESI-MS was used to confirm the mass of the pure peptide, which was then lyophilized to dryness.

Circular dichroism spectroscopy

Circular dichroism spectroscopy was performed on a Jasco CD-Spectropolarimeter with a 1 cm pathlength quartz cuvette. Guanidinium hydrochloride (GuHCl) titrations were performed with a 10 μM peptide solution in 10 mM potassium phosphate, pH 7.5 at 25 °C. A solution containing 10 μM peptide, 10 mM potassium phosphate, and concentrated GuaHCl was titrated into the cuvette in 0.05 M GuaHCl steps to 7 M GuaHCl with 30 seconds of stirring at 450 rpm between each addition. The absorbance at 222 nm was monitored after each addition.

^{207}Pb NMR

^{207}Pb NMR was performed with unbuffered peptide solutions containing 3-5 mM trimer with 0.9 equivalents of isotopically enriched Pb per trimer in 10% D_2O prepared from a new ampule for each experiment. The pH was adjusted with small aliquots of KOH. The reported pH does not consider the deuterium concentration. Spectra were collected for 5-12 hours at 25 °C with no spin, 0.020 ms relaxation time, and 20 ms acquisition time, and a direct delay receiver time constant of ~90 at 145.95 MHz on a 700 MHz Varian NMR Spectrometer. All spectra were referenced to 1 M $Pb(NO_3)_2$ in D_2O (δ=-2990 ppm relative to $Pb(CH_3)_4$). Backwards linear prediction was performed to generate the reported Fourier transforms. The most intense peak in the FID, typically occurring between points 15 and 25, was selected as the point from which linear prediction was performed and the predicted number of points was equivalent to the number of excluded points. The peak area is dependent upon the point of linear prediction. The earliest, most intense point in the FID was chosen as the point of linear prediction (Figure 2-10, blue). This results in the most intense peak in the ^{207}Pb NMR (Figure 2-11). Spectra were exported directly from the acquisition software and were not processed in software such as MestReNova as the default frequency for Pb is inaccurate. Note that the original NMR probe broke had to be replaced halfway through this work with a probe of lower sensitivity, resulting in lower signal to noise spectra.

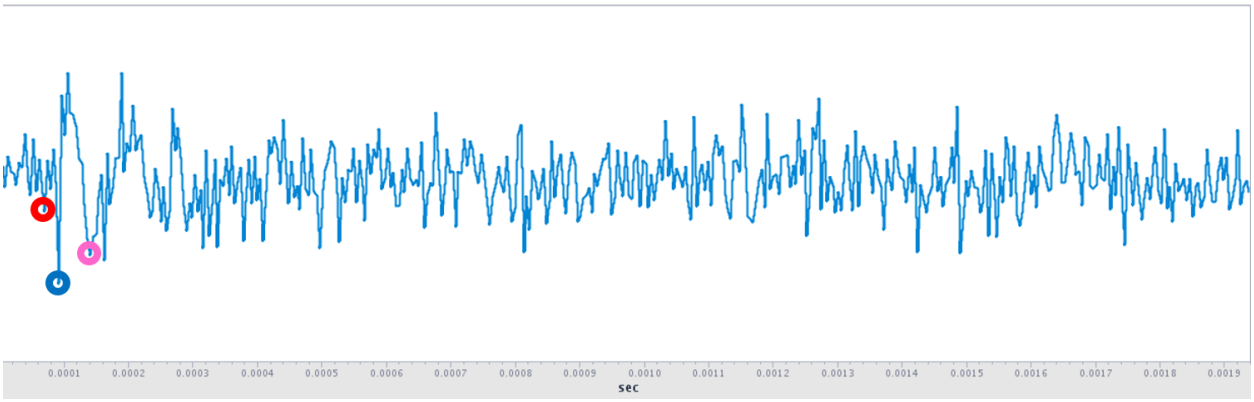

Figure 2-10 FID of a 12 hour acquisition for $Cys_3^dAla_3^a$ with point 17 in red, 22 in blue, and 32 in pink

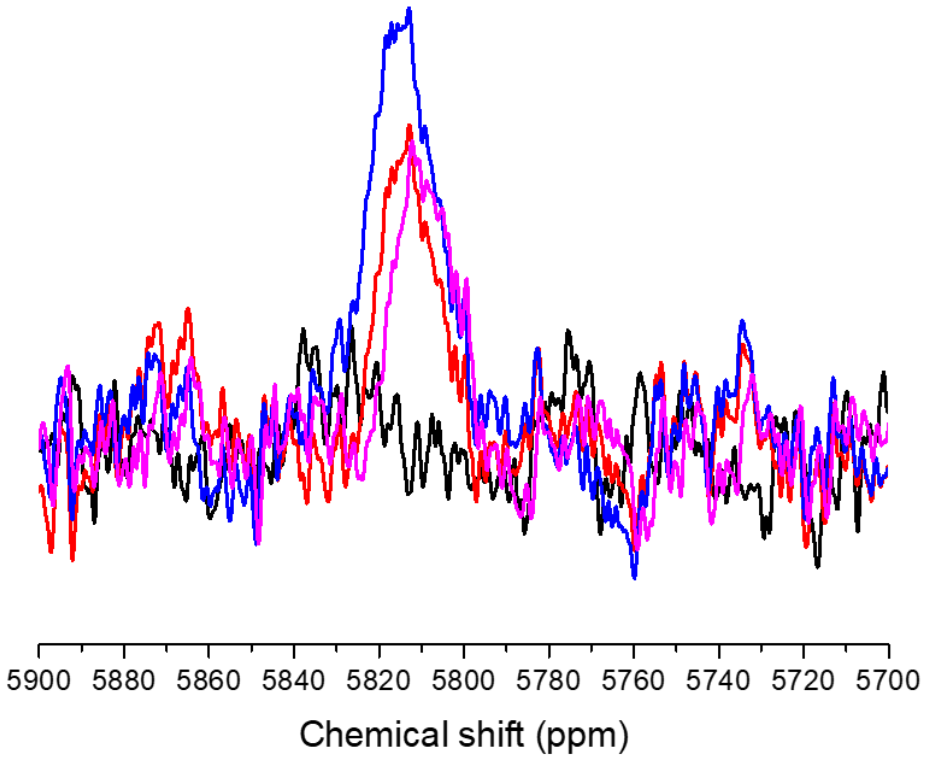

Figure 2-11 ^{207}Pb NMR of $Cys_3^dAla_3^a$ after a 12 hour acquisition with no linear prediction in black, linear prediction from point 17 in red, 22 in blue, and 32 in pink

Pb(II) titrations

UV-visible data was acquired on a Cary 100 Bio UV/Vis Spectrometer with a 1 cm pathlength quartz cuvette. A solution of 180 μM peptide at pH 7.5 in 50 mM HEPES is titrated with 0.1

equivalents of 10 mM $Pb(NO_3)_2$ with 10 minutes of stirring between each addition. The absorbance of the Pb-S_3 LMCT chromophore is monitored from 200 to 400 nm.

pH titrations

UV-visible data was acquired on a Cary 100 Bio UV/Vis Spectrometer with a 1 cm pathlength quartz cuvette. An unbuffered solution containing 180 μM peptide and 60 μM $Pb(NO_3)_2$ was titrated with KOH from pH ~3-10. The pH was measured and the absorbance of the Pb-S_3 LMCT band (λ_{max}=340-350 nm) was monitored after each addition. The resulting spectra were fit to four different deprotonation models. The first three models consider only the deprotonation of Cys sidechains in a fully formed 3SCC by three different processes: (i) single proton deprotonation, (ii) two proton simultaneous deprotonation, and (iii) two proton stepwise deprotonation. The fourth model considers the pH dependence of the 2SCC to 3SCC conversion in addition to the deprotonation of the Cys sidechain. The source of these protons are denoted as H_C for protons released by the Cys and H_E for protons released by the Glu residues to form the 3SCC.

In the single proton deprotonation model, we observe the following equilibrium:

Equation 2-1

$$Pbpep_3H_C \rightleftharpoons Pbpep_3^- + H^+$$

With the following K_a:

Equation 2-2

$$K_a = \frac{[H^+][Pbpep_3^-]}{[Pbpep_3H_C]}$$

Rearrangement of this equation yields:

Equation 2-3

$$[Pbpep_3H_C] = \frac{[H^+][Pbpep_3^-]}{K_a}$$

The following mass balance equation can also be applied:

Equation 2-4

$$[pep_3]_T = [Pbpep_3^-] + [Pbpep_3H_C]$$

Rearrangement of Equation 2-4 and substitution into Equation 2-3 yields the following:

Equation 2-5

$$[pep_3]_T = [Pbpep_3^-]\left(\frac{[H^+]}{K_a} + 1\right)$$

The absorbance of the peptide species in Equation 2-5 is proportional to its concentration as related by Beer's law:

Equation 2-6

$$Abs = \varepsilon * l * [pep_3]_T$$

Where ε is the extinction coefficient at the wavelength of maximum absorbance and l is the pathlength of the cuvette.

Substitution of Equation 2-5 into Equation 2-6 yields:

Equation 2-7

$$Abs = \varepsilon * l * \left([Pbpep_3^-]\left(\frac{[H^+]}{K_a} + 1\right)\right)$$

This equation can then be modified to represent progress along a normalized absorbance spectrum, in which x is pH, y is Abs, and y_{max} is the absorbance at 100% $Pbpep_3^-$ and K_a can be fit in Origin with Equation 2-8:

Equation 2-8

$$y = \frac{y_{max}}{\frac{10^{-x}}{K_a} + 1}$$

The second case, a simultaneous two proton deprotonation, is expressed by the following equilibrium:

Equation 2-9

$$Pbpep_3H_{2,C}^+ \rightleftharpoons Pbpep_3^- + 2H^+$$

The K_a for this expression is as follows:

Equation 2-10

$$K_{a2} = \frac{[H^+]^2[Pbpep_3^-]}{[Pbpep_3H_{2,C}^+]}$$

Substitution of the mass balance outlined in Equation 2-4 and rearrangement of terms in Equation 2-10 yields

Equation 2-11

$$[pep_3]_T = [Pbpep_3^-]\left(\frac{[H^+]^2}{K_{a2}} + 1\right)$$

As before, this can be substituted into Equation 2-6 to yield

Equation 2-12

$$Abs = \varepsilon * l * \left([Pbpep_3^-]\left(\frac{[H^+]^2}{K_{a2}} + 1\right)\right)$$

This equation can then be modified to represent progress along a normalized absorbance spectrum, in which x is pH, y is Abs, and y_{max} is the absorbance at 100% $Pbpep_3^-$ and K_{a2} can be fit in Origin with

Equation 2-13

$$y = \frac{y_{max}}{\frac{10^{-2x}}{K_{a2}} + 1}$$

This fit gives a combined K_a value for both deprotonation events, meaning the K_a of the simultaneous two proton deprotonation is ½ K_{a2}.

The final case, a step-wise two proton deprotonation is described by the following equilibria:

Equation 2-14

$$Pbpep_3H_{2,C}^+ \rightleftharpoons H^+ + Pbpep_3H_C \rightleftharpoons H^+ + Pbpep_3^-$$

K_{a1} describes the K_a of the transition from the doubly protonated to the singly protonated species as follows:

Equation 2-15

$$K_{a1} = \frac{[H^+][Pbpep_3H_C]}{[Pbpep_3H_{2,C}^+]}$$

K_{a2} describes the K_a of the transition from the singly protonated species to the deprotonated species as follows:

Equation 2-16

$$K_{a2} = \frac{[H^+][Pbpep_3^-]}{[Pbpep_3H_C]}$$

As in this model there are three peptide species, the mass balance equation is as follows:

Equation 2-17

$$[pep_3]_T = \left[Pbpep_3H_{2,C}^{+}\right] + [Pbpep_3H_C] + [Pbpep_3^{-}]$$

Rearrangement of Equation 2-15 and Equation 2-16 and subsequent substitution into Equation 2-17 yields:

Equation 2-18

$$[Pbpep_3]_T = [Pbpep_3^{-}]\left(\frac{[H^+]^2}{K_{a1}K_{a2}} + \frac{[H^+]}{K_{a2}} + 1\right)$$

Substitution of Equation 2-18 into Equation 2-6 yields:

Equation 2-19

$$Abs = \varepsilon * b * [Pbpep_3^{-}]\left(\frac{[H^+]^2}{K_{a1}K_{a2}} + \frac{[H^+]}{K_{a2}} + 1\right)$$

This equation can then be modified to represent progress along a normalized absorbance spectrum, in which x is pH, y is Abs, and y_{max} is the absorbance at 100% $Pbpep_3^-$. K_{a1} and K_{a2} can be fit in Origin by the following equation:

Equation 2-20

$$y = \frac{y_{max}}{\frac{10^{-2x}}{K_{a1}K_{a2}} + \frac{10^{-x}}{K_{a2}} + 1}$$

Each spectrum was fit to all three models and the best fit was determined to be the model with the lowest associated error.

For 30Cys[a], this model was modified to consider different extinction coefficients for each term in Equation 2-17 as determined by Pb(II) binding curves at pH 6, 7.5, and 9. Thus,

Equation 2-21

$$Abs = \varepsilon_1 * l * \left[Pbpep_3H_{2,C}\right] + \varepsilon_2 * l * [Pbpep_3H_C] + \varepsilon_3 * l * [Pbpep_3^{-}]$$

The extinction coefficients for each term are reported as fractions of the extinction coefficient for the $Pbpep_3^-$ species because the fit was performed with a normalized absorbance curve. Therefore,

Equation 2-22

$$y = \frac{y_{max}}{0.47\left(\frac{10^{-2x}}{K_{a1}K_{a2}}\right) + 0.63\left(\frac{10^{-x}}{K_{a2}}\right) + 1}$$

The pH titrations were also fit to a model considering Pb(II) binding as a function of 3SCC formation:

Equation 2-23

$$Pbpep_2H_E + pepH_C \rightleftharpoons Pbpep_3 + 2H^+$$

The K_a of $Pbpep_3$ formation is described by

Equation 2-24

$$K_a = \frac{[Pbpep_3][H^+]^2}{[Pbpep_2H_E][pepH_C]}$$

With three peptide species, the mass balance is as follows:

Equation 2-25

$$[pep]_T = [pepH_C] + 2[Pbpep_2H_E] + 3[Pbpep_3]$$

Note that this considers concentration of single peptide strands rather than 3SCC concentration. A second mass balance considering Pb(II) species can also be written as follows:

Equation 2-26

$$[Pb]_T = [Pbpep_2] + [Pbpep_3]$$

Rearrangement of Equation 2-25 and Equation 2-26 and insertion into Equation 2-24 yields

Equation 2-27

$$[Pbpep_3]^2 + [Pbpep_3]([Pb]_T - [pep]_T - K_a[H^+]^2) + [Pb]_T[pep]_T - 2[Pb]_T^2 = 0$$

The real solution of this equation can be substituted into Beer's law (Equation 2-6) where the extinction coefficient is determined by the absorbance of 1 equivalent of Pb(II) bound to each peptide as in Figure 2-15.

Crystallography

The crystal structure for GRCS $Cys_3^dAla_3^a$ was obtained via sitting drop vapor diffusion at 20 °C, with drops containing 0.75 μL: 0.75 μL ratio of peptide/precipitant solutions. The peptide solutions were prepared from 20 mg/mL peptide, 15 mM $Zn(OAc)_2$, 0.5 mM Tris buffer pH 8.5 and 1 eq. of $Pb(NO_3)_2$ per 3SCC. The crystal (PDB ID: 6MCD) was crystallized in 30% (v/v) PEG-600, 10% (v/v) glycerol, 0.1 M MES pH 6.0 and 5% (w/v) PEG-1000. Data were collected at the Advanced Photon Source on the LS-CAT Beamline 21-ID-G equipped with a Mar 300 CCD detector with a 1° oscillation. The crystal diffracted to 1.50 Å resolution and the data were processed and scaled to R32 space group using HKL 2000,[14] corresponding to one helix per

asymmetric unit (ASU). The combination of the three adjacent ASUs that are constrained by the threefold axis, generated a well-folded, parallel 3SCC structure. The phases of $Cys_3^dAla_3^a$ were obtained by using the **GC**$L12_DLL16C$ (PDB ID: 6EGL) structure as a starting model in Arp/warp.[15] The structure consequently underwent iterative rounds of electron density fitting and refining in Coot[16] and Buster 2.11.2,[17] resulting in $R_{working}/R_{free}$ of 20.6/20.6%. The validity of the models was verified using MolProbity.[18] All the residues were present within allowed regions of the Ramachandran plot. The crystallographic data collections and refinement statistics of both crystal structures are shown in

Table 2-3.

Table 2-3 Data collection and refinement statistics for $Cys_3^dAla_3^a$

Peptide	**Pb(II)(GC-L12CL16A)$_3$ (Pb(II)$Cys_3^dAla_3^a$)**
PDB ID	**6MCD**
Data collection	
Space Group	R32
Cell dimensions	
a, b, c (Å)	38.304, 38.304, 141.141
α, β, γ (°)	90.00, 90.00, 120.00
Wavelength (Å)	0.97856
Resolution (Å)[1]	1.50 (1.53-1.50)
R_{sym} (%)[2]	6.3 (49.3)
$\langle I/\sigma I \rangle$[3]	>50 (2)
Completeness (%)[4]	99.8 (100)
Redundancy	15.6 (16.0)
Refinement	
Resolution (Å)	1.50
R-Factor (%)[5]	20.6
R_{free} (%)[6]	20.6
Protein atoms	279
Metal ions	1/3 Pb(II) at the twelfth position
Water Molecules	1 Zn(II) on helical surface
Unique Reflections	51
R.m.s.d.[7]	6703
Bonds	
Angles	0.01
MolProbity Score[8]	1.05
Clash Score[8]	0.50
	0

[1]Statistics for highest resolution bin of reflections in parentheses.
[2]$R_{sym} = \Sigma_h \Sigma_j \mid I_{hj} - \langle I_h \rangle \mid / \Sigma_h \Sigma_j I_{hj}$, where I_{hj} is the intensity of observation j of reflection h and $\langle I_h \rangle$ is the mean intensity for multiply recorded reflections.
[3]Intensity signal-to-noise ratio.
[4]Completeness of the unique diffraction data.
[5]R-factor = $\Sigma_h \mid IF_oI - IF_cI \mid / \Sigma_h |F_o|$, where F_o and F_c are the observed and calculated structure factor amplitudes for reflection h.
[6]R_{free} is calculated against a 10% random sampling of the reflections that were removed before structure refinement.
[7]Root mean square deviation of bond lengths and bond angles.
[8]From the Buster program[17]

All other structures discussed herein were previously collected and refined by Dr. Leela Ruckthong.

Computations

The complexation energies for all systems in the Pb(II) bound and apo forms were computed using two-layer Quantum Mechanics/Molecular Mechanics (QM/MM) ONIOM[19-20] calculations

by Dr. Rajeev Prabhakar at the University of Miami. This method does not require explicit QM-MM coupling terms and the bond between the QM and MM regions is treated using the link atom method.[21] In the ONIOM method, the MM energy [E_{MM} (model)] of the QM (model) part is subtracted from the sum of the QM energy of the model [E_{QM} (model)] and MM energy [E_{MM} (real)] of the whole (real) system i.e. E_{ONIOM}(QM/MM) = E_{QM} (model) + E_{MM} (real) - E_{MM} (model). This procedure corrects the artifacts introduced by the link atom. The details and applications of this method were reviewed recently.[22]

The structures of both homonuclear and heteronuclear strands were created through L16A mutations in the X-ray structures of Cys_3^d. The QM/MM calculations were performed using both X-ray structures and their equilibrated conformations (only for the apo form) provided by molecular dynamics (MD) simulations. They were performed at the B3LYP[23-24]/AMBER[25] level of theory using the Gaussian 09 program.[26] The following basis sets were used for atoms in the QM part in these calculations: Lanl2dz [with corresponding Hay-Wadt effective core potential[27] (ECP)] for Pb and Zn metals; 6-311G(d) for the O, N and S atoms; and 6-31G for the C and H atoms. The interactions between the QM and MM parts were treated by mechanical embedding.[28-29] All MD simulations were performed utilizing the AMBER03[30-31] force field and TIP3P[32] model for water molecules as implemented in the GROMACS program.[33-34] In the ONIOM calculations, the QM part includes Zn, Pb, Cys16, Glu31, Glu34 and His35 (157 atoms) for the metal bound form and either Cys16 or Cys19 residue (30 atoms) for the apo form. The rest of the system was included in the MM part (~1600 atoms for the metal bound and ~1350 for the apo form).

Results

Stability determination of apo-peptides by chemical denaturation

The stabilities of apo-Cys_3^d and apo-$Cys_3^dAla_3^a$ were determined by chemical denaturation with Guanidinium Hydrochloride (GuHCl). Apo-Cys_3^d folded into an alpha-helical coiled coil with characteristic absorption minima at 208 nm and 222 nm (Figure 2-12). The increase in signal below 210 nm in the final scan (red) is due to detector overload from the high concentration of GuHCl.

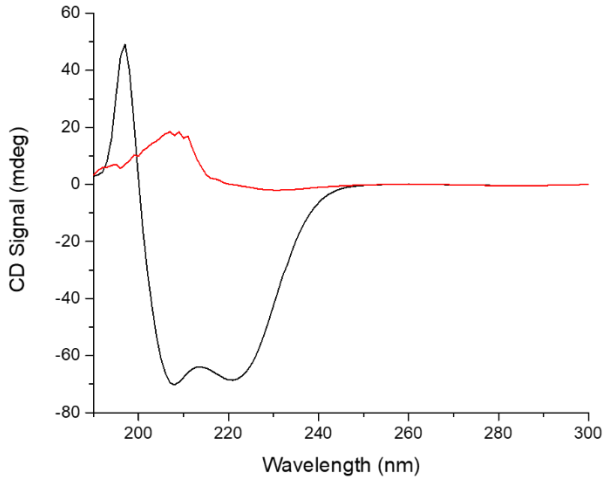

Figure 2-12 Initial (black) and final (red) CD spectra of 10 μM apo-Cys_3^d in 10 mM potassium phosphate pH 7.5

Similarly, apo-$Cys_3^dAla_3^a$ folded into an alpha-helical coiled coil (Figure 2-13). There is no difference in initial stability between the two peptides as determined by the signal at 222 nm.

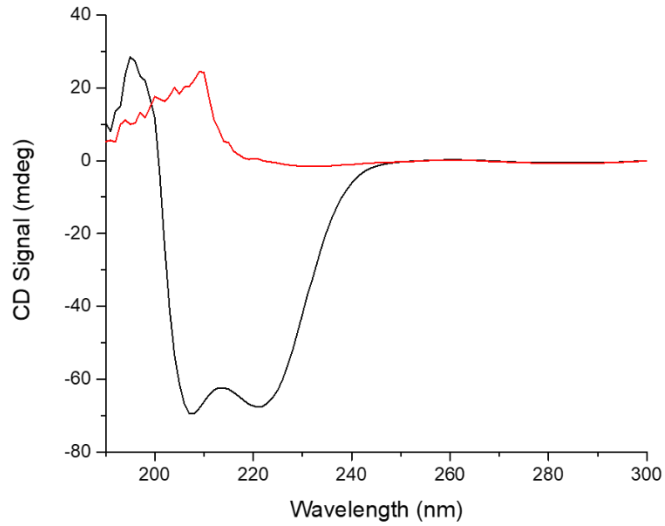

Figure 2-13 Initial (black) and final (red) CD spectra of 10 μM apo-$Cys_3^dAla_3^a$ in 10 mM potassium phosphate pH 7.5

Chemical denaturation with GuHCl was performed. The denaturation curves were not fit to a two state unfolding model because an initial plateau was not present (Figure 2-14). Apo-$Cys_3^dAla_3^a$ unfolded more with lower concentrations of GuHCl, with a midpoint of unfolding of 1.45 M vs. 1.85 M for apo-Cys_3^d.

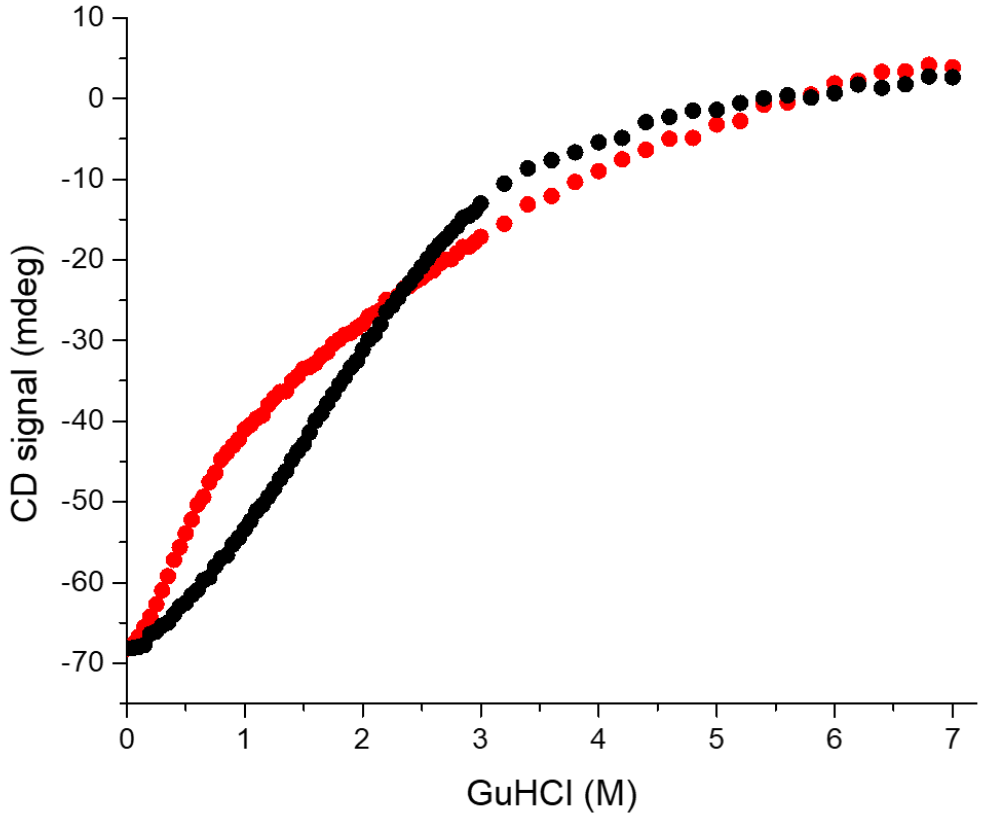

Figure 2-14 CD denaturation spectra of 10 μM Cys_3^d (black) and $Cys_3^dAla_3^a$ (red) in 10 mM potassium phosphate pH 7.5

Pb(II) binding

$Pb(NO_3)_2$ was titrated into a solution of apo peptide to determine the binding stoichiometry and λ_{max} of the Pb-S_3 LMCT. Pb(II) bound Cys_3^d, $Cys_3^dAla_3^a$, and heterotrimeric mixtures all bound Pb(II) in a 1:3 ratio (metal to monomer, Figure 2-15). Pb(II)-Cys_3^d had the highest energy LMCT band at 339 nm and Pb(II)-$Cys_3^dAla_3^a$ had the lowest energy band at 342 nm, with the maximum absorbance of heterotrimeric species at energies between the two homotrimeric signals.

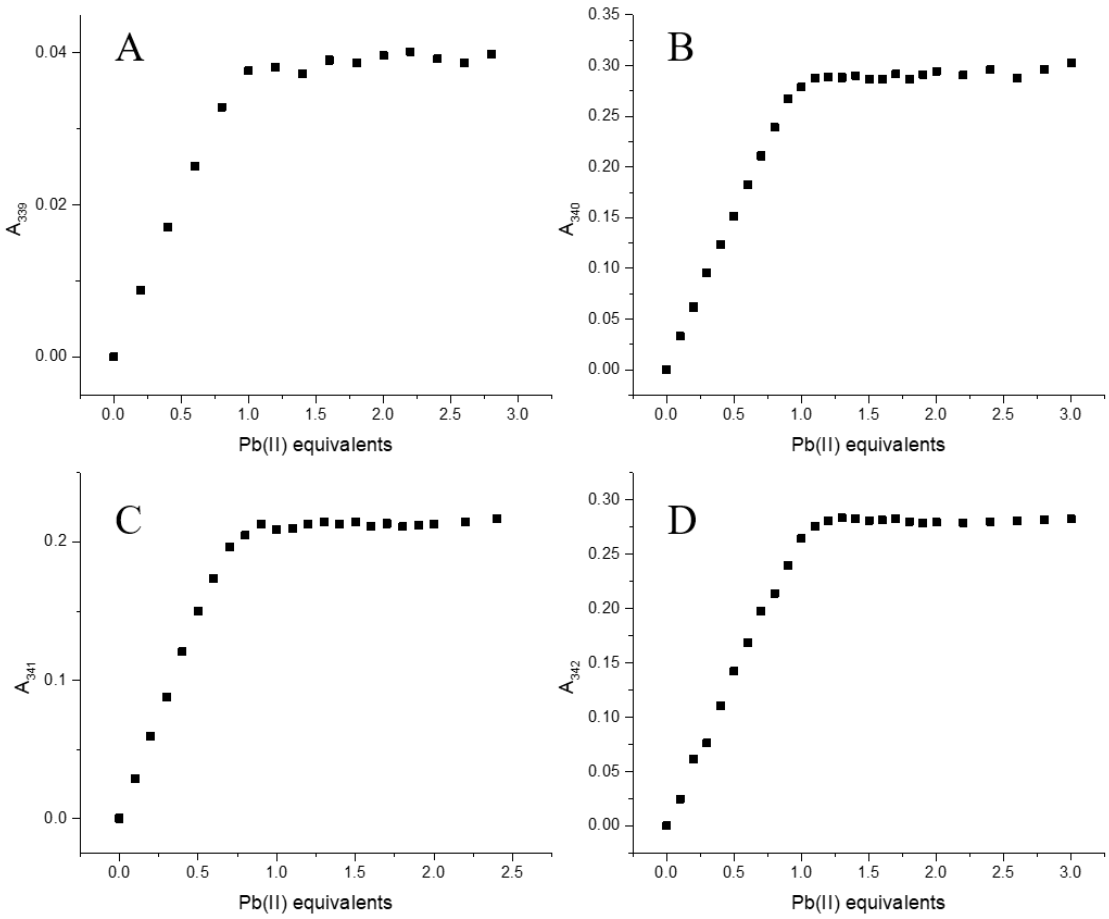

Figure 2-15 Titration curves of (A) Cys_3^d, (B) $Cys_3^dAla_1^a$, (C) $Cys_3^dAla_2^a$, and (D) $Cys_3^dAla_3^a$ at λ_{max} of the Pb-S_3 LMCT with Pb(II) equivalents relative to trimer concentration. Data are truncated at the point of precipitation. Experiments were performed with 60 μM 3SCC and 60 μM equivalent of $Pb(NO_3)_2$ in 50 mM HEPES pH 7.5.

pH dependence of Pb-S_3 complexation

The pH dependence of Pb(II) complexation was determined by titration of KOH into a solution of apo peptide and $Pb(NO_3)_2$. Previous work in the Pecoraro group has considered the pH dependence of Pb(II) complexation occurring only in fully formed 3SCCs where the protons being lost are only from the cysteine sidechains. As such, the first fits tried for the Cys^d peptides were a one proton deprotonation, simultaneous two proton deprotonation, and a stepwise two proton deprotonation. Before discussing these results, we must first consider $30Cys^a$ as this case provides necessary context for determination of the best fit.

$30Cys^a$ places the Cys substitution in the most C-terminal **a** site, which proved to have significant effects on the pH dependence of Pb(II) complexation. Unlike previously reported

constructs, two spectral features were observed in the near-UV region, one with maximum absorbance at 324 nm and a second with maximum absorbance at 346 nm (Figure 2-16). The higher energy feature is predominant below pH 6 but is converted to the lower energy feature, that of PbS_3, above pH 7. This transition occurs with an isosbestic point at 337 nm, indicating that this shift in λ_{max} is the conversion of one species to another.

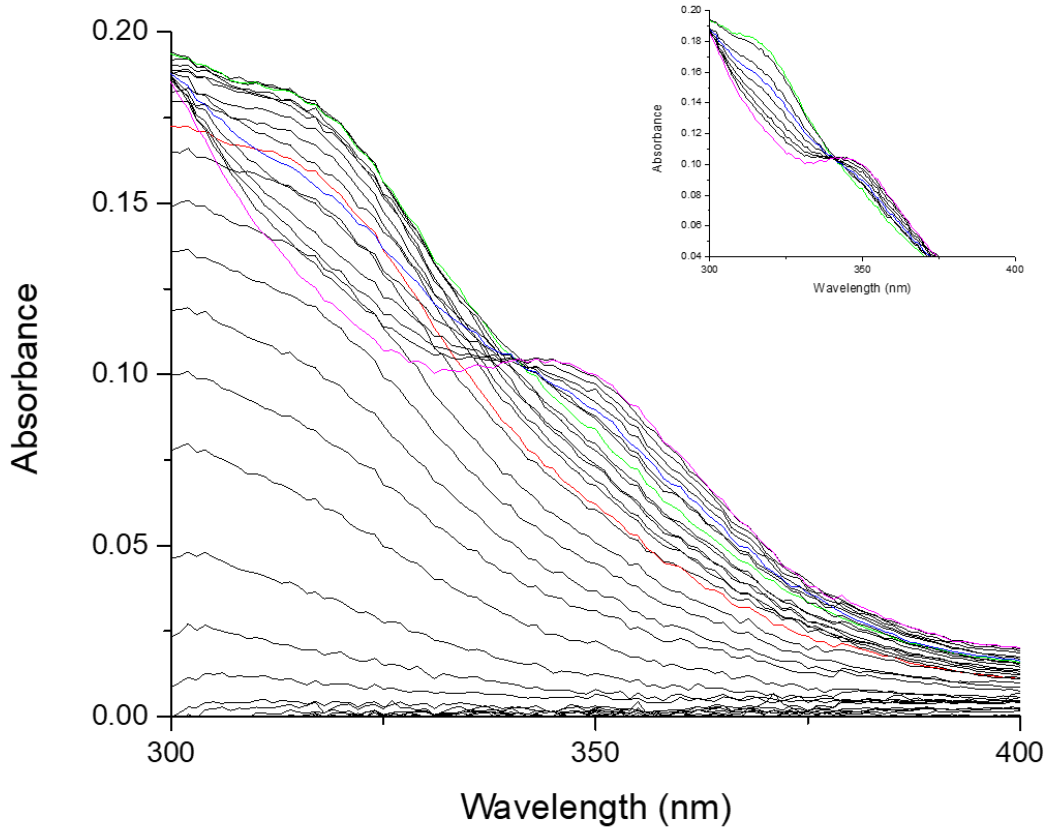

Figure 2-16 UV-visible spectra of 60 μM Pb(II) bound 60 μM 30Cys$_3$[a] from pH 3 to 10 with pH6 highlighted in red, pH 7 in green, pH 8 in blue, and pH 9 in pink. pH 7 to 9 is displayed as an inset to highlight the isosbestic conversion.

The titration curve at 346 nm is also indicative of a stepwise deprotonation (Figure 2-17). The fits for this peptide are discussed in the following section regarding alternate Cys positions. This case is discussed here as it is the first peptide in which there is spectroscopic evidence for an intermediate species. While the identity of this intermediate is not known, it is either the PbS_2SH species or a PbS_2 species, in which the third sulfur does not associate in strongly acidic conditions. Thus, for an intermediate species to exist in the trimers discussed herein, one would

expect to see a UV signal around 325 nm. The Pb-S_3 UV absorption profile occurs over a very limited range (338 to 346 nm), with Cys^d trending at higher energy than Cys^a, though this trend is not absolute. As such, one would expect the λ_{max} of the intermediate species to fall within a narrow range as well. Consideration of a stepwise fit, therefore, is dependent upon observation of a higher energy species.

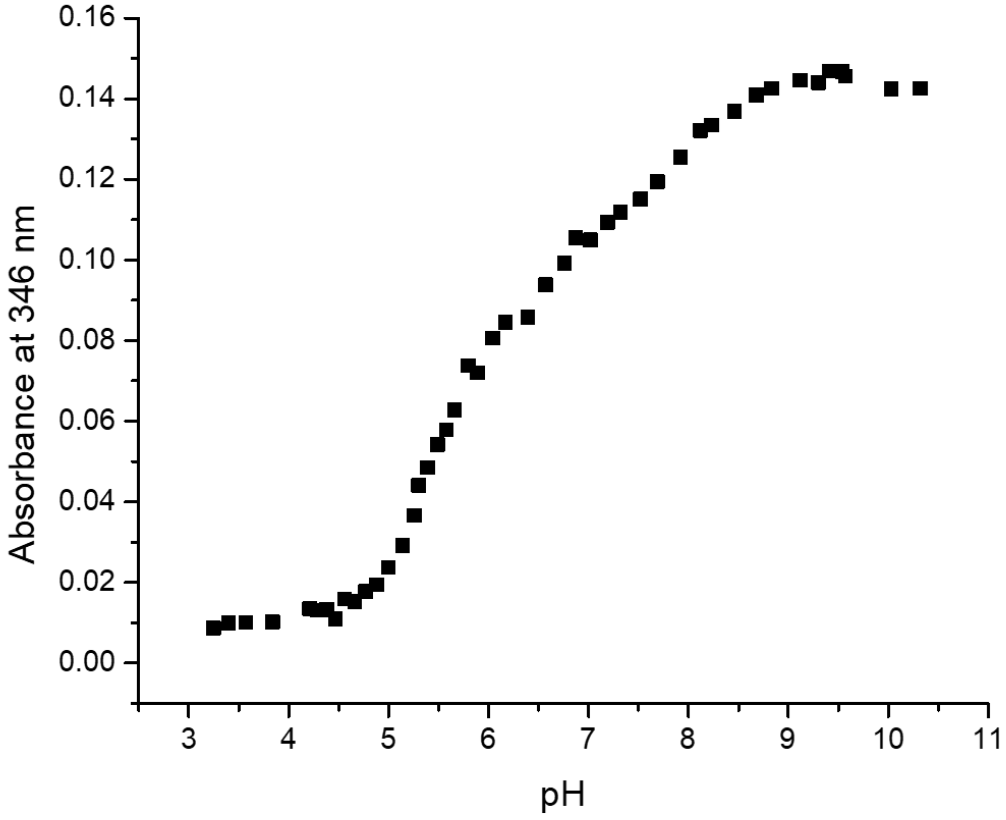

Figure 2-17 pH dependence of Pb-S_3 formation for $30Cys_3^a$

In the case of the Cys^d peptides, the transition from free thiol to Pb-S_3 occurred between pH 5 and 7, with full Pb-S_3 observed above pH 7.5. The titration curves were fit to a one proton deprotonation, simultaneous two proton deprotonation, and stepwise two proton deprotonation model. All peptides best fit to a simultaneous two step deprotonation model, though none of these models accurately fit all areas of the curve (Table 2-4). The spectra of these four peptides

do not have any feature indicative of the intermediate observed in 30Cys[a] (Figure 2-18). Thus, while a stepwise fit was attempted it is not supported by the spectroscopy.

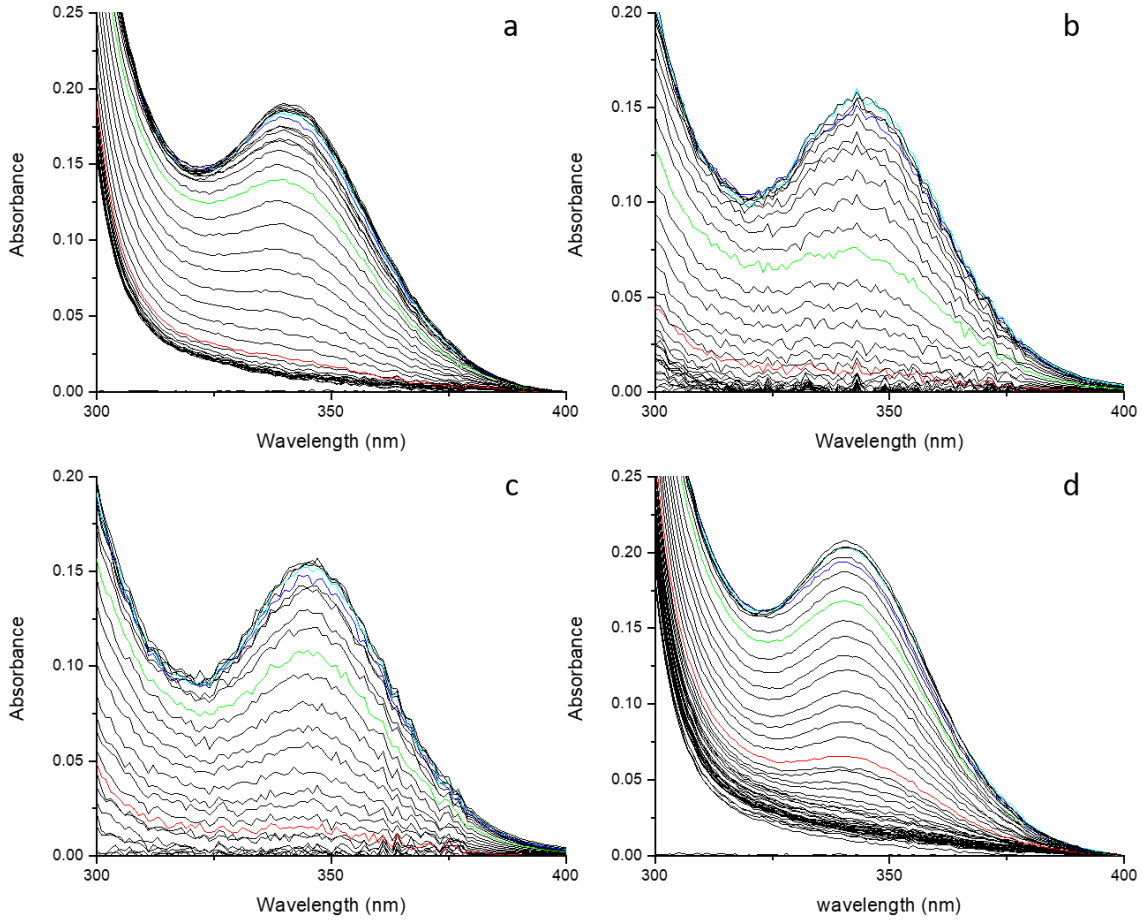

Figure 2-18 pH dependent absorption profiles of (a) Cys_3^d, (b) $Cys_3^dAla_1^a$, (c) $Cys_3^dAla_2^a$, and (d) $Cys_3^dAla_3^a$ with the spectra from pH 3 to 10 with pH 5 highlighted in red, pH 6 in green, pH 7 in dark blue, and pH 8 in light blue. All spectra contain 60 μM $Pb(NO_3)_2$ and 60 μM 3SCC.

$Cys_3^dAla_3^a$ fit with the most acidic pK_a, 11.2 ± 0.2 (Figure 2-19). The best fit across triplicate runs was determined to be the simultaneous two proton deprotonation, though Figure 2-19b depicts the limitations of this model to accurately fit the high pH region of the curve.

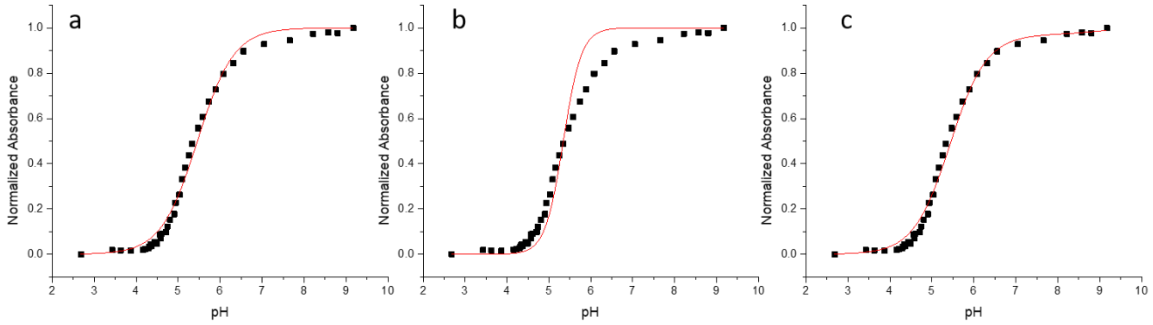

Figure 2-19 pH profile of PbS_3 formation for $Cys_3^dAla_3^a$ fit to (a) one proton deprotonation, (b) simultaneous two proton deprotonation, and (c) stepwise two proton deprotonation models. All spectra contain 60 μM $Pb(NO_3)_2$ and 60 μM 3SCC.

Both $Cys_3^dAla_2^a$ and $Cys_3^dAla_1^a$ also fit best to a simultaneous two proton deprotonation (Figure 2-20 and Figure 2-21, respectively). While the stepwise two proton deprotonation mechanism visually fits well, in both cases either the first or second step fit well, but not both. Additionally, as described above with $30Cys_3^a$, an intermediate lead-sulfur species of higher energy than the Pb-S_3 species fit to the stepwise model. These spectra, therefore, do not support a stepwise fit as no intermediate is observed. With the simultaneous two proton model, these spectra fit to pK_a's of 11.6 ± 0.2 and 11.9 ± 0.2, respectively. The single proton deprotonation mechanism also provided a good visual fit, but with higher error than the simultaneous two proton deprotonation model.

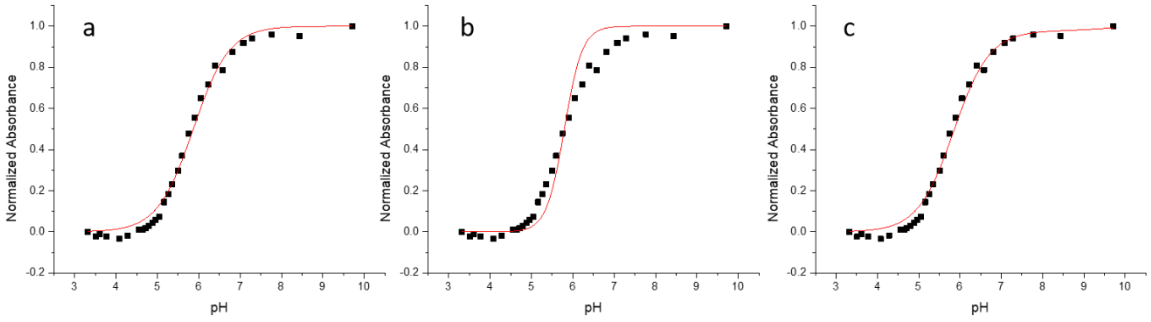

Figure 2-20 pH profile of PbS_3 formation for $Cys_3^dAla_2^a$ fit to (a) one proton deprotonation, (b) simultaneous two proton deprotonation, and (c) stepwise two proton deprotonation model. All spectra contain 60 μM $Pb(NO_3)_2$ and 60 μM 3SCC.s

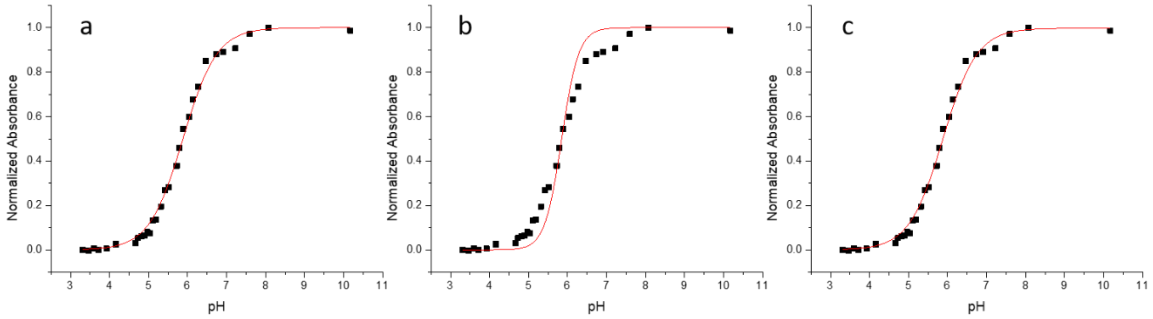

Figure 2-21 pH profile of PbS_3 formation for $Cys_3^dAla_1^a$ fit to (a) one proton deprotonation, (b) simultaneous two proton deprotonation, and (c) stepwise two proton deprotonation model. All spectra contain 60 μM $Pb(NO_3)_2$ and 60 μM 3SCC.

The Cys_3^d homotrimer also fit best to a simultaneous two proton deprotonation with a pK_a of 11.7 ± 0.2 (Figure 2-22). Again, the stepwise model fits well visually but is not supported by the data. Both heterotrimers have a pK_a within error of this value.

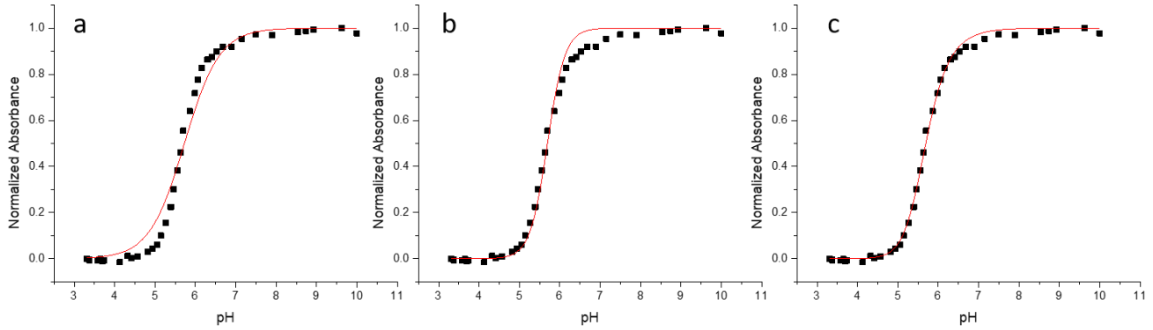

Figure 2-22 pH profile of PbS_3 formation for Cys_3^d fit to (a) one proton deprotonation, (b) simultaneous two proton deprotonation, and (c) stepwise two proton deprotonation model. All spectra contain 60 μM $Pb(NO_3)_2$ and 60 μM 3SCC.

Table 2-4 pK_a values for the formation of Pb-S_3 fit to one proton, two proton simultaneous, and two proton stepwise equations as described in the methods section

Peptide	One proton	Two proton simultaneous	Two proton stepwise
Cys_3^d	6.2 ± 0.4	11.7 ± 0.2	6.0 ± 0.2 12.3 ± 0.5
$Cys_3^dAla_1^a$	6.0 ± 0.2	11.9 ± 0.2	6.0 ± 0.1 11.3 ± 0.4
$Cys_3^dAla_2^a$	5.87 ± 0.2	11.6 ± 0.2	5.7 ± 0.5 10.4 ± 0.2
$Cys_3^dAla_3^a$	5.68 ± 0.6	11.2 ± 0.2	5.7 ± 0.1 11.8 ± 0.3

As none of these models accurately fit the entire curve, another model was considered in which Pb(II) binding is dependent not only on deprotonation of the Cys sidechain but also on the formation of the 3SCC from the 2SCC. Cys_3^d and $Cys_3^dAla_1^a$ had the lowest K_d values of 90 ± 20 and 60 ± 20 nM, respectively (Figure 2-23). $Cys_3^dAla_2^a$ forms a 3SCC with a K_d of 120 ± 10 nM and $Cys_3^aAla_3^a$ forms with a K_d of 360 ± 20 nM.

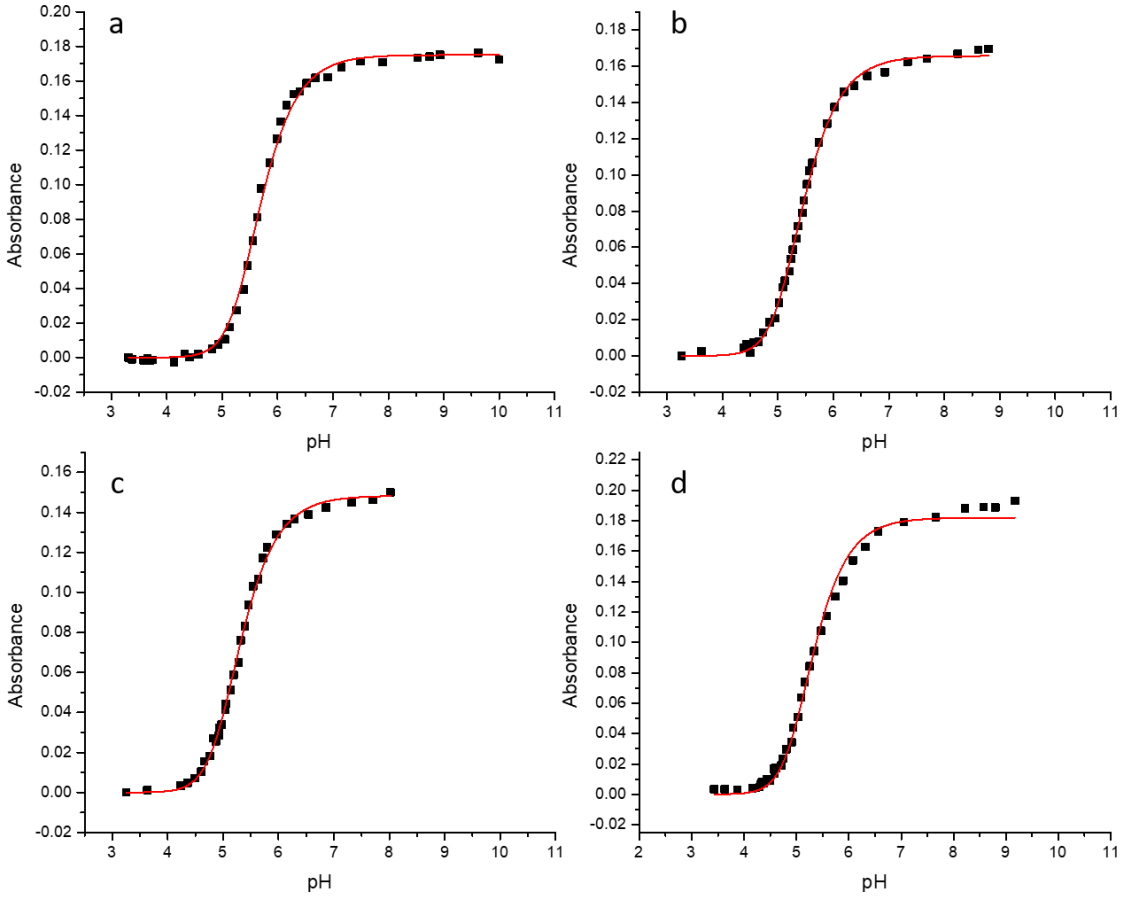

Figure 2-23 pH profile of PbS_3 formation fit to a PbS_2 to PbS_3 model for (a) Cys_3^d, (b) $Cys_3^dAla_1^a$, (c) $Cys_3^dAla_2^a$, and (d) $Cys_3^dAla_3^a$

Given these results, I re-examined the pH titrations done by Dr. Mocny to determine if a 2SCC to 3SCC transition should be considered. It is important to note that all of this data was collected using the TRI length peptide, not the GR length peptide. This model fit well over the entirety of the curve (Figure 2-24). Cys_3^a fit to the tightest K_d of 66 ± 6 nM followed by $Ala_1^dCys_3^a$ at 390 ± 20 nM, $Ala_3^dCys_3^a$ at 550 ± 50 nM, and $Ala_2^dCys_3^a$ at 970 ± 50 nM. It is

interesting to note that the selective heterotrimer also has the weakest affinity for the third peptide strand.

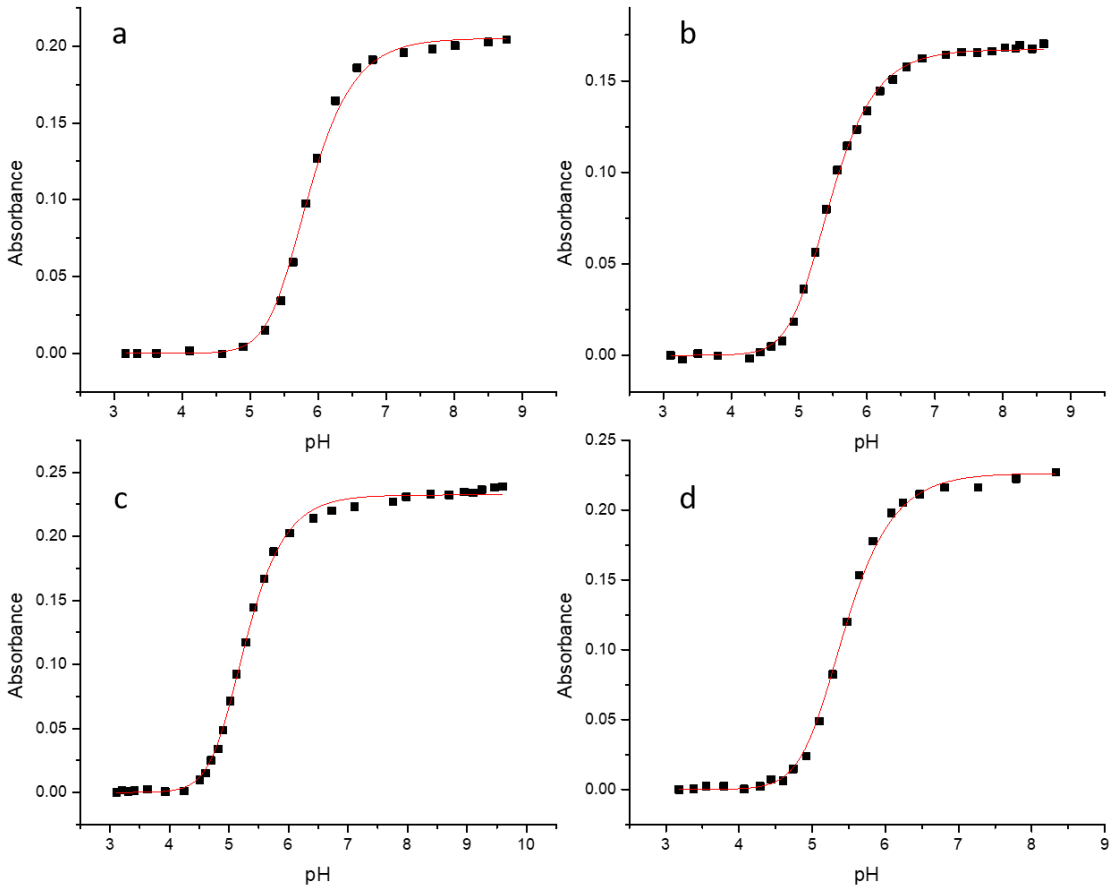

Figure 2-24 pH profile of PbS_3 formation fit to a PbS_2 to PbS_3 model for (a) Cys_3^a, (b) $Ala_1^dCys_3^a$, (c) $Ala_2^dCys_3^a$, and (d) $Ala_3^dCys_3^a$

Analytical ultracentrifugation of Cys_3^a by Dr. Borries Demeler at pH 5.3 and 7.8 support these results. At pH 5.3, he found a mix of dimer, trimer, and tetramer species for apo Cys_3^a, with the dimer being the predominant species (Figure 2-25). At pH 7.8, however, almost all apo Cys_3^a complexes as a trimer. This speciation does, however, depend upon the fitting algorithm used and has only been done for the apo peptide. This work cannot inform us on the effect of sulfur deprotonation and Pb(II) complexation to drive 3SCC formation.

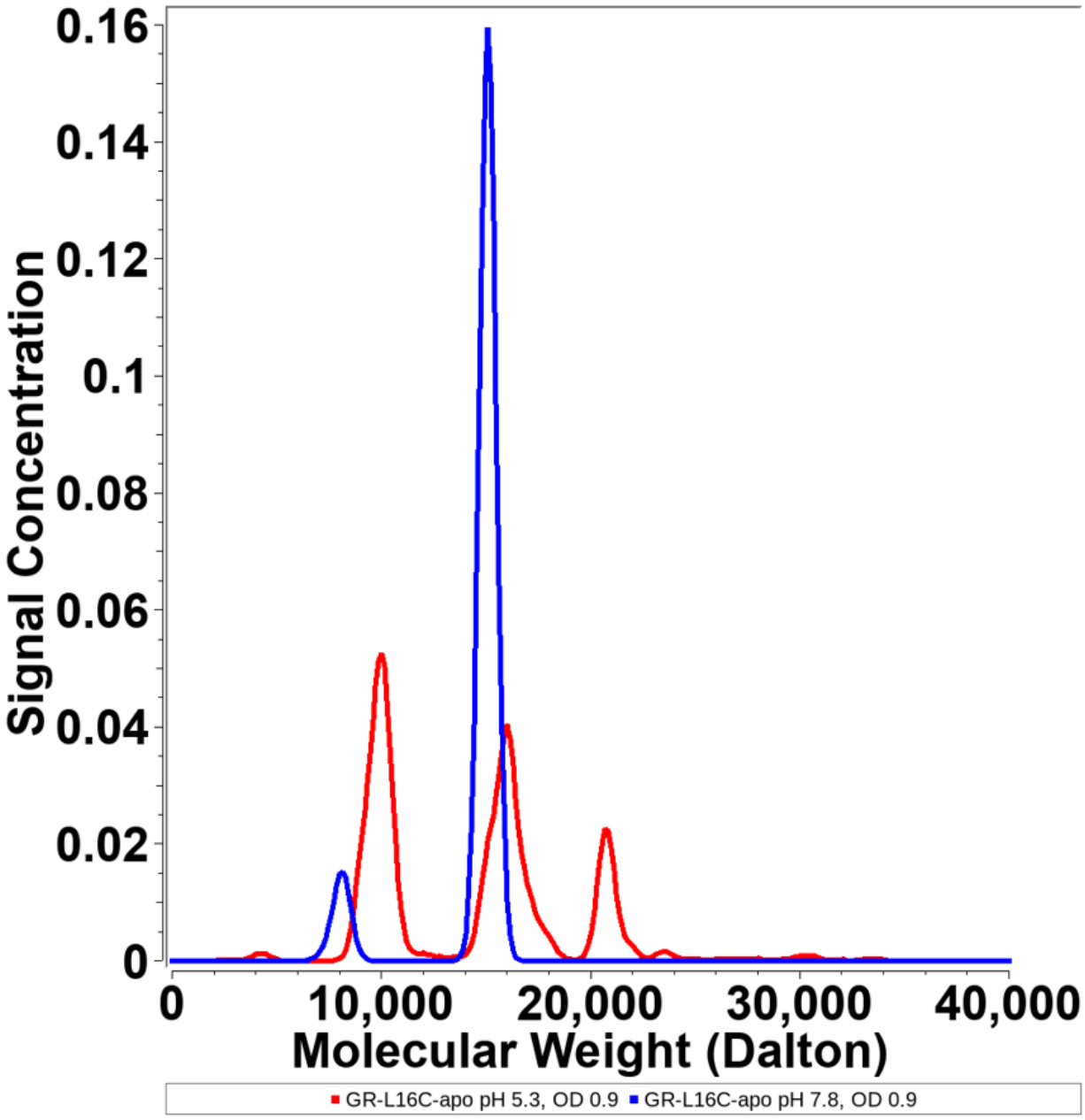

Figure 2-25 Speciation diagram from analytical ultracentrifugation with Cys_3^a at pH 5.3 in red and Cys_3^a at pH 7.8 in blue. The peaks correspond to dimer, trimer, and tetramer with increasing molecular weight.

^{207}Pb NMR of homo- and heterotrimers

^{207}Pb NMR was used to probe the Pb(II) environment in each of the four peptides. A single resonance at 5789 ppm was observed for Cys_3^d (Figure 2-26), in agreement with a previously published **d** site Cys, Baby L9C, at 5786 ppm.[35] $Cys_3^dAla_3^a$ had a resonance slightly upfield at 5762 ppm. The heterotrimeric mixtures, $Cys_3^dAla_2^a$ and $Cys_3^dAla_1^a$, both had resonances downfield of the homotrimeric peptides at 5875 ppm and 5803 ppm, respectively.

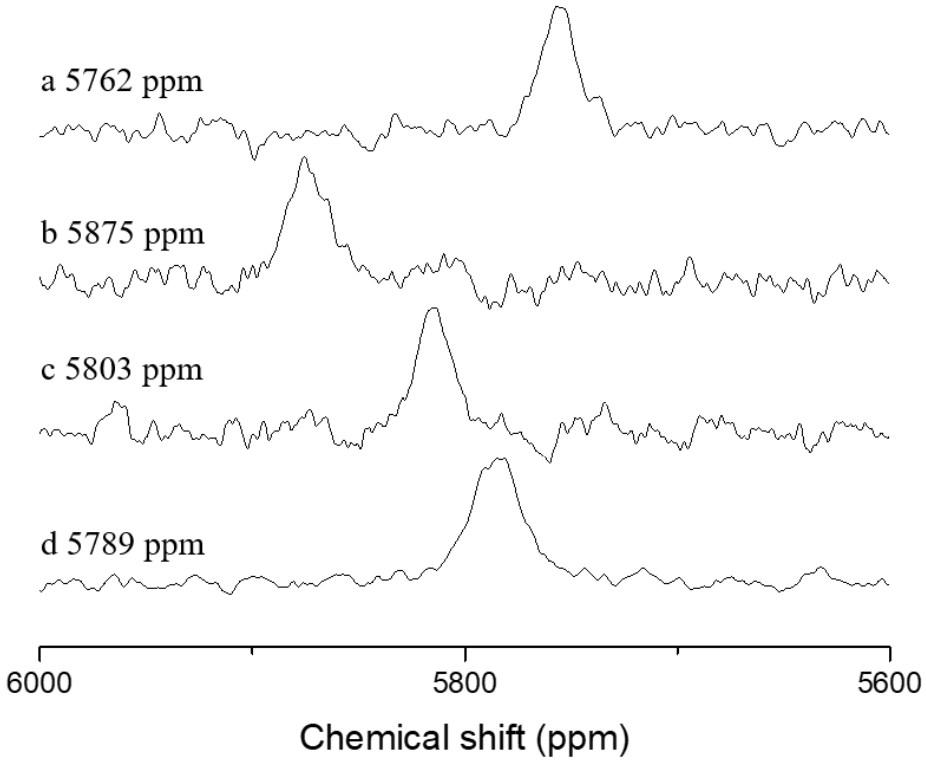

Figure 2-26 ^{207}Pb NMR of (a) $Cys_3^dAla_3^a$, (b) $Cys_3^dAla_2^a$, (c) $Cys_3^dAla_1^a$, and (d) Cys_3^d at pH 7.5. All spectra contain 3.5-5 mM 3SCC and 0.9 equivalents of $Pb(NO_3)_2$ (relative to trimer) in 10% D_2O.

X-ray crystallography of $Cys_3^dAla_3^a$

A 1.50 Å resolution structure of $Cys_3^dAla_3^a$ with 60% Pb(II) occupancy was obtained (PDB: 6MCD). The Pb(II) binds in an *endo* configuration (i.e. on the same side of the S_3 plane as the Cys β carbons) with a Pb-S distance of 2.7 Å and S-S distance of 3.4 Å (Figure 2-27). This S-S distance is too long to allow for disulfide bond formation. The Cys χ1 dihedral angle defined by N-Cα-Cβ-S is -167.3°, which is similar to previously observed dihedral angles for $Hg(II)Cys_3^a$ (-151.88°) and $Hg(II)Cys_3^aAla_3^d$ (-147.85°)[36] The $Pb(II)Cys_3^a$ structure, however, has a dihedral angle of -68.38°. In the space created by the Leu to Ala mutation, a single water molecule is able to coordinate at 3.4 Å from a single Cys residue. Instead of remaining on the helical interface, the water molecules orient closer to the center of the coiled coil than in $Ala_3^dCys_3^a$, directly below each Cys side chain. This orientation prevents interactions between the water molecules and multiple Cys residues.

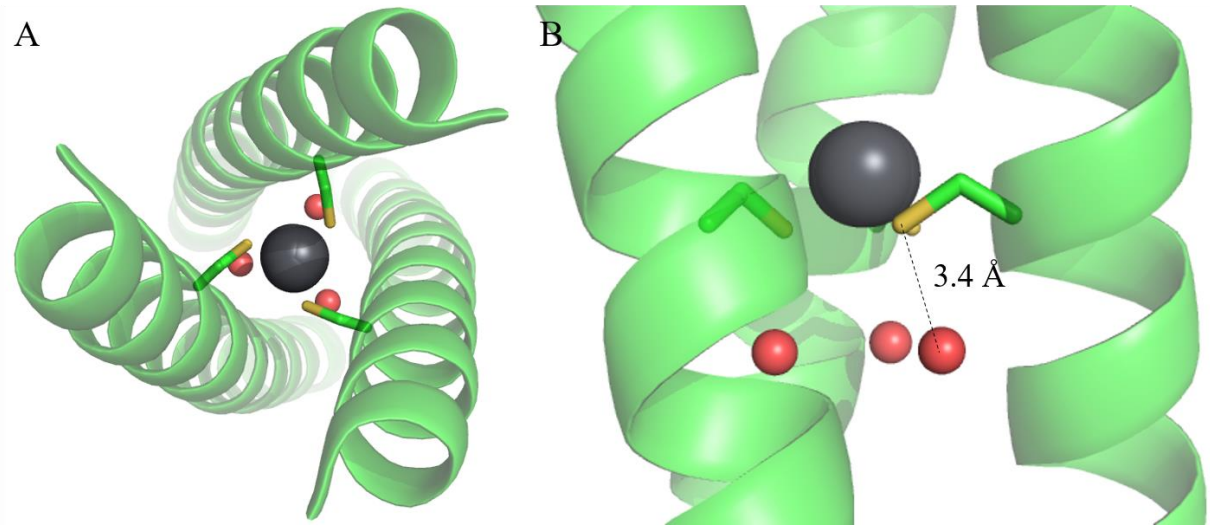

Figure 2-27 Top down (A) and side (B) view of $Cys_3^dAla_3^a$ (6MCD) with Pb(II) shown as a grey sphere, water as red spheres, and sulfur in yellow

QM/MM characterization

In collaboration with Dr. Rajeev Prabhakar's research group, the complexation energies of Cys_3^d, $Cys_3^dAla_3^a$, Cys_3^a, $Ala_3^dCys_3^a$, and all heterotrimers were determined via QM/MM. Dr. Thomas Paul in the Prabhakar group found that, for Cys^a constructs, the fully selective $Ala_2^dCys_3^a$ construct has the lowest complexation energy (Table 2-5). The nonselective heterotrimer, $Ala_1^dCys_3^a$, complexes with only 8.5 kcal/mol more energy. The homotrimers Cys_3^a and $Ala_3^dCys_3^a$ have the highest complexation energies, 17 kcal/mol and 32 kcal/mol higher than $Ala_2^dCys_3^a$, respectively.

Table 2-5 Complexation energies of Cys^a and Cys^d peptides

Cys^a peptide	Complexation energy (kcal/mol)	Cys^d peptide	Complexation energy (kcal/mol)
Cys_3^a	17	Cys_3^d	53.9
$Ala_1^dCys_3^a$	8.5	$Cys_3^dAla_1^a$	12.9
$Ala_2^dCys_3^a$	0	$Cys_3^dAla_2^a$	0
$Ala_3^dCys_3^a$	32	$Cys_3^dAla_3^a$	33

In Cys^d constructs, the analogous 2 Ala construct, $Cys_3^aAla_2^d$, also has the lowest complexation energy. A 12.9 kcal/mol gap separates that construct from $Cys_3^aAla_1^d$. $Cys_3^dAla_3^a$ complexes with 33 kcal/mol more energy than $Cys_3^dAla_2^a$, similar to Cys^a constructs, but Cys_3^d requires 53.9 kcal/mol more energy. The orientation of water and Pb(II) in these binding sites was also determined computationally. For both Cys^a and Cys^d systems, the 2 Ala: 1 Leu

heterotrimer complexed with the least amount of energy, but the Pb(II) environment exhibits notable differences between the two heterotrimers. In $Ala_2{}^dCys_3{}^a$ the single Leu residue is reoriented to allow for symmetric Pb(II) coordination (Figure 2-28). In $Cys_3{}^dAla_2{}^a$, however, the Leu orientation is maintained and Pb(II) binds dissymmetrically.

Cys^a and Cys^d peptides also differ in water coordination to Cys sulfur atoms. The water molecules in $Ala_3{}^dCys_3{}^a$ coordinate with the Cys-S and backbone of the Ala layer and are oriented along the helical interface. $Cys_3{}^dAla_3{}^a$, however, coordinated the water closer to the center of the helix and hydrogen bond only to the Cys-S. In both models, the computational structures agreed with the crystal structures reported above in regards to metal-sulfur distance and angle. Because the Leu does not reorient in $Cys_3{}^dAla_2{}^a$, one of these hydrogen bonds is lost as the Leu disrupts the hydrogen bonding network. This difference in hydrogen bonding network is not observed in Cys^a systems. Thus, the orientation of Leu residues and placement of waters results in fully selective Cys^d heterotrimers and only full selectivity for $Ala_2{}^dCys_3{}^a$.

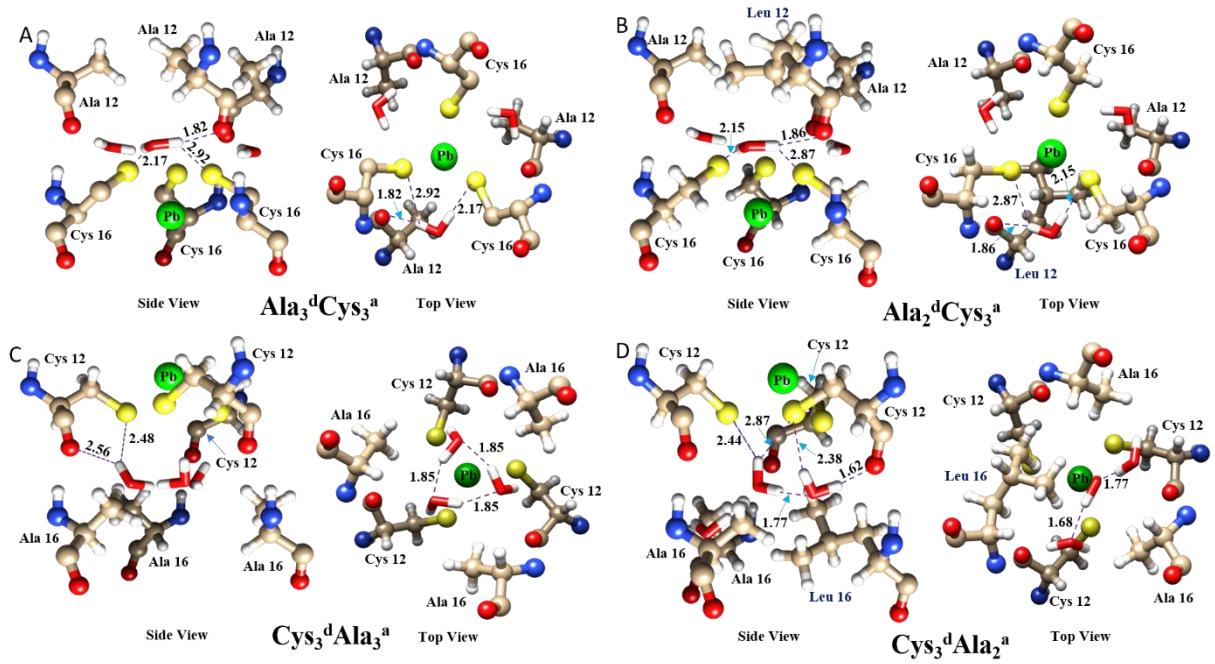

Figure 2-28 The hydrogen bonding interactions of (A) $Ala_3{}^dCys_3{}^a$, (B) $Ala_2{}^dCys_3{}^a$, (C) $Cys_3{}^dAla_3{}^a$, and (D) $Cys_3{}^dAla_2{}^a$ with the coordinated water molecules are shown in both side and top views with Pb(II) in green and sulfur in yellow.

Alternate interior Cys^a position: 23Cys^a

23Cys^a was also studied as an alternate position to complex Pb(II) for heterotrimer formation. This site is one heptad C-terminal of the Cys^a site described by Dr. Mocny and maintains the interstrand distances. At the 16th position, the location of Cys^a, the interstrand α carbons are 6.9 Å apart, while at the 23rd position the α carbons are 7.1 Å apart. ^{207}Pb NMR was done to determine if a similar Pb(II) binding environment was observed. 23Cys$_3^a$ had a chemical shift of 5645 ppm and Ala$_3^d$23Cys$_3^a$ had a chemical shift of 5574 ppm, identical to Ala$_3^d$Cys$_3^a$ (Figure 2-29). The analog of the selective heterotrimer, Ala$_2^d$23Cys$_3^a$, appears to be selective in this position as well, with a single resonance at 5597 ppm, although the spectrum is sufficiently noisy not to preclude a small amount of Ala$_1^d$23Cys$_3^a$. This is especially true as no signal for Ala$_1^d$23Cys$_3^a$ was observed after 12 hours.

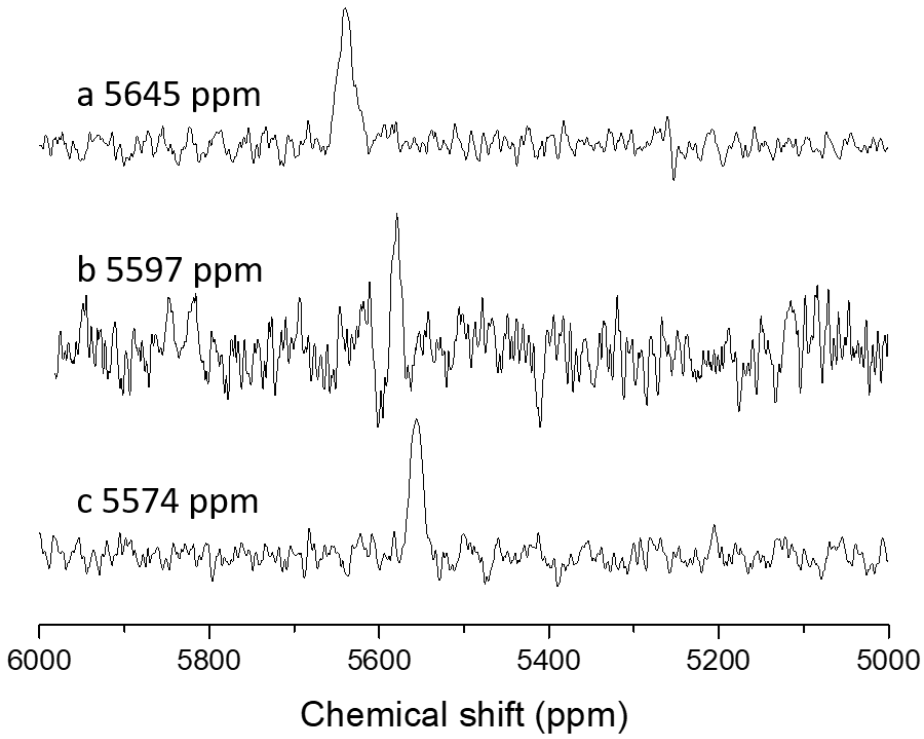

Figure 2-29 ^{207}Pb NMR of (a) Ala$_3^d$23Cys$_3^a$, (b) Ala$_2^d$23Cys$_3^a$, and (c) 23Cys$_3^a$ at pH 7.5. All spectra contain 3.5-5 mM 3SCC and 0.9 equivalents of Pb(NO$_3$)$_2$ (relative to trimer) in 10% D$_2$O.

Alternate terminal Cys^a position: 30Cys^a

The most C-terminal **a** site, 30Cys^a, was also studied for heterotrimer formation. This site displays significant fraying relative to the 16th and 23rd positions.[36] In 30Cys$_3^a$, two different UV

signals were observed at 328 nm and 346 nm with an isosbestic point at 337 nm (Figure 2-30). The species with maximum absorbance at 328 nm increases in absorbance to about pH 7 (green curve) and then decreases, while the species at 346 nm increases in absorbance with increasing pH.

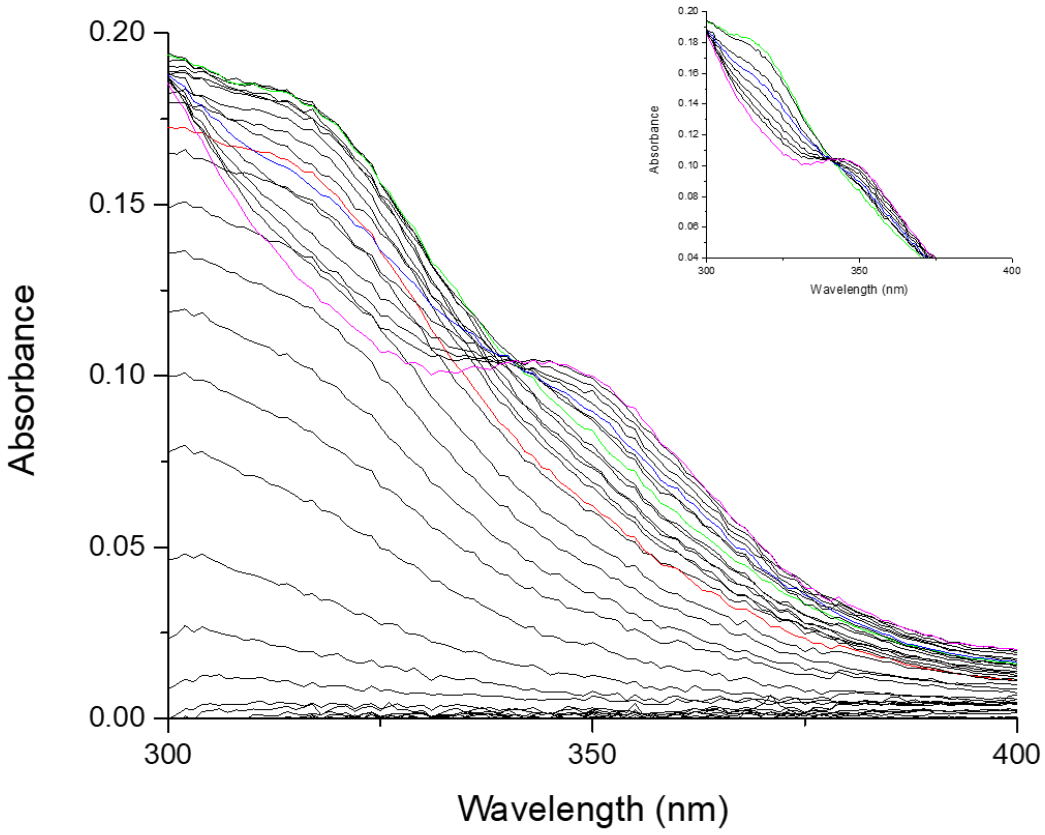

Figure 2-30 UV-visible spectra of 60 μM Pb(II) and 60 μM 30Cys$_3$[a] from pH 3 to 10 with pH6 highlighted in red, pH 7 in green, pH 8 in blue, and pH 9 in pink. pH 7 to 9 is displayed as an inset.

As previously mentioned, the species absorbing at 346 nm is attributed to the Pb-S_3 complex. A two-step process is observed for the formation of this complex. The first step occurs below pH 7, at which point the predominant species being formed has maximum absorbance at 324 nm. This species cannot be identified based solely on this spectrum but is likely either the PbS_2SH or PbS_2 intermediate. Both of these species would absorb at a lower wavelength than PbS_3 because the charge transfer is higher energy. Between pH 7 and 9, this species decreases in absorbance as the Pb-S_3 complex increases in absorbance with an isosbestic point at 337 nm. This isosbestic point indicates the conversion of one species to another rather than the

destruction and creation of two unrelated species. Maximum absorbance of the Pb-S_3 species is not observed until pH 9 (Figure 2-31).

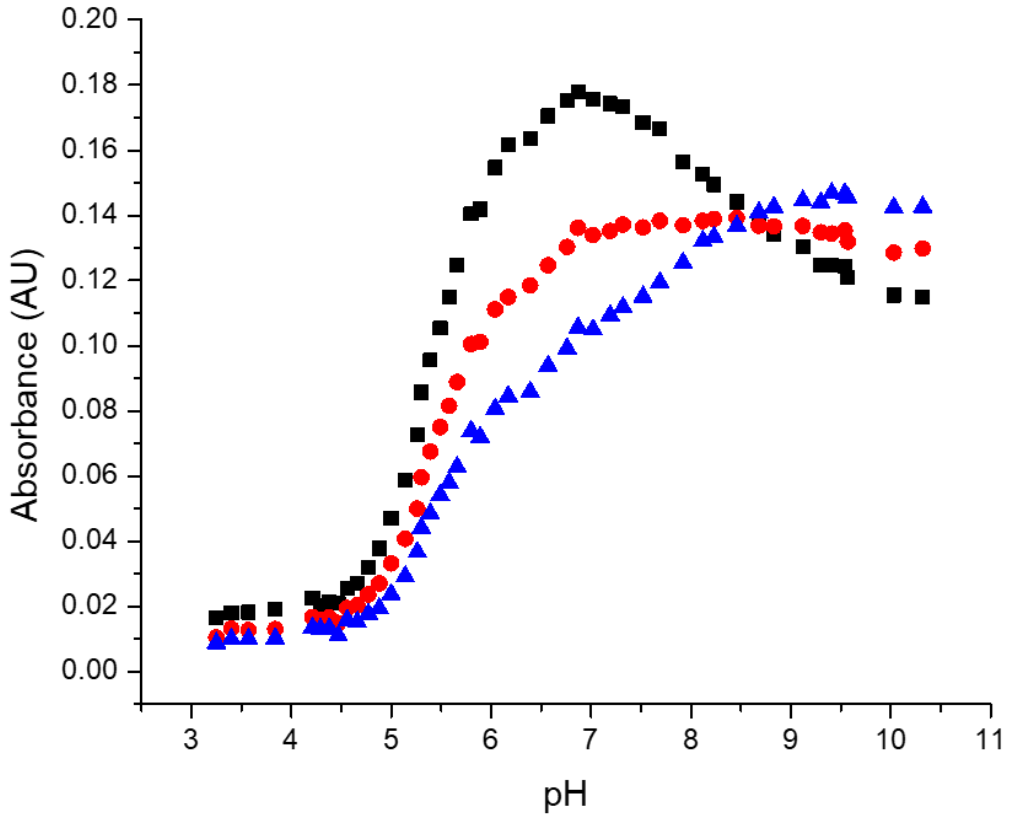

Figure 2-31 Absorbance profiles of the pH dependence of Pb-S_3 formation for 30Cys$_3^a$ at 324 nm (black squares), the isosbestic point at 337 nm (red circles), and 346 nm (blue triangles)

As discussed previously, the formation of the Pb-S_3 complex was fit to a two-step process, one step in acidic conditions and one step in neutral and basic conditions because there was spectroscopic evidence for an intermediate species (Figure 2-32). The pK_a's for this process are 5.58 ± 0.02 and 7.9 ± 0.1. Thus, the Pb-S_3 complex is not fully formed until pH 8.9.

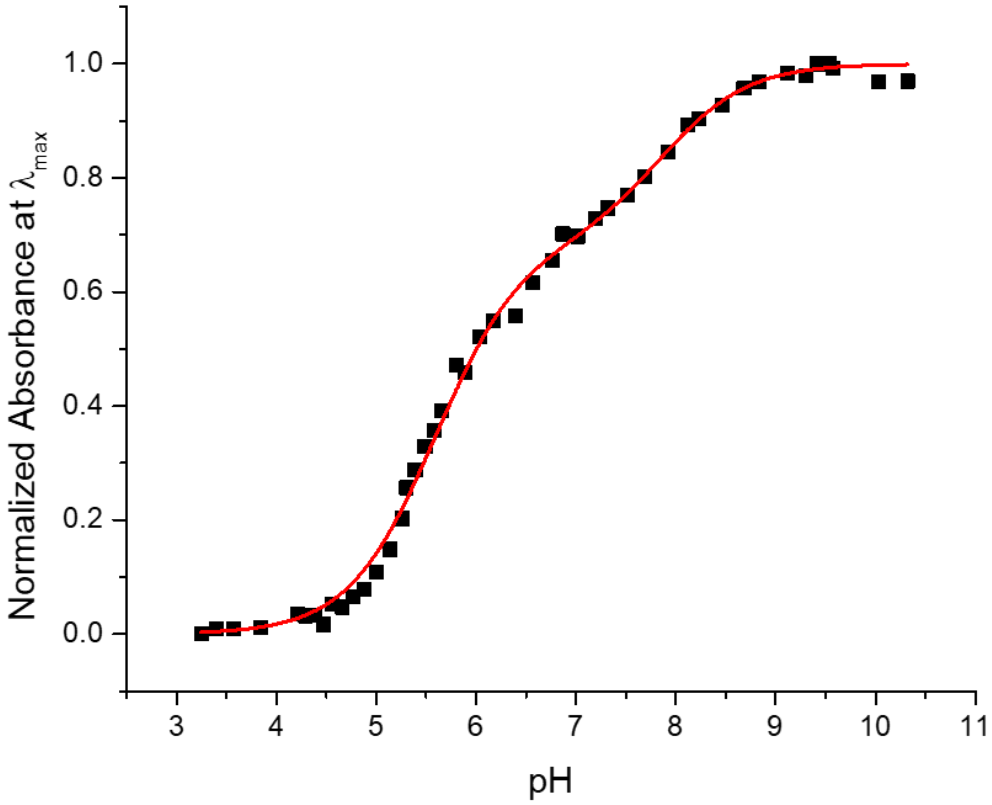

Figure 2-32 Pb-S_3 LMCT absorbance of 30Cys_3^a with a fit to a stepwise two proton deprotonation

Due to the high pK_a of this Cys_3^a site, this location was not pursued further for heterotrimer formation as many of the applications of a heterotrimeric scaffold in enzymatic reactions require that the assembly be fully and stably formed below pH 8.

Alternate interior Cys^d position: 19Cys^d

An alternate Cys^d position was also explored for heterotrimer formation. As with 23Cys^a, 19Cys^d is structurally similar to Cys^d. ^{207}Pb NMR showed that heterotrimers form at this position in a similar manner to Cys^d. The homotrimers are the most upfield shifted at 5811 ppm for 19$Cys_3^dAla_3^a$ and 5799 ppm for 19Cys_3^d (Figure 2-33). The heterotrimeric mixtures are also downfield of the range of homotrimeric peaks at 5850 ppm for 19$Cys_3^dAla_2^a$ and 5901 ppm for

19Cys$_3^d$Ala$_1^a$. The feature at 5920 ppm in spectrum b is noise as linear prediction had no effect on the intensity of the peak.

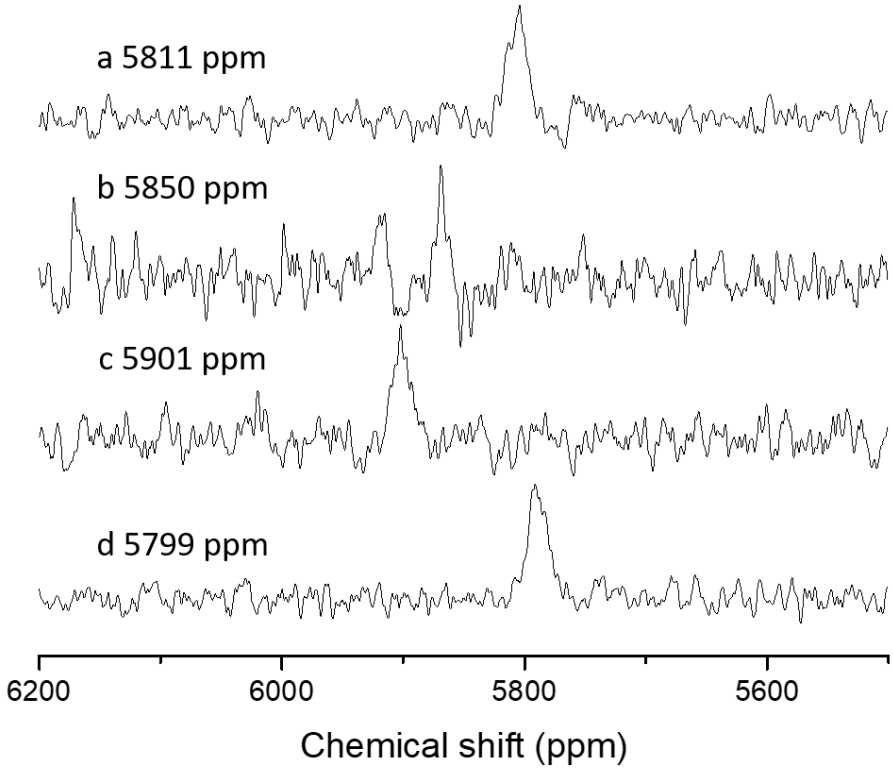

Figure 2-33 ^{207}Pb NMR of (a) 19Cys$_3^d$Ala$_3^a$, (b) 19Cys$_3^d$Ala$_2^a$, (c) 19Cys$_3^d$Ala$_1^a$, and (d) 19Cys$_3^d$ at pH 7.5. All spectra contain 3.5-5 mM 3SCC and 0.9 equivalents of Pb(NO$_3$)$_2$ (relative to trimer) in 10% D$_2$O.

Incorporation of a second metal binding site

As the goal of this work is to investigate asymmetric transition metal centers, the Cys$_3^d$ was probed with the addition of a distant His$_3$ site and with the addition of Zn(II). The Pb(II) center was not perturbed by the addition of the His$_3$ site at the 30th position or the bound Zn(II) as determined by ^{207}Pb NMR (Figure 2-34). The increase in noise for the spectrum with Zn(II) is due to the use of a less sensitive probe and not to disorder of the sample. Thus, one can incorporate a transition metal into a heterotrimeric peptide without perturbing the Pb(II) site.

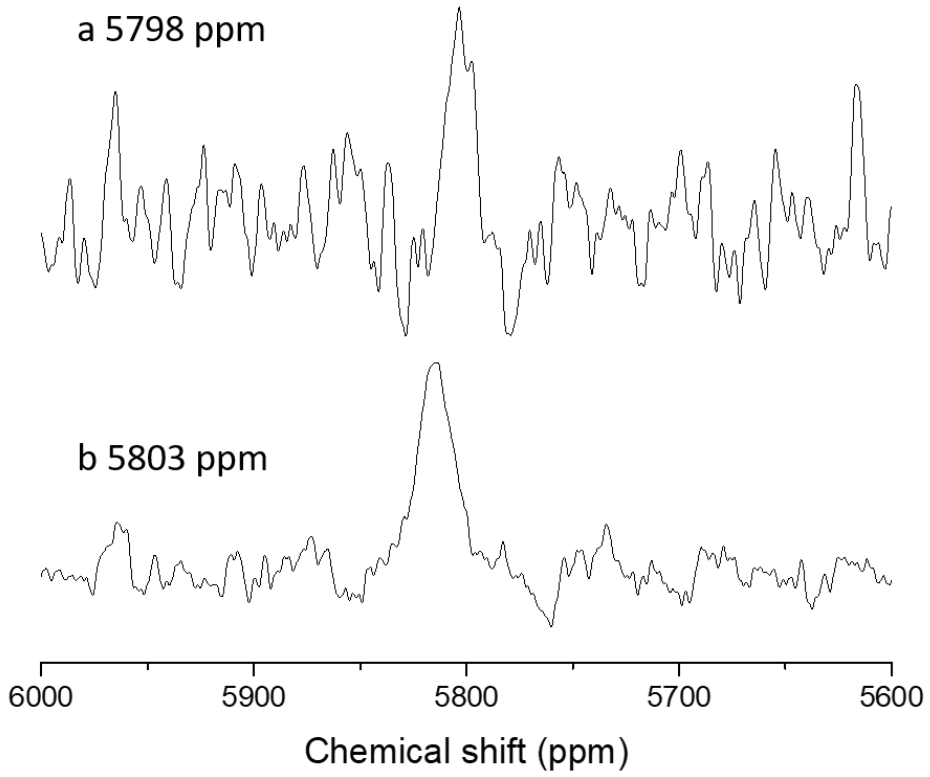

Figure 2-34 ^{207}Pb NMR of (a) $Ala_2^dCys_3^a$ with a distant His_3 site (L30H) and Zn(II) and (b) $Cys_3^dAla_2^a$ at pH 7.5. All spectra contain 3.5-5 mM 3SCC and 0.9 equivalents of $Pb(NO_3)_2$ (relative to trimer) in 10% D_2O.

Heterotrimer formation at increased pH

The ability to form heterotrimers was also investigated as a function of increased pH. No change to the ^{207}Pb NMR chemical shift was observed from pH 7.5 to pH 9.5 (Figure 2-35). This is corroborated by the pH profiles of each spectrum. Thus, as with Cys^a sites, Cys^d sites can be used at increased pH.

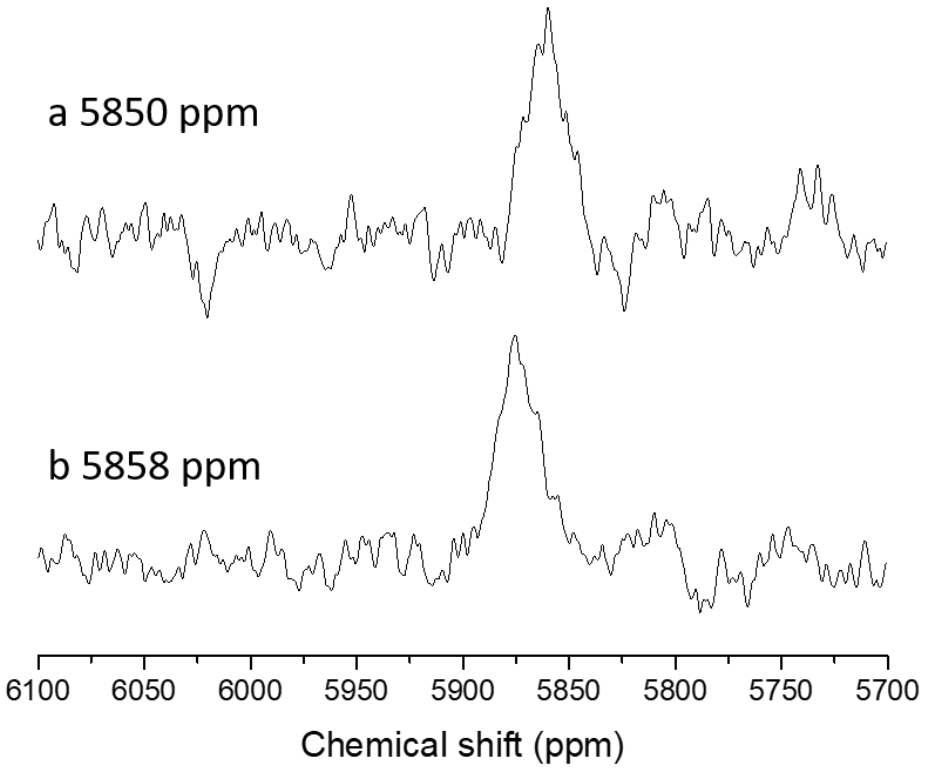

Figure 2-35 ^{207}Pb NMR of $Cys_3^dAla_2^a$ at (a) pH 7.5 and (b) pH 9.5. All spectra contain 3.5-5 mM 3SCC and 0.9 equivalents of $Pb(NO_3)_2$ (relative to trimer) in 10% D_2O.

Discussion

A self-assembling, asymmetric heterotrimeric three stranded coiled coil (3SCC) was developed by Dr. Kosh Neupane and characterized by Dr. Catherine Mocny using **a** site cysteine and **d** site alanine substitution of core leucine hydrophobes in adjacent layers, but the scaffolds were lacking full selectivity. In this chapter, I have described an improvement to this method that affords full asymmetric selectivity. This method still utilizes a Cys_3 site, Pb(II), and an adjacent mixed Ala/Leu layer, but in a different position within the heptad. By moving the Cys from an **a** layer (Cys^a) to a **d** layer (Cys^d), we aimed to utilize a different Cys orientation to achieve full heterotrimer selectivity.

In the previously described Cys_3^a peptide,[5] the Pb(II) bound Cys residues are oriented towards the center of the 3SCC, with a S-S distance of 3.4 Å. The Pb(II) binds in an *endo* conformation (*i.e.* on the same side of the Cys-S as the β carbon) with a Cys-S-Pb distance between 2.5 and 2.6 Å (Figure 2-2). When Pb(II) is bound to Cys_3^d, the Cys residues still orient

towards the center of the 3SCC, but three fold symmetry around the Pb(II) is no longer present. Instead, there are S-S distances of 2.6 Å, 3.3 Å, and 3.6 Å. The Cys-S-Pb distance of 2.6 Å and *endo* orientation are, however, maintained (Figure 2-8).

Interestingly, more apparent differences between Cys^a and Cys^d positions are observed in the presence of an adjacent Ala layer. The Ala substitution was introduced either directly above or below the Cys layer, depending on the placement of the Pb(II). In the Cys^a peptide, the endo Pb(II) configuration places the center of the Pb(II) below the sulfur plane. In the Cys^d peptide, however, the Pb(II) is above the sulfur plane. Thus, the Ala layer goes above Cys^a (Ala^dCys^a) and below Cys^d (Cys^aAla^d). Pb(II)$Ala_3^dCys_3^a$ coordinates three solvent molecules at the interface between each helical interface, 3.0 Å and 3.4 Å from the adjacent Cys-S atoms (Figure 2-7). In Pb(II)$Cys_3^dAla_3^a$, however, this hydrogen bonding network is reorganized. Each Cys-S coordinates a single solvent molecule at a distance of 3.4 Å. These waters are also much closer to the center of the 3SCC than those of Pb(II)$Ala_3^dCys_3^a$. Dr. Mocny hypothesized that heterotrimer formation was the result of peak stability from both hydrophobic packing of the native Leu residues and the hydrogen bonding network introduced by the reduced steric bulk of the Ala residues. By modifying the hydrogen bonding network in Pb(II)$Cys_3^dAla_3^a$, we hypothesized that fully selective heterotrimers could be generated.

CD spectroscopy of apo homotrimers showed that both Cys_3^d and $Cys_3^dAla_3^d$ fold into coiled coils. The additional leucine substitution in $Cys_3^dAla_3^a$ destabilized apo trimer formation under denaturing conditions, but under buffered conditions at pH 7.5, there is no difference in stability between Cys_3^d and $Cys_3^dAla_3^a$. The four trimer combinations also bind Pb(II) tightly in 1:1 ratios (Pb(II)/3SCC). Cys_3^d has the highest energy Pb-S_3 LMCT transition and $Cys_3^dAla_3^a$ has the lowest, with heterotrimers at stepwise intervals between the homotrimers. This may be due to the introduction of water to the sulfur site. The decrease in LMCT energy occurs as more sulfur atoms are able to hydrogen bond to solvent. This hydrogen bonding decreases the electron density of the sulfur atom, decreasing the energy gap between the ligand and metal orbitals. The peaks are so broad, however, that further characterization of the Pb(II) environment in these peptides is not possible.

The pH dependence of Pb-S_3 complexation was also examined to determine if a similar acid shifting of heterotrimeric pK_a's were observed as with Cys^a heterotrimers. Rather than fitting to a simultaneous two proton deprotonation, which has previously been demonstrated to

model this system well,[5, 37-38] the best model was determined to be dependent upon formation of the 3SCC. Below pH 4.5, all peptides exist as 2SCCs. The transition from 2SCC to 3SCC is dependent on the location of the Cys layer, with Cys^a having a lower pK_a than Cys^d.[39] The transition from 2SCC to 3SCC occurs simultaneously with Pb-S_3 complexation for the Cys^d peptides. No spectroscopic evidence of an intermediate is found for these systems as in $30Cys_3^a$, indicating that the release of this proton occurs simultaneously with association of the third peptide strand.

This is unlike what was previously reported for Cys^a systems, in which the 3SCCs were fully formed before Pb(II) bound. Dr. Mocny's analysis showed that the heterotrimeric constructs had pK_a's for the deprotonation of the Cys side chains that were more acidic than a predicted mixture of homotrimeric species. For the Cys^a system, this provided further support for the formation of heterotrimers as these values cannot arise from a mixture of homotrimeric species. Given these new results for the Cys^d system, however, this transition was reexamined as the conversion of a 2SCC to a 3SCC that occurs simultaneously with Pb(II)-S_3 coordination. This model also fit the data quite well, but the results are seemingly contradictory. The species with the most acidic pKa also had the weakest affinity for the third peptide strand. One would assume that a higher affinity for the third peptide strand would result in the most acidic transition, but this assumption does not consider the order that residues are deprotonated.

The model I have derived considers the release of only two protons, which is a simplification of this system. One proton must be released from the Cys-SH to yield the Cys-S^- that coordinates Pb(II), but the data presented here cannot provide any information on the number of protons that are released by Glu residues to form the requisite salt bridges. It is possible that there is one key layer that must be deprotonated to cause the entire coiled coil to pack as a 3SCC or that the single proton incorporated in this model is an average of every Glu-OH deprotonation. More work must be done for one to determine the nuances of this process. The deprotonation events could be tracked through 2D ^1H ^{15}N NMR or by ^1H NMR monitoring of His protons in the presence of Cu(I) as was done by Dr. Tegoni.[40] What is being considered herein is the pH at which a 3SCC exists and not the mechanism by which the transition occurs.

The order of deprotonation of Cys vs Glu residues contributes to the seemingly contradictory affinity and pK_a values. Based on the sidechain pK_a values of the free aqueous amino acid, one would expect all Glu residues to be deprotonated well before the Cys residues,

but the impact of the local environment can have drastic effects on these pK_a values. That is to say, 3SCC formation in the presence of a Cys_3 site may be driven either by Cys deprotonation to form the Pb-S_3 site, inducing 3SCC formation or Glu deprotonation to form the 3SCC, inducing Cys deprotonation. This data suggests the former is more likely because computational data has shown that the $Ala_2^dCys_3^a$ heterotrimer has the lowest complexation energy and also the lowest pK_a for Pb-S_3 formation, but the weakest affinity for the third peptide strand. With the most stable Cys site driving formation of the 3SCC, one would expect this transition to occur under more acidic conditions even if the trimer is less stable.

The same can be said for the Cys^d systems. In these peptides, the transition occurs at a less acidic pH than for Cys^a peptides, but the affinity is not reflective of the stability of the trimers at pH 7.5 as determined by computations. The relative acidity of the sulfur proton is affected by the location in the heptad such that peptides with fewer Ala residues have a stronger affinity for Pb-S_3 formation. There is not, however, a significant difference in the pK_a of this transition. This may be due to a more stable 2SCC generated by the GR construct instead of the TRI construct. Ultimately, no conclusions on the selectivity of heterotrimers can be made from the pH dependence of Pb-S_3 formation because this system has proven to be far more complicated than we have previously considered. The complexation of metal concurrent with 3SCC formation was only observed once before for Cd(II) binding to TRI $Ala_3^dCys_3^a$.[37] This data instead suggests that the metal dependent supramolecular assembly of 3SCCs is affected by the length of the peptide, the position of the metal binding site, or both.

This data cannot confirm or refute the formation of selective heterotrimers in this system. Instead, this presents a limit to the Cys^d system that is not observed in the Cys^a system. This system cannot be used in acidic conditions to investigate reactions such as nitrite reductase, which is monitored at pH 5.9, because a mixture of 2SCC and 3SCC species exists under these conditions. It must be noted, however, that Dr. Mocny reported Cys^a pK_a values for the TRI system, not the GR system. It remains to be seen if this model is a result of shifting from **a** site to **d** site Cys within the GR scaffold or from elongating the scaffold from TRI to GR. Nevertheless, the enzymatic systems discussed later in this work are investigated in neutral and basic pH and are therefore unaffected by the elevated pK_a of the 2SCC to 3SCC conversion for these systems.

The selectivity of these heterotrimeric mixtures is, however, elucidated by ^{207}Pb NMR. Single resonances are observed for Cys_3^d, $Cys_3^dAla_1^a$, $Cys_3^dAla_2^a$, and $Cys_3^dAla_3^a$ with both

heterotrimeric mixtures downfield of the range of homotrimeric resonances. As both heterotrimeric signals are downfield of the range of the homotrimers, these signals must arise from unique species, not a combination of homotrimeric species. In the Cys^a system, heterotrimeric signals were within the range of the homotrimeric chemical shifts and therefore could have arisen from coalescence of homotrimeric systems. Further evidence provided by pK_a determinations and ^{207}Pb NMR with alternate ratios of peptide strands were necessary to confirm the formation of heterotrimers. For Cys^d, however, the ^{207}Pb NMR provides sufficient evidence for this, which is not disproven by the pK_a of Pb-S_3 formation. Thus, shifting from Cys^a to Cys^d results in fully selective heterotrimers of both A_2B and AB_2 types.

A crystal structure of $Cys_3^dAla_3^a$ was obtained at 1.50 Å resolution. This structure was similar to $Ala_3^dCys_3^a$ in that three solvent molecules were able to hydrogen bond to the Cys sulfur atoms but the orientation was different. The solvent molecules in $Cys_3^dAla_3^a$ were oriented directly C-terminal of the sulfur atoms and were hydrogen bonding distance to only a single sulfur atom. This is in contrast to the Cys^a structure, in which the solvent molecules were aligned at the helical interface and were able to hydrogen bond to sulfur atoms on both adjacent peptide strands. As hypothesized, shifting the Cys site to a **d** layer did allow for a different hydrogen bonding network.

Crystal structures of the heterotrimers, however, remain elusive. While the interior of the 3SCC is asymmetric, no asymmetry inducing mutations have been made to the exterior of the CC. Thus, when packing in three dimensional space, the A strand of an A_2B heterotrimer is not oriented in an ordered fashion. This disorder results in an averaged electron density map that cannot conclusively be fit around the metal center. Redesign of the exterior of the 3SCC is necessary to obtain asymmetric crystal structures.

As these crystal structures have remained elusive, we turned to computations to explain why Cys^d constructs form fully selectively but Cys^a constructs do not. In both Cys^a and Cys^d constructs the 2 Ala: 1 Leu complexed with the lowest energy. This explains the selectivity seen with $Ala_2^dCys_3^a$ as this construct is most pre-disposed to form. The small barrier between that and $Ala_1^dCys_3^a$ may contribute to the lack of full selectivity with this construct. A smaller energy barrier between these two trimers allows for some peptide to complex in the lowest energy trimer. The Cys^d construct also gains selectivity from a negative design element. The homotrimeric Cys_3^d requires 54 kcal/mol more energy than the lowest energy $Cys_3^dAla_2^a$, which

is significantly destabilized over Cys_3^a. Thus, heterotrimers are more strongly favored in Cys^d constructs than Cys^a constructs.

The orientation of water and Pb(II) in these binding sites was also determined computationally and was found to affect heterotrimer formation. It is unknown experimentally if the individual strands of the heterotrimers maintain the same side chain rotamers as in the homotrimeric crystal structures or if a rearrangement is observed. QM/MM work showed that a rearrangement of the leucine residue in $Ala_2^dCys_3^a$ occurs to maintain Pb-S_3 symmetry. This maintained symmetry is observed in the ^{207}Pb NMR of Cys^a constructs. The change in chemical shift may be due only to increasing solvation of the sulfur atoms and not to modifications in Pb-S orbital overlap. This could result in a stepwise downfield shift as Ala residues are introduced and the Pb(II) remains in a symmetric environment but electron donating character of the sulfur ligand is changed.

In Cys^d, however, the leucine residue remains in the same orientation in both Cys_3^d and $Cys_3^dAla_2^a$. This forces the Pb(II) to bind $_{dissym}$metrically, leading to tighter packing of the 3SCC and greater orbital overlap of lead and sulfur. This may explain the downfield shift of heterotrimers relative to homotrimers as observed by ^{207}Pb NMR. The primary coordination sphere of the lead is modified in an asymmetric environment, leading to a more significant change in chemical shift than in Cys^a.

With a well-defined system to generate selective asymmetric trimers, I examined whether this binding site was transferrable to other heptad positions in the 3SCC. Dr. Zastrow found that the kinetic parameters k_{cat} and K_M were dependent on the location of a Zn(II)His_3 catalytic site, though catalytic efficiency was unchanged.[4] Thus, the ability to move the Pb(II)Cys_3 site would allow for fine tuning of specific kinetic parameters. Repositioning the Pb(II)Cys_3 site in the N-terminal direction one heptad to positions 5 or 9 was not attempted due to stability concerns as this would be too close to the N-terminal Trp. Moving the Cys layer in the C-terminal direction one heptad resulted in $19Cys^d$ or $23Cys^a$. These sites are 2 heptads from the C-terminus while the previously described Cys^a and Cys^d were 2 heptads from the N-terminus so these new sites were predicted to behave similarly. As with Cys^a and Cys^d, the Ala layer was introduced either above the **a** layer (Ala^d23Cys^a) or below the **d** layer ($19Cys^dAla^a$). The homotrimeric and heterotrimeric mixtures were probed by ^{207}Pb NMR to determine if selective heterotrimers can be produced from this binding site and produced similar results.

Homotrimeric $23Cys_3^a$ and $Ala_3^d23Cys_3^a$ have identical chemical shifts to Cys_3^a and $Ala_3^dCys_3^a$. The analog of the fully selective $Ala_2^dCys_3^a$, $Ala_2^d23Cys_3^a$ had a single resonance, but with a much lower signal to noise ratio. No signal was observed for $Ala_1^d19Cys_3^a$, the analog of non-selective $Ala_1^dCys_3^a$. This indicates that the lack of selectivity is increased at this position. To determine a reason for this, crystal structures of the homotrimeric peptides are necessary for QM/MM analysis.

$19Cys^d$ constructs behaved analogously to Cys^d constructs, with heterotrimers downfield of the range of homotrimeric chemical shifts. Thus, this site may be used as a heterotrimer nucleation site. The chemical shift values for $19Cys^d$ peptides are all downfield of their Cys^d analogs. This downfield shift could occur for a myriad of reasons. It is possible that the S-OH_2 bond distance is changed, that Cys rotamers are different, or that Leu rotamers are different. As with $23Cys^a$, crystal structures of the homotrimers are necessary to determine bond distances or to perform QM/MM calculations.

The most C-terminal a site, $30Cys^a$ was hypothesized to increase the stability of the trimer through the introduction of a Pb(II) binding site, reducing the amount of fraying. Instead, the fraying disrupted solvent accessibility and hydrogen bonding to increase the pK_a of Pb-S_3 complexation. The Pb-S_3 complexation is not fully formed until pH 8.3, prohibiting the use of this site for studies at physiological pH. As heterotrimer formation is tied to the hydrogen bonding network present in each position, such a modification to solvent accessibility likely prohibits formation of heterotrimers as well. I hypothesize that heterotrimer formation is limited to internal heptads as they afford control over the hydrogen bonding network.

All work described up to this point shows that Cys^d systems selectively form heterotrimers at two interior heptad positions. This presents a significant advancement over the previous Cys^a systems, in which only one heterotrimer forms selectively. The goal of this work, however, is to utilize these heterotrimers to study asymmetry at a distant transition metal center. This system must also be stable across a range of pH values for use in multiple enzyme systems. ^{207}Pb NMR demonstrates that no perturbation of the Pb(II) site is observed up to pH 9.5. Additionally, the inclusion of a His_3^a layer at the most C-terminal position does not perturb the Pb(II) binding site with the addition of Zn(II). Thus, the Cys^d system is a robust scaffold to study asymmetric peptides as both A_2B and AB_2 type systems form fully selectively in neutral and basic pH with the addition of a distant transition metal binding site.

Conclusion

In this chapter I have described a novel approach to form fully selective, self-assembling A_2B and AB_2 type heterotrimers utilizing a Cys_3 layer, Pb(II), and an adjacent layer of reduced steric bulk for hydrogen bonding. Dr. Mocny previously characterized a construct with Cys_3 in an **a** layer that afforded full selectivity for only the A_2B-type trimer, $Ala_2^aCys_3^d$. By shifting this site to a **d** layer, full selectivity is afforded for both the A_2B and AB_2-type trimers. This distinction is necessary as it allows for the study of both X_1His_3 and X_2His_3 type sites at a distant transition metal binding site without a significant loss in stability. The previous scaffold was limited to X_1His_3 sites due to limitations on the number of leucine substitutions possible per strand.

^{207}Pb NMR of these Cys^d constructs showed that all chemical shifts are ~200 ppm downfield of the Cys^a constructs. The homotrimeric peaks for Cys_3^d and $Cys_3^dAla_3^a$ were the most upfield. Single resonances were observed for both $Cys_3^dAla_1^a$ and $Cys_3^dAla_2^a$ downfield of the range of the homotrimeric peaks. Thus, these signals must arise from unique species and not a coalescence of homotrimeric signals. UV-visible spectroscopy confirmed that 1 equivalent of Pb(II) binds to each trimer, but the Pb-S_3 LMCT chromophore is not sensitive enough to provide further evidence for heterotrimer formation. Additionally, the pK_a of Pb-S_3 complexation is dependent upon formation of the 3SCC, not deprotonation of Cys within a fully formed 3SCC and as such neither supports nor refutes the formation of heterotrimers above pH 7. While the pH dependence of Pb-S_3 formation does not provide additional evidence for heterotrimer formation, the ^{207}Pb NMR spectroscopy is conclusive evidence of this.

Computational studies confirmed these results and provided insights into the lack of selectivity for Cys^a constructs. In both systems, the 2 Ala: 1 Leu heterotrimer had the lowest complexation energy, explaining the full selectivity of these constructs. In Cys^a systems, the energy differences between constructs are comparatively small, preventing selectivity in the $Ala_1^dCys_3^a$ construct. The Cys_3^d construct is sufficiently destabilized by Leu orientation to provide an additional element of negative design in this system. Thus, one can form fully selective A_2B and AB_2 heterotrimers using Cys^d systems.

I also showed that this method is transferrable to other interior heptads within the 3SCC. $19Cys^d$ also affords full selectivity to both A_2B and AB_2 heterotrimers, as observed by NMR. The chemical shifts of this system are downfield of the original Cys^d trimers, so the sites are not

fully identical. These differences present an area of future study to determine the structural differences that contribute to this. 23Cys^{a} systems have identical chemical shifts to the original Cys^{a} system. If, however, one shifts to the C-terminal Cys^{a}, Pb(II)-S_3 complexation is not observed until above pH 7.5. The solvent accessibility of this site is much higher than the interior sites, preventing the formation of heterotrimers in this position.

Not only can Cys^{d} sites be used to selectively form both A_2B and AB_2 type heterotrimers, but a distant His$_3^{a}$ site can be incorporated for transition metal binding. This allows for the investigation of asymmetry in catalytic systems which was previously unobtainable. Additionally, these systems are stable up to pH 9.5.

This work presents the first system to generate fully selective, asymmetric, self-assembling A_2B and AB_2 type heterotrimers. This method requires only a single heptad and utilizes natural amino acids, allowing for simple synthesis and possible incorporation of other binding sites within the trimer. Future studies will be done on using this system using a distant site to incorporate the metal binding sites of metalloenzymes with asymmetry in the first or second coordination sphere. Additionally, the transferability of this site to other positions within the 3SCC will allow for repositioning of the catalytic site to take advantage of different kinetic properties.

References

1. Christianson, D. W.; Fierke, C. A., Carbonic Anhydrase: Evolution of the Zinc Binding Site by Nature and by Design. *Acc. Chem. Res.* **1996,** *29*, 331-339.

2. Kiefer, L. L.; Paterno, S. A.; Fierke, C. A., Hydrogen Bond Network in the Metal Binding Site of Carbonic Anhydrase Enhances Zinc Affinity and Catalytic Efficiency. *J. Am. Chem. Soc.* **1995,** *117* (26), 6831-6837.

3. Zastrow, M. L.; Peacock, A. F.; Stuckey, J. A.; Pecoraro, V. L., Hydrolytic catalysis and structural stabilization in a designed metalloprotein. *Nat. Chem.* **2011,** *4* (2), 118-23.

4. Zastrow, M. L.; Pecoraro, V. L., Influence of active site location on catalytic activity in de novo-designed zinc metalloenzymes. *J. Am. Chem. Soc.* **2013,** *135* (15), 5895-903.

5. Mocny, C. S. Ph.D. Dissertation, Examining the metal selectivity of thiol rich de novo designed peptides as a strategy to make asymmetric alpha- helical protein assemblies. 2016.

6. Astrin, K. H.; Bishop, D. F.; Wetmur, J. G.; Kaul, B.; Davidow, B.; Desnick, R. J., delta-Aminolevulinic acid dehydratase isozymes and lead toxicity. *Ann. N. Y. Acad. Sci.* **1987,** *514*, 23-9.

7. Cangelosi, V.; Ruckthong, L.; Pecoraro, V. L., Lead (II) Binding in Natural and Artificial Proteins. (Ii), 1-85.

8. Zampella, G.; Neupane, K. P.; De Gioia, L.; Pecoraro, V. L., The importance of stereochemically active lone pairs for influencing Pb(II) and As(III) protein binding. *Chemistry* **2012,** *18* (7), 2040-50.

9. Schnarr, N. A.; Kennan, A. J., Peptide Tic-Tac-Toe: Heterotrimeric Coiled-Coil Specificity from Steric Matching of Multiple Hydrophobic Side Chains. *J. Am. Chem. Soc.* **2001,** *124*, 9779-9783.

10. Tolbert, A. E.; Ervin, C. S.; Ruckthong, L.; Paul, T. J.; Jayasinghe-Arachchige, V. M.; Neupane, K. P.; Stuckey, J. A.; Prabhakar, R.; Pecoraro, V. L., Heteromeric 3-Stranded Coiled Coils Designed Using a Pb(II)(Cys)3 Template Mediated Strategy. *Nature Chem.* **2019,** *In press*.

11. Ruckthong, L.; Zastrow, M. L.; Stuckey, J. A.; Pecoraro, V. L., A Crystallographic Examination of Predisposition versus Preorganization in de Novo Designed Metalloproteins. *J. Am. Chem. Soc.* **2016,** *138* (36).

12. Touw, D. S. Structural and spectroscopic studies of heavy metal binding to de novo designed coiled coil peptides. University of Michigan, United States, 2007.

13. *Fmoc Solid Phase Peptide Synthesis: A Practical Approach*. 2 ed.; Oxford University Press: New York, 2000.

14. Otwinowski, Z.; Minor, W., Processing of X-ray diffraction data collected in oscillation mode. *Methods Enzymol.* **1997,** *276*, 307-326.

15. Langer, G.; Cohen, S. X.; Lamzin, V. S.; Perrakis, A., Automated macromolecular model building for X-ray crystallography using ARP/wARP version 7. *Nat. Protoc.* **2008,** *3* (7), 1171-9.

16. Emsley, P.; Cowtan, K., Coot: model-building tools for molecular graphics. *Acta Crystallogr. D Biol. Crystallogr.* **2004,** *60* (Pt 12 Pt 1), 2126-32.

17. Bricogne, G.; Blanc, E.; Brandl, M.; Flensburg, C.; Keller, P.; Paciorek, W.; Roversi, P.; Sharff, A.; Smart, O. S.; Vonrhein, C.; Womack, T. O. *BUSTER version 2.11.2*, United Kingdom: Global Phasing Ltd: Cambridge.

18. Chen, V. B.; Arendall, W. B., 3rd; Headd, J. J.; Keedy, D. A.; Immormino, R. M.; Kapral, G. J.; Murray, L. W.; Richardson, J. S.; Richardson, D. C., MolProbity: all-atom structure validation for macromolecular crystallography. *Acta Crystallogr. D Biol. Crystallogr.* **2010,** *66* (Pt 1), 12-21.

19. Dapprich, S.; Komáromi, I.; Byun, K. S.; Morokuma, K.; Frisch, M. J., A new ONIOM implementation in Gaussian98. Part I. The calculation of energies, gradients, vibrational frequencies and electric field derivatives1. *Journal of Molecular Structure: THEOCHEM* **1999,** *461*, 1-21.

20. Vreven, T.; Morokuma, K.; Farkas, Ö.; Schlegel, H. B.; Frisch, M. J., Geometry optimization with QM/MM, ONIOM, and other combined methods. I. Microiterations and constraints. *J. Comput. Chem.* **2003,** *24* (6), 760-769.

21. Senn, H. M.; Thiel, W., QM/MM methods for biomolecular systems. *Angew. Chem. Int. Ed. Engl.* **2009,** *48* (7), 1198-229.

22. Chung, L. W.; Sameera, W. M.; Ramozzi, R.; Page, A. J.; Hatanaka, M.; Petrova, G. P.; Harris, T. V.; Li, X.; Ke, Z.; Liu, F.; Li, H. B.; Ding, L.; Morokuma, K., The ONIOM Method and Its Applications. *Chem. Rev.* **2015,** *115* (12), 5678-796.

23. Becke, A. D., Density-functional exchange-energy approximation with correct asymptotic behavior. *Phys. Rev. A* **1988,** *38* (6), 3098-3100.

24. Becke, A. D., Density-functional thermochemistry. III. The role of exact exchange. *The Journal of chemical physics* **1993,** *98* (7), 5648-5652.

25. Cornell, W. D.; Cieplak, P.; Bayly, C. I.; Gould, I. R.; Merz, K. M.; Ferguson, D. M.; Spellmeyer, D. C.; Fox, T.; Caldwell, J. W.; Kollman, P. A., A Second Generation Force Field for the Simulation of Proteins, Nucleic Acids, and Organic Molecules. *J. Am. Chem. Soc.* **1995,** *117* (19), 5179-5197.

26. Frisch, M. J.; Trucks, G.; Schlegel, H. B.; Scuseria, G.; Robb, M.; Cheeseman, J.; Scalmani, G.; Barone, V.; Mennucci, B.; Petersson, G., Gaussian 09, revision A. 1. *Gaussian Inc. Wallingford CT* **2009,** *27*, 34.

27. Hay, P. J.; Wadt, W. R., Ab initio effective core potentials for molecular calculations. Potentials for the transition metal atoms Sc to Hg. *The Journal of chemical physics* **1985,** *82* (1), 270-283.

28. Weiner, S. J.; Singh, U. C.; Kollman, P. A., Simulation of formamide hydrolysis by hydroxide ion in the gas phase and in aqueous solution. *J. Am. Chem. Soc.* **1985,** *107* (8), 2219-2229.

29. Bakowies, D.; Thiel, W., Hybrid Models for Combined Quantum Mechanical and Molecular Mechanical Approaches. *The Journal of Physical Chemistry* **1996,** *100* (25), 10580-10594.

30. Case, D. A.; Cheatham, T. E.; Darden, T.; Gohlke, H.; Luo, R.; Merz, K. M.; Onufriev, A.; Simmerling, C.; Wang, B.; Woods, R. J., The Amber biomolecular simulation programs. *J. Comput. Chem.* **2005,** *26* (16), 1668-1688.

31. Case, D.; Cheatham, T.; Darden, T.; Gholke, R.; Luo, R.; Merz, K.; Onufriev, A.; Simmerling, C.; Wang, J.; Woods, R., Case. *DA, Cheatham, TEI, Darden, TA, Gholke, R., Luo, R., Merz, KM, Onufriev, A., Simmerling, CL, Wang, J., and Woods* **2018**, 1668-1688.

32. Price, D. J.; Brooks III, C. L., A modified TIP3P water potential for simulation with Ewald summation. *The Journal of chemical physics* **2004,** *121* (20), 10096-10103.

33. Lindahl, E.; Hess, B.; Van Der Spoel, D., GROMACS 3.0: a package for molecular simulation and trajectory analysis. *Molecular modeling annual* **2001,** *7* (8), 306-317.

34. Oostenbrink, C.; Villa, A.; Mark, A. E.; Van Gunsteren, W. F., A biomolecular force field based on the free enthalpy of hydration and solvation: the GROMOS force-field parameter sets 53A5 and 53A6. *J. Comput. Chem.* **2004,** *25* (13), 1656-1676.

35. Neupane, K. P.; Pecoraro, V. L., Probing a homoleptic PbS3 coordination environment in a designed peptide using 207Pb NMR spectroscopy: Implications for understanding the molecular basis of lead toxicity. *Angewandte Chemie - International Edition* **2010,** *49* (44), 8177-8180.

36. Ruckthong, L. Crystallographic comparison of tris-thiolate sites in designed proteins to control metal geometries. University of Michigan, Ann Arbor, MI, 2016.

37. Iranzo, O.; Jakusch, T.; Lee, K.-H.; Hemmingsen, L.; Pecoraro, V. L., The correlation of 113Cd NMR and 111mCd PAC spectroscopies provides a powerful approach for the characterization of the structure of Cd(II)-substituted Zn(II) proteins. *Chemistry (Weinheim an der Bergstrasse, Germany)* **2009,** *15* (15), 3761-72.

38. Touw, D. S. Structural and spectroscopic studies of heavy metal binding to de novo designed coiled-coil peptides. University of Michigan, Ann Arbor, Michigan, 2007.

39. Peacock, A. F. A.; Iranzo, O.; Pecoraro, V. L., Harnessing natures ability to control metal ion coordination geometry using de novo designed peptides. *Dalton Trans.* **2009,** *9226* (13), 2271-80.

40. Tegoni, M.; Yu, F.; Bersellini, M.; Penner-Hahn, J. E.; Pecoraro, V. L., Designing a functional type 2 copper center that has nitrite reductase activity within α-helical coiled coils. *Proceedings of the National Academy of Sciences* **2012,** *109* (52), 1-6.

Chapter 3 Spectroscopic Characterization of Transition Metal Binding to Symmetric and Asymmetric Peptide Scaffolds

Introduction

While Chapter 2 describes a method to selectively form both A_2B and AB_2 heterotrimers, the goal of this work is to incorporate a transition metal binding center to study catalysis in an asymmetric scaffold. Dr. Catherine Mocny has previously described a His_3 layer with 1-3 Asp residues in an adjacent layer.[1] The focus of this chapter is to determine if the asymmetric properties observed in Cys^a heterotrimers were transferrable to Cys^d heterotrimers. Additionally, this work will expand the scope of transition metals in the asymmetric environment from Co(II) and Zn(II) described by Dr. Mocny to include Cu(I/II).

The ultimate goal of this work is to model both primary and secondary coordination spheres of native metalloenzyme active sites. This chapter will first examine Zn(II) and Co(II) coordination to $Glu_x{}^dHis_3{}^a$ sites, where x is between 1 and 3, as an expansion of the work done by Dr. Melissa Zastrow and Dr. Mocny.[1-3] Peptides described in this chapter will follow a similar format as in Chapter 2 but will instead list only the mutations from the GR sequence at the transition metal site. Thus, formation of the $Glu_3{}^dHis_3{}^a$ homotrimer requires 3 equivalents of the Glu^dHis^a peptide listed in Table 3-1, which has only the Cys^d mutation at the Pb(II) binding site. The alternate homotrimer, $His_3{}^a$, is formed from 3 equivalents of the His^a strand, containing both the Ala^a and Cys^d mutations at the Pb(II) binding site. Heterotrimers containing intermediate numbers of Glu resides contain a mixture of these two strands to achieve the desired Glu stoichiometry. The fully selective heterotrimers are induced by the mixed Cys^d and Ala^aCys^d layers at the Pb(II) site from the Glu^dHis^a and His^a strands, respectively.

Previous work in the Pecoraro lab has focused on building a *de novo* model of carbonic anhydrase (CA), a zinc metalloenzyme. The native enzyme coordinates Zn(II) with three His residues in a pseudotetrahedron with an exogenous solvent molecule (Figure 3-1).[4] Dr. Zastrow was able to construct this site in a TRI peptide, TRI L9CL23H, generating the best aqueous model of the native reaction and, at the time, the best esterase model of CA, a secondary function

of the enzyme (Table 3-1).[3] Thus proving that the TRI family is an excellent scaffold in which to explore hydrolytic zinc chemistry.

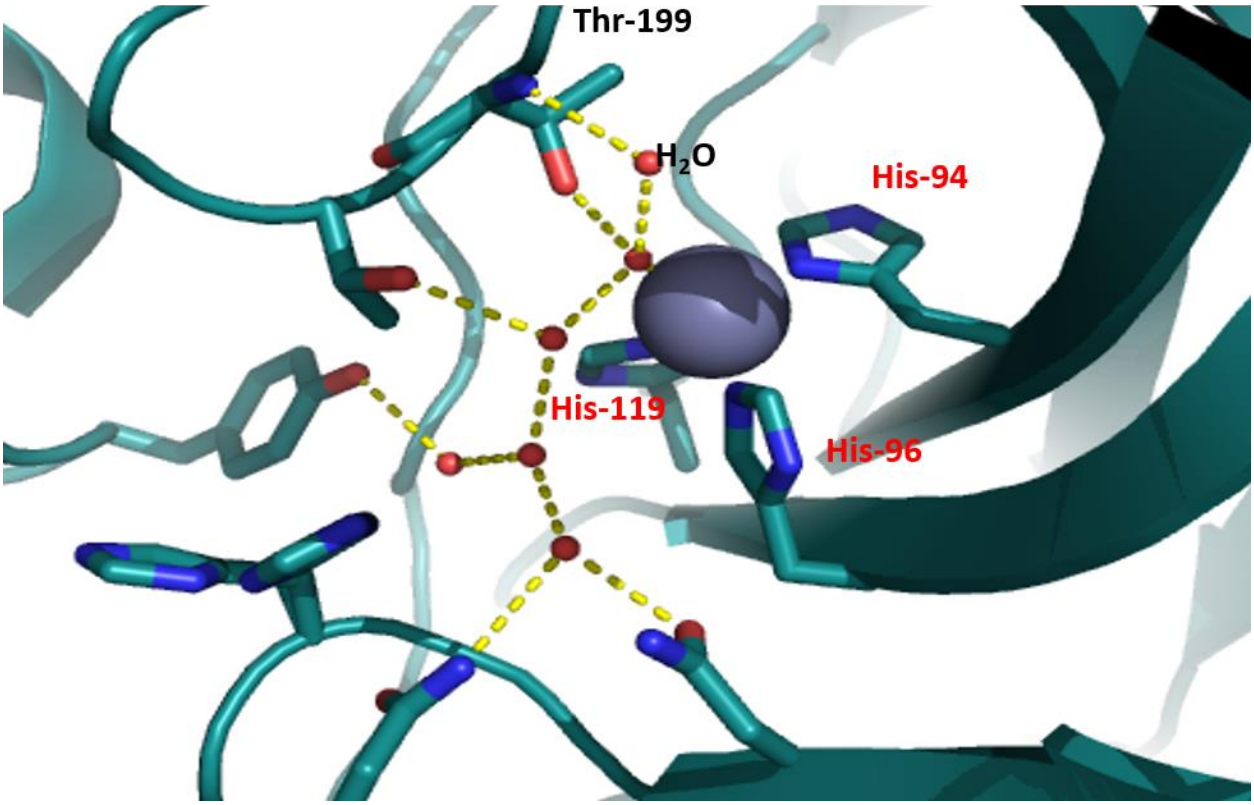

Figure 3-1Active site of CAII (PDB: 2CBA)[5]

*Table 3-1 List of peptide sequences discussed in this chapter with substitutions at the lead binding site in **bold green** and at the transition metal binding site in **bold red**.*

Abbreviation	Sequence
TRI L9CL23H	Ac-G WKALEEK **C**KALEEK LKALEEK **H**KALEEK G-NH_2
TRI His^a	Ac-G WKALEEK LKALEEK LKALEEK **H**KALEEK G-NH_2
His^a	Ac-G WKALEEK LKA**C**EEK **A**KALEEK LKALEEK **H**KALEEK G-NH_2
Asp^dHis^a	Ac-G WKALEEK LKA**C**EEK LKALEEK LKA**D**EEK **H**KALEEK G-NH_2
Glu^dHis^a	Ac-G WKALEEK LKA**C**EEK LKALEEK LKA**E**EEK **H**KALEEK G-NH_2
His^d	Ac-G WKALEEK LKA**C**EEK **A**KALEEK LKA**H**EEK LKALEEK G-NH_2
His^dHis^a	Ac-G WKALEEK LKA**C**EEK LKALEEK LKA**H**EEK **H**KALEEK G-NH_2
His^aGlu^d	Ac-G WKALEEK LKALEEK **C**KALEEK LKALEEK **H**KA**E**EEK G-NH_2
His^aAsp^d	Ac-G WKALEEK LKALEEK **C**KALEEK LKALEEK **H**KA**D**EEK G-NH_2
GRCS L16CL30H	Ac-E WEALEKK LAALESK **C**QALEKK LQALEKK **H**EALEHG-NH_2

This model, while an excellent reconstruction of the primary coordination sphere, was limited in that it could not also incorporate a second coordination sphere hydrogen bonding residue. The native enzyme contains a threonine residue in the active site that hydrogen bonds to the Zn(II)-coordinated solvent molecule, mediating the pK_a of the active site.[6-8] The removal of

this hydrogen bonding residue increases the pK_a of the active site by ~2 pH units and decreases the catalytic efficiency by a factor of 100. The TRI His_3^a model characterized by Dr. Zastrow has a pKa ~ 2 pH units above that of the native enzyme and is ~400-fold less efficient. It was hypothesized, therefore, that the introduction of a second coordination sphere hydrogen bonding residue could decrease the active site pK_a and increase the reaction rate.

To this end, Dr. Mocny explored both threonine and aspartate residues in the **d** layer directly N-terminal of the His_3^a site in the GR scaffold. The kinetic parameters of these sites are discussed in Chapter 4. Herein, we must consider if the spectroscopic properties of Zn(II) or Co(II), used as a probe for Zn(II), were perturbed if an asymmetric number of hydrogen bonding residues are placed adjacent to the His_3^a site. Dr. Mocny first found that the addition of an aspartate binding site did not perturb Pb(II) binding and no change to the Pb(II)-S_3 LMCT band was observed with a $Asp_3^dHis_3^a$ site in addition to a Cys_3^a site.[1]

The ability of an asymmetric peptide binding site to confer asymmetry on a transition metal was determined via perturbations to cobalt d-d UV-visible transitions. The homotrimeric His_3^a peptide had a symmetric peak with an extinction coefficient corresponding to a 6-coordinate Co(II) species (Figure 3-2). The other homotrimer, $Asp_3^dHis_3^a$, had a similar UV-visible absorption band (slightly red shifted), but with slightly higher extinction coefficient. The $Asp_1^dHis_3^a$ and $Asp_2^dHis_3^a$ heterotrimers, however, had asymmetric absorption profiles with extinction coefficients corresponding to 5-coordinate structures. The coordination environment of these $Asp_x^dHis_3^a$ species was confirmed via Co(II) EXAFS, in which the heterotrimers best fit to 5-coordinate species while the homotrimers best fit to 6-coordination. The Zn(II) EXAFS, however, best fit to 4-coordinate for all trimers with indistinguishable fits for 2 His and 2 oxygen ligands or 3 His and 1 oxygen ligand. This work proved that an asymmetric scaffold can confer asymmetry on a distant transition metal binding site. Cobalt, however, in this system is not an accurate spectroscopic probe for zinc active site structure.

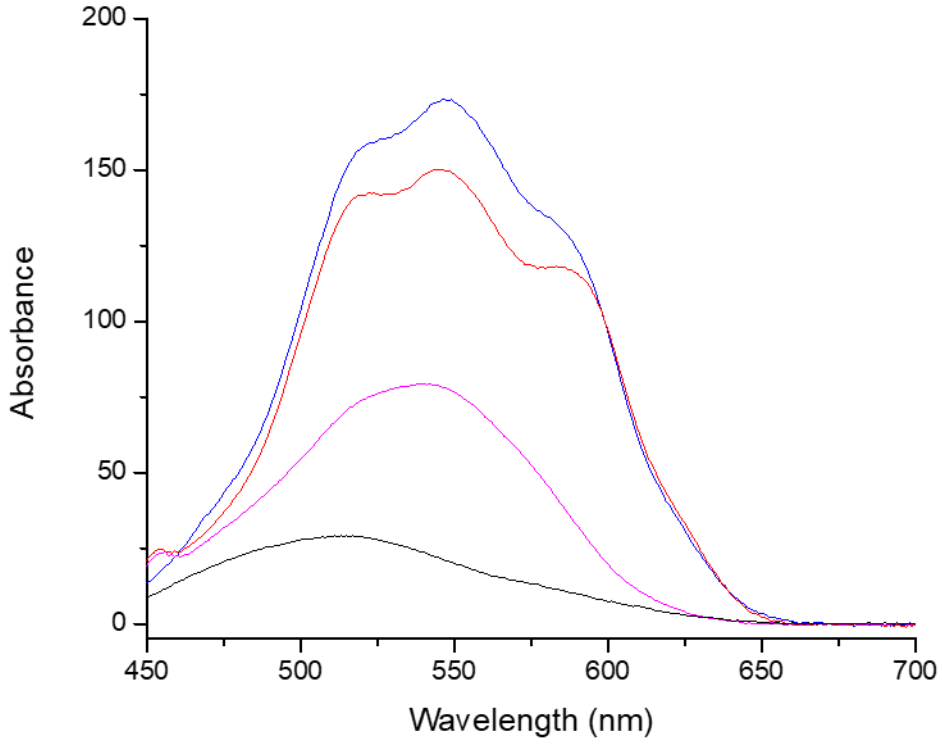

Figure 3-2 Co(II) absorption spectra of His_3^a (black), $Asp_3^dHis_3^a$ (pink), $Asp_2^dHis_3^a$ (blue), and $Asp_1^dHis_3^a$ (red). All spectra contain 0.5 mM 3SCC and 0.5 mM $CoSO_4$ in 50 mM HEPES pH 7.5.

In addition to the work with Zn(II) and Co(II) to investigate a CA active site, Cu(I) and Cu(II) binding environments will be probed as a model of Cu-only SOD. This enzyme is asymmetric in the first coordination sphere, with three His ligands in the Cu(I) bound form and four His ligands in the Cu(II) bound form (Figure 3-3).[9] Extensive work has been done on copper binding to three-fold symmetric His_3^a sites in the TRI peptide, but most of this work was done at pH 5.9 as a model of Cu NiR. Dr. Fangting Yu was able to characterize Cu(I) and Cu(II) binding to TRI His_3^a by EPR and XAS spectroscopies. Cu(I) XAS showed that the metal was three-coordinate with an average bond distance of 1.93 Å. This was consistent with a three-coordinate species observed at pH 5.9. Cu(II) UV-visible and EPR spectroscopies were consistent with a Type 2 copper center containing 3 His residues and 2 exogenous solvent molecules. The EPR spectra were invariant between pH 5.19 and 7.80. These data suggest that work done by Dr. Yu with TRI His_3^a at pH 5.9 should be consistent with work done at pH 7.5 as a study of Cu-only SOD.

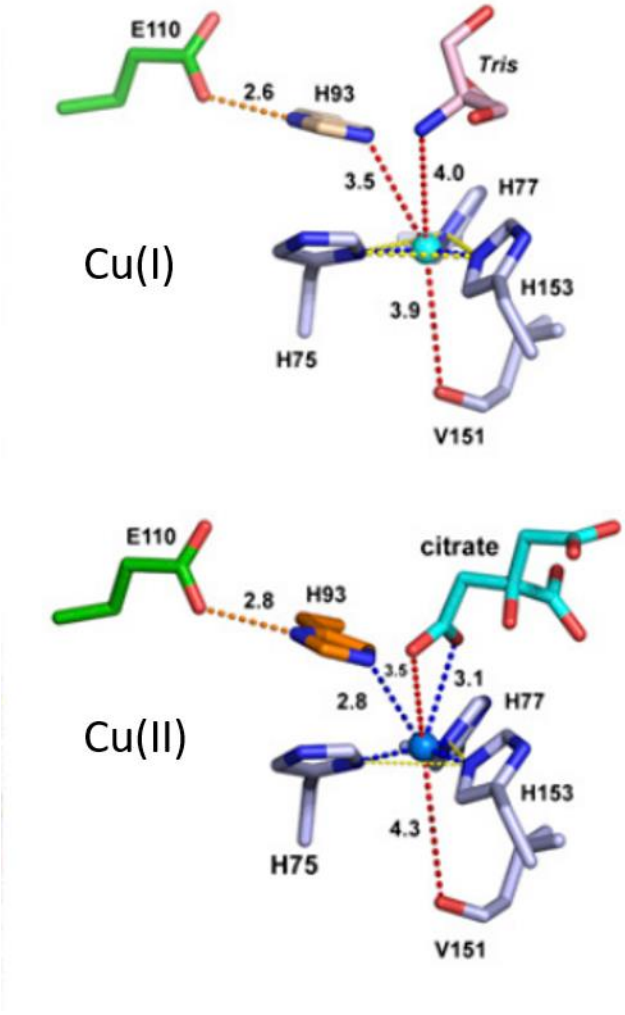

Figure 3-3 Cu(I) (top) and Cu(II) (bottom) coordination environments in Cu-only SOD[9]

Herein, the effects on Cu(I) and Cu(II) spectroscopy will be explored for His_3^a, His_3^d, and mixed $His_x^dHis_{3-x}^a$ species in the GR scaffold. This will serve to probe both the effects of the angle of the His_3 plane relative to the helical axis and if His_3^d and His_3^a sites behave differently with copper. Dr. Zastrow found that there was no change to Zn(II) kinetic properties with a **d** site His layer,[10] but this has not previously been studied with copper. Given the drastic changes observed in Pb(II) binding to **a** vs **d** layers, one can imagine other metals could bind differently to binding sites in alternate layers as well. His_4 binding sites will also be investigated as a model of the Cu(II) bound form of the enzyme.

Copper binding will also be investigated in sites with mixed histidine and carboxylate ligands. These sites are reminiscent of Fe/Mn SODs, which bind either Fe or Mn with two histidine and one aspartate in equatorial positions and an additional axial histidine.[11] These sites

aim to determine the effect of negatively charged amino acids on copper binding and catalysis as well as the selectivity of different *de novo* SOD models for different redox active metals. In fact, in our GRα_3D SOD models, there was no difference in reaction rate of His_3 and His_3Asp models.[12] These sites allow for a study of both asymmetry in *de novo* systems and structure-function relationships as copper is incorporated into systems that utilize iron or manganese in nature.

The first aim of this chapter is to confirm the Co(II) spectroscopy of Cys^a systems with a Cys^d heterotrimer. This will ensure that modification of the Pb(II) binding site does not disrupt transition metal binding. It was previously shown in Chapter 2 that transition metal binding does not perturb Pb(II) binding to Cys^d heterotrimers, but the reverse must be true as well. Then, the effects on cobalt and zinc binding to $Glu_x{}^dHis_3{}^a$ systems will be explored as a study of CA chemistry. Previous work by Dr. Mocny with the $Asp_x{}^dHis_3{}^a$ peptides did show asymmetry in the Co(II) binding environment, but no improvement to CA ester hydrolysis activity was observed over TRI $His_3{}^a$.[1] It was hypothesized that, rather than forming the intended water hydrogen bond, the Asp residue was instead forming a chelate motif with a His residue and preventing the Zn(II) from coordinating all 3 His residues. This work aims to characterize a Zn(II) binding site with longer carboxylate chain with the aim of removing this chelate motif and instead generating the desired hydrogen bond in the center of the 3SCC. This work will then explore copper binding to His_3, His_4, and $His_3(Carboxy)_x$ systems to determine how both the cuprous and cupric ions bind to different positions in the heptad and with different local charges as a model of Cu-only and Fe/Mn SOD. This chapter will conclude with an analysis of how different metal ions interact differently with identical protein ligand environments.

Methods

Peptide synthesis and purification

Peptides were synthesized on a Biotage Initiator+ Alstra peptide synthesizer using Fmoc-rink amide-methylbenzhydrylamine (MBHA) resin. Standard deprotection and coupling protocols with HOBt/HBTU/DIEA were used.[13] Peptides were cleaved from the resin using trifluoroacetic acid, thioanisole, ethanedithiol, and anisole (90:5:3:2) for four hours, precipitated with cold ether, and redissolved in double distilled water. The crude peptide was then lyophilized to dryness. The peptide was purified using a Waters 600 HPLC with a reverse phase C-18 column. A linear

gradient from 70% A (0.1% trifluoroacetic acid in double distilled water) 30% B (0.1 % trifluoroacetic acid, 10% double distilled water, 90% acetonitrile) to 20% A/80% B was utilized at a flow rate of 20 mL/min over 35 minutes. ESI-MS was used to confirm the mass of the pure peptide, which was then lyophilized to dryness.

Circular dichroism spectroscopy

Circular dichroism spectroscopy was performed on a Jasco CD-Spectropolarimeter with a 1 cm pathlength quartz cuvette. Guanidinium hydrochloride (GuHCl) titrations were performed with a 10 μM peptide solution in 10 mM potassium phosphate, pH 7.5 at 25 °C. A solution containing 10 μM peptide, 10 mM potassium phosphate, and concentrated GuHCl was titrated into the cuvette in 0.05 M GuHCl steps to 7 M GuHCl with 30 seconds of stirring at 450 rpm between each addition. The absorbance at 222 nm was monitored after each addition.

^{207}Pb NMR

^{207}Pb NMR was performed with unbuffered peptide solutions containing 3-5 mM trimer with 0.9 equivalents of isotopically enriched $^{207}Pb(NO_3)_2$ per trimer in 10% D_2O prepared from a new ampule for each experiment. Samples with Co(II) also contain 0.9-1 equivalents of $CoSO_4$. The pH was adjusted with small aliquots of KOH. The reported pH does not correct for the deuterium concentration. Spectra were collected for 5-12 hours at 25 °C without spinning, 0.020 ms relaxation time, and 20 ms acquisition time, and a direct delay receiver time constant of ~90 at 145.95 MHz on a 700 MHz Varian NMR Spectrometer. All spectra were referenced to 1 M $Pb(NO_3)_2$ in D_2O (δ=-2990 ppm relative to $Pb(CH_3)_4$). Backwards linear prediction was performed to generate the reported Fourier transforms. The most intense peak in the FID, typically occurring between points 15 and 25, was selected as the point from which linear prediction was performed and the predicted number of points was equivalent to the number of excluded points. Spectra were exported directly from the acquisition software and were not processed in software such as MestReNova as the default frequency for Pb is inaccurate.

Co(II) titrations

UV-visible data was acquired on a Cary 100 Bio UV/Vis Spectrometer with a 1 cm pathlength quartz cuvette. A solution containing 1.5 mM peptide and 0.5 mM $Pb(NO_3)_2$ in 50 mM HEPES, pH 7.5 was titrated with 0.1 equivalents of 16 mM $CoSO_4$ with 8 minutes of stirring between

each addition. The absorbance of the Co(II) d-d transition was monitored from 200 to 800 nm. The concentration of metal stock solutions was determined by ion coupled plasma mass spectrometry with a Perkin-Elmer Nexion 2000 ICP-MS and equivalencies added were adjusted based on the corrected concentration.

The Co(II) affinity was determined for these peptides by monitoring the absorbance at λ_{max} and fitting the resulting curve by the following method:

The equilibrium for the association of Co(II) can be described by the following equation

Equation 3-1

$$Co(II) + PbPep_3 \rightleftharpoons CoPbPep_3$$

Which can be described by the following equilibrium expression:

Equation 3-2

$$K_d = \frac{[PbPep_3]_F[Co]_F}{[CoPbpep_3]}$$

And the following mass balance expressions can be applied:

Equation 3-3

$$[Co]_T = [Co]_F + [CoPbPep_3]$$

Equation 3-4

$$[PbPep_3]_T = [PbPep_3]_F + [CoPbPep_3]$$

Rearrangement of Equation 3-3 and Equation 3-4 followed by substitution into Equation 3-2 yields the following expression

Equation 3-5

$$K_d = \frac{([PbPep_3]_T - [CoPbPep_3])([Co]_T - [CoPbPep_3])}{[CoPbPep]_3}$$

No correction for pH was required since the histidines are deprotonated at the examined pH and hydrolysis of the metal does not begin until approximately pH 10. The absorbance of the Co(II) bound peptide was monitored and the concentration of this species was determined via Beer's law:

Equation 3-6

$$A = \varepsilon * l * [CoPbPep_3]$$

Equation 3-5 was rearranged to solve for the concentration of Co(II) bound peptide, the real solution of which was substituted into Equation 3-6 to solve for K_d.

Cu(II) titrations

UV-visible data was acquired on a Cary 100 Bio UV/Vis Spectrometer with a 1 cm pathlength quartz cuvette. A solution containing 750 μM peptide and 250 μM $Pb(NO_3)_2$ in 50 mM HEPES, pH 7.5 was titrated with 0.1 equivalents of 9.36 mM $CuCl_2$. The solution was stirred for 8 minutes between each addition. The absorbance of the Cu(II) d-d transition was monitored from 200 to 800 nm. The concentration of metal stock solutions was determined by ion coupled plasma mass spectrometry with a Perkin-Elmer Nexion 2000 ICP-MS.

Co(II) EPR spectroscopy

Co(II) EPR spectroscopy was performed on a Bruker EMX electron spin resonance spectrometer with a liquid helium cryostat. EPR samples contained 6 mM peptide, 2 mM $Pb(NO_3)_2$, and 1 mM $CoSO_4$ in 50 mM HEPES, pH 7.5 with 30% glycerol as a glassing agent. Spectra were collected at 4 K with a spectral range of 5000 G, spectrum center of 3000 G, attenuation of 10 dB, and modulation amplitude of 16 G..

Cu(II) EPR spectroscopy

Cu(II) EPR spectroscopy was performed on a Bruker EMX electron spin resonance spectrometer with a liquid nitrogen cryostat. EPR samples contained 900 μM peptide, 300 μM $Pb(NO_3)_2$, and 150 μM $CuCl_2$ in 50 mM HEPES, pH 7.5 with 30% glycerol as a glassing agent. Spectra were collected at 110 K with a spectral range of 2000 G, spectrum center of 3000 G, attenuation of 10 dB, and modulation amplitude of 4 G. EPR spectra were fit with the software Spincount.[14]

X-ray absorption spectroscopy

Samples for X-ray absorption spectroscopy were made with 6 mM peptide, 2 mM $Pb(NO_3)_2$, and 1 mM transition metal ($CoSO_4$, ZnOAc, $CuCl_2$) in 50 mM HEPES buffer, pH 7.5 with 50% glycerol as a glassing agent. Cu(I) samples were prepared with $CuCl_2$ and ~50 equivalents of sodium ascorbate as a reducing agent in degassed solvents. Samples were then loaded into sample cells and frozen in liquid nitrogen.

Measurements were conducted at the Stanford Synchrotron Radiation Lightsource beamline 9-3 which is equipped with a Si(220) double crystal monochrometer and a flat Rh-coated vertically collimating harmonic rejection mirror. The beam was calibrated with absorption spectra of Cu, Co, or Zn foils as a reference then the fluorescence excitation spectra were measured with a 100-

element Ge detector. Points were collected with 0.25 eV steps in the XANES region (1 second integration) and 0.05 $Å^{-1}$ in the EXAFS region (1-20 second integration) up to k=13.5 $Å^{-1}$. Samples were kept below 10 K during data collection with an Oxford Instruments liquid helium cryostat.

XAS fitting was performed with edges assigned as 8879 eV for Cu, 7709 eV for Co, and 9659 eV for Zn. Spectra were fit with the EXAFSPAK programs[15] with phase and amplitude calculations performed with FEFF 9.[16] Multiscattering fits of His residues were performed using metal-His models found in the Cambridge Crystallographic data base and Debye-Waller factors were taken from calculations by Bunker *et al*.[17] Pre-edge spectra were normalized with the program MBack.[18]

Results

Stability of apo peptides

The stabilities of apo $Glu_3^dHis_3^a$, $His_3^dHis_3^a$, and $His_3^aGlu_3^d$ were determined by chemical denaturation with GuHCl. Apo-$Glu_3^dHis_3^a$ folded into an alpha helical coiled coil with characteristic absorption minima at 208 and 222 nm (Figure 3-4a). The initial stability of this peptide is comparable to that of $Asp_3^dHis_3^a$ as determined by Dr. Mocny.[1] A denaturation profile was not fit to this peptide as no initial plateau in stability was observed under denaturing conditions (Figure 3-4b). The midpoint of unfolding was determined to be 2 M GuHCl, which is significantly more stable than $Asp_3^dHis_3^a$ with a midpoint of unfolding of 1 M GuHCl.

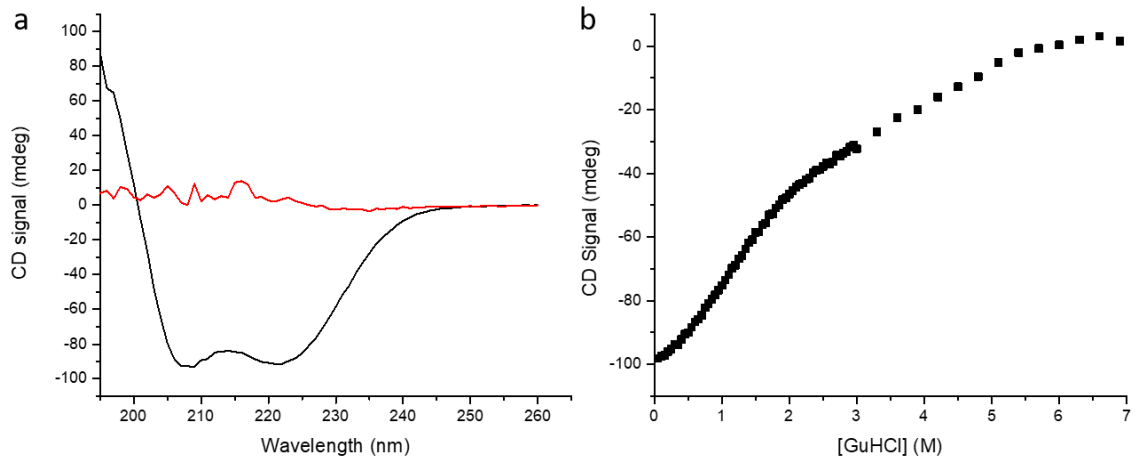

Figure 3-4 CD spectra of 10 μM $Glu_3^dHis_3^a$ (a) initial (black) and final (red) spectra and (b) Guanidinium denaturation curve in 10 mM potassium phosphate, pH 7.5

When the Glu residues are repositioned below the His_3^a plane, a similar initial stability is observed (Figure 3-5a). As with $Glu_3^dHis_3^a$, $His_3^aGlu_3^d$ cannot be fit to a two-step denaturation profile as no initial plateau is observed under denaturing conditions (Figure 3-5b). The midpoint of unfolding is 2.4 M GuHCl, which is comparable to $His_3^aAsp_3^d$ with a midpoint of 2.5 M GuHCl as measured by Dr. Mocny.[1]

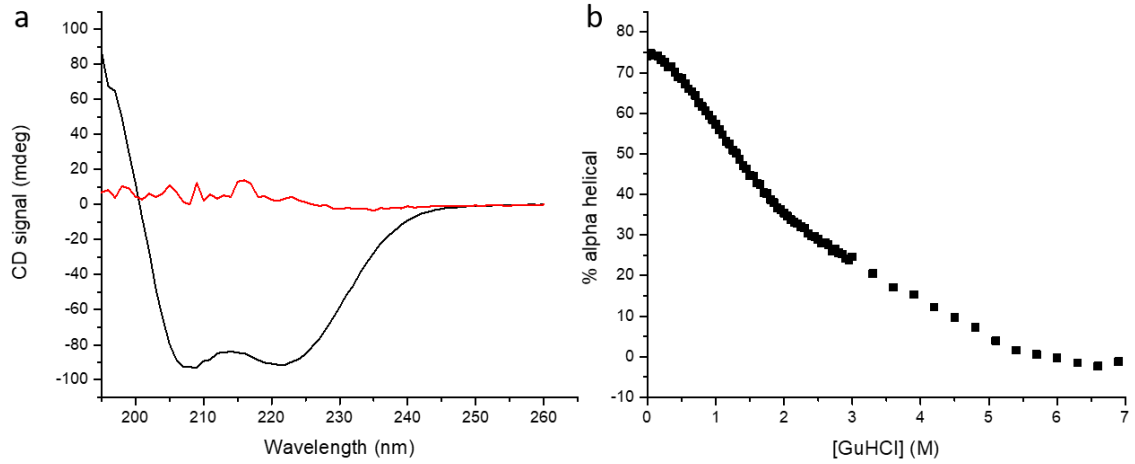

Figure 3-5 CD spectra of 10 μM $His_3^aGlu_3^d$ (a) initial (black) and final (red) spectra and (b) Guanidinium denaturation curve in 10 mM potassium phosphate, pH 7.5

The initial stability of $His_3^dHis_3^a$ is less than all other substitutions, but this peptide still folds into an alpha helical coiled coil (Figure 3-6a). As with the other constructs discussed here, a denaturation profile could not be fit because an initial plateau was not observed. The midpoint of

unfolding is 1.7 M GuHCl with an initial folding to 50% alpha helical (Figure 3-6b). Given the increased bulk of the additional His residue, these results are unsurprising.

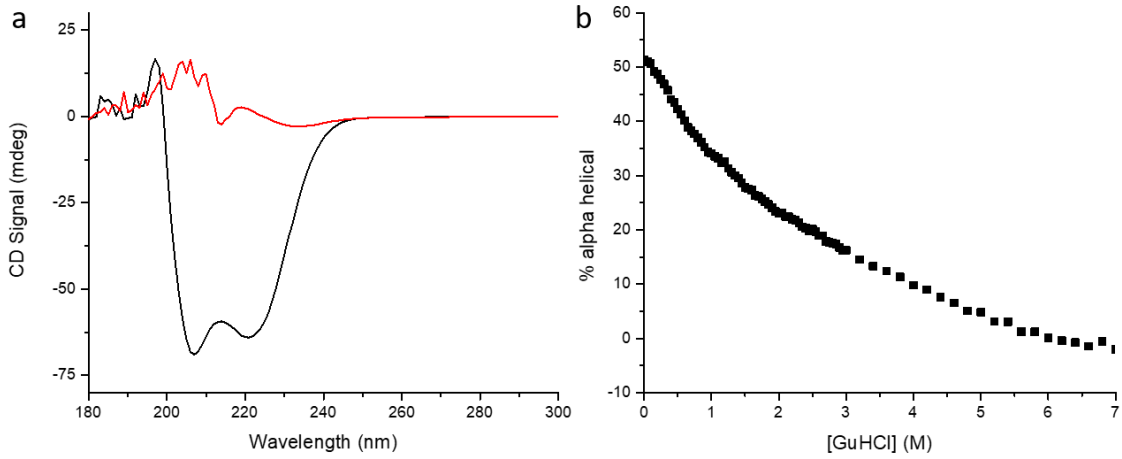

Figure 3-6 CD spectra of 10 μM $His_3{}^dHis_3{}^a$ (a) initial (black) and final (red) spectra and (b) Guanidinium denaturation curve in 10 mM potassium phosphate, pH 7.5

Pb(II) binding

The Pb(II) binding equivalency was determined for $Glu_3{}^dHis_3{}^a$ as Pb(II) may have some affinity for the carboxylate site. One equivalent of Pb(II) bound preferentially to the $Cys_3{}^d$ site per trimer with an absorption profile similar to $Asp_3{}^dHis_3{}^a$ (Figure 3-7).[1] In the absence of a transition metal, no ^{207}Pb NMR signal is observed for this species, which is indicative of fast exchange of a Pb(II) between the Cys_3 site and the transition metal site. This exchange may account for the curve of the titration approaching 1 equivalent of Pb(II). The extinction coefficient at 1 equivalent, however, is consistent with previously characterized Pb(II)-S_3 constructs.

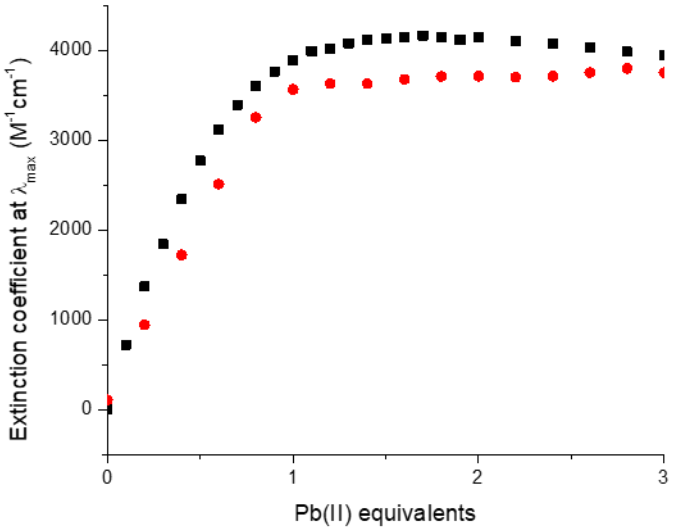

Figure 3-7 Pb(II) titration into 60 μM (Cys_3^a)$Glu_3^dHis_3^a$ (black) and Cys_3^d with no distant His site (red) in 50 mM HEPES with Pb(II) equivalents determined relative to trimer concentration

The Pb(II) binding equivalency was also determined for $His_3^dHis_3^a$. Given the increased bulk of adjacent His residues, it is possible that this peptide would no longer fold into a 3SCC. One equivalent of Pb(II) bound per trimer with an extinction coefficient consistent with previous Pb-S_3 peptides (Figure 3-8).

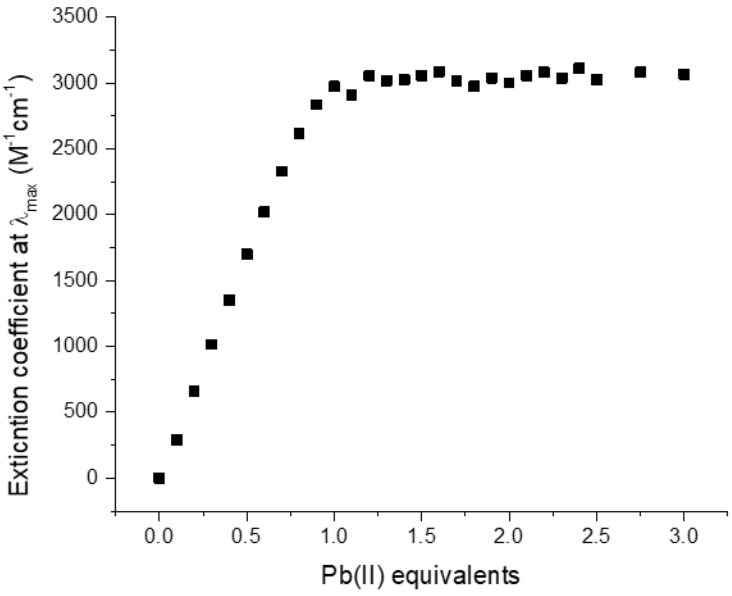

Figure 3-8 Pb(II) binding titration of 60 μM $His_3{}^dHis_3{}^a$ in 50 mM HEPES pH 7.5 with Pb(II) equivalents measured relative to trimer concentration

^{207}Pb NMR

The Pb-S_3 environment of $Glu_x{}^dHis_3{}^a$ peptides was further characterized by ^{207}Pb NMR. Only the $Glu_1{}^dHis_3{}^a$ peptide had a signal for the Pb-S_3 in the absence of Co(II). The chemical shift was similar in both the presence and absence of an additional transition metal (Figure 3-9).

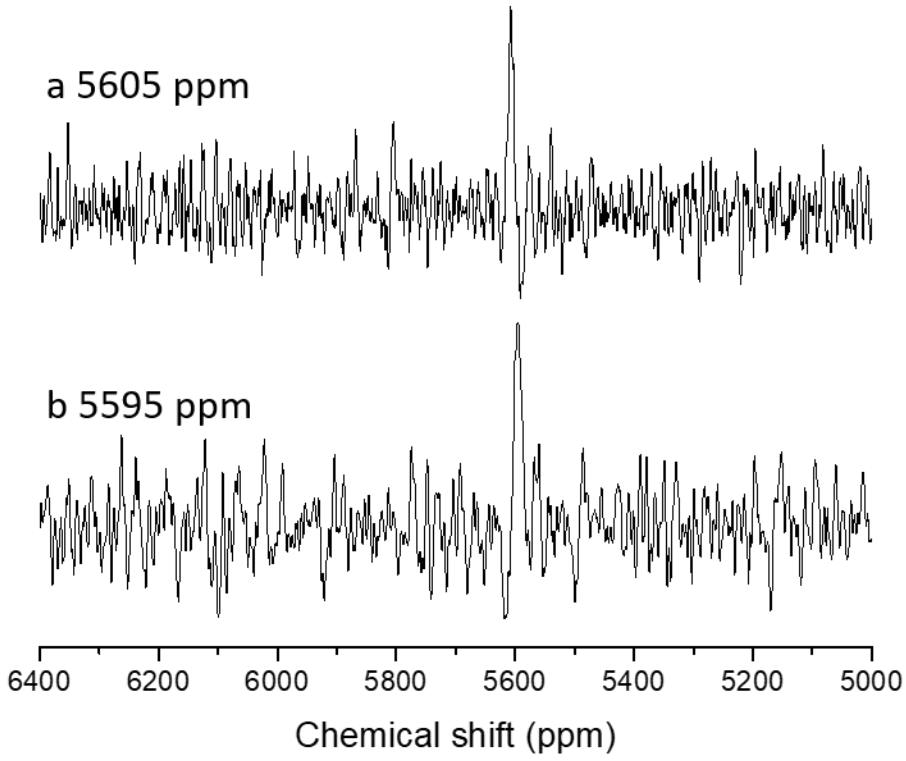

Figure 3-9 ^{207}Pb NMR of $Glu_1{}^dHis_3{}^a$ in the presence (a) and absence (b) of 1 equivalent of Co(II) at pH 7.5. All spectra contain 3.5-5 mM 3SCC and 1 equivalent of $Pb(NO_3)_2$ (relative to trimer) in 10% D_2O. NB this data is for Pb(II) binding to a Cys^a layer, not the transition metal site.

No ^{207}Pb NMR signal was observed for $Glu_2{}^dHis_3{}^a$ or $Glu_3{}^dHis_3{}^a$ in the absence of a transition metal. With the addition of 1 equivalent of Co(II), however, the chemical shifts observed are consistent with the appropriate heterotrimer shift for Cys^a peptides (Figure 3-10). As was observed by Dr. Mocny,[1] the addition of a transition metal to a carboxylate containing site provides full selectivity for both the $Ala_1{}^dCys_3{}^a(Glu_2{}^dHis_3{}^a)$ and $Ala_2{}^dCys_3{}^a(Glu_1{}^dHis_3{}^a)$ heterotrimers.

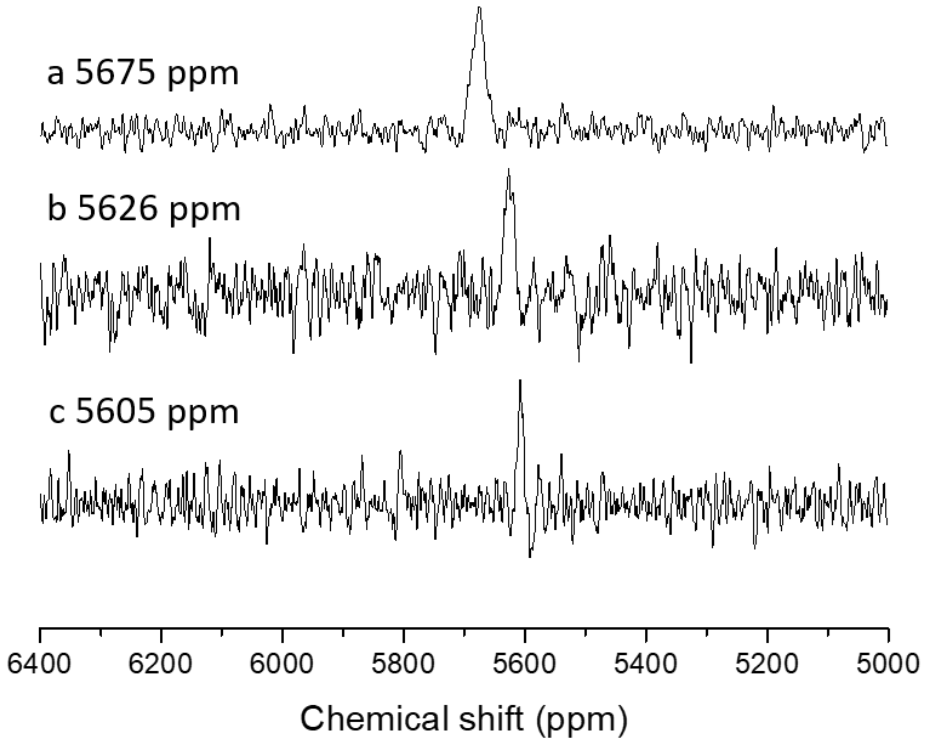

Figure 3-10 ^{207}Pb NMR of (a) $Glu_3^dHis_3^a$, (b) $Glu_2^dHis_3^a$, and (c) $Glu_1^dHis_3^a$ with 1 equivalent of Co(II) at pH 7.5. All spectra contain 3.5-5 mM 3SCC and 1 equivalent of $Pb(NO_3)_2$ (relative to trimer) in 10% D_2O. NB this data is for Pb(II) binding to a Cys^a layer, not the transition metal site.

Co(II) UV-visible spectroscopy

The Co(II) absorption profile was determined for $Glu_x^dHis_3^a$ peptides, where x is between 0 and 3 in Cys^a and Cys^d constructs. Cys^a constructs were used for direct comparison to the Asp_xHis_3 peptides characterized by Dr. Mocny while Cys^d constructs were used to ensure that full selectivity of the scaffold was achieved even in the absence of a transition metal. No significant differences were observed at the His_3 site between the Cys^a and Cys^d systems (Figure 3-11). The His_3^a homotrimer had the lowest extinction coefficient, consistent with 6-coordinate Co(II), and highest energy maximum absorbance. The other homotrimer, $Glu_3^dHis_3^a$, had a higher extinction coefficient and a less symmetric peak than His_3^a with a lower energy maximum absorbance. The two heterotrimers, $Glu_1^dHis_3^a$ and $Glu_2^dHis_3^a$ had significantly higher extinction coefficients consistent with 5-coordinate Co(II) complexes with similar peak shapes and maximum absorbance as $Glu_3^dHis_3^a$.

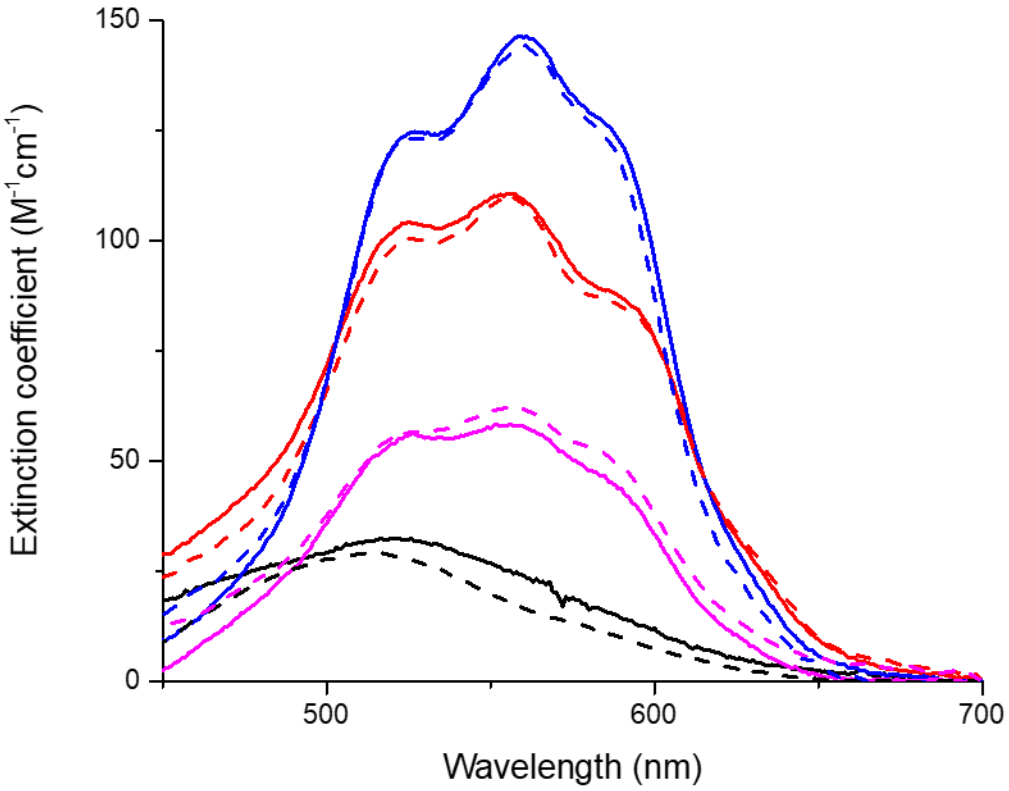

Figure 3-11 Co(II) absorption spectra of His_3^a (black), $Glu_3^dHis_3^a$ (pink), $Glu_2^dHis_3^a$ (blue), and $Glu_1^dHis_3^a$ (red). Cys^a systems are shown as dashed lines and Cys^d systems are shown as solid lines.

With the Asp containing trimers Dr. Mocny found that the maximum absorbance was slightly higher in energy (18180 cm^{-1}) than for the Glu trimers (17860 cm^{-1}, Figure 3-12). Additionally, the $Asp_3^dHis_3^a$ homotrimer had a single, smooth peak. Homotrimeric peptides had smooth, symmetric peaks with extinction coefficients consistent with 6-coordinate species. The shape of the heterotrimeric peaks was consistent between the $Asp_x^dHis_3^a$ and $Glu_x^dHis_3^a$ systems.

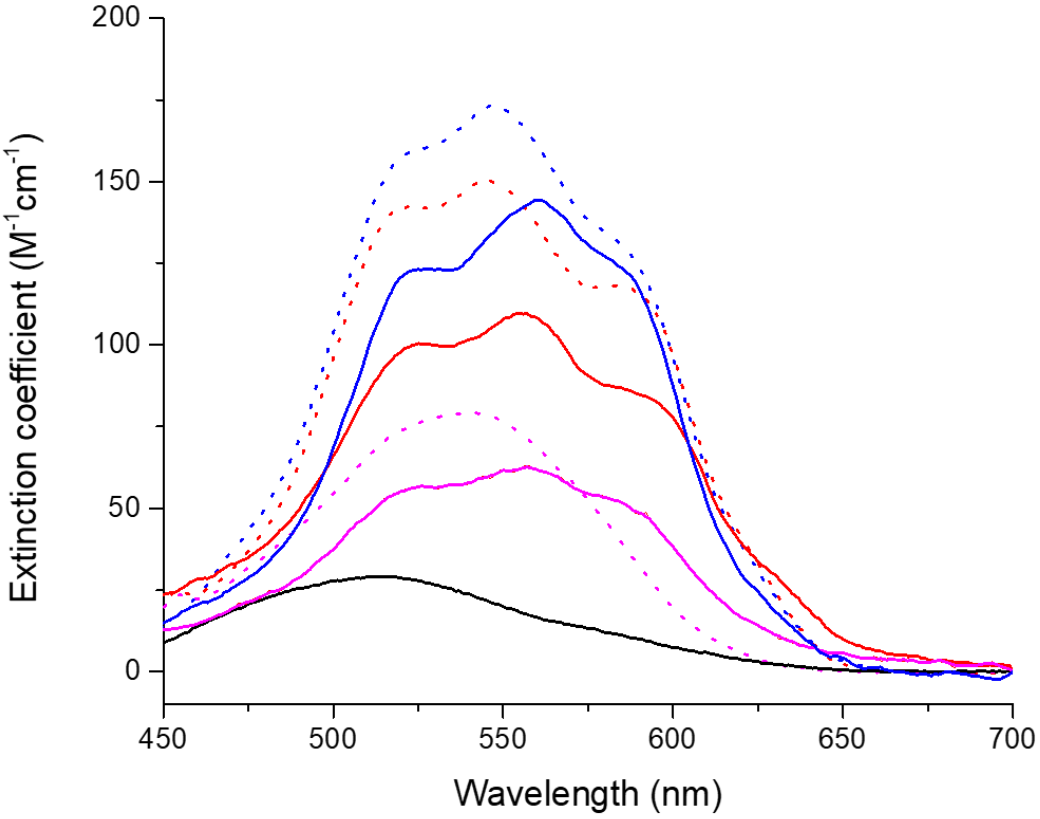

Figure 3-12 Co(II) absorption spectra of His_3^a (solid black), $Glu_3^dHis_3^a$ (solid pink), $Asp_3^dHis_3^a$ (dashed pink), $Glu_2^dHis_3^a$ (solid blue), $Asp_2^dHis_3^a$ (dashed blue), $Glu_1^dHis_3^a$ (solid red), and $Asp_1^dHis_3^a$ (dashed red) at pH 7.5. His_3^a and all Asp data were acquired by Dr. Mocny.[1]

The Co(II) d-d transition was also examined for peptides in which the Glu residue is in the **d**-layer C-terminal to the His^a site (His^aGlu^d). In these peptides, there was no difference in the absorbance profile between the homotrimer and two heterotrimers (Figure 3-13). This is consistent with data collected by Dr. Mocny on His^aAsp^d peptides.[1] As the introduction of varying numbers of carboxylate residues did not affect Co(II) d-d transitions, these peptides were not investigated further.

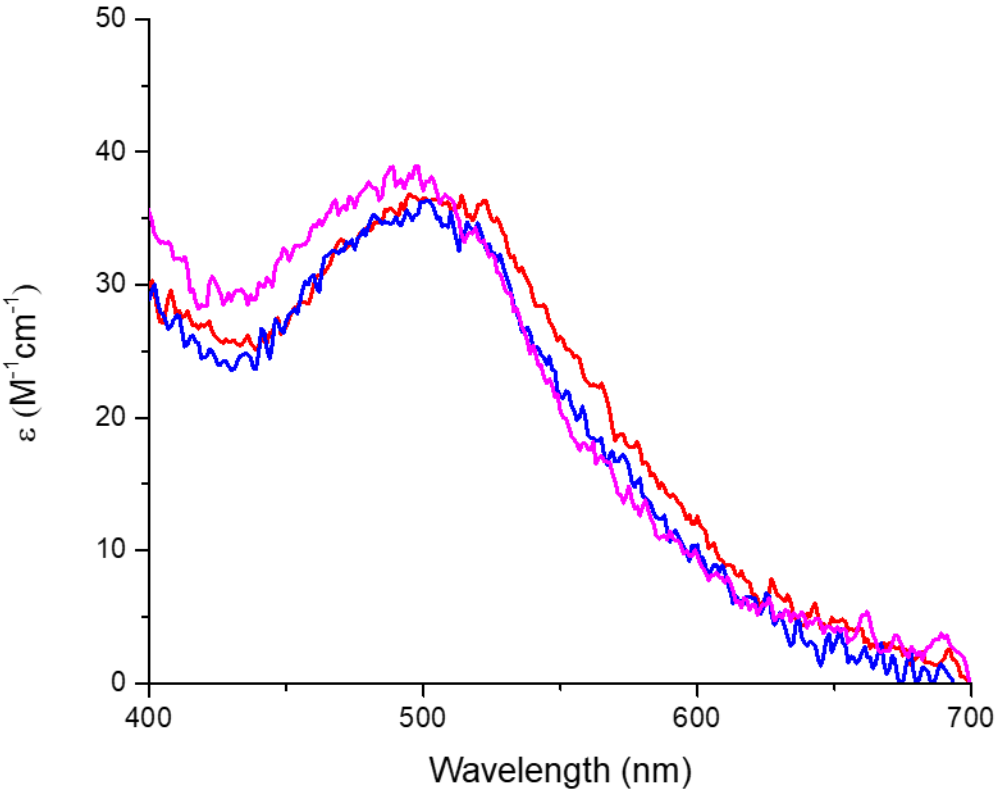

Figure 3-13 Co(II) absorption spectra of $His_3^aGlu_3^d$ (pink), $His_3^aGlu_2^d$ (blue), and $His_3^aGlu_1^d$ (red). This data was collected with Cys^a peptides.

Co(II) Affinity

The affinity of Co(II) for the $Glu_x^dHis_3^a$ peptides was determined spectroscopically from Co(II) titrations (Figure 3-14-Figure 3-16). The heterotrimers had the tightest cobalt binding at 13 and 10 μM for 1 and 2 Glu residues, respectively, though these values are within error of one

another (Table 3-2). The homotrimer, $Glu_3^dHis_3^a$, bound Co(II) significantly weaker at 28 ± 8 μM, though this binding is still tighter than His_3^a (41 ± 6 μM).

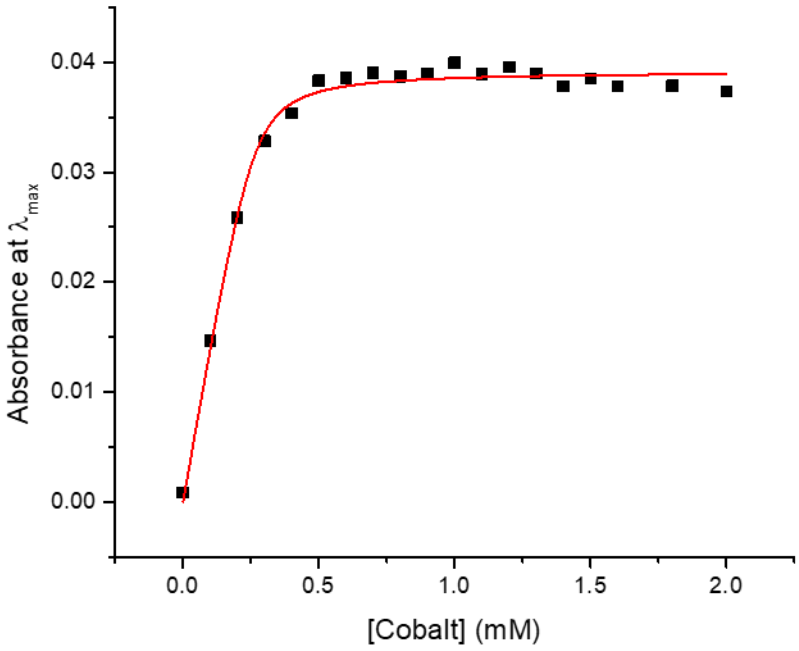

Figure 3-14 Co(II) affinity determination with 500 μM $Glu_1^dHis_3^a$ in 50 mM HEPES pH 7.5 with data in black and fit in red.

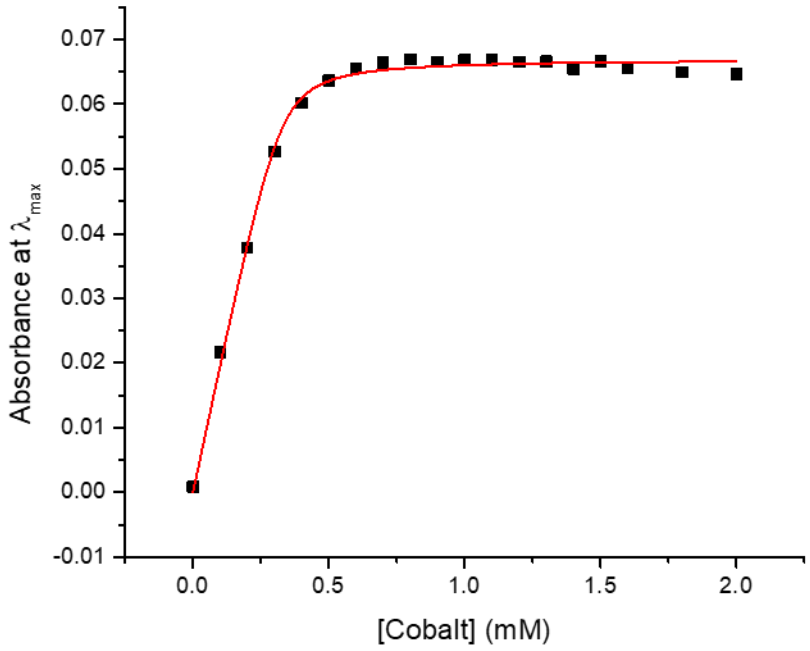

Figure 3-15 Co(II) affinity determination with 500 μM $Glu_2^dHis_3^a$ in 50 mM HEPES pH 7.5 with data in black and fit in red.

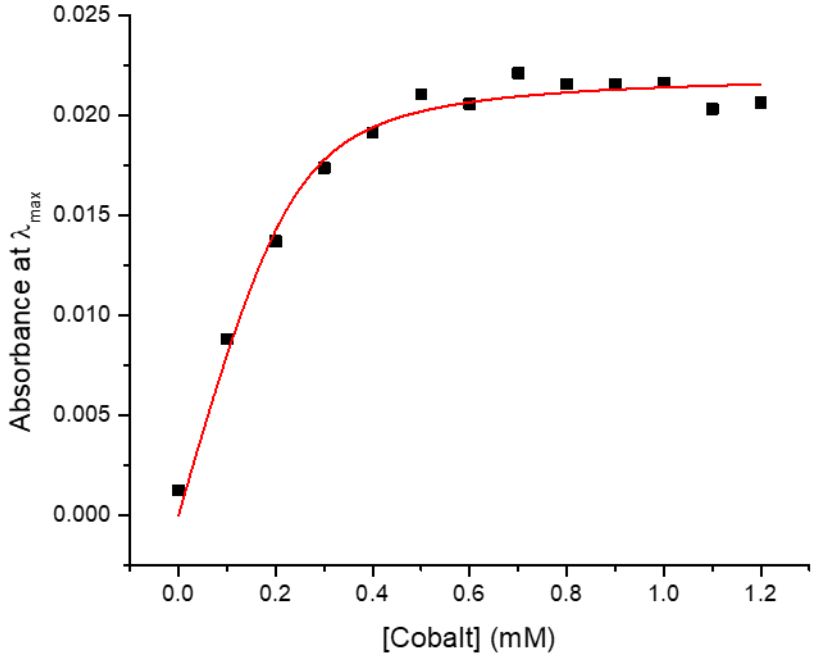

Figure 3-16 Co(II) affinity determination with 500 μM $Glu_3{}^dHis_3{}^a$ in 50 mM HEPES pH 7.5 with data in black and fit in red.

Table 3-2 Co(II) binding affinities (average ± S.D) for carboxylate containing peptides. $Glu_x{}^dHis_3{}^a$ peptides contain a Cys^d site while $His_3{}^a$ and $Asp_x{}^dHis_3{}^a$ peptides contain a Cys^a site and were collected by Dr. Mocny.[1]

Peptide	Affinity (μM)
$Glu_1{}^dHis_3{}^a$	13 ± 5
$Glu_2{}^dHis_3{}^a$	10 ± 3
$Glu_3{}^dHis_3{}^a$	28 ± 8
$His_3{}^a$	41 ± 6
$Asp_1{}^dHis_3{}^a$	20 ±2
$Asp_2{}^dHis_3{}^a$	7.9 ± 3.9
$Asp_3{}^dHis_3{}^a$	50 ± 8

Co(II) EXAFS

The extended X-ray absorption fine structure (EXAFS) of Co(II) bound to $Glu_x{}^dHis_3{}^a$ systems was determined. The homotrimer fit equally well to a 6-coordinate system with 3 oxygen and 3 histidine model (Figure 3-17) and a 5-coordinate system with 3 oxygen and 2 histidines. The 6-coordinate system fit with a longer oxygen scatterer at 2.11 Å and histidine at 1.98 Å for an average bond distance of 2.05 Å. The 5-coordinate system fit to the same histidine

distance but a shorter oxygen distance at 2.10 Å. The intensity of the backscattering feature is better fit by the 6-coordinate system, though statistically there is no difference between the two models (

Table 3-3). A fit to 3 histidine and 2 oxygen ligands was also attempted but was statistically unreasonable with negative debye-waller factors and was excluded from this discussion.

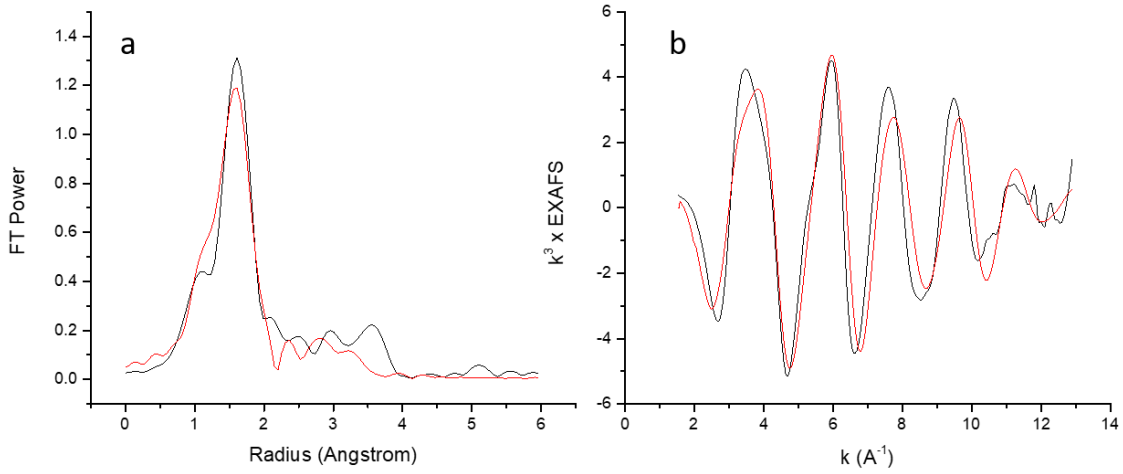

Figure 3-17 FT (a) and EXAFS (b) of Co(II) bound $Glu_3{}^dHis_3{}^a$ with 2 mM 3SCC and 1 mM $CoSO_4$ in 50 mM HEPES pH 7.5 with data in black and fit to 3 O and 3 His in red

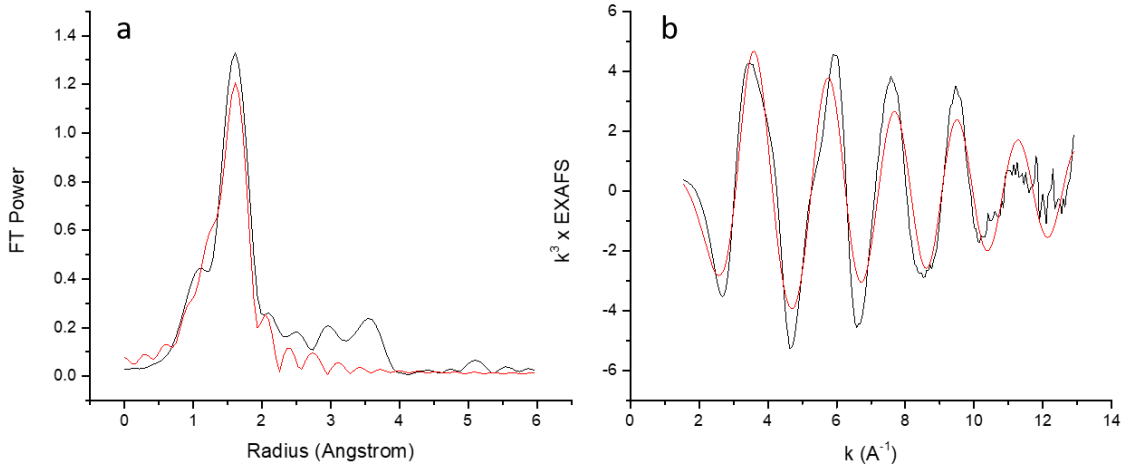

Figure 3-18 FT (a) and EXAFS (b) of Co(II) bound $Glu_3{}^dHis_3{}^a$ with 2 mM 3SCC and 1 mM $CoSO_4$ in 50 mM HEPES pH 7.5 with data in black and fit to 3 O and 2 His in red

$Glu_2^dHis_3^a$ also fit equally well to the same models as for the homotrimer. The 6-coordinate system fit with three oxygen at 2.09 Å and three histidines at 1.95 Å, giving an average bond distance of 2.02 Å (Figure 3-19). The five-coordinate model fit to 3 oxygens at 2.08 Å and 2 histidines at 1.94 Å for an average bond distance of 2.02 Å (Figure 3-20). Again, a fit to 3 histidines and 2 oxygens resulted in a statistically unreasonable model and was not included.

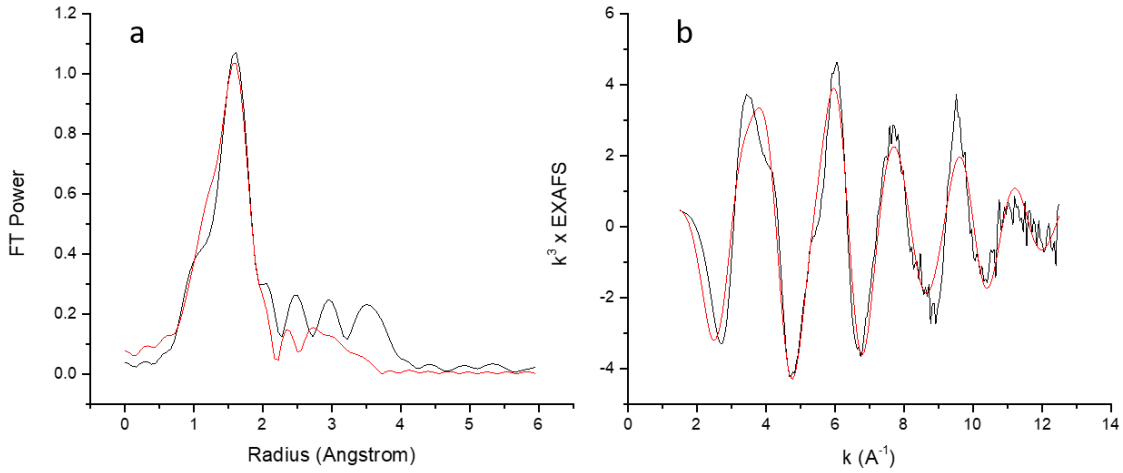

Figure 3-19 FT (a) and EXAFS (b) of Co(II) bound $Glu_2^dHis_3^a$ with 2 mM 3SCC and 1 mM $CoSO_4$ in 50 mM HEPES pH 7.5 with data in black and fit to 3 O and 3 His in red

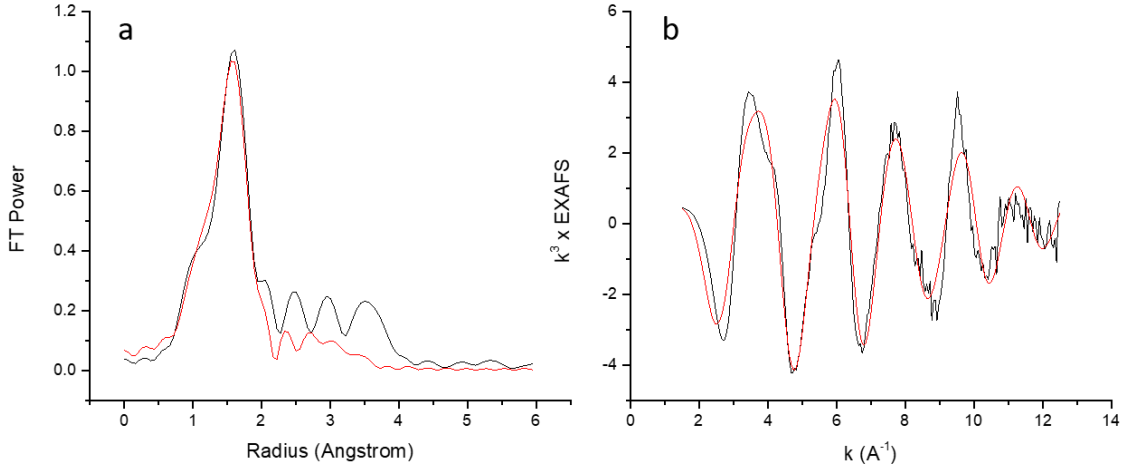

Figure 3-20 FT (a) and EXAFS (b) of Co(II) bound $Glu_2^dHis_3^a$ with 2 mM 3SCC and 1 mM $CoSO_4$ in 50 mM HEPES pH 7.5 with data in black and fit to 3 O and 2 His in red

The alternate heterotrimer, $Glu_1{}^dHis_3{}^a$, fit equally well to similar models as the other Glu peptides. A 6-coordinate model fit 3 His at 2.09 Å and 3 oxygen at 2.02 Å for an average bond distance of 2.06 Å (Figure 3-21). In this model, the His residues fit best at a longer distance whereas the previous constructs fit best the oxygen ligands at a longer distance. A 5-coordinate model was also fit but unlike the 2 and 3 Glu constructs, this fit best to 3 His at 2.08 Å and 2 O at 2.02 Å, for an average bond distance of 2.06 Å (Figure 3-22). The alternate 5-coordinate model of 3 O and 2 His resulted in a statistically unreasonable fit and was not included. While statistically there is not a best model for this data, the first shell is best fit by the 6-coordinate model while the histidine backscattering is best fit by the 5-coordinate model.

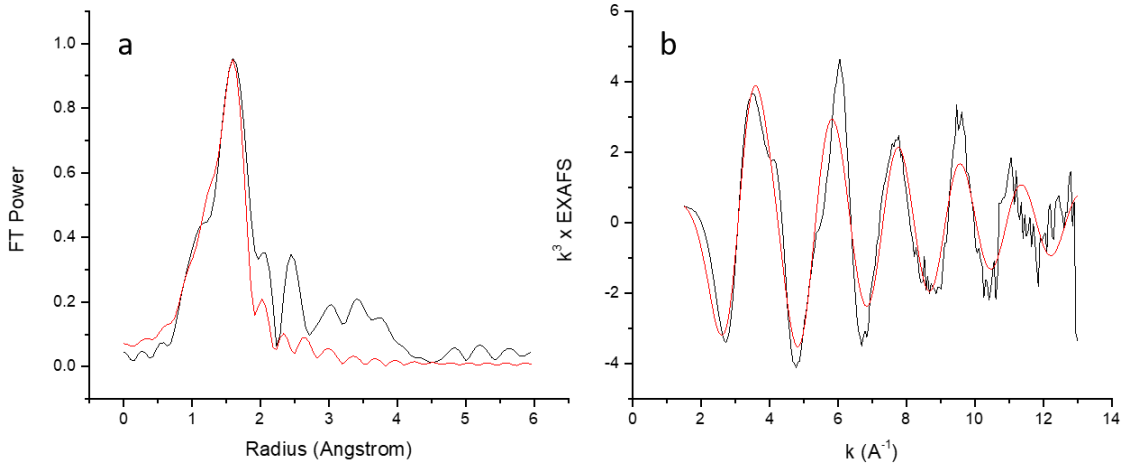

Figure 3-21 FT (a) and EXAFS (b) of Co(II) bound $Glu_1{}^dHis_3{}^a$ with 2 mM 3SCC and 1 mM $CoSO_4$ in 50 mM HEPES pH 7.5 with data in black and fit to 3 O and 3 His in red

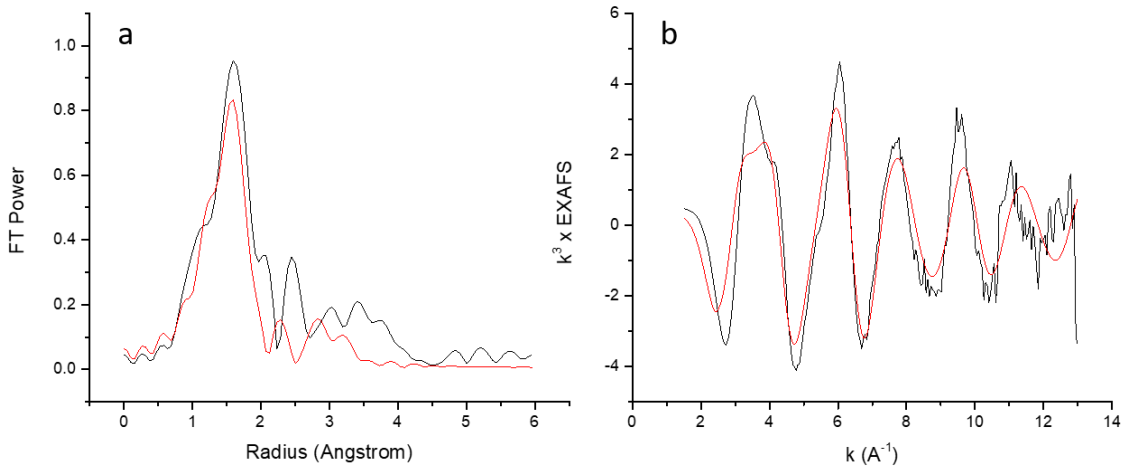

Figure 3-22 FT (a) and EXAFS (b) of Co(II) bound $Glu_1{}^dHis_3{}^a$ with 2 mM 3SCC and 1 mM $CoSO_4$ in 50 mM HEPES pH 7.5 with data in black and fit to 2 O and 3 His in red

Table 3-3 Co(II) EXAFS fitting parameters

Peptide	Number of O ligands	Oxygen R (Å)	σ^2	Number of His ligands	Histidine R (Å)	σ^2	Goodness of Fit	Average bond distance (Å)
$Glu_3{}^dHis_3{}^a$	3	2.11	0.0086	3	1.98	0.00535	116	2.045
	3	2.10	0.0084	2	1.98	0.00535	116	2.052
$Glu_2{}^dHis_3{}^a$	3	2.09	0.00242	3	1.95	0.00944	107	2.02
	3	2.08	0.00241	2	1.94	0.00775	110	2.024
$Glu_1{}^dHis_3{}^a$	3	2.02	0.008	3	2.09	0.01074	261	2.055
	2	2.02	0.00598	3	2.08	0.00855	296	2.056

Co(II) XANES

The pre-edge feature of the Co(II) bound $Glu_x{}^dHis_3{}^a$ peptides was analyzed via X-ray absorption near edge spectroscopy (XANES). A pre-edge feature for the forbidden 1s to 3d transition is observed for Co(II) and the intensity of this feature is a direct reflection of the symmetry of the site. This transition is symmetry forbidden so as symmetry restrictions are relaxed the intensity of the pre-edge feature is increased. Thus, one would expect that a lower coordinate system would have a more intense pre-edge feature. The least intense pre-edge was observed for the homotrimer, which correlates well with the lower extinction coefficient observed by UV-visible spectroscopy (Figure 3-23). The heterotrimers had more intense pre-

edge features, indicating a decrease in symmetry in these systems. Again, this is consistent with the higher extinction coefficients observed by UV-visible spectroscopy.

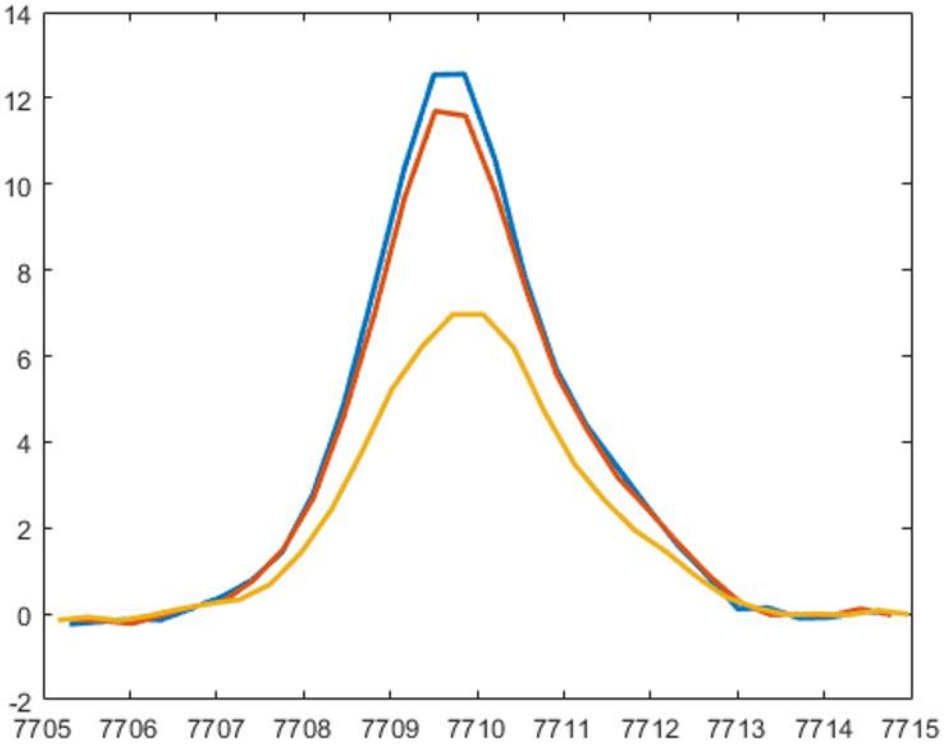

Figure 3-23 1s→3d pre-edge regions with $Glu_1^dHis_3^a$ in blue, $Glu_2^dHis_3^a$ in red, and $Glu_3^dHis_3^a$ in yellow with 2 mM 3SCC and 1 mM $CoSO_4$ in 50 mM HEPES pH 7.5.

Co(II) EPR

Co(II) binding was also investigated by EPR. The complexity of Co(II) EPR prohibits us from fitting these spectra with confidence, but comparisons can be made between the $Asp_x^dHis_3^a$ and $Glu_x^dHis_3^a$ peptides. With one or two carboxylate residues, the Co(II) EPR spectra are very different (Figure 3-24 and Figure 3-25, respectively). Three carboxylate residues, however, are much more similar and also overlay well with His_3^a (Figure 3-26). The feature at 2000 G is different for $Glu_3^dHis_3^a$ as compared to $Asp_3^dHis_3^a$ and His_3^a. This is more similar to what is seen for the heterotrimeric glutamate peptides, where a broad negative feature is seen at 2000 G. These results suggest that cobalt coordination is different in glutamate heterotrimers as compared to aspartate heterotrimers and that the glutamate homotrimer has a unique cobalt ligand environment compared to the other homotrimers.

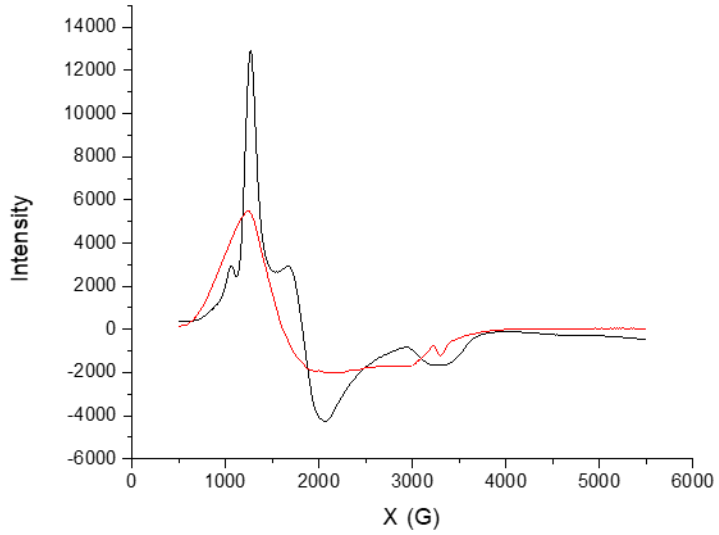

Figure 3-24 Co(II) EPR of $Glu_1^dHis_3^a$ (red) and $Asp_1^dHis_3^a$ (black) from Dr. Mocny[1] with 2 mM 3SCC and 1 mM $CoSO_4$ in 50 mM HEPES pH 7.5 with 30% glycerol as a glassing agent

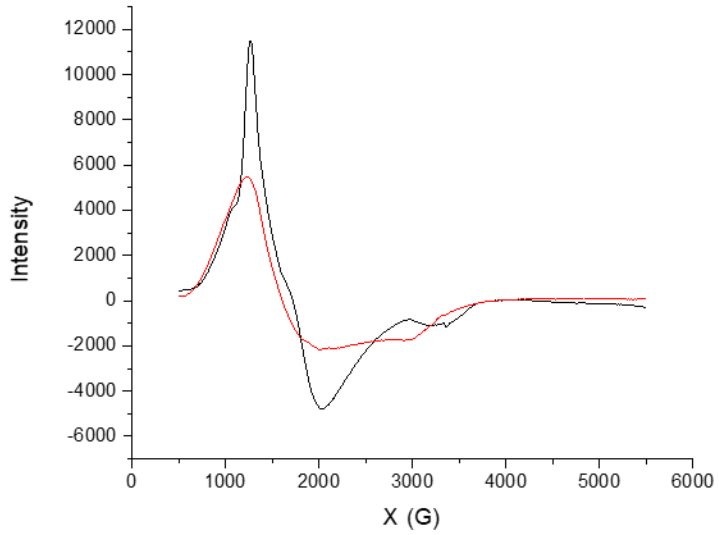

Figure 3-25 Co(II) EPR of $Glu_2^dHis_3^a$ (red) and $Asp_2^dHis_3^a$ (black) from Dr. Mocny[1] with 2 mM 3SCC and 1 mM $CoSO_4$ in 50 mM HEPES pH 7.5 with 30% glycerol as a glassing agent

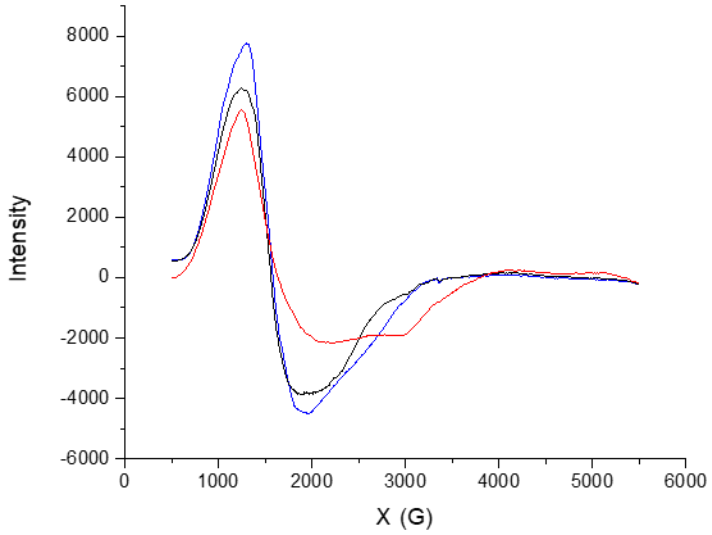

Figure 3-26 Co(II) EPR of $Glu_3^dHis_3^a$ (red), $Asp_3^dHis_3^a$ (black), His_3^a (blue). Aspartate and His_3^a data from Dr. Mocny[1] with 2 mM 3SCC and 1 mM $CoSO_4$ in 50 mM HEPES pH 7.5 with 30% glycerol as a glassing agent

Zn(II) EXAFS

Zn(II) bound to $Glu_x^dHis_3^a$ systems was investigated by XAS. This allows for direct examination of the zinc coordination environment without the use of a spectroscopic probe such as cobalt. As such, Zn(II) bound peptides were investigated at pH 7.5, where other spectroscopic characterization has been done, and 9.5, where CA kinetic parameters were determined (see Chapter 4). At pH 7.5, the homotrimer $Glu_3^dHis_3^a$ fit equally well to 2 histidine and 2 oxygen ligands (Figure 3-27) or 3 histidine and one oxygen ligand (Figure 3-28). The first case fits the intensity of the first shell scattering well with a His distance of 1.94 Å and an oxygen distance of 2.01 Å. With three histidine residues, the fit is better at approximating the backscattering intensity but does not model the first shell intensity as well. In this case, three histidine residues fit to a distance of 1.94 Å and one oxygen fit to 2.04 Å.

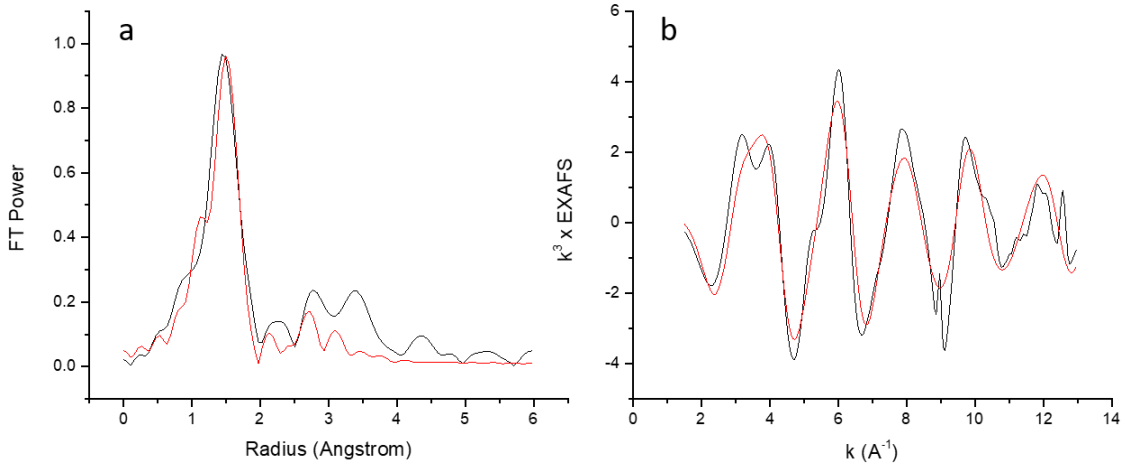

Figure 3-27 FT (a) and EXAFS (b) of Zn(II) bound $Glu_3^dHis_3^a$ with 2 mM 3SCC and 1 mM ZnOAc in 50 mM HEPES pH 7.5 with data in black and fit to 2 His and 2 O ligands in red

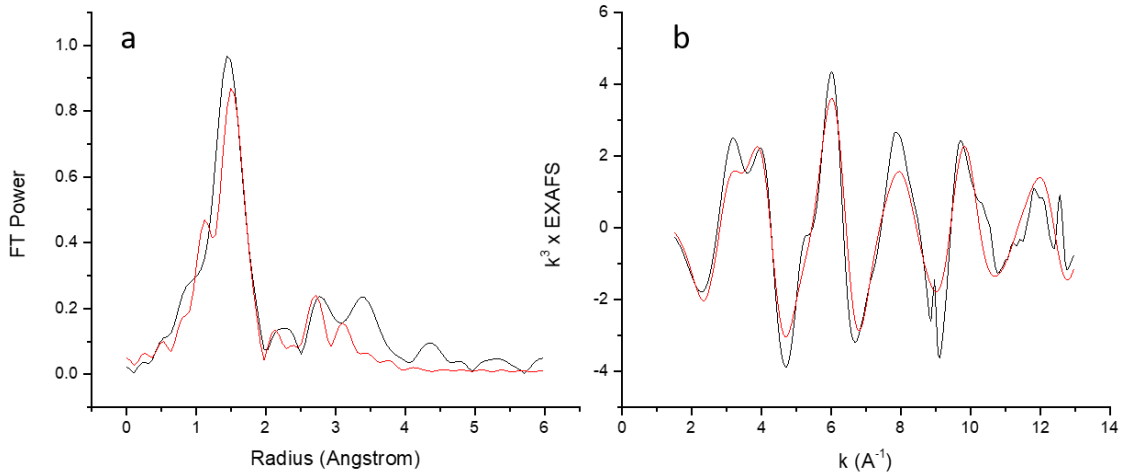

Figure 3-28 FT (a) and EXAFS (b) of Zn(II) bound $Glu_3^dHis_3^a$ with 2 mM 3SCC and 1 mM ZnOAc in 50 mM HEPES pH 7.5 with data in black and fit to 3 His and 1 O ligands in red

At pH 9.5, very similar fits were observed. Again, a fit to 2 oxygen ligands at 2.02 Å and 2 His ligands at 1.95 Å approximated the intensity of the first shell very well (Figure 3-29). A fit with 3 histidine ligands at 1.95 Å and 1 oxygen at 2.04 Å provided a better approximation for the backscattering intensity (Figure 3-30). The peak at 3 Å^{-1} is also better approximated by the 2 His, 2 O model. Statistically, neither fit is better than the other.

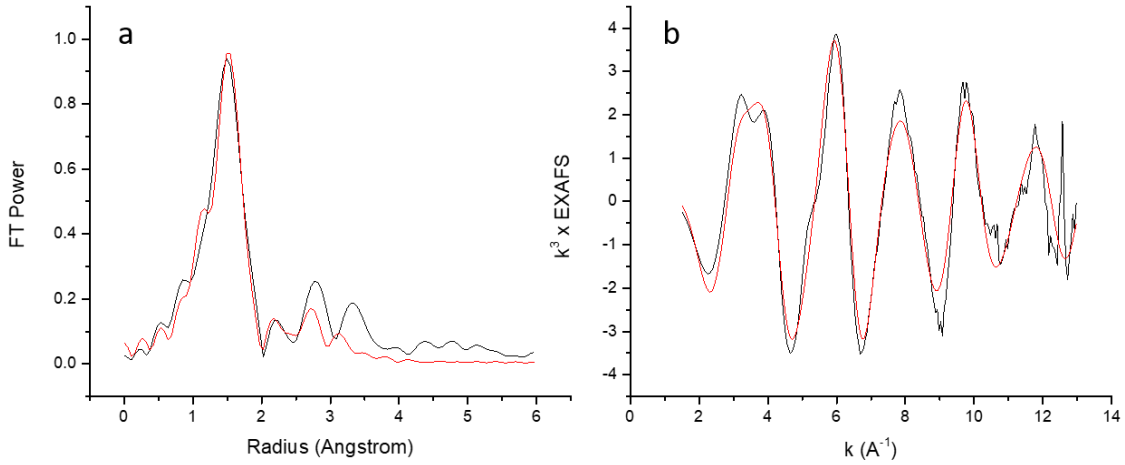

Figure 3-29 FT (a) and EXAFS (b) of Zn(II) bound $Glu_3^dHis_3^a$ with 2 mM 3SCC and 1 mM ZnOAc in 50 mM CHES pH 9.5 with data in black and fit to 2 His and 2 O ligands in red

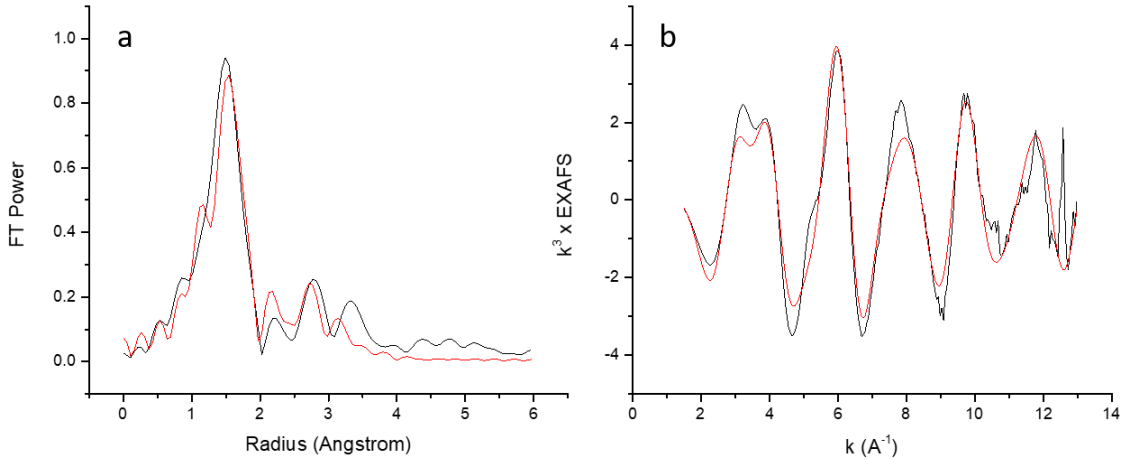

Figure 3-30 FT (a) and EXAFS (b) of Zn(II) bound $Glu_3^dHis_3^a$ with 2 mM 3SCC and 1 mM ZnOAc in 50 mM CHES pH 9.5 with data in black and fit to 3 His and 1 O ligands in red

Both the two oxygen, two histidine and one oxygen, three histidine models fit equally well to this data at both pH 7.5 and pH 9.5. Consistently, the model with more oxygen ligands fit the intensity of the first shell better while the model with more histidine ligands fit the backscattering better. A comparison of the XAS spectra at both pH values shows that there are no significant differences in the EXAFS or FT as a function of pH (Figure 3-31). Thus, while the exact Zn(II) environment cannot be determined based solely on this data, it is consistent across the range of pH values examined herein.

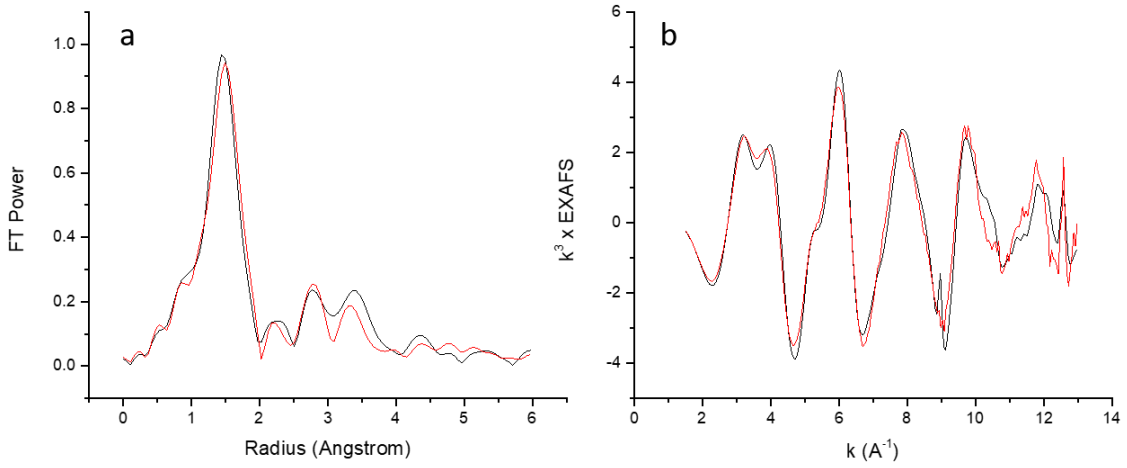

Figure 3-31 FT (a) and EXAFS (b) of Zn(II) bound $Glu_3{}^dHis_3{}^a$ at pH 7.5 (black) and 9.5 (red)

At pH 7.5, $Glu_2{}^dHis_3{}^a$ fit best to a four-coordinate model with 2 His ligands and 2 oxygen ligands (*Figure 3-32*). The His ligands have a bond distance of 1.93 Å and the oxygen ligands have a bond distance of 2.01 Å. A statistically unreasonable fit was derived for a ligand environment with 3 His and 1 oxygen ligands and is not discussed here.

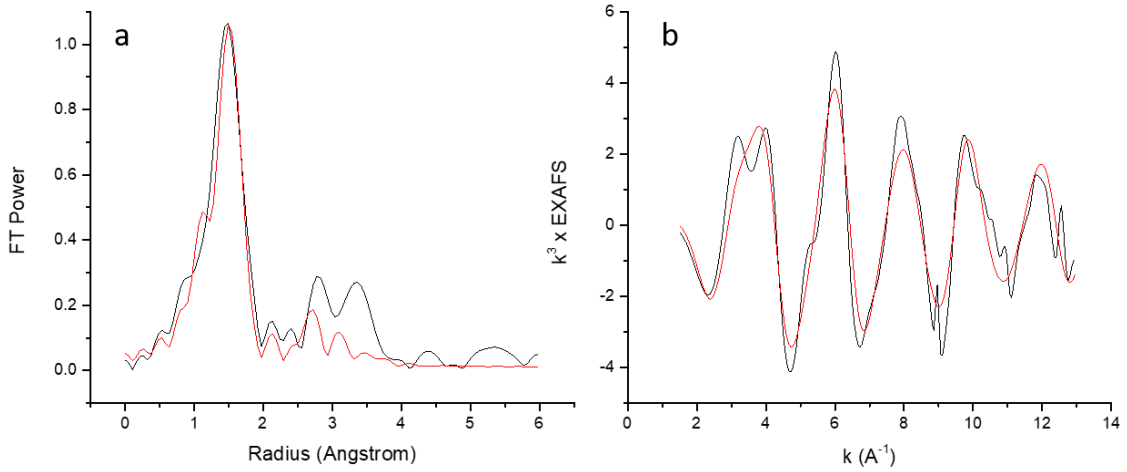

Figure 3-32 FT (a) and EXAFS (b) of Zn(II) bound $Glu_2{}^dHis_3{}^a$ with 2 mM 3SCC and 1 mM ZnOAc in 50 mM HEPES pH 7.5 with data in black and fit to 2 His and 2 O ligands in red

At pH 9.5 both a 2 His, 2 O model and a 3 His, 1 O model fit the data equally well. The first model fit two oxygen ligands at 2.00 Å and 2 His at 1.96 Å (Figure 3-33). The second model fit three His ligands at 1.95 Å and 1 oxygen at 2.02 Å (Figure 3-34). As with the $Glu_3{}^dHis_3{}^a$

homotrimer, more oxygen ligands better approximated the intensity of the first shell but more histidine ligands better fit the backscattering intensity.

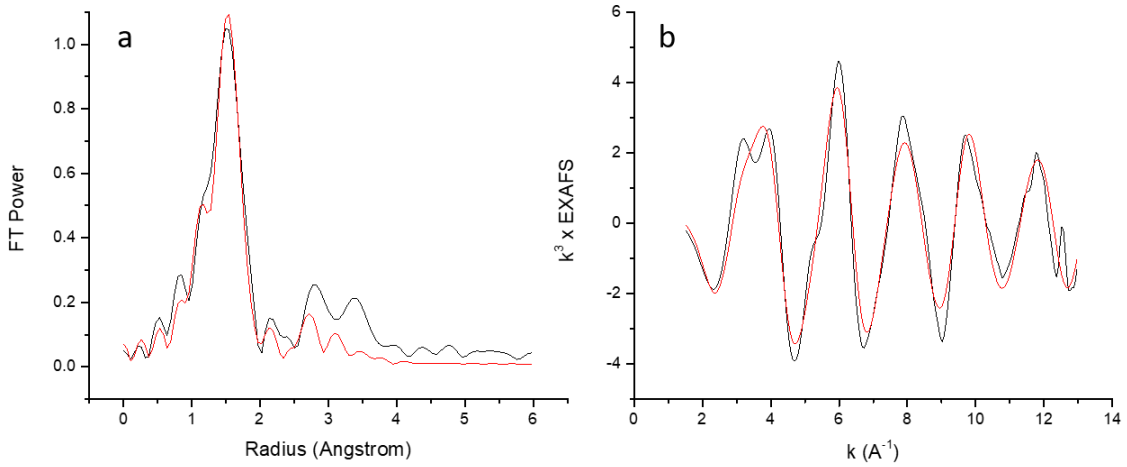

Figure 3-33 FT (a) and EXAFS (b) of Zn(II) bound $Glu_2^dHis_3^a$ with 2 mM 3SCC and 1 mM ZnOAc in 50 mM CHES pH 9.5 with data in black and fit to 2 His and 2 O ligands in red

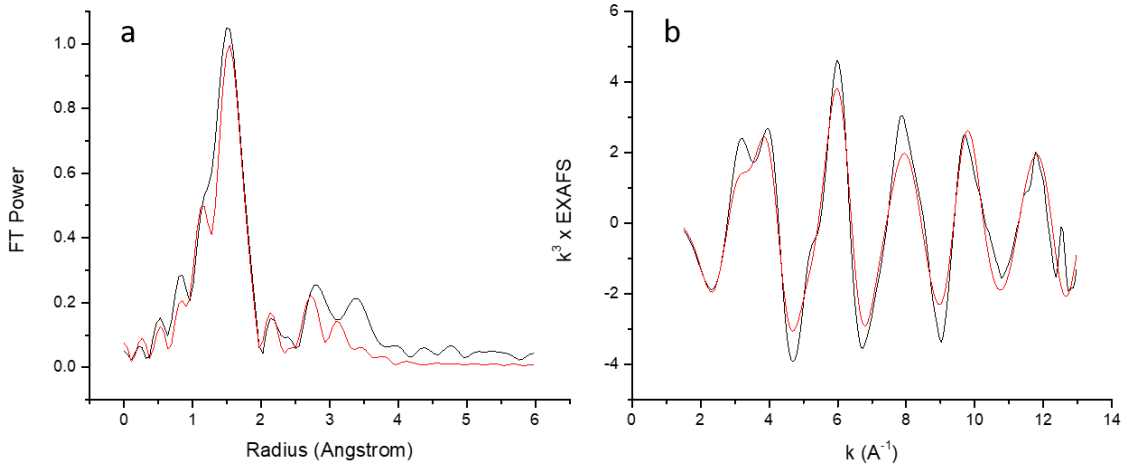

Figure 3-34 FT (a) and EXAFS (b) of Zn(II) bound $Glu_2^dHis_3^a$ with 2 mM 3SCC and 1 mM ZnOAc in 50 mM CHES pH 9.5 with data in black and fit to 3 His and 1 O ligands in red

A comparison of the spectra at both pH 7.5 and pH 9.5 showed that the coordination environment does not change significantly as a function of pH (Figure 3-35). This suggests that the 2 His, 2 O coordination may be the more likely Zn(II) ligand environment at pH 9.5 as this is the best fit model at pH 7.5.

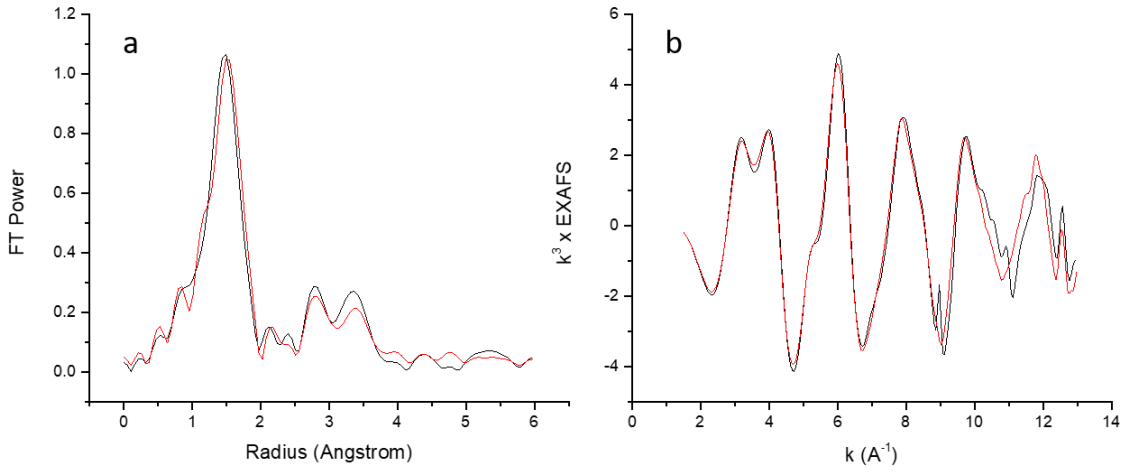

Figure 3-35 FT (a) and EXAFS (b) of Zn(II) bound $Glu_2{}^dHis_3{}^a$ at pH 7.5 (black) and 9.5 (red)

The other heterotrimer, $Glu_1{}^dHis_3{}^a$, also best fit to a 2 His, 2 O model at pH 7.5. This model fit to two oxygen ligands at 2.01 Å and two histidine ligands at 1.93 Å (Figure 3-36). A statistically unreasonable model was derived for the 3 His, 1 O model.

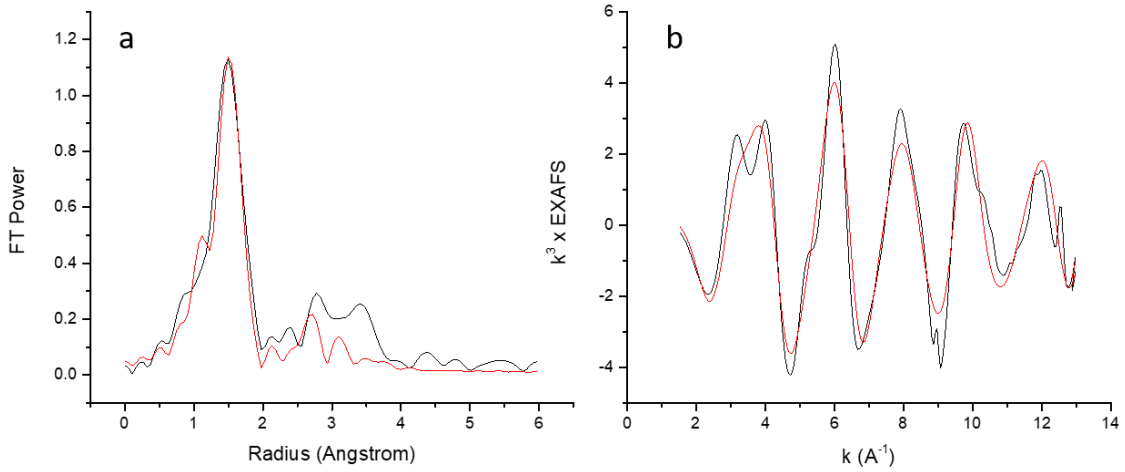

Figure 3-36 FT (a) and EXAFS (b) of Zn(II) bound $Glu_1{}^dHis_3{}^a$ with 2 mM 3SCC and 1 mM ZnOAc in 50 mM HEPES pH 7.5 with data in black and fit to 2 His and 2 O ligands in red

At pH 9.5, an equally good fit was determined for $Glu_1{}^dHis_3{}^a$ with both 2 His, 2 O and 3 His, 1 O models. In the first case, two His residues were fit at 1.95 Å and 2 O ligands at 2.0 Å (Figure 3-37). The second model fit to a His distance of 1.94 Å and an oxygen distance of 2.03 Å (Figure 3-38). As with $Glu_3{}^dHis_3{}^a$ and $Glu_2{}^dHis_3{}^a$, the model with more His residues better fit the backscattering while the model with more oxygen ligands better fit the first shell.

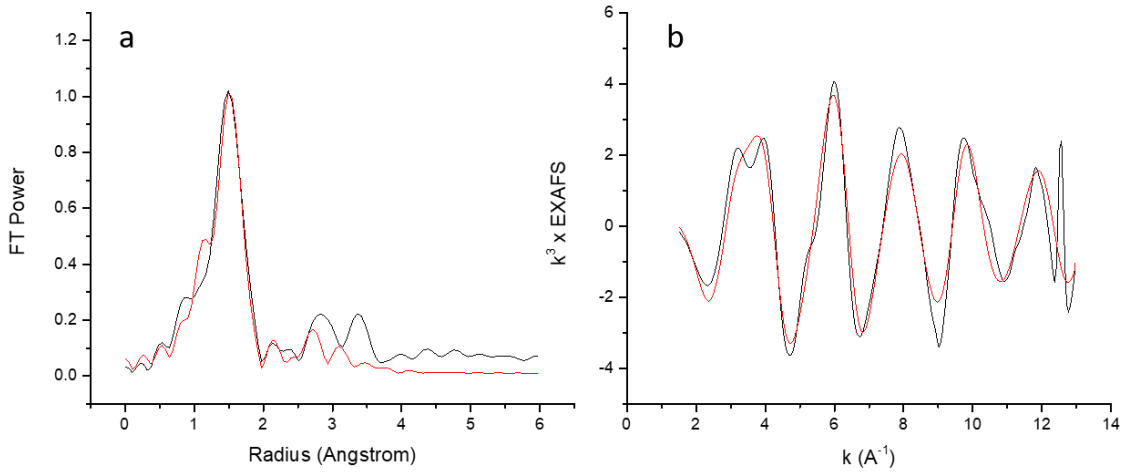

Figure 3-37 FT (a) and EXAFS (b) of Zn(II) bound $Glu_1^dHis_3^a$ with 2 mM 3SCC and 1 mM ZnOAc in 50 mM CHES pH 9.5 with data in black and fit to 2 His and 2 O ligands in red

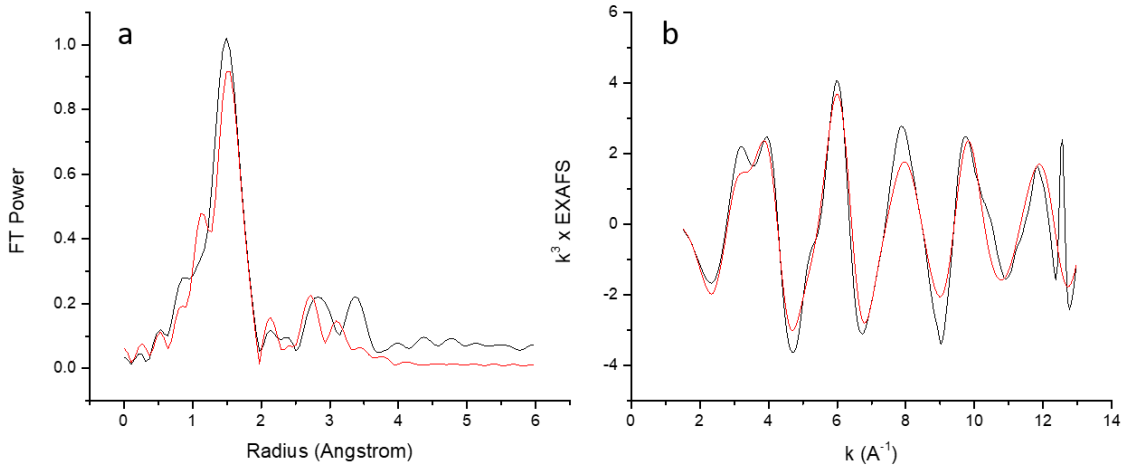

Figure 3-38 FT (a) and EXAFS (b) of Zn(II) bound $Glu_1^dHis_3^a$ with 2 mM 3SCC and 1 mM ZnOAc in 50 mM CHES pH 9.5 with data in black and fit to 3 His and 1 O ligands in red

The FT and EXAFS do not change significantly with pH, suggesting that the Zn(II) binding environment is not affect by pH (Figure 3-39).

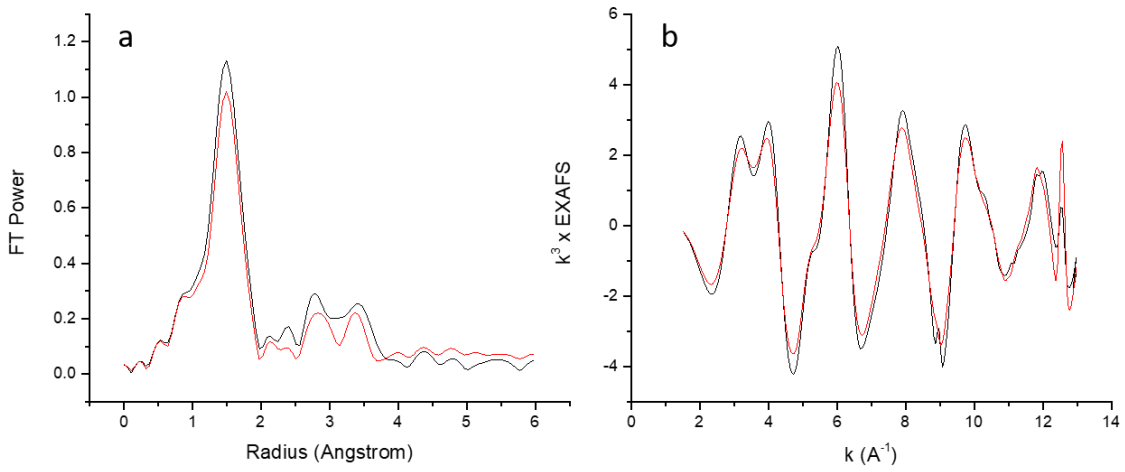

Figure 3-39 FT (a) and EXAFS (b) of Zn(II) bound $Glu_1{}^dHis_3{}^a$ at pH 7.5 (black) and 9.5 (red)

Table 3-4 XAS fitting parameters for $Glu_x{}^dHis_3{}^a$ peptides

Peptide	pH	Number of O ligands	Oxygen R (Å)	σ^2 (10^{-3})	Number of His ligands	His R (Å)	σ^2 (10^{-3})	Goodness of Fit	Average bond distance (Å)
$Glu_1{}^dHis_3{}^a$	7.5	2	2.01	2.58	2	1.93	6.71	102	1.97
	9.5	2	2.00	4.69	2	1.95	7.44	62	1.98
		1	2.03	1.21	3	1.94	8.00	63	1.96
$Glu_2{}^dHis_3{}^a$	7.5	2	2.01	3.27	2	1.93	6.84	92	1.97
	9.5	2	2.00	3.85	2	1.96	7.62	68	1.98
		1	2.02	0.46	3	1.95	8.00	66	1.97
$Glu_3{}^dHis_3{}^a$	7.5	2	2.01	4.87	2	1.94	7.21	82	1.98
		1	2.04	1.26	3	1.94	7.53	79	1.97
	9.5	2	2.02	3.91	2	1.95	7.64	53	1.99
		1	2.04	0.5	3	1.95	8.54	52	1.97

Cu(II) UV-visible spectroscopy

Cu(II) binding to the transition metal site was characterized by UV-visible spectroscopy. With one equivalent of Cu(II) per trimer, no difference in extinction coefficient or maximum absorbance wavelength was observed for $His_3{}^d$, $His_2{}^dHis_1{}^a$, and $His_1{}^dHis_2{}^a$ (Figure 3-40). $His_3{}^a$ however, has a higher energy Cu(II) d-d transition with a higher extinction coefficient (Table 3-5).

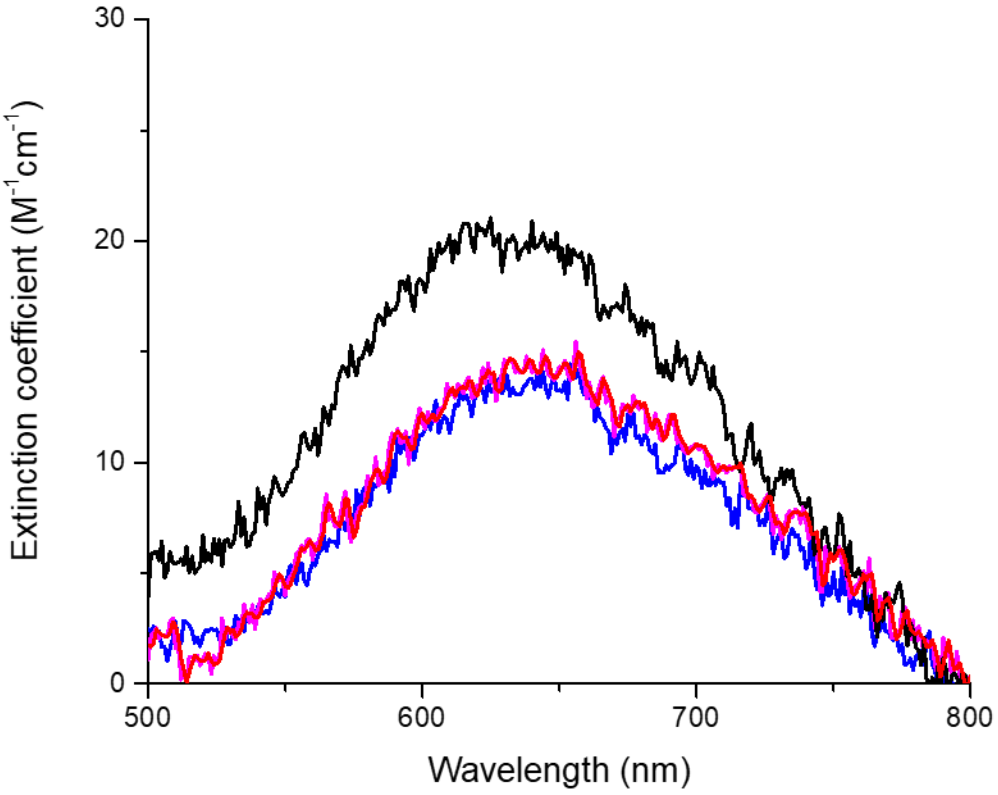

Figure 3-40 Cu(II) UV-Visible spectra of His_3^a (black), His_3^d (red), $His_2^dHis_1^a$ (blue), and $His_1^dHis_2^a$ (pink) at pH 7.5. All spectra collected with 250 μM 3SCC in 50 mM HEPES pH 7.5.

The His_4 models both had higher extinction coefficients than the His_3 homotrimers, but with a λ_{max} equivalent to His_3^a.

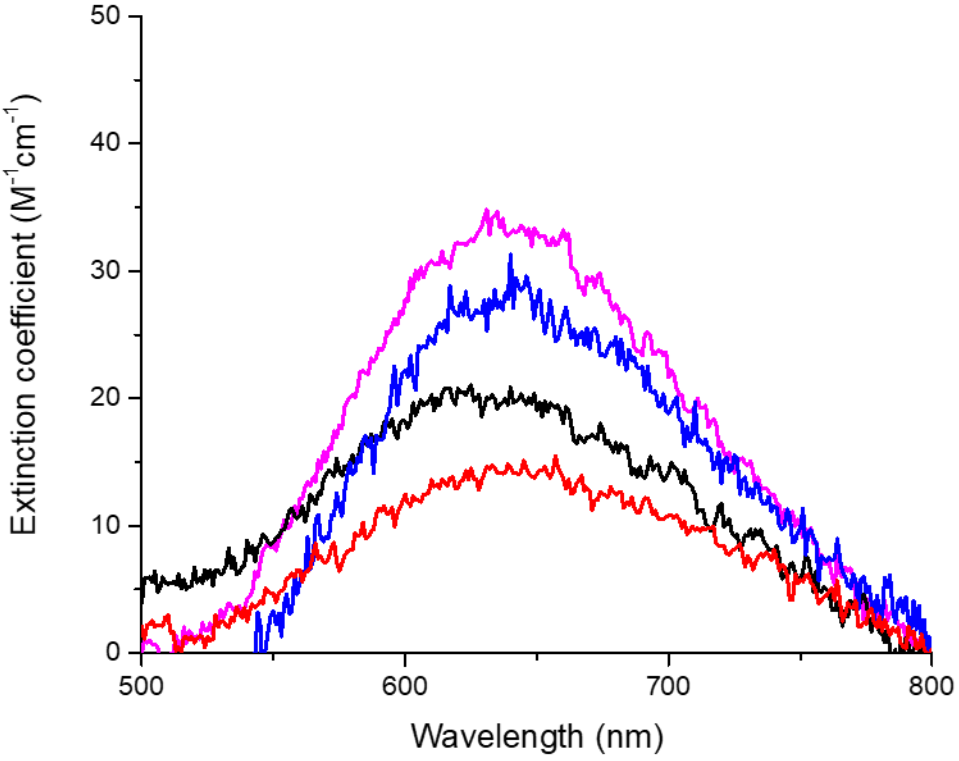

Figure 3-41 Cu(II) UV-Visible spectra of His_3^a (black), His_3^d (red), $His_1^dHis_3^a$ (blue), and $His_3^dHis_1^a$ (pink) at pH 7.5. All spectra collected with 250 μM 3SCC in 50 mM HEPES pH 7.5.

The Asp containing peptides all had maximum absorbance between 639 and 652 nm (Figure 3-42). $Asp_1^dHis_3^a$ and $Asp_2^dHis_3^a$ had the highest extinction coefficients, though the noise in these spectra may make this difference negligible.

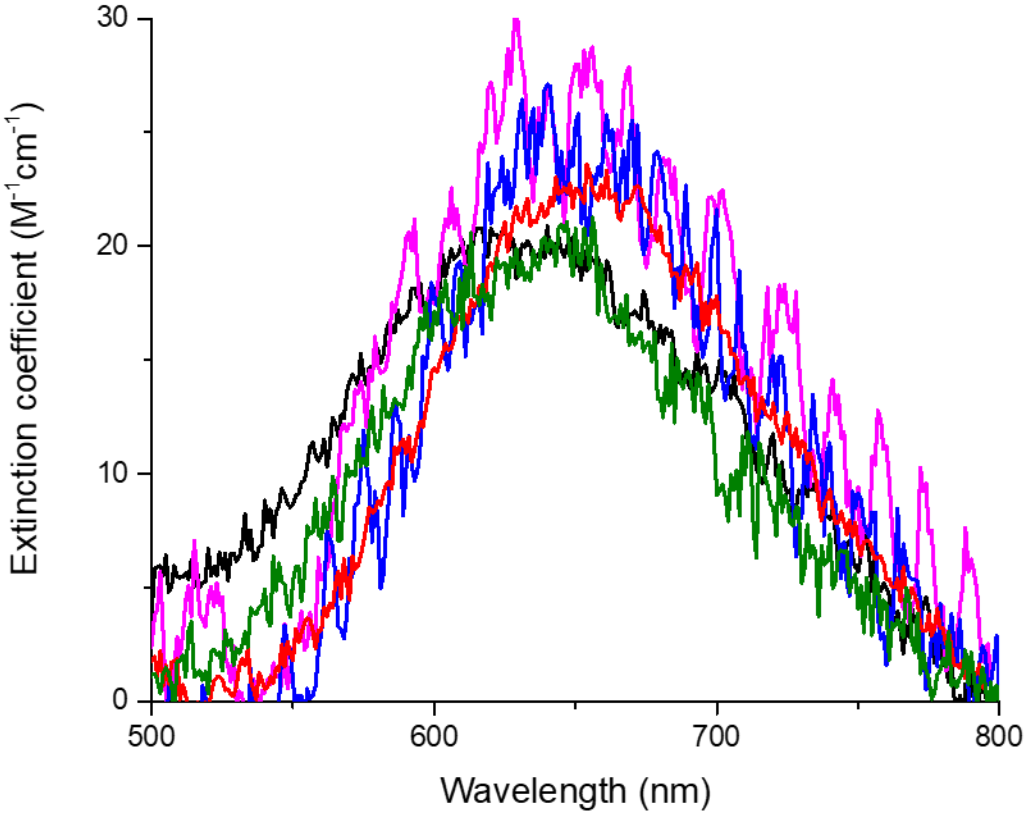

Figure 3-42 Cu(II) UV-Visible spectra of His_3^a (black), $Asp_3^dHis_3^a$ (red), $Asp_2^dHis_3^a$ (blue), $Asp_1^dHis_3^a$ (pink), and $His_2^dAsp_1^dHis_1^a$ (green) at pH 7.5. All spectra collected with 250 μM 3SCC in 50 mM HEPES pH 7.5.

The Glu containing peptides all have a similar energy for the maximum absorbance ~645 nm (Figure 3-43). The extinction coefficient for this d-d transition increased as the number of glutamate residues increased.

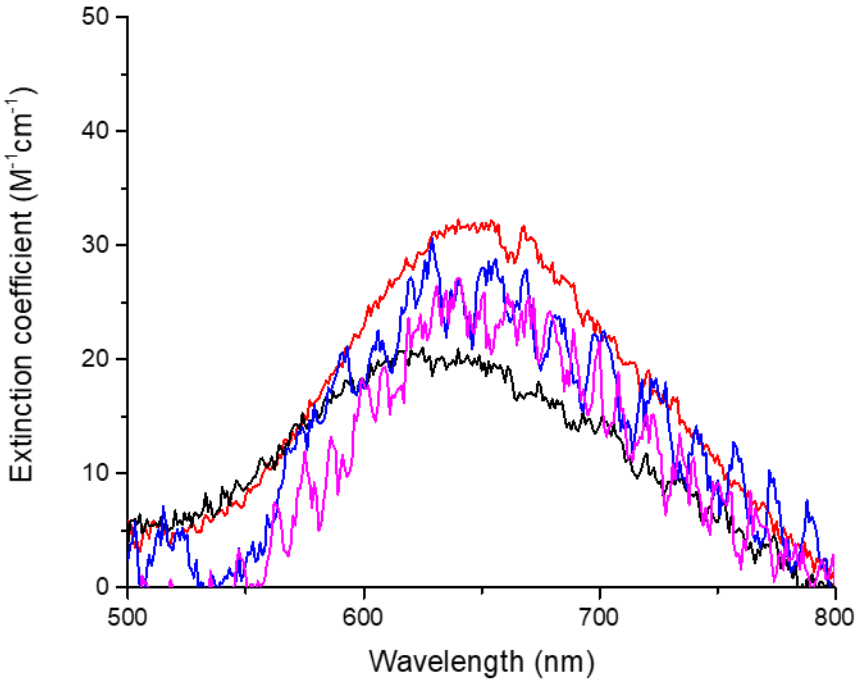

Figure 3-43 Cu(II) UV-Visible spectra of His_3^a (black), $Glu_3^dHis_3^a$ (red), $Glu_1^dHis_3^a$ (blue), and $Glu_2^dHis_3^a$ (pink) at pH 7.5. All spectra collected with 250 μM 3SCC in 50 mM HEPES pH 7.5.

Table 3-5 Cu(II) absorbance properties for relevant peptides at pH 7.5

Peptide	Extinction coefficient at λ_{max} ($M^{-1}cm^{-1}$)	λ_{max} (nm)	Wavenumbers (cm^{-1})
His_3^a	21	623	16100
$His_1^dHis_2^a$	14	640	15600
$His_2^dHis_1^a$	14	640	15600
His_3^d	14	640	15600
$His_3^dHis_1^a$	32	622	16100
$His_1^dHis_3^a$	28	622	16100
$Asp_1^dHis_3^a$	26	639	15700
$Asp_2^dHis_3^a$	24	642	15600
$Asp_3^dHis_3^a$	24	652	15300
$His_2^dAsp_1^dHis_1^a$	21	644	15500
$Glu_1^dHis_3^a$	26	645	15500
$Glu_2^dHis_3^a$	25	644	15500
$Glu_3^dHis_3^a$	32	649	15400

Cu(II) EPR

The Cu(II) EPR of all homo- and heterotrimeric systems was measured to determine the Cu(II) binding geometry. The fits for His_3^a agree with those reported for TRI His_3^a at pH 7.80, with $g_\perp$ of ~2.04 and $g_\parallel$ of 2.27 (Figure 3-44,

Table 3-6).[19] These values are similar for His_3^d, though the **d**-layer His system has a larger hyperfine coupling constant. The heterotrimers, however, fit best to a mixture of species. $His_2^dHis_1^a$ had identical $g_\perp$ values in the two models, with 90% of this mixture matching well with His_3^d. The remaining 10% has a much lower $g_\parallel$ and higher $A_\parallel$. The alternate heterotrimer, $His_2^dHis_1^a$, has 55% that matches His_3^d parameters well and 45% that matches His_3^a parameters well.

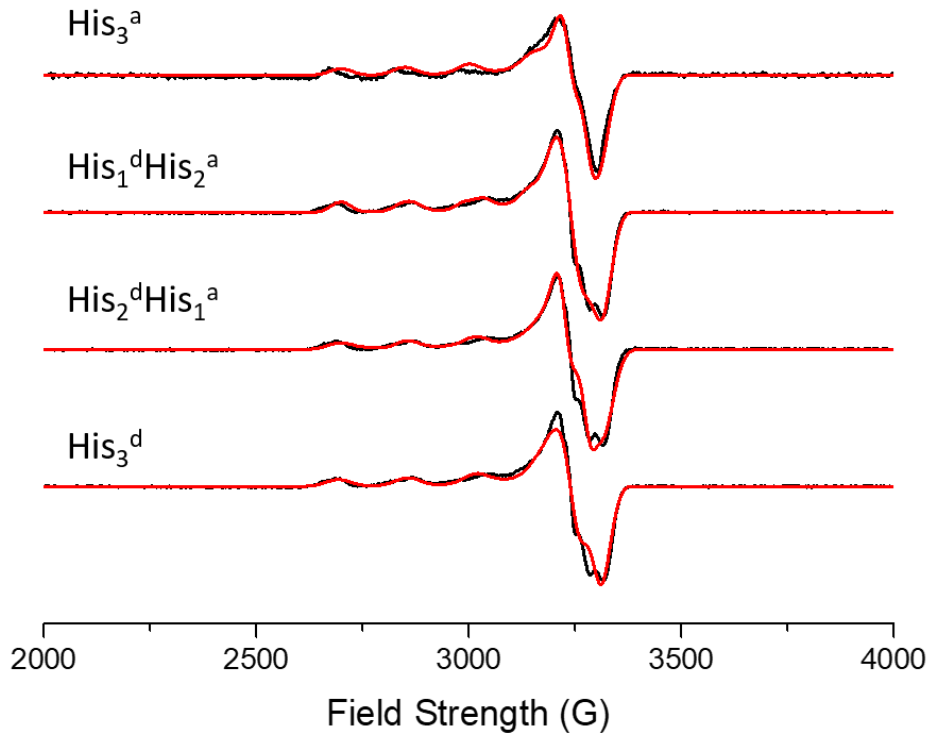

Figure 3-44 Cu(II) EPR of His_3 systems at pH 7.5 with data in black and fits in red. All spectra collected with 300 mM 3SCC and 150 mM CuCl2 in 50 mM HEPES pH 7.5 and 30% glycerol as a glassing agent.

Table 3-6 Cu(II) EPR fitting parameters for His_3 systems at pH 7.5

Peptide	%	g_x	g_y	g_z	$A_{\|\|}$ (10^{-4} cm^{-1})	$f = A_{\|\|}/g_z$
His_3^a	100	2.0297	2.0576	2.2731	159	142
$His_1^dHis_2^a$	10	2.0609	2.0304	2.1969	178	123
	90	2.0652	2.0332	2.2665	167	135
$His_2^dHis_1^a$	55	2.0444	2.043	2.2507	171	131
	45	2.0531	2.0524	2.2792	161	142
His_3^d	100	2.0442	2.059	2.2661	172	142

$His_3^dHis_1^a$ fit to a single Cu(II) species with parameters identical to His_3^d (Figure 3-45,

Table 3-7). $His_1{}^dHis_3{}^a$, however, fit to a mix of Cu(II) species. The major species (65%) was similar to $His_3{}^d$ while the minor species had a smaller $g_{\|}$ and a larger $A_{\|}$.

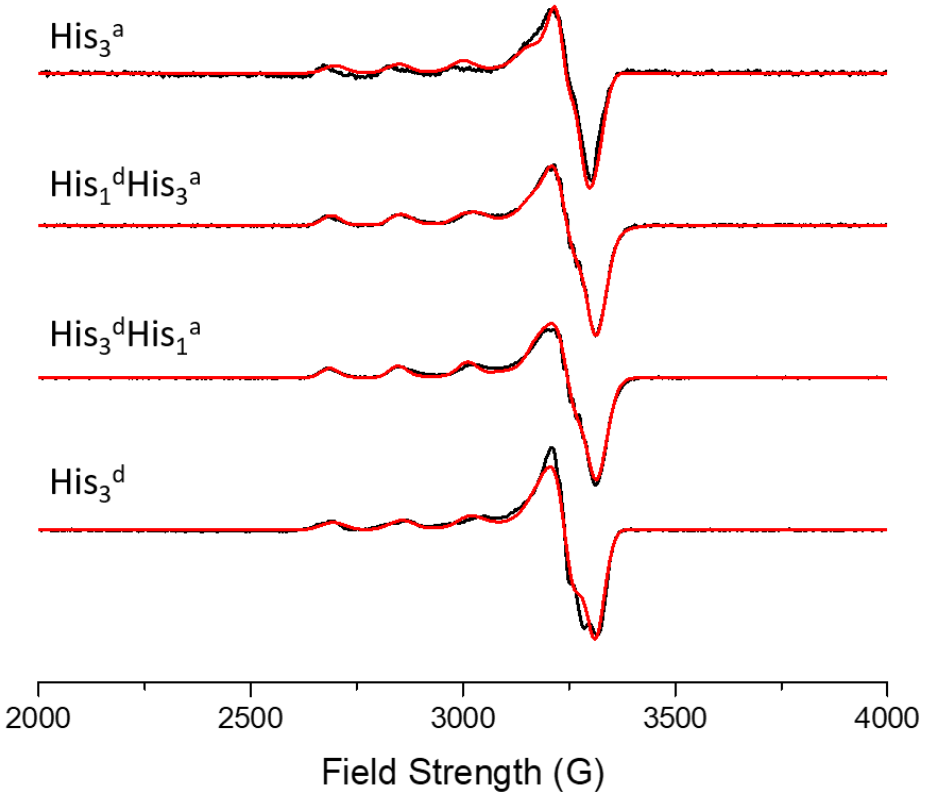

Figure 3-45 Cu(II) EPR of His_3 homotrimers and His_4 heterotrimers at pH 7.5 with data in black and fits in red. All spectra collected with 300 mM 3SCC and 150 mM CuCl2 in 50 mM HEPES pH 7.5 and 30% glycerol as a glassing agent.

Table 3-7 Cu(II) EPR fitting parameters for His_3 homotrimer and His_4 heterotrimer systems at pH 7.5

Peptide	%	g_x	g_y	g_z	$A_{\|\|}$ (10^{-4} cm^{-1})	$f = A_{\|\|}/g_z$
His_3^a	100	2.0297	2.0576	2.2731	159	142
$His_1^dHis_3^a$	65	2.0492	2.0287	2.2705	168	135
	35	2.0589	2.0293	2.2465	182	123
$His_3^dHis_1^a$	100	2.0489	2.0293	2.2648	171	132
His_3^d	100	2.0442	2.059	2.2661	172	142

The $Asp_1^dHis_3^a$ heterotrimer was a mix of species. The predominant species (70%) was similar to His_3^a, though with a smaller hyperfine coupling constant (Figure 3-46, Table 3-8). The other species was different from both previously described homotrimers with a more rhombic environment. The $Asp_2^dHis_3^a$ and $Asp_3^dHis_3^a$ systems were more similar to the predominant axial signal in $Asp_1^dHis_3^a$. The $His_2^dAsp_1^dHis_1^a$ heterotrimer was also axial but with two species of differing $A_{\|}$ fits. One species had a hyperfine coupling constant similar to His_3^a while the other species had the highest hyperfine coupling of all species reported herein at 182.

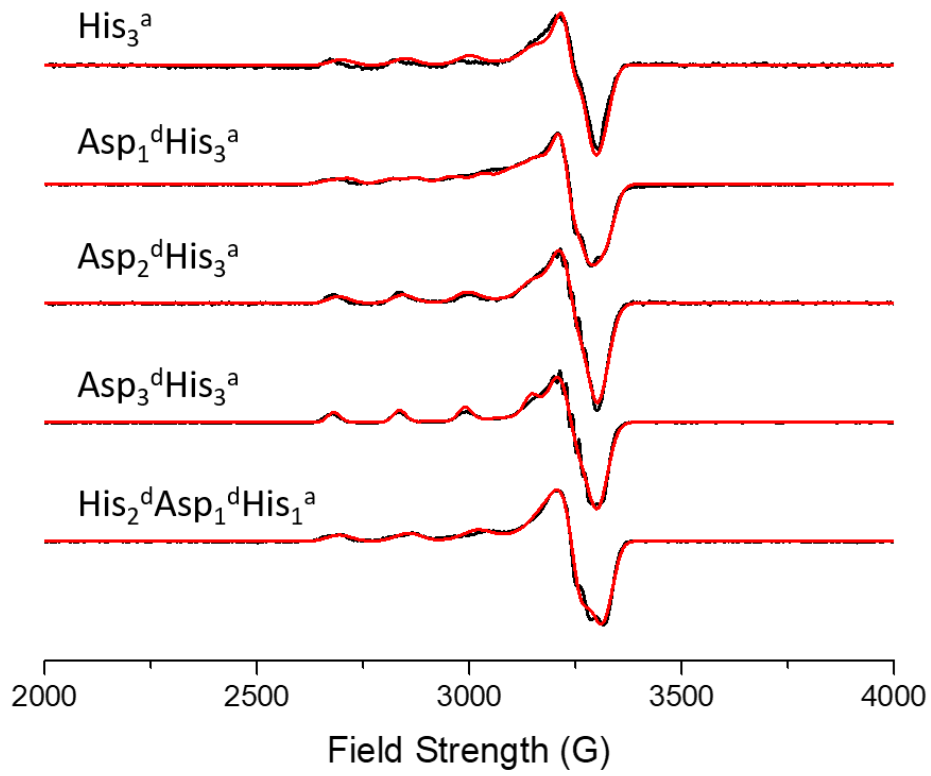

Figure 3-46 Cu(II) EPR of Asp containing 3SCCs with His_3^a for comparison at pH 7.5 with data in black and fits in red. All spectra collected with 300 mM 3SCC and 150 mM CuCl2 in 50 mM HEPES pH 7.5 and 30% glycerol as a glassing agent.

Table 3-8 Cu(II) EPR fitting parameters for Asp systems at pH 7.5

Peptide	%	g_x	g_y	g_z	$A_{\|}$ (10^{-4} cm^{-1})	$f = A_{\|}/g_z$
His_3^a	100	2.0297	2.0576	2.2731	159	142
$Asp_1^dHis_3^a$	30	2.0403	2.0977	2.2494	163	138
	70	2.0225	2.0581	2.2987	151	153
$Asp_2^dHis_3^a$	100	2.0574	2.0309	2.276	161	141
$Asp_3^dHis_3^a$	100	2.0607	2.0334	2.2805	165	138
$His_2^dAsp_1^dHis_1^a$	55	2.0411	2.0592	2.2558	162	140
	45	2.0362	2.0592	2.2558	182	123

The Cu(II) bound Glu containing systems were also investigated by EPR. The $Glu_3^dHis_3^a$ homotrimer best fit to a single species with parameters similar to His_3^d (Figure 3-47, Table 3-9). The $Glu_1^dHis_3^a$ heterotrimer was a mix of two species, one rhombic with a relatively low $A_{\|}$ as compared to the other systems. The second species was axial with a relatively high $A_{\|}$. $Glu_2^dHis_3^a$ had the same two species observed, though with a higher proportion of the rhombic species.

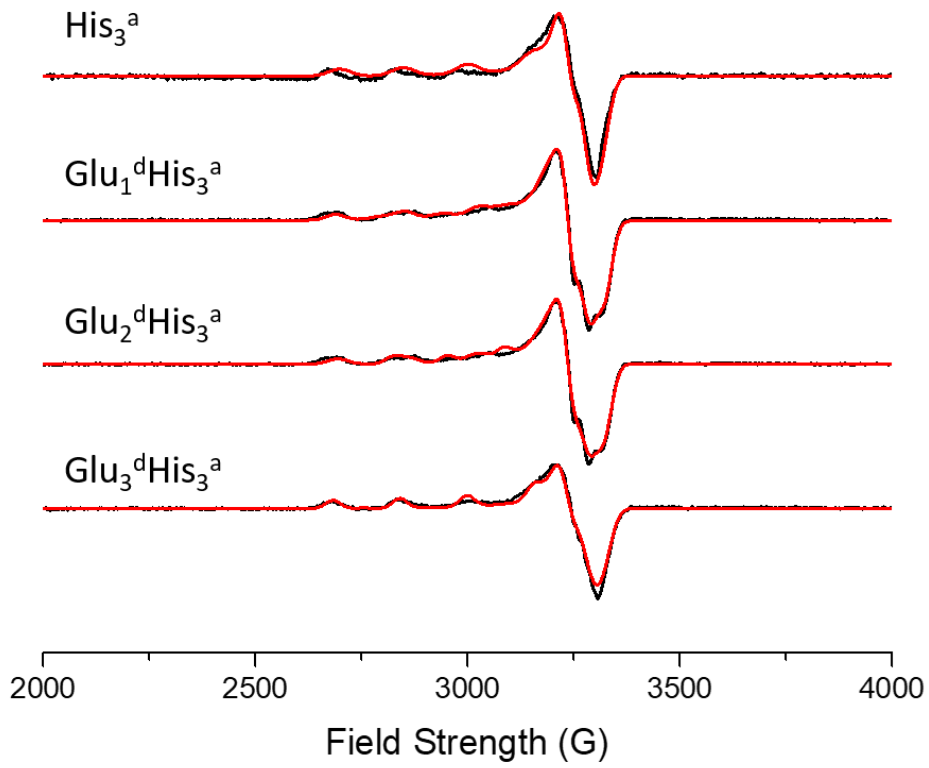

Figure 3-47 Cu(II) EPR of Glu containing 3SCCs with His_3^a for comparison at pH 7.5 with data in black and fits in red. All spectra collected with 300 mM 3SCC and 150 mM CuCl2 in 50 mM HEPES pH 7.5 and 30% glycerol as a glassing agent.

Table 3-9 Cu(II) EPR fitting parameters for Glu systems at pH 7.5

Peptide	%	g_x	g_y	g_z	$A_{\|\|}$ (10^{-4} cm^{-1})	$f = A_{\|\|}/g_z$
His_3^a	100	2.0297	2.0576	2.2731	159	142
$Glu_1^dHis_3^a$	55	2.0654	2.0349	2.2608	176	129
	45	2.0576	2.0524	2.2086	140	158
$Glu_2^dHis_3^a$	65	2.0562	2.0371	2.2589	174	130
	35	2.0724	2.0523	2.2001	136	161
$Glu_3^dHis_3^a$	100	2.0586	2.028	2.2739	168	135

Cu(I) EXAFS

The Cu(I) binding environment of these peptides was investigated by XAS. The His_3^d homotrimer was fit to several different ligand environments, 3 His (Figure 3-48), 2 His 1 O (Figure 3-49), and 1 His 3 O (Figure 3-50). The average bond distance was between 2.01 Å and 2.02 Å, which is longer than the 1.93 Å distance reported for TRI His_3^a (

Table 3-10).[19]

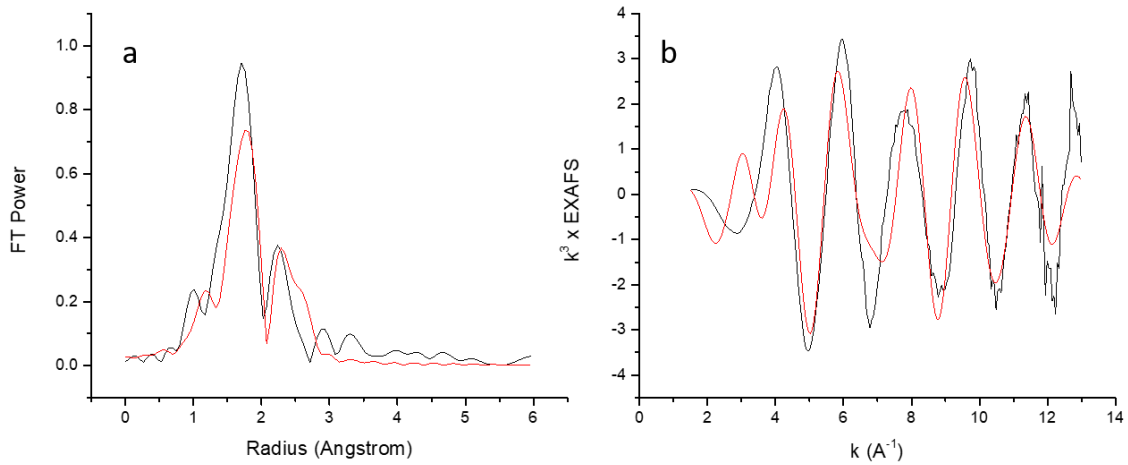

Figure 3-48 Cu(I) FT(a) and EXAFS (b) of His_3^d with 2 mM 3SCC, 2 mM $Pb(NO_3)_2$, 1 mM $CuCl_2$, ~50 equivalents of sodium ascorbate, and 50 mM HEPES pH 7.5 with data in black and fit to 3 His in red

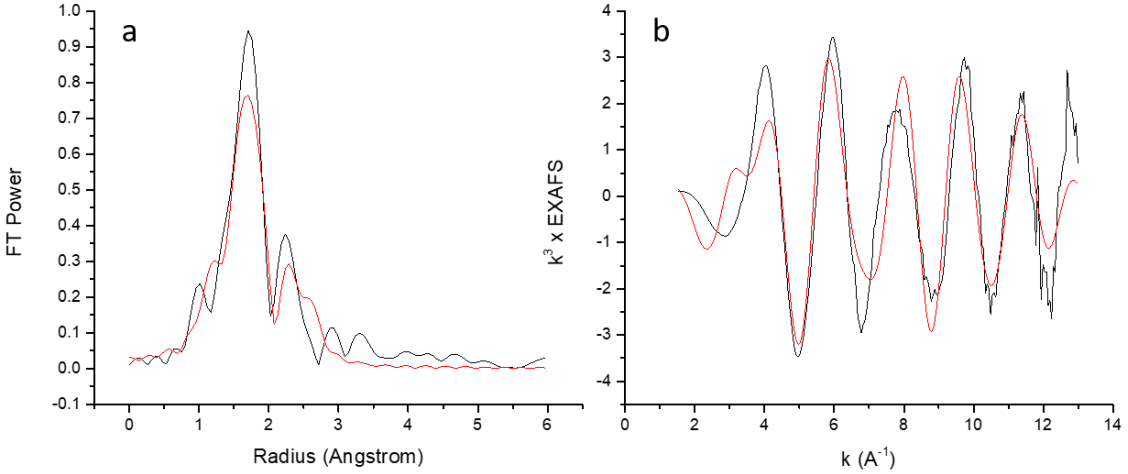

Figure 3-49 Cu(I) FT (a) and EXAFS (b) of His_3^d with 2 mM 3SCC, 2 mM $Pb(NO_3)_2$, 1 mM $CuCl_2$, ~50 equivalents of sodium ascorbate, and 50 mM HEPES pH 7.5 with data in black and fit to 2 His and 1 O in red

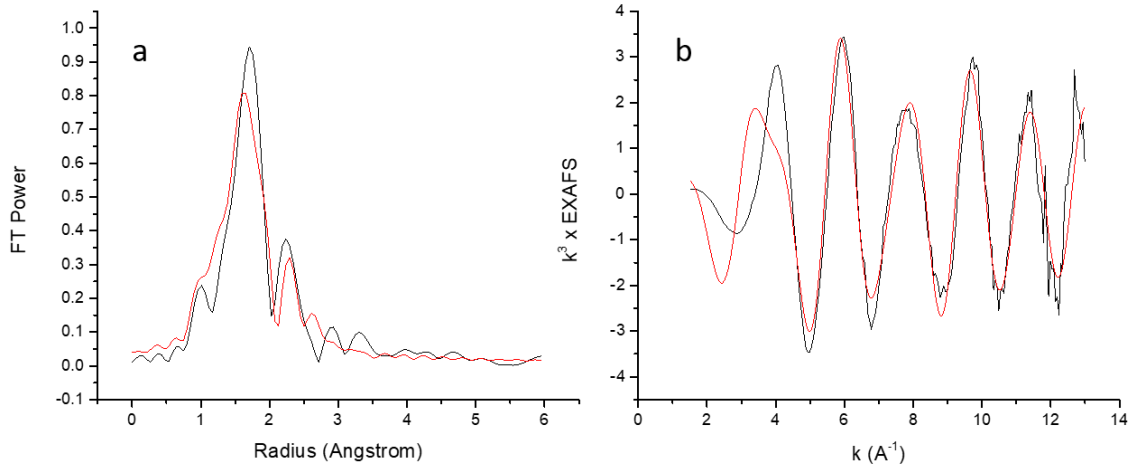

Figure 3-50 Cu(I) FT(a) and EXAFS (b) of His_3^d with 2 mM 3SCC, 2 mM $Pb(NO_3)_2$, 1 mM $CuCl_2$, ~50 equivalents of sodium ascorbate, and 50 mM HEPES pH 7.5 with data in black and fit to 2 His and 2 O in red

The His_3 heterotrimers also best fit to models with average bond distances between 1.96 Å and 1.98 Å, longer than TRI His_3^a. The best statistical fit to $His_2^dHis_1^a$ was a model with 3 His ligands and 1 O ligand, though all fits were poor (Figure 3-51). $His_1^dHis_2^a$ also fit well to this model (Figure 3-52) and to a 2 His 2 O model (Figure 3-53).

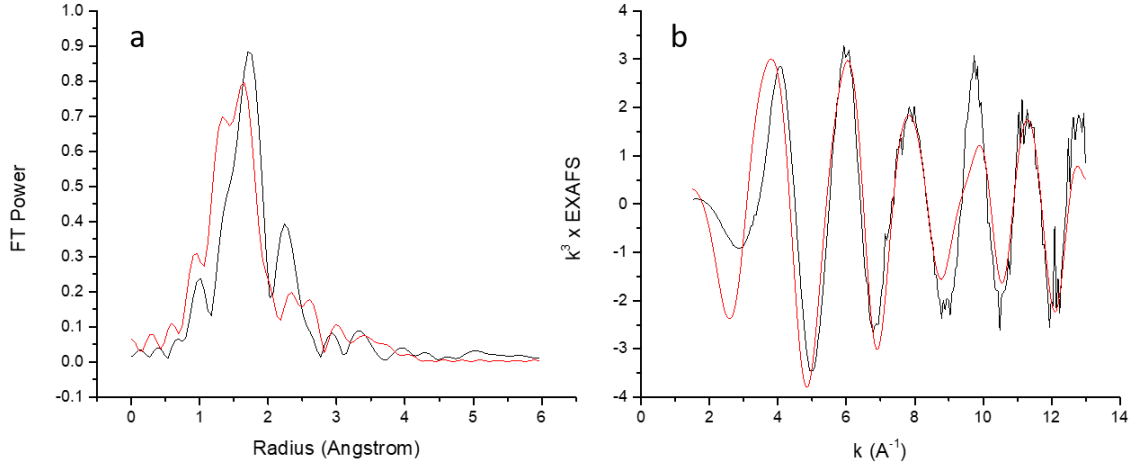

Figure 3-51 Cu(I) FT (a) and EXAFS (b) of $His_2^dHis_1^a$ with 2 mM 3SCC, 2 mM $Pb(NO_3)_2$, 1 mM $CuCl_2$, ~50 equivalents of sodium ascorbate, and 50 mM HEPES pH 7.5 with data in black and fit to 1 His and 3 O in red

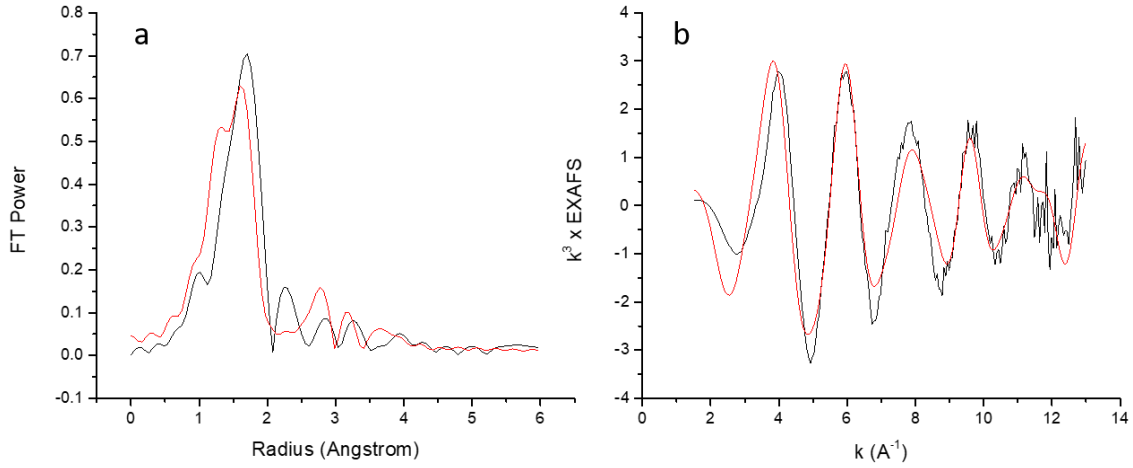

Figure 3-52 Cu(I) FT(a) and EXAFS (b) of $His_1{}^dHis_2{}^a$ with 2 mM 3SCC, 2 mM $Pb(NO_3)_2$, 1 mM $CuCl_2$, ~50 equivalents of sodium ascorbate, and 50 mM HEPES pH 7.5 with data in black and fit to 1 His and 3 O in red

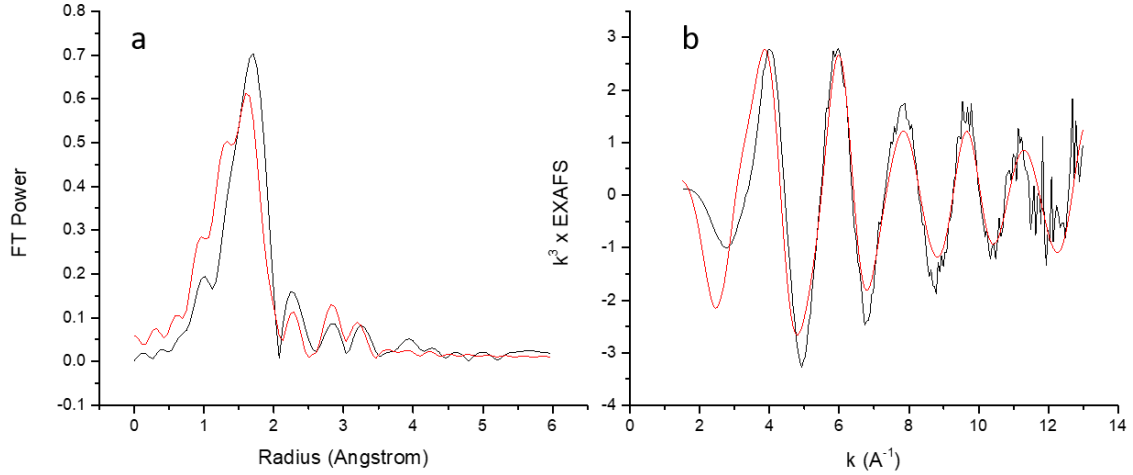

Figure 3-53 Cu(I) FT (a) and EXAFS (b) of $His_1{}^dHis_2{}^a$ with 2 mM 3SCC, 2 mM $Pb(NO_3)_2$, 1 mM $CuCl_2$, ~50 equivalents of sodium ascorbate, and 50 mM HEPES pH 7.5 with data in black and fit to 2 His and 2 O in red

The aspartate containing heterotrimers, $Asp_1{}^dHis_3{}^a$ and $His_2{}^dAsp_1{}^dHis_1{}^a$, both visually fit well to a 3 His 1 O model (Figure 3-54 and Figure 3-56, respectively), but the Debye-Waller factor for this model is negative, indicating a statistically impossible fit. Given the apparent disorder of these systems these fits are still reported herein. The other best fit for $Asp_1{}^dHis_3{}^a$ is 1 His 3 O (Figure 3-55) and both fits reported have an average bond distance between 1.96 Å and

1.99 Å. $His_2{}^dAsp_1{}^dHis_1{}^a$ also fit well to a model with 2 His and 2 O ligands (Figure 3-57) with an average bond distance of 1.97 Å.

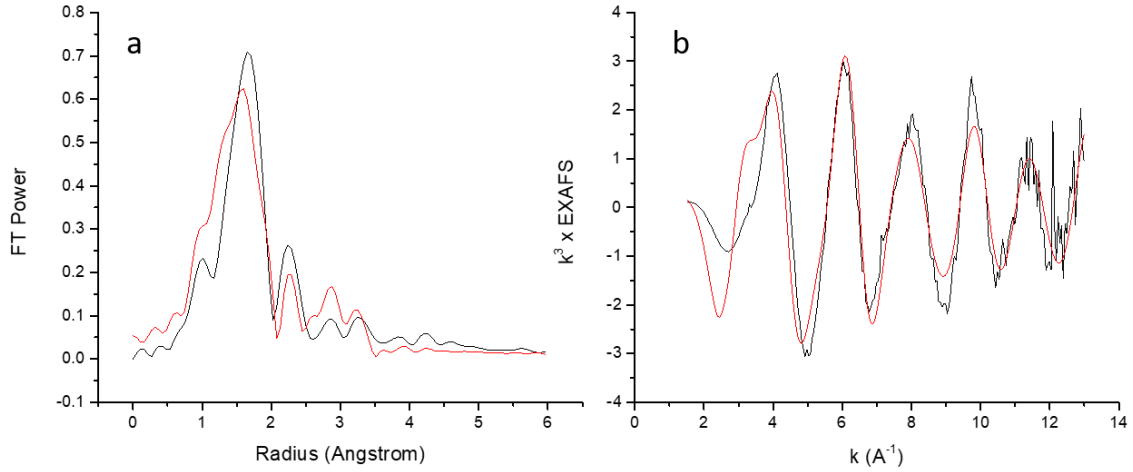

Figure 3-54 Cu(I) FT (a) and EXAFS (b) of $Asp_1{}^dHis_3{}^a$ with 2 mM 3SCC, 2 mM $Pb(NO_3)_2$, 1 mM $CuCl_2$, ~50 equivalents of sodium ascorbate, and 50 mM HEPES pH 7.5 with data in black and fit to 3 His and 1 O in red

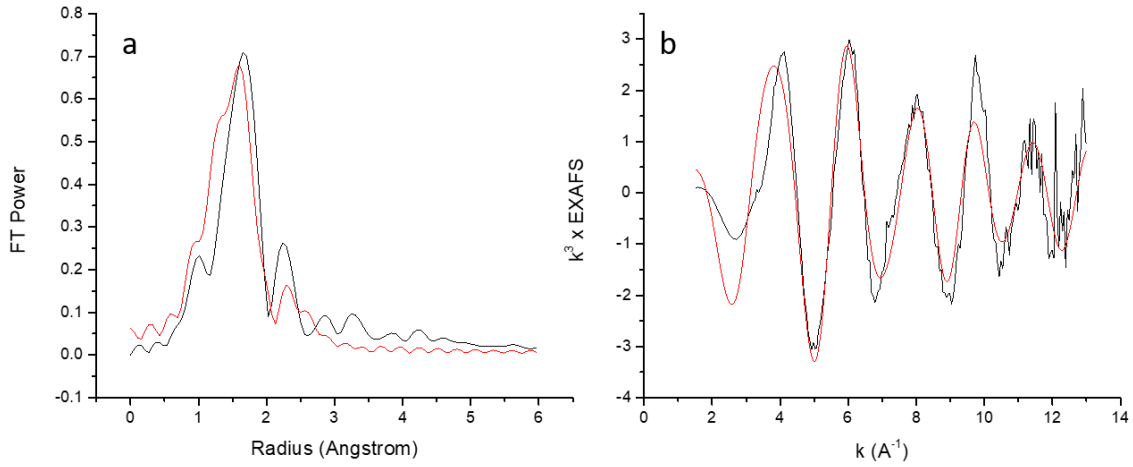

Figure 3-55 Cu(I) FT (a) and EXAFS (b) of $Asp_1{}^dHis_3{}^a$ with 2 mM 3SCC, 2 mM $Pb(NO_3)_2$, 1 mM $CuCl_2$, ~50 equivalents of sodium ascorbate, and 50 mM HEPES pH 7.5 with data in black and fit to 1 His and 3 O in red

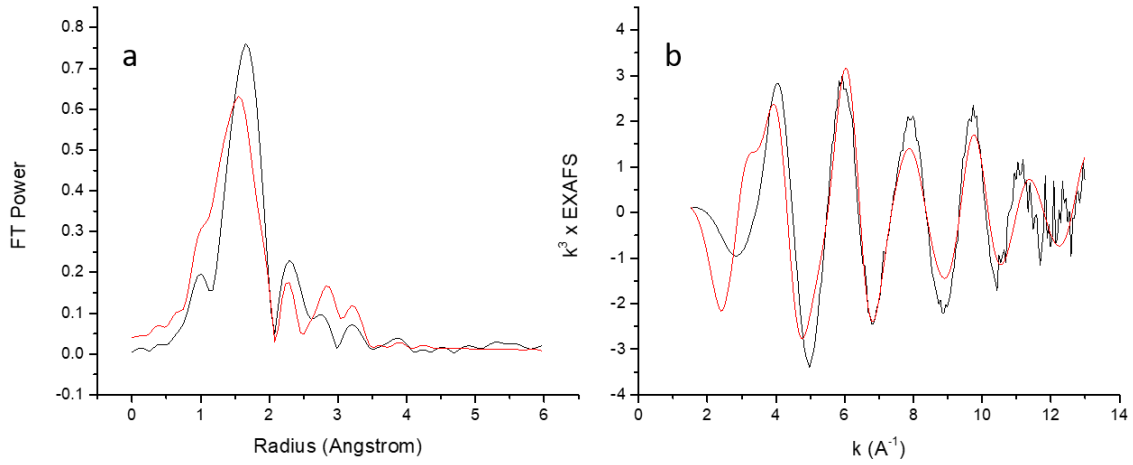

Figure 3-56 Cu(I) FT (a) and EXAFS (b) of $His_2{}^dAsp_1{}^dHis_1{}^a$ with 2 mM 3SCC, 2 mM $Pb(NO_3)_2$, 1 mM $CuCl_2$, ~50 equivalents of sodium ascorbate, and 50 mM HEPES pH 7.5 with data in black and fit to 3 His and 1 O in red

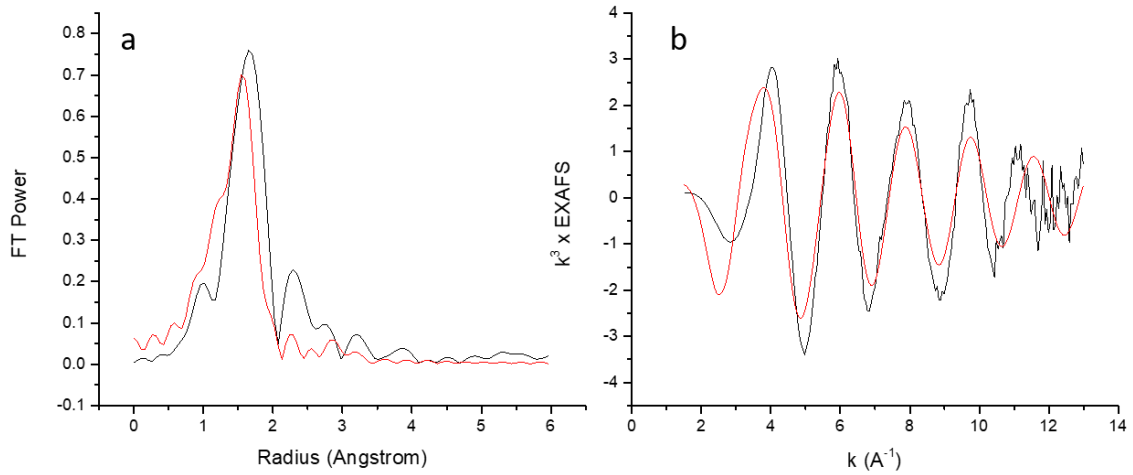

Figure 3-57 Cu(I) FT (a) and EXAFS (b) of $His_2{}^dAsp_1{}^dHis_1{}^a$ with 2 mM 3SCC, 2 mM $Pb(NO_3)_2$, 1 mM $CuCl_2$, ~50 equivalents of sodium ascorbate, and 50 mM HEPES pH 7.5 with data in black and fit to 2 His and 2 O in red

The glutamate containing trimers were also examined by XAS. $Glu_1{}^dHis_3{}^a$ fit best visually to a model containing 3 His and 1 O (Figure 3-58), but with a negative Debye-Waller factor for the oxygen ligand. This fit is still reported herein due to the high disorder of this system. The best statistical model for this system was a fit to 2 His and 2 O ligands, though this poorly approximates the histidine backscattering (Figure 3-59). The $Glu_3{}^dHis_3{}^a$ homotrimer also fit to a 2 His 2 O model with an average bond distance of 1.98 Å (Figure 3-60). This system also

fit very well to a 3 S 1 Cu model similar to reports from Dr. Mocny with a Cu-S distance of ~2.2 Å (Figure 3-61).[1] Note that this model was examined for the other trimers reported in this chapter but unreasonably short Cu-S distances were determined.

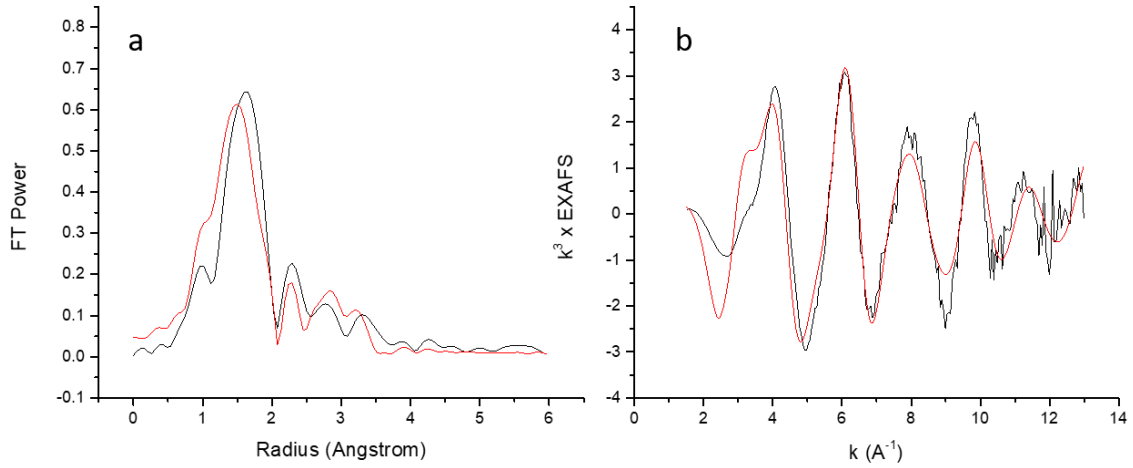

Figure 3-58 Cu(I) FT (a) and EXAFS (b) of $Glu_1^dHis_3^a$ with 2 mM 3SCC, 2 mM $Pb(NO_3)_2$, 1 mM $CuCl_2$, ~50 equivalents of sodium ascorbate, and 50 mM HEPES pH 7.5 with data in black and fit to 3 His and 1 O in red

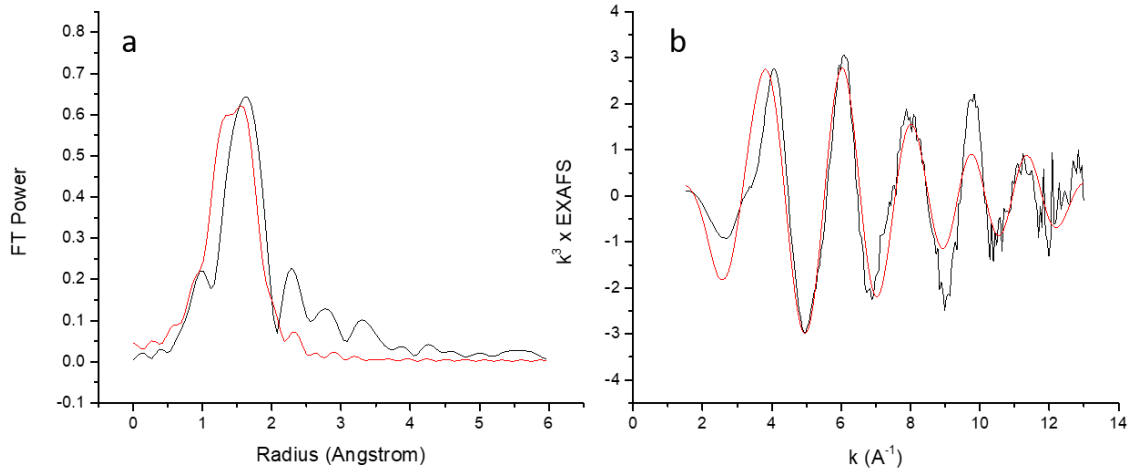

Figure 3-59 Cu(I) FT (a) and EXAFS (b) of $Glu_1^dHis_3^a$ with 2 mM 3SCC, 2 mM $Pb(NO_3)_2$, 1 mM $CuCl_2$, ~50 equivalents of sodium ascorbate, and 50 mM HEPES pH 7.5 with data in black and fit to 2 His and 2 O in red

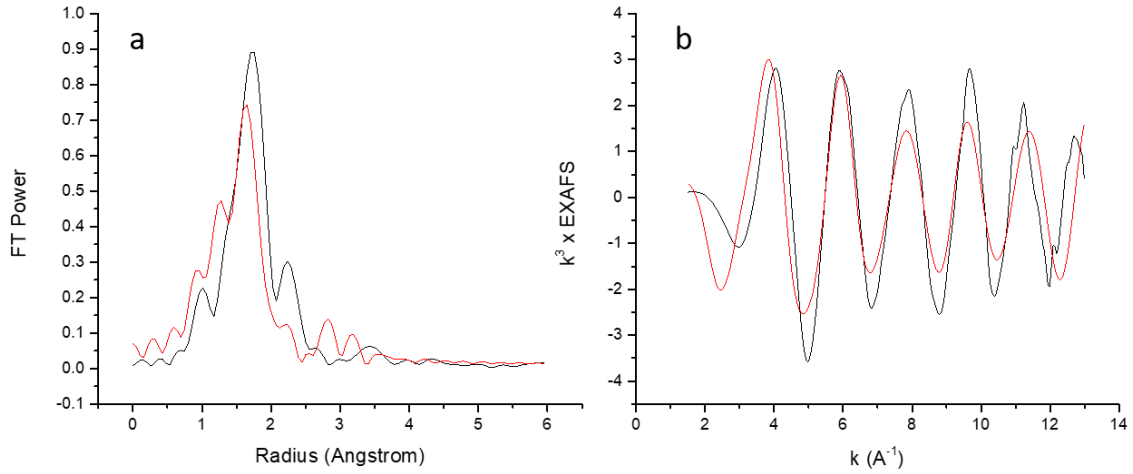

Figure 3-60 Cu(I) FT (a) and EXAFS (b) of $Glu_3^dHis_3^a$ with 2 mM 3SCC, 2 mM $Pb(NO_3)_2$, 1 mM $CuCl_2$, ~50 equivalents of sodium ascorbate, and 50 mM HEPES pH 7.5 with data in black and fit to 2 His and 2 O in red

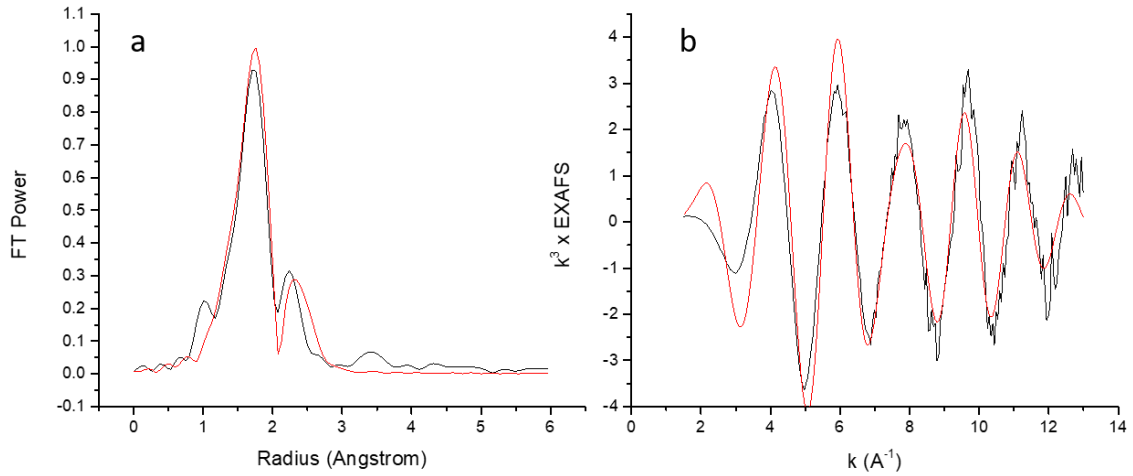

Figure 3-61 Cu(I) FT (a) and EXAFS (b) of $Glu_3^dHis_3^a$ with 2 mM 3SCC, 2 mM $Pb(NO_3)_2$, 1 mM $CuCl_2$, ~50 equivalents of sodium ascorbate, and 50 mM HEPES pH 7.5 with data in black and fit to 3 S and 1 Cu in red

*Table 3-10 Cu(I) XAS parameters for displayed fits. *TRI His_3^a data from Dr. Fangting Yu[19] #Cys_3^a data from Dr. Mocny in a GR peptide[1]*

Peptide	Number of O ligands	Oxygen R (Å)	σ^2 (10^{-3})	Number of His ligands	His R (Å)	σ^2 (10^{-3})	Goodness of Fit	Average R (Å)
His_3^d				3	2.02	7.39	198	2.02
	1	2.00	5.28	2	2.03	6.30	143	2.02
	2	2.06	1.18	2	1.95	7.87	135	2.01
$His_2^dHis_1^a$	3	2.02	2.50	1	1.85	3.22	184	1.98
$His_1^dHis_2^a$	2	2.04	2.16	2	1.88	8.95	87	1.96
	3	1.97	10.39	1	2.06	3.99	88	1.99
TRI His_3^a*				3	1.93	9	35	1.93
$His_3^dHis_1^a$	1	1.91	0.072	3	2.03	6.63	155	2.00
				4	1.98	10.85	197	1.98
$His_1^dHis_3^a$	1	2.06	1.44	3	1.93	9.49	73	1.96
				4	1.97	1.157	89	1.97
$Asp_1^dHis_3^a$	1	2.05	-1.1	3	1.93	8.78	99	1.96
	3	1.97	10.17	1	2.05	5.34	80	1.99
$His_2^dAsp_1^dHis_1^a$	1	2.07	-0.57	3	1.94	8.83	128	1.97
	2	2.02	2.88	2	1.90	1.807	139	1.96
$Glu_1^dHis_3^a$	1	2.06	-0.56	3	1.93	8.50	86	1.96
	2	1.93	4.9	2	2.05	4.59	98	1.99
$Glu_3^dHis_3^a$	2	2.05	0.90	2	1.90	8.14	187	1.98
	Number of S ligands	Sulfur R (Å)	σ^2 (10^{-3})	Number of Cu ligands	Cu R (Å)	σ^2 (10^{-3})	Goodness of Fit	
	3	2.22	8.39	1	2.66	8.74	123	
$Cys_3^{a\#}$	3	2.20	6.44	1	2.66	7.61	129	

Cu(I) XANES

The XANES spectra were investigated to determine likely coordination numbers for these peptides. The pre-edge feature of His_3^d and His_3 heterotrimers is less intense than was measured for a three coordinate system, TRI His_3^a,[20] indicating a mix of three and four coordinate environments (Figure 3-62).

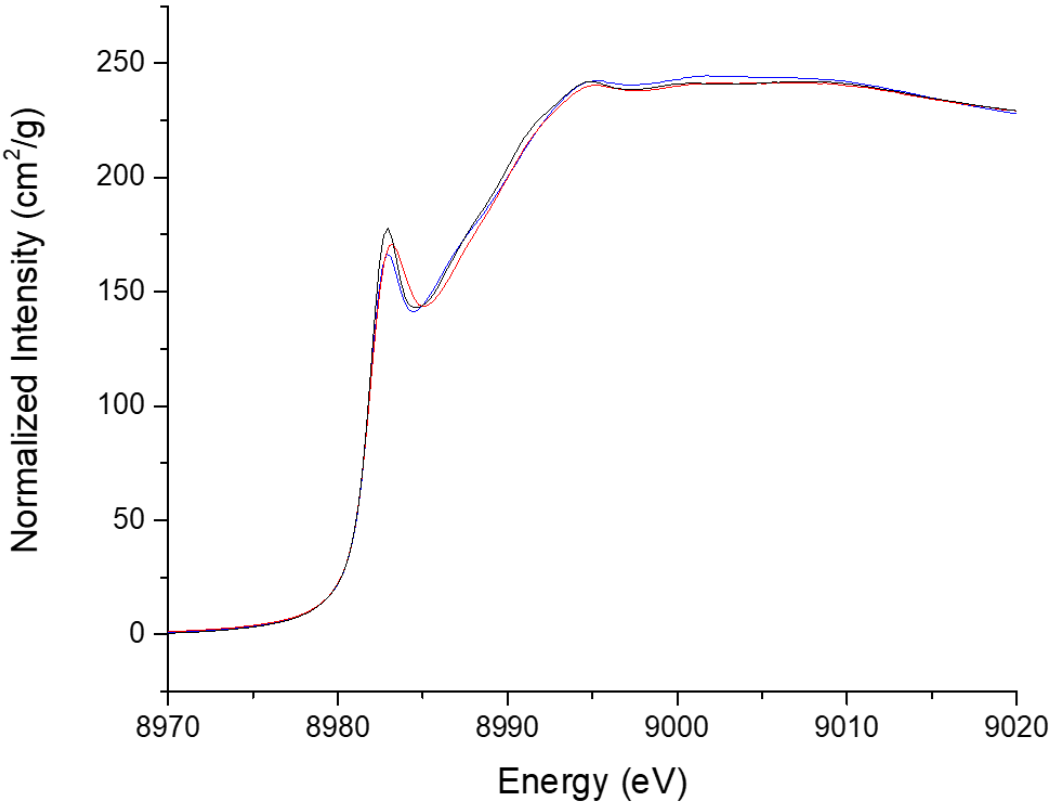

Figure 3-62 XANES of Cu(I) bound to His_3^d (black), $His_2^dHis_1^a$ (red), and $His_1^dHis_2^a$ (blue) at pH 7.5

The pre-edge feature is less intense for the His_4 systems than His_3^d, which is indicative of a higher coordination number (Figure 3-63).

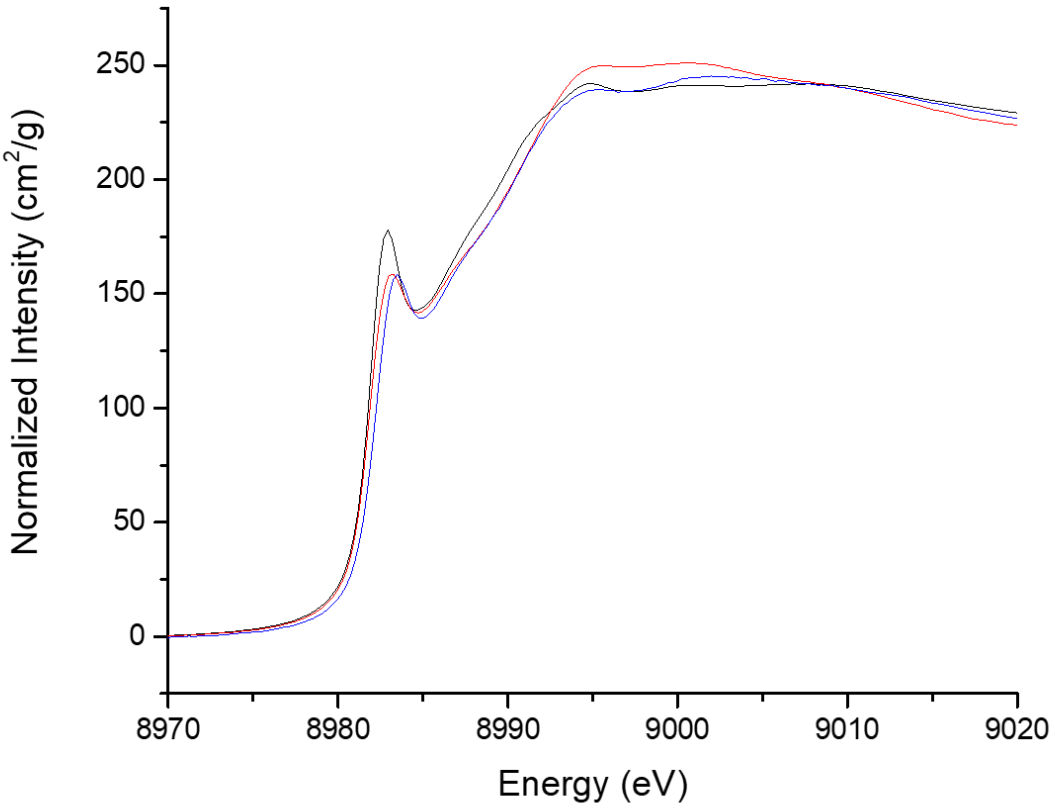

Figure 3-63 XANES of Cu(I) bound to His_3^d (black), $His_1^dHis_3^a$ (red), and $His_3^dHis_1^a$ (blue) at pH 7.5

There is no difference in the pre-edge feature of the Asp heterotrimers ($Asp_1^dHis_3^a$ and $His_2^dAsp_1^dHis_1^a$) as compared to His_3^d (Figure 3-64). The heterotrimer containing only one Glu residue, however, has a much less intense pre-edge transition than the $Glu_3^dHis_3^a$ homotrimer (Figure 3-65).

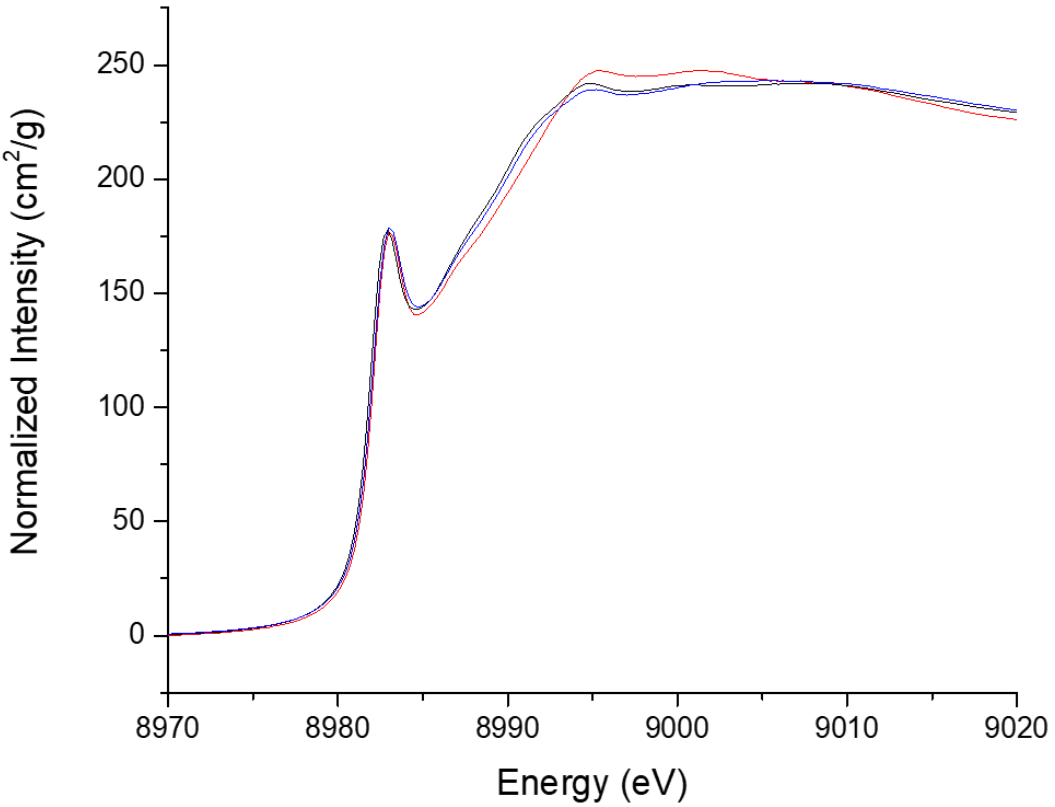

Figure 3-64 XANES of Cu(I) bound to His_3^d (black), $Asp_1^dHis_3^a$ (red), and $His_2^dAsp_1^dHis_1^a$ (blue) at pH 7.5

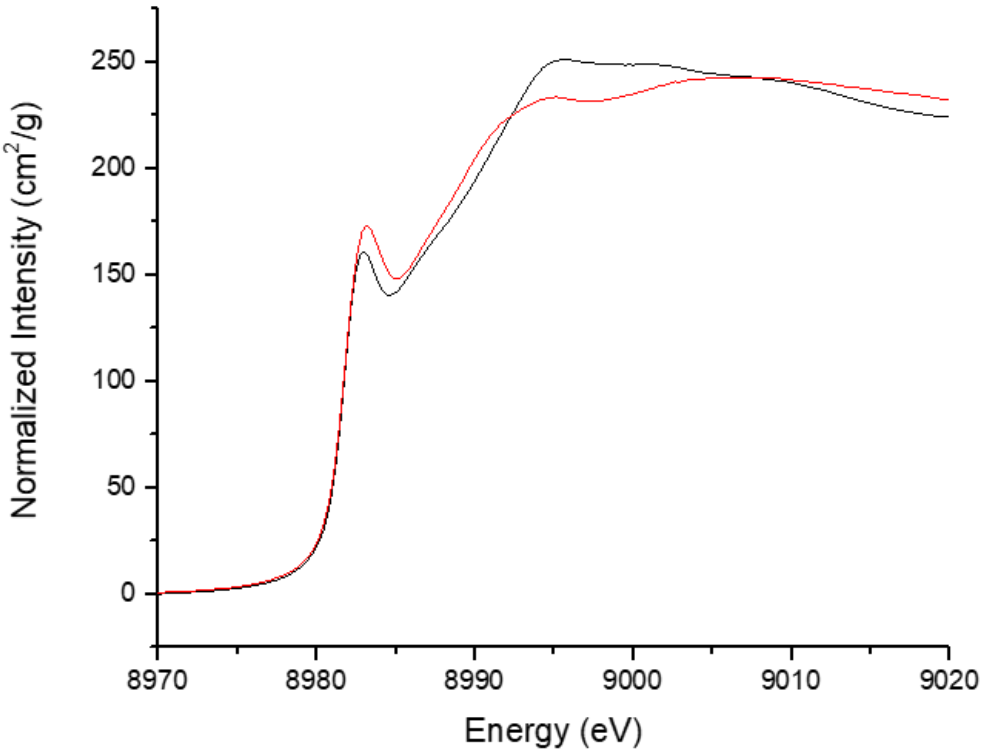

Figure 3-65 XANES of Cu(I) bound to $Glu_1{}^dHis_3{}^a$ (black) and $Glu_3{}^dHis_3{}^a$ (red) at pH 7.5

Discussion

In this chapter I have described how transition metal binding is affected by coordination in an asymmetric protein environment. Previous work by Dr. Catherine Mocny with Asp containing heterotrimers showed that asymmetry induced by the Cys^a site was conferred to the distant transition metal site. This work included Co(II) UV-visible, EPR, and X-ray absorption spectroscopies in which $Asp_1{}^dHis_3{}^a$ and $Asp_2{}^dHis_3{}^a$ peptides were of lower coordination number than $His_3{}^a$ and $Asp_3{}^dHis_3{}^a$ homotrimers. The heterotrimers were more 5-coordinate while the homotrimers were 6-coordinate. Zn(II) bound to these same sites, however, remained 4-coordinated with either His_3O or His_2O_2 ligand environments, showing that Co(II) was not a faithful spectroscopic probe for Zn(II).

This chapter also expands upon the copper work described by Dr. Fangting Yu. She investigated copper binding to $His_3{}^a$ homotrimers as a model of CuNiR at pH 5.9 but also did

some characterization at physiological pH. Dr. Yu found that Cu(I) was 3-coordinate while Cu(II) was 5-coordinate in His_3^a. In this chapter I have described spectroscopic properties of both Cu(I) and Cu(II) in His_3^a systems with Asp and Glu residues and in His_3^d systems at pH 7.5 as a model of Cu-only SOD.

In Chapter 2, I showed via ^{207}Pb NMR that a distant His_3 layer and a transition metal could be added to the Cys^d heterotrimeric scaffold without perturbing heterotrimer formation. In order to work with trimers containing carboxylate residues, it first needs to be confirmed that these residues do not affect Pb(II) binding to the Cys_3^d layer. Dr. Mocny previously showed that Co(II) bound to His_3^a, $Asp_3^dHis_3^a$, $Asp_2^dHis_3^a$, and $Asp_1^dHis_3^a$ did not disrupt Pb(II) binding to the Cys_3^a site as monitored by ^{207}Pb NMR. In fact, the addition of the transition metal resulted in only a single signal for all trimers, indicating that the transition metal induced full selectivity when carboxylate residues are present in addition to the His_3^a layer.[1] The same is true for the Glu containing homo- and heterotrimers in the presence of Co(II). No signal is observed for $Glu_2^dHis_3^a$ and $Glu_3^dHis_3^a$ in the absence of a transition metal, which was also observed for $Asp_2^dHis_3^a$. This lack of signal is likely due to fast exchange of Pb(II) from the Cys_3 site to the carboxylate site.

This exchange of Pb(II) between the two sites is reflected in the Pb(II) titration into $Glu_3^dHis_3^a$. In this titration, rather than a linear increase in absorbance to exactly one equivalent of Pb(II) per trimer as was observed in Chapter 2, the $Glu_3^dHis_3^a$ trimer instead shows a level of competition for Pb(II) between the Cys_3^d and $Glu_3^dHis_3^a$ sites (Figure 3-7). Still a 3SCC is formed based both on the Pb(II) binding equivalency to the Cys_3 site and the Pb(II)-S_3 NMR signal. . This competition between the sulfur and oxygen/nitrogen sites will be discussed further as it relates to Co(II) affinity to the $Glu_3^dHis_3^a$ site. With only His ligands, no such competition is observed. This is true for both His_3^a peptides as discussed in Chapter 2 as well as the $His_3^dHis_3^a$ homotrimer described above (Figure 3-8). This His_6 peptide binds only 1 equivalent of Pb(II) with an extinction coefficient consistent with previously observed Pb(II)-S_3 sites. These results, along with CD spectra, show that, while the His^dHis^a peptide strand is less stable than the other peptides discussed in this work, it still folds into an alpha helical coiled coil that is capable of binding Pb(II) at the distant Cys_3^d site. This homotrimer is not explored further in this work as it is unknown if one or two binding sites would result from two adjacent layers of His residues.

This peptide is instead used as a single strand in a heterotrimer to generate a His_4 site and will be discussed further with copper spectroscopy work.

The Glu containing peptides were initially designed to model the second coordination sphere interactions of CA. The native Zn(II) is spectroscopically silent, so Co(II) UV-visible spectroscopy was performed to determine how an asymmetric peptide scaffold influenced transition metal binding. The homotrimeric His_3^a peptide bound one equivalent of Co(II) with maximum absorbance for the d-d transition at 515 nm (Figure 3-12). The $Glu_3^dHis_3^a$ homotrimer also bound one equivalent of Co(II) but with a maximum absorbance at 560 nm. Unlike the His_3^a homotrimer, this is not a single smooth peak but instead has a higher energy shoulder at 515 nm and a lower energy shoulder at ~590 nm. For both homotrimers the extinction coefficients were consistent with 6-coordinate Co(II) species. The $Glu_1^dHis_3^a$ and $Glu_2^dHis_3^a$ heterotrimers had similar peak shapes and positions to the $Glu_3^dHis_3^a$ homotrimer, but with higher extinction coefficients that are more consistent with 5-coordinate Co(II) complexes. The absorbances at lower energy are consistent with 5-coordinate Co(II) substituted CA.[21-22] These spectra are invariant between Cys^a and Cys^d systems (Figure 3-11), further verifying that the addition of a transition metal to a peptide containing a distant mixed carboxylate/histidine site results in a fully selective heterotrimer for Cys systems.

The Co(II) UV-visible spectroscopy of Glu containing trimers was also compared to the results Dr. Mocny obtained with Asp containing trimers. The homotrimeric $Asp_3^dHis_3^a$ was significantly different from $Glu_3^dHis_3^a$, containing only a single smooth peak at higher energy than the Glu homotrimer. The shape of the heterotrimeric peaks was similar between the two systems, but the Asp containing system was at higher energy and had higher extinction coefficients. These extinction coefficients were still consistent with 5-coordinate Co(II) complexes.

The cobalt binding affinity was directly determined from titrations of Co(II) into the $Glu_x^dHis_3^a$ peptides (Table 3-2). The two heterotrimers had the tightest affinity (~10 μM), which is not significantly different than the affinity of $Asp_2^dHis_3^a$ for Co(II) as determined by Dr. Mocny (8 μM). The $Glu_3^dHis_3^a$ homotrimer has an affinity ~2.5x weaker than the heterotrimers (28 μM), but still tighter than the His_3^a homotrimer (41 μM). This result is interesting as one would expect tighter binding with an increase in oxygen ligands. As was discussed previously with the Pb(II) binding data, the lead ion also has some affinity for the oxygen rich site. With

more oxygen ligands, the Co(II) binding curve is not a direct reflection of Co(II) binding to an apo $Glu_x^dHis_3^a$ site, rather it is a competition titration of Pb(II) and Co(II) for this site. Likely, one equivalent of Pb(II) binds to the Cys_3 site and one equivalent can bind to the $Glu_3^dHis_3^a$ site, although spectroscopic characterization of this binding was not performed. The true binding constant of Co(II) to $Glu_3^dHis_3^a$ would require a peptide lacking the Cys_3^a site. It is possible that the Pb(II) binding affinity for this site could be extracted based on the Co(II) affinity and the Pb(II)-S_3 binding curve.

An examination of the EPR spectra of the Co(II) environment showed that Asp and Glu containing systems are quite different. The interpretation of Co(II) EPR is complex, so all statements herein are qualitative. All $Glu_x^dHis_3^a$ peptides are more similar to the $Asp_3^dHis_3^a$ and His_3^a spectra than to the heterotrimeric Asp spectra (Figure 3-24-Figure 3-26). These features are reminiscent of small molecule Co(II) complexes with 3 N and 2 O ligands.[23] A six-coordinate Co(II) complex with oxygen and nitrogen ligands is expected to have a negative peak at ~2500 G rather than ~2000 G as was observed with the Glu peptides.

These coordination environments were also examined by Co(II) XAS. Both 5- and 6-coordinate environments were fit to these spectra with no single best model for any trimer. The average bond distance was between 2.02 and 2.05 Å but the goodness of fit indicated that some disorder was present in these systems (Table 3-3). The XANES spectra of the heterotrimers had a much more intense pre-edge feature than $Glu_3^dHis_3^a$ (Figure 3-23). Because this feature is due to a forbidden transition from the 1s to 3d orbitals, a higher intensity of this feature indicates a lower symmetry, which typically correlates with a lower coordination number. The lower coordination number of the heterotrimers agrees well with the observed UV-visible spectra. Thus, the heterotrimers are likely 5-coordinate though some disorder may be attributed to a 6-coordinate species while all homotrimeric data best fits a 6-coordinate model.

Models of the six-coordinate complexes were generated in Pymol based on the crystal structure of GRCS L16CL30H (PDB: 5KB0). Co(II) coordinated to His_3^a was best modeled by a 6-coordinate Co(II) with the cobalt ion C-terminal to the His_3^a plane (Figure 3-66). This is opposite from Zn(II) binding in all crystal structures of His_3^a in which the Zn(II) is N-terminal to the His_3^a site, but the addition of two more solvent molecules in the center of the 3SCC required the additional space of the fraying trimer to avoid significant steric clash with the native Leu

residues (Figure 3-67). In these models, all ligands are at 2.1 Å but distance measurements have been excluded for clarity.

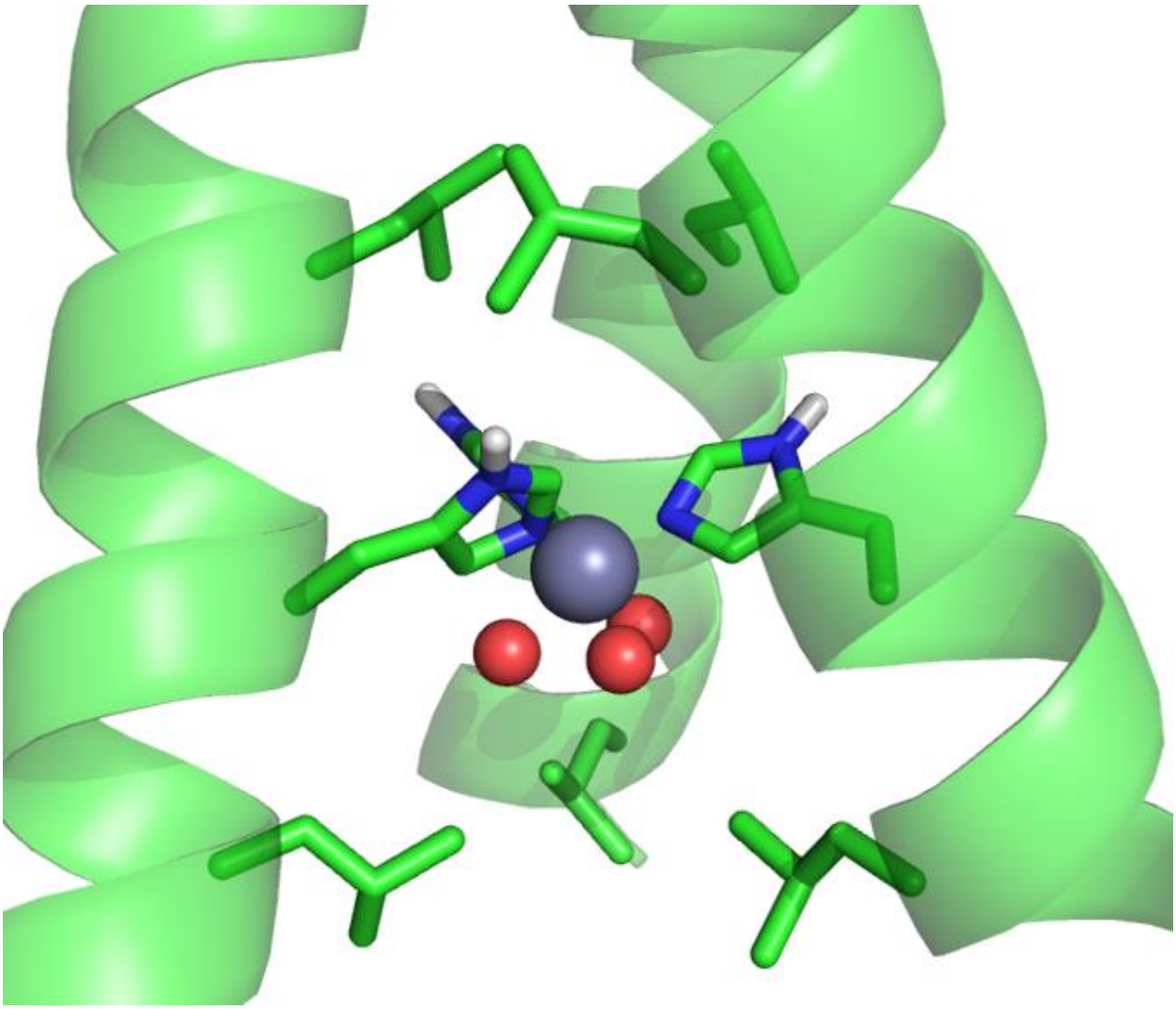

Figure 3-66 Side view of Pymol model of Co(II) His_3^a based on the structure 5KB0

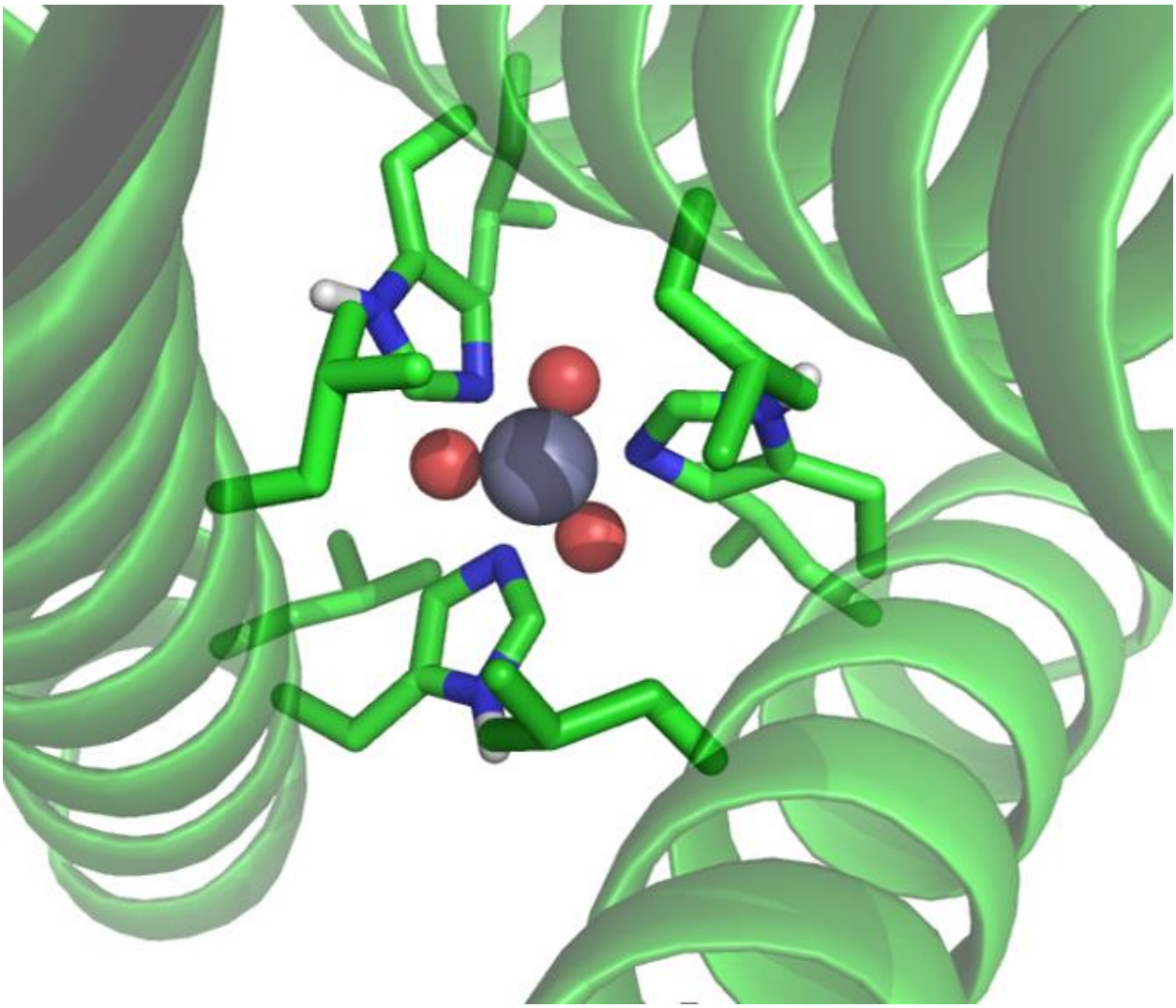

Figure 3-67 Top down view of Pymol model of Co(II)His_3^a based on the structure 5KB0

The $Glu_3^dHis_3^a$ Pymol models allowed for either Co(II) coordination above (N-terminal) or below (C-terminal) the His3a plane. With the Co(II) below the His_3^a plane, there is no perturbation to the binding site shown above, instead, the Glu residues are able to hydrogen bond to the protonated delta-nitrogen of the His residues at a distance of 2.4 Å (Figure 3-68). Note that these models do not show a linear hydrogen bond due to limits of possible side chain orientations in Pymol. This disparity is further highlighted in the top down view (Figure 3-69), though one could expect rotation of the carboxylate group to accommodate this bond. As with the His_3^a models, all ligands are at 2.1 Å but these measurements have been omitted for clarity.

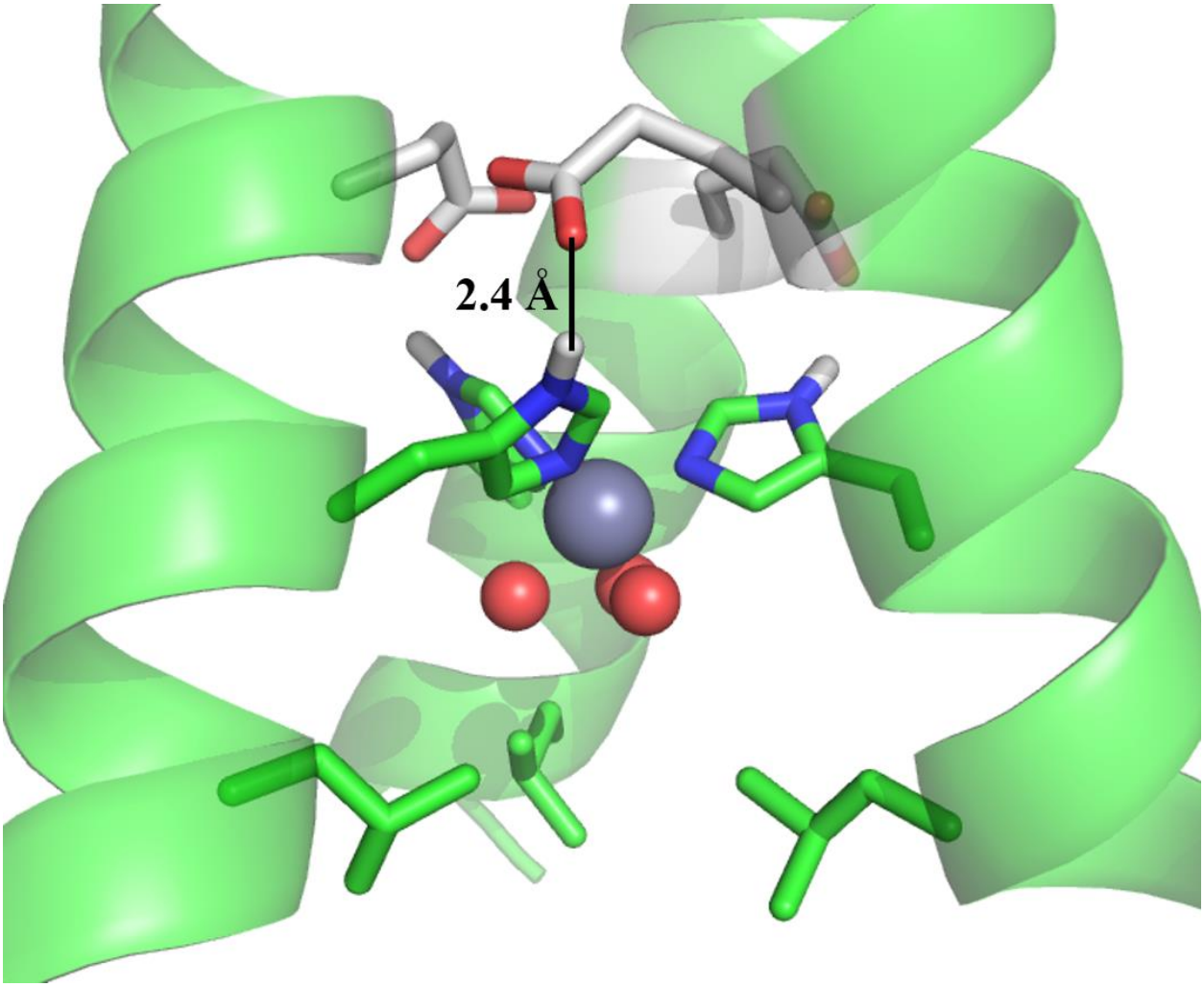

Figure 3-68 Side view of Pymol model of Co(II)$Glu_3^dHis_3^a$ with one hydrogen bond shown. Note that hydrogen bonds may be present on all three strands but have been omitted for clarity. Based on the structure 5KB0

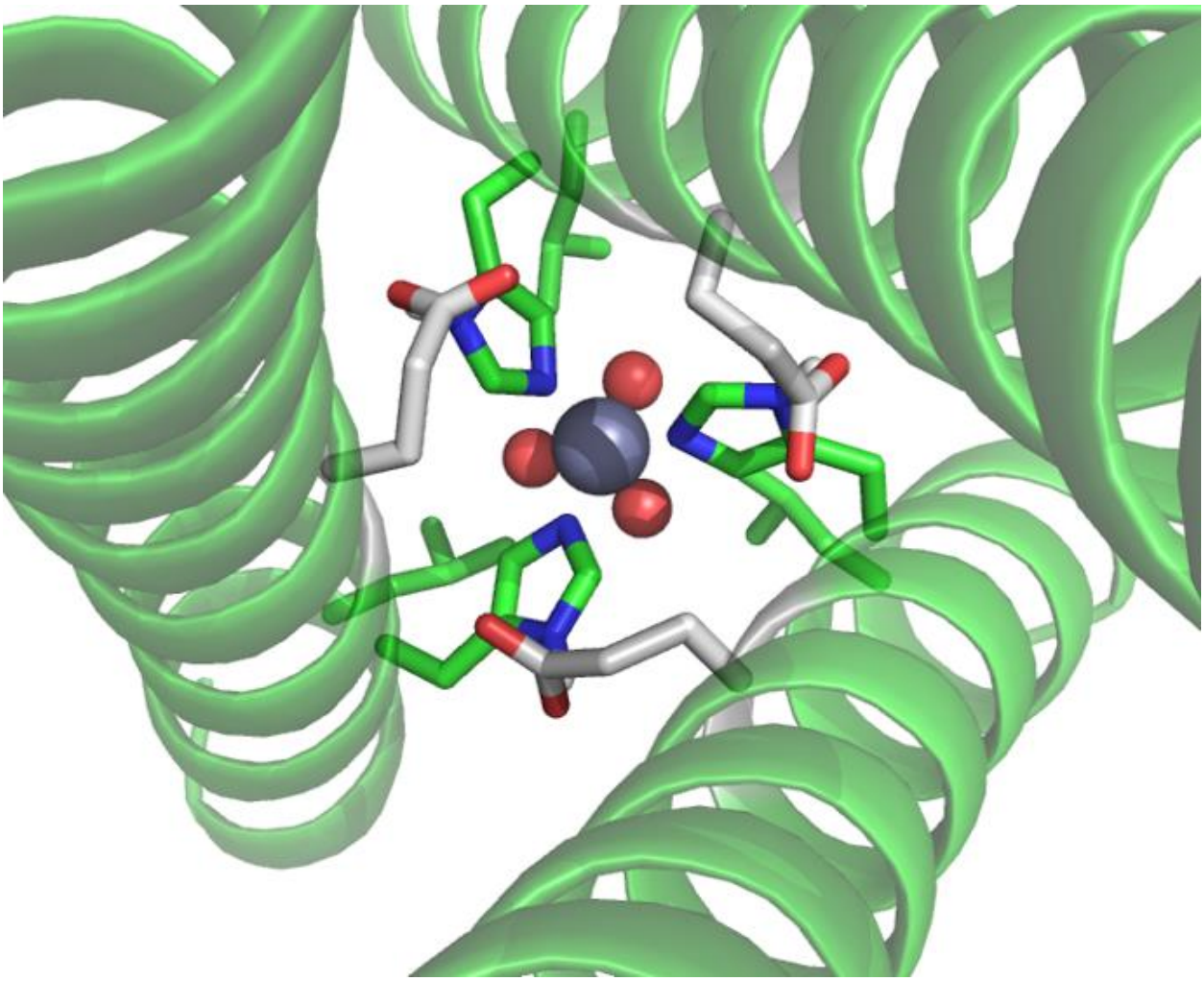

Figure 3-69 Top down view of Co(II)$Glu_3^dHis_3^a$ with the Co(II) below the His_3^a plane. Based on the structure 5KB0

The Glu substitution also allows for the Co(II) to orient above the His_3^a plane in the site that Zn(II) occupies. Three solvent molecules are able to coordinate in the space generated by the Glu substitution (Figure 3-70, Figure 3-71). Again, a Glu—His hydrogen bond may form at 2.4 Å and all ligands are at 2.1 Å. Note that all three Glu residues cannot directly coordinate the Co(II) due to steric clashes between the three Glu and the His residues. It is possible that one or two Glu residues may displace the solvent molecules to directly coordinate Co(II), which agrees with the decrease in symmetry in this environment as observed in the Co(II) UV-visible spectroscopy (Figure 3-12).

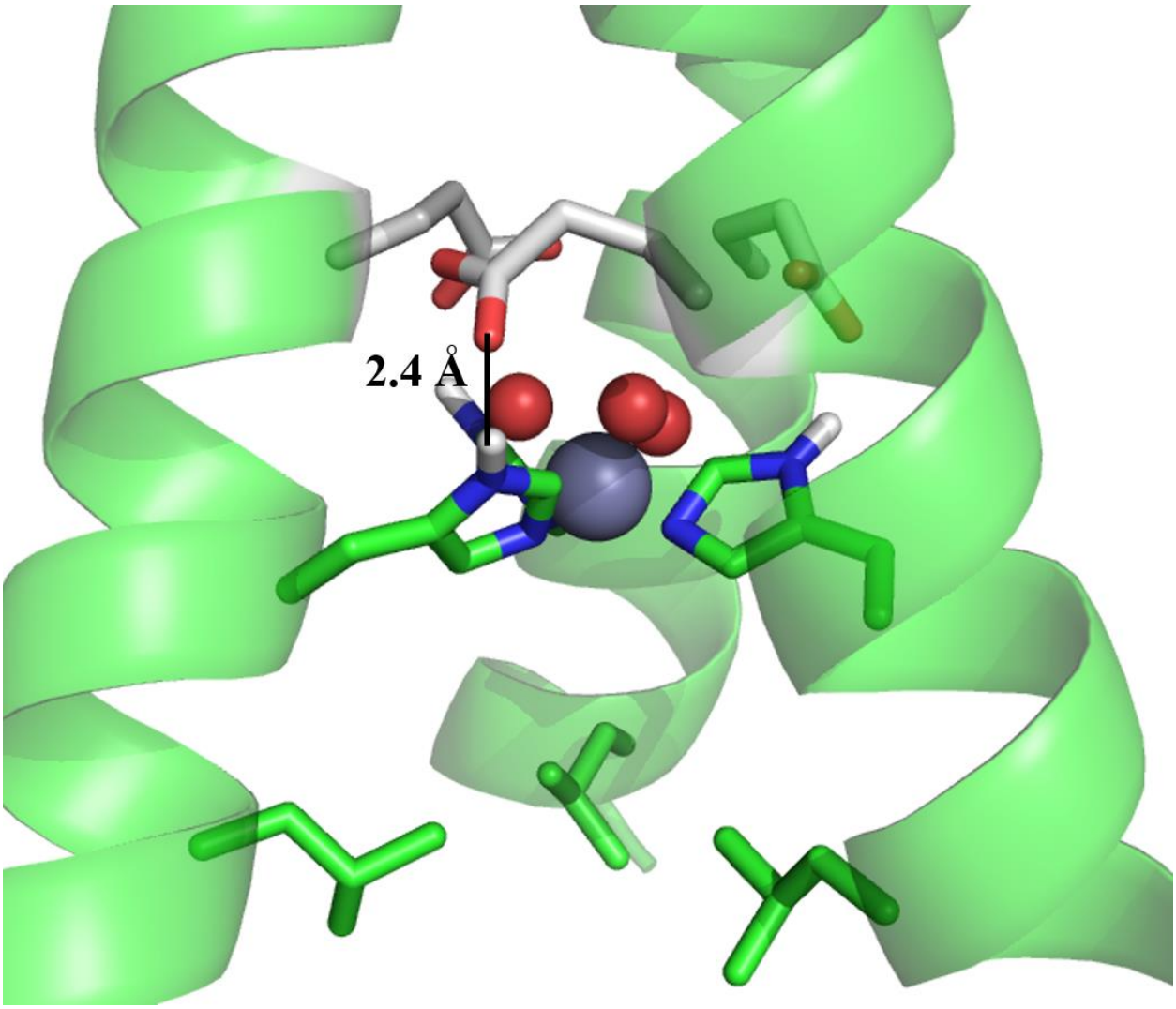

Figure 3-70 Side view of a Pymol model of Co(II)Glu$_3^d$His$_3^a$ with Co(II) above the His$_3^a$ plane. Based on the structure 5KB0

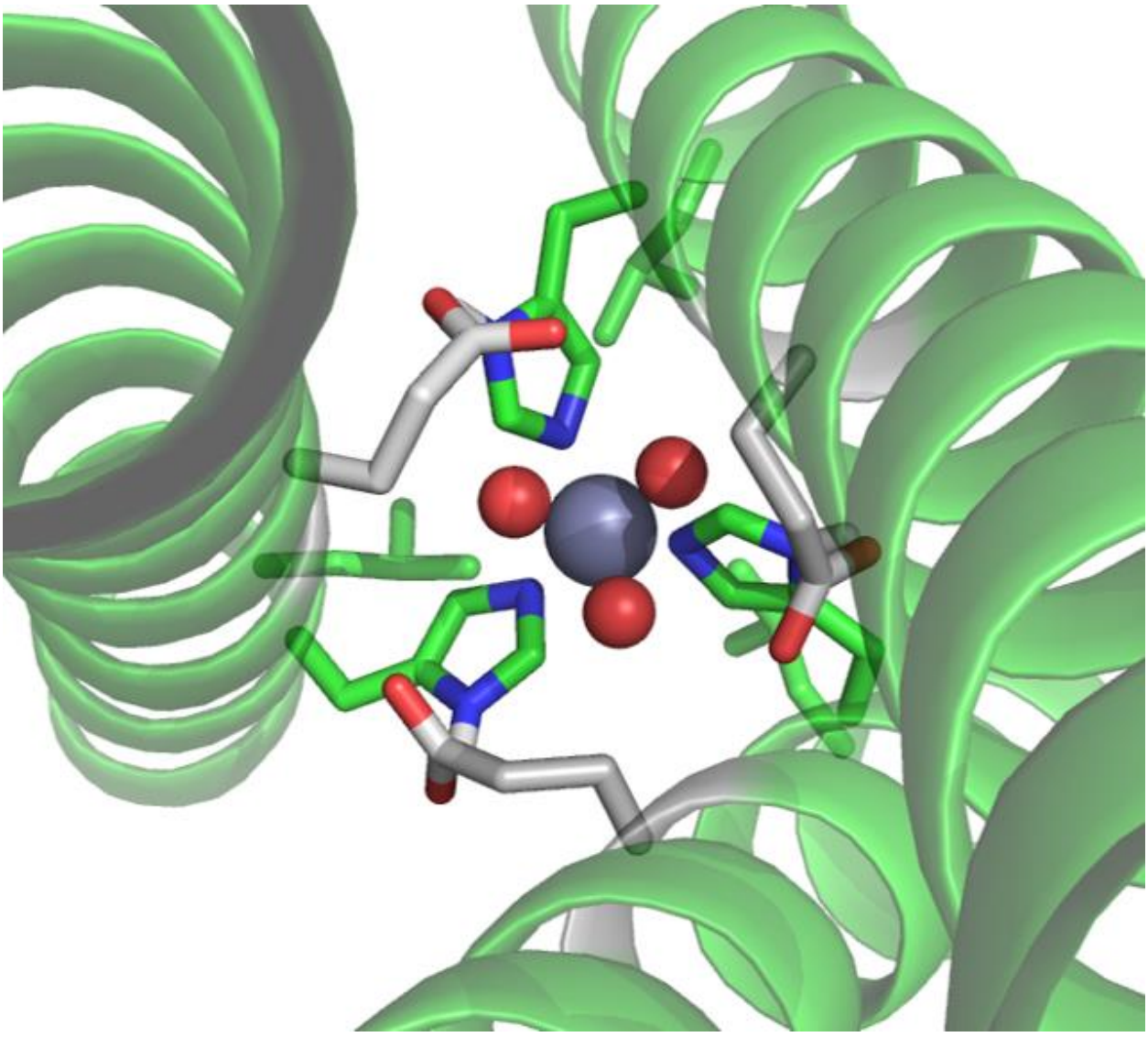

Figure 3-71 Top down view of Co(II)$Glu_3^dHis_3^a$ with Co(II) above the His_3^a plane. Based on the structure 5KB0

The $His_3^aGlu_3^d$ homotrimer was closely similar spectroscopically to His_3^a with bound Co(II). A Pymol model of this mutation shows that, even with the Co(II) N-terminal to the His_3^a plane, a Glu residue in this position cannot coordinate the metal ion (Figure 3-72). Thus, regardless of the symmetry of the scaffold, no spectroscopic changes should be observed because the carboxylate residues are too far to interact with the metal ion.

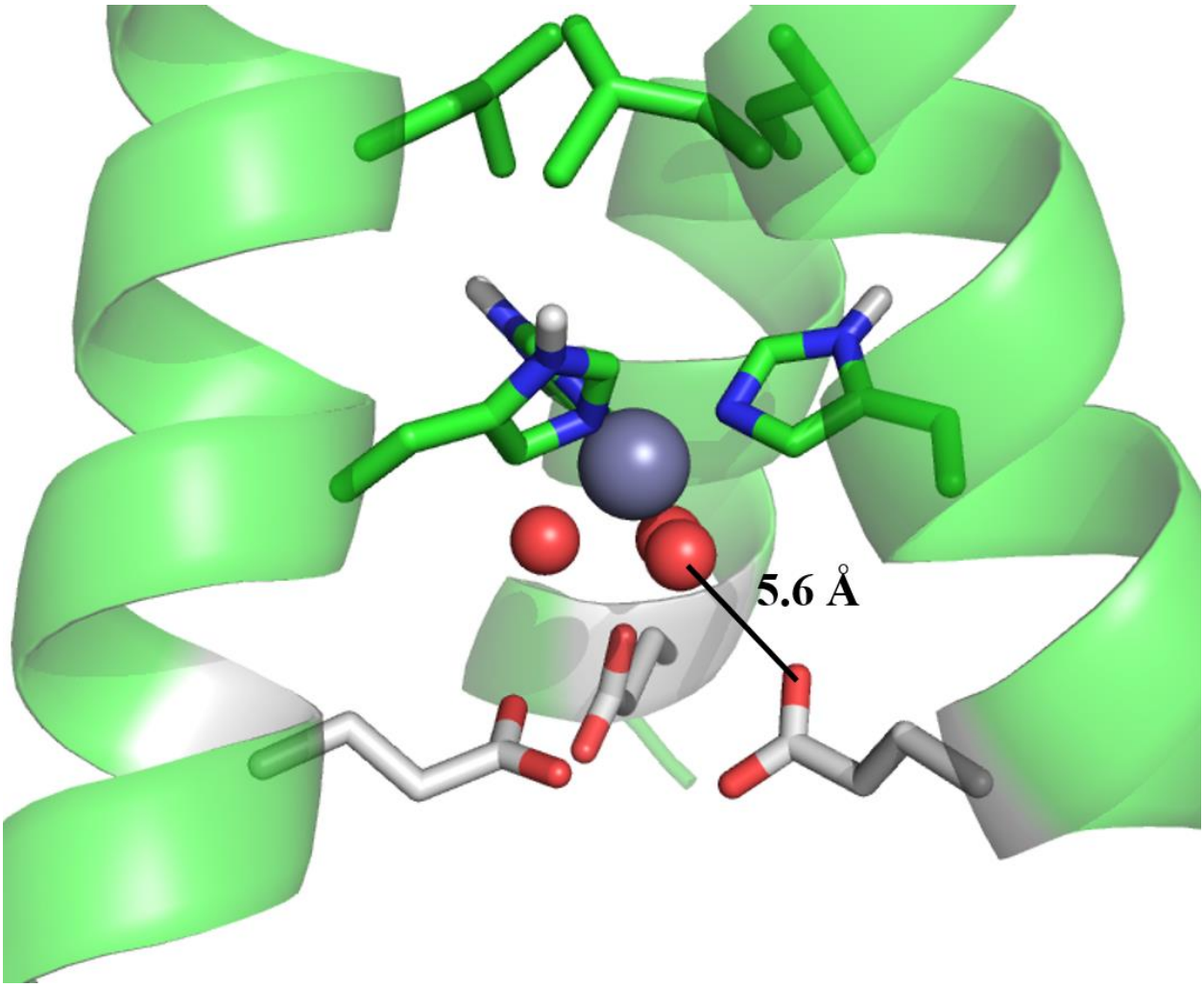

Figure 3-72 Side view of Co(II)$His_3^aGlu_3^d$ with the shortest water-Glu distance shown. Based on the structure 5KB0

The Glu containing heterotrimers better fit to 5-coordinate structures based on all spectroscopic evidence previously described. These 5-coordinate environments are likely formed with equatorial His residues and axial solvent molecules (Figure 3-73). As shown above, there is sufficient space below the His_3^a plane for solvent coordination, but only one solvent molecule is likely to coordinate above the His_3^a plane as with the Zn(II) structures (Figure 3-74). Only the $Glu_1^dHis_3^a$ heterotrimer is shown here as $Glu_2^dHis_3^a$ is expected to coordinate similarly. All ligands in the 5-coordinate model are set between 2.0 and 2.1 Å.

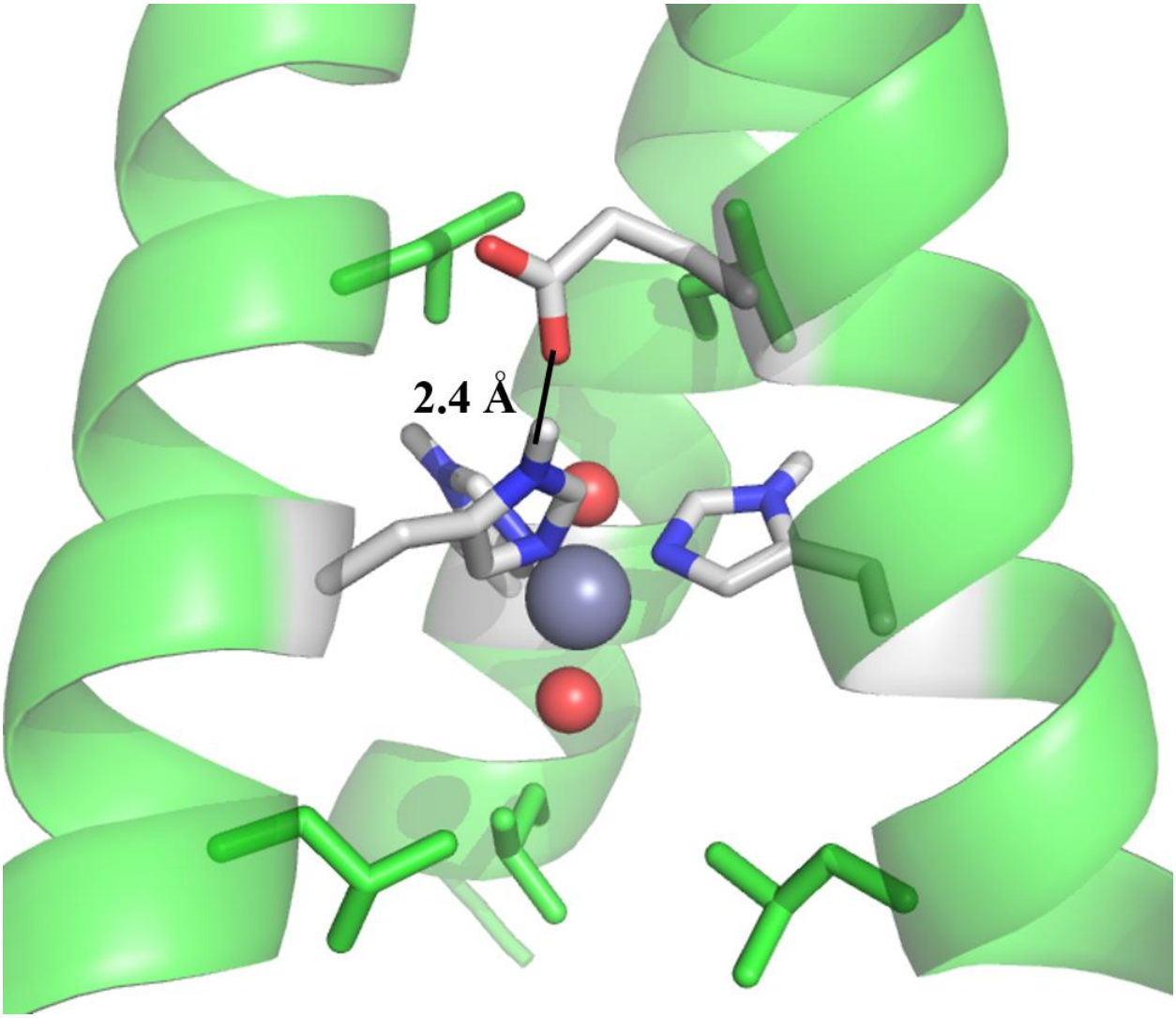

Figure 3-73 Side view of Co(II)Glu$_1^d$His$_3^a$ based on the structure 5KB0

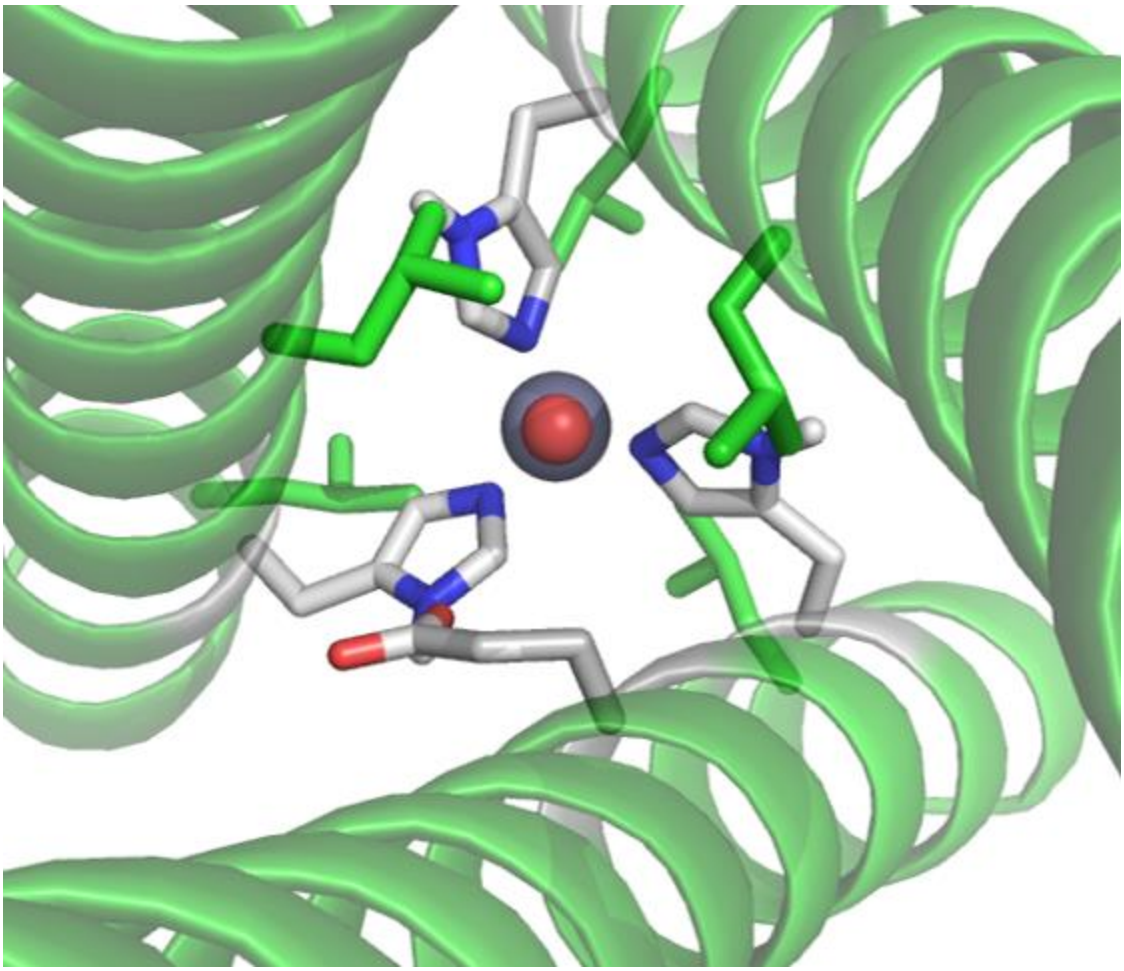

Figure 3-74 Top down view of Co(II)$Glu_1^dHis_3^a$ based on the structure 5KB0

The Zn(II) XAS reported herein does not provide enough information to determine the exact coordination environment of zinc in the Glu containing trimers. As with the Asp containing trimers described by Dr. Mocny, the 5- and 6-coordinate Co(II) was found to be an unfaithful spectroscopic probe for Zn(II), despite a wealth of literature suggesting Co(II) substitution in metalloenzymes mimics Zn(II) coordination.[24-27] All Zn(II) spectra best fit to 4-coordinate species regardless of pH (Table 3-4). Unfortunately, this data is unable to distinguish between His_3O and His_2O_2 coordination environments. The Zn(II) affinity for these peptides is discussed in Chapter 4 as it relates to activity and further interpretation of the Zn(II) environment is discussed in relation to that data.

Cu(II) binding in these environments is different from both the Co(II) and Zn(II) binding environments. Cu(II) remains 4-coordinate regardless of the ligand environment. Without X-ray crystallography or XAS data, one cannot deduce the exact ligands, but the UV-visible

spectroscopy provides some possibilities. A perfectly symmetric Cu(II)$His_3(OH_2)$ complex was predicted to have a maximum absorbance for the d-d transition at 634 nm.[28] This agrees well with the maximum absorbance for the peptides reported herein, ranging from 620-652 nm. Note that these wavelengths are not exact as noise in the spectra required estimation of the peak maximum from a smoothed spectrum. A predicted Cu(II)$His_2(OH_2)_2$ spectrum was expected to have a d-d transition at much lower energy, 692 nm.[28] It is possible that some of these species are shifting towards this coordination environment, though the broadness of the d-d transition does not change across trimers (Figure 3-40-Figure 3-43). If a broader peak were observed with a lower energy transition this may have indicated a higher population of the His_2O_2 environment. Instead, this may reflect the lack of symmetry in these sites. The calculated d-d transitions assumed symmetric His coordination but this seems unlikely in these systems. Crystal structures of Cu(II) in both Cu,Zn SOD and Cu-only SOD have shown that the copper is coordinated to 4 His residues with variable geometry.[9, 29-33] It was even shown crystallographically that Cu(II) may have two different coordination environments in Cu, Zn SOD.[34] These are still histidine environments, but with slightly different ligand distances. Thus, it is not unlikely for disorder to be present in SOD systems or within the 3SCC models.

This disorder is reflected in the EPR spectra. All the spectra are reminiscent of Type 2 copper centers containing a square planar copper coordinated by nitrogen and oxygen ligands. In these systems, $g_\perp$ is less than $g_\parallel$ and $A_\parallel$ is greater than 0.014 cm^{-1} (Figure 3-44-Figure 3-47).[35-36] Native Cu,Zn SODs have been reported with a rhombic copper, $g_\parallel$ ~2.26, and $A_\parallel$ between 0.014 and 0.016 cm^{-1}.[37-38] Both axial and rhombic features were fit in the 3SCC spectra. All homotrimers fit to a single axial species with $A_\parallel$ between 0.0150 and 0.0170 cm^{-1} and $g_\parallel$ ~2.27. The heterotrimers, however, typically fit best to a mixture of two species. The exceptions being $Asp_2{}^dHis_3{}^a$ and $His_3{}^dHis_1{}^a$. The parameters fit to all these peptides did not vary greatly amongst the different species. All had $g_x \approx g_y \approx 2.05$, g_z ~2.27, and $A_\parallel$ between 0.0140 and 0.0180 cm^{-1}, except one of two species of $His_2{}^dHis_1{}^a$, $Glu_1{}^dHis_3{}^a$, and $Glu_2{}^dHis_3{}^a$ in which g_z was ~2.20. These parameters are relatively close to the native enzyme, but do reflect disorder in the system as multiple species are observed.

The Cu(I) system also reflects this disorder. The intensity of the pre-edge transition of the XANES spectrum is less than was observed for Cu(I) bound to TRI $His_3{}^a$ (Figure 3-62-Figure 3-65).[19] This is indicative of a higher coordination number, though 4-coordinate Cu(I) is

expected to have little to no pre-edge features.[39] Thus, there is likely a mixture of three- and four-coordinate Cu(I) in these systems. The His_4 systems in particular have a significant reduction in Cu(I) pre-edge intensity. Interestingly, there is no change in the edge energy with modifications to the His_3^a site. It was previously observed with 3SCC models of Cu NiR that the edge energy correlated with activity.[19, 40-41] These studies were all performed at pH 5.9 and by increasing the pH to 7.5 this relationship was lost. The intensity of this pre-edge is related to factors including structure, ligand environment, and ligand orbital overlap. These results contradict our previously published work in which constructs with reduced steric bulk were able to coordinate Cu(I) in a linear geometry with two His ligands.[41] At pH 7.5, no linear coordination environments were observed, both based on the pre-edge intensity, which is expected to be much higher for 2-coordinate copper, and the Cu-ligand distance in the EXAFS region. This may be a result of different geometries afforded by His^d residues or by mixing His ligands between **a** and **d** sites, precluding an opening of this site as was hypothesized at pH 5.9.

The EXAFS analysis of these sites proved to be just as disordered as the Cu(II) spectroscopy. There was no single best fit for any spectra presented herein. Statistically better fits were achieved with 4-coordinate models than with 3-coordinate models, but all fits underestimated the intensity of the first shell scatterer. Fits with 1-3 His residues were all attempted but only the two best fits are displayed above (Figure 3-48-Figure 3-61). It is possible that this disorder in coordination number is exacerbated by non-equivalent His ligand distances. The fits have all assumed that the His ligands are at an equivalent distance, but this may not be true. With a mixture of **a** and **d** layer His residues or even a mix of His and carboxylate residues, there may be multiple coordinated His residues at different distances. Computational limits prevent the modeling of these interactions which may contribute to poor fit quality in both the first shell and the backscattering. Thus, no conclusive coordination environments can be determined solely from this data for all trimers except $Glu_3^dHis_3^a$.

The $Glu_3^dHis_3^a$ homotrimer fit best not to a His based Cu(I) environment but instead to a Cys based Cu(I) environment. Previous investigations into Cu(I)-Cys_3^a systems by Dr. Mocny showed that a binuclear copper center is formed with Cu-S distances of ~2.2 Å and a Cu-Cu distance of ~2.6 Å.[1] The $Glu_3^dHis_3^a$ homotrimer also contains a Cys_3^d site for Pb(II) coordination and best fit to a ligand environment like the $Cu(I)_2Cys_3^a$ spectrum (Figure 3-61). It is important to note that a fit to this ligand environment was attempted for all peptides but resulted in a Cu-S

distance of ~2 Å which better agreed with a N/O environment. Thus, this was the only case where the Cu(I) ion bound to the Cys_3^d site rather than the intended transition metal site. Pb(II) binding to $(Cys_3^d)Glu_3^dHis_3^a$ was found to be competitive between the two metal binding sites. As previously described, the addition of Co(II) resulted in Pb(II) binding solely to the sulfur site. This was attributed to the relative affinity of Co(II) for the N/O site over the S site, forcing Pb(II) to bind to the sulfur site. Cu(I), however, will also bind to sulfur-rich sites with high affinity. Thus, if Pb(II) binds competitively between the two sites, Cu(I) does not have a strong enough preference to force the Pb(II) ion into a single site. This was not observed for the Asp containing peptides or for the heterotrimer containing a single glutamate residue which all fit best to His-containing models. Cu(I) was not found to bind to the sulfur layer if an apo transition metal site was present[1] and no perturbation to the Pb-S_3 signal was observed for these peptides (discussed in Chapter 5). The Cu(I)-S_3 coordination observed for $Glu_3^dHis_3^a$ is unique to this trimer and presents the only case observed thus far with interference between the two metal binding sites.

Conclusions

In this chapter, I have shown spectroscopic evidence for the coordination environments of Co(II), Zn(II), and Cu(I/II) to a transition metal binding site within Pb(II)-scaffolded homo- and heterotrimeric systems. First, this work showed that Pb(II) still binds solely to the Cys_3 site with additional histidine residues at a distant transition metal site though it is able to bind to a $Glu_3^dHis_3^a$ site. The addition of a transition metal with relatively low affinity for the Cys_3 site (Co(II)) forces the Pb(II) to bind only to the sulfur site as observed by ^{207}Pb NMR and Co(II) binding affinities, though a transition metal with higher relative affinity for the sulfur site than Co(II) (Cu(I)) does not ensure that all Pb(II) binds to the sulfur site as observed by Cu(I) XAS. The Co(II) spectroscopy further showed that there is no difference in binding between Cys^a and Cys^d Pb(II) site peptides, allowing for direct comparison of previous work done by Dr. Mocny to the work described herein. The UV-visible spectra of Co(II) bound to $Asp_x^dHis_3^a$ and $Glu_x^dHis_3^a$ systems showed similar peak shapes for Glu and Asp heterotrimers, though all Glu transitions were at lower energy. The $Glu_3^dHis_3^a$ heterotrimer also showed a splitting of the peaks indicating a lower symmetry environment. Co(II) EPR also showed that the Glu based systems have much more similar coordination environments than the Asp based trimers do. XAS agreed with UV-visible spectroscopy in coordination number assignment for 5-coordinate heterotrimers and 6-

coordinate homotrimers. Thus, an asymmetric peptide scaffold does induce asymmetry in transition metal binding.

This asymmetry was not reflected in Zn(II) XAS. All Zn(II) spectra remained 4-coordinate regardless of the ligand environment or pH (7.5 or 9.5) with equally good fits to 2 or 3 His ligands. The unchanging coordination number of Zn(II) is not unexpected given it is a d_{10} ion, but this work does prove that Co(II) is not always a faithful probe of Zn(II). Further characterization of the Zn(II) center is described in Chapter 4 as it relates to CA activity. While this work does not provide definitive evidence for the Zn(II) environment in these peptides, the activity is nevertheless affected by the heterotrimeric ligand environments though coordination number is unchanged.

Cu(II) spectroscopy showed that all homo- and heterotrimers described herein are more likely $His_3(OH_2)$ coordinated than $His_2(OH_2)_2$ coordinated as determined by the energy of the d-d transition. There is disorder in these heterotrimers as well, with multiple species observed in the EPR spectra. All parameters agree well with native Cu,Zn SOD and the Type 2 copper center in NiR except for a few species with a lower $g_{\|}$ than was reported in the native enzymes. Disorder was also observed in the Cu(I) XAS spectra, where a single best fit was not observed. All peptides fit equally well to 3- and 4-coordinate Cu(I) with an average bond distance intermediate to previously described 3-coordinate Cu(I) and expected 4-coordinate systems. Thus, an asymmetric peptide scaffold can induce asymmetry in transition metal coordination as observed in the Co(II) system, but these scaffolds are unable to induce only a single ligand environment as observed by the disorder in XAS of the Zn(II) and Cu(I) systems. Copper binding is further explored in Chapter 5 as it relates to SOD activity.

References

1. Mocny, C. S. Ph.D. Dissertation, Examining the metal selectivity of thiol rich de novo designed peptides as a strategy to make asymmetric alpha- helical protein assemblies. 2016.

2. Zastrow, M. L. De novo designed metalloenzymes: structural stabilization and hydrolytic catalysis in a family of α-helical coiled coils. 2013.

3. Zastrow, M. L.; Peacock, A. F.; Stuckey, J. A.; Pecoraro, V. L., Hydrolytic catalysis and structural stabilization in a designed metalloprotein. *Nat. Chem.* **2011,** *4* (2), 118-23.

4. Maren, T. H., Carbonic Anhydrase: Chemistry, Physiology, and Inhibition. *Physiol. Rev.* **1967,** *47*, 597-781.

5. Hakansson, K.; Carlsson, M.; Svensson, L. A.; Liljas, A., Structure of Native and Apo Carbonic Anhydrase II and Structure of Some of Its Anion-Ligand Complexes. *J. Mol. Biol.* **1992,** *227*, 1192-1204.

6. Kiefer, L. L.; Paterno, S. A.; Fierke, C. A., Hydrogen Bond Network in the Metal Binding Site of Carbonic Anhydrase Enhances Zinc Affinity and Catalytic Efficiency. *J. Am. Chem. Soc.* **1995,** *117* (26), 6831-6837.

7. Krebs, J. F.; Ippolito, J. A.; Christianson, D. W.; Fierke, C. A., Structural and Functional Importance of a Conserved Hydrogen Bond Network in Human Carbonic Anhydrase II. *The Journal of Biological Chemistry* **1993,** *268* (36), 27458-27466.

8. Liang, Z.; Xue, Y.; Behravan, G.; Jonsson, B.-H.; Lindskog, S., Importance of the conserved active-site residues Try7, Glu106 and Thr199 for the catalytic function of human carbonic anhydrase II. *Eur. J. Biochem.* **1993,** *211* (3), 821-827.

9. Gleason, J. E.; Galaleldeen, A.; Peterson, R. L.; Taylor, A. B.; Holloway, S. P.; Waninger-Saroni, J.; Cormack, B. P.; Cabelli, D. E.; Hart, P. J.; Culotta, V. C., Candida albicans SOD5 represents the prototype of an unprecedented class of Cu-only superoxide dismutases required for pathogen defense. *Proc. Natl. Acad. Sci. U. S. A.* **2014,** *111* (16), 5866-5871.

10. Zastrow, M. L.; Pecoraro, V. L., Influence of active site location on catalytic activity in de novo-designed zinc metalloenzymes. *J. Am. Chem. Soc.* **2013,** *135* (15), 5895-903.

11. Kerfeld, C. A.; Yoshida, S.; Tran, K. T.; Yeates, T. O.; Cascio, D.; Bottin, H.; Berthomieu, C.; Sugiura, M.; Boussac, A., The 1.6 Å resolution structure of Fe-superoxide dismutase from the thermophilic cyanobacterium Thermosynechococcus elongatus. *J. Biol. Inorg. Chem.* **2003,** *8* (7), 707-714.

12. Mathieu, E.; Tolbert, A. E.; Koebke, K. J.; Tard, C.; Iranzo, O.; Penner-Hahn, J.; Policar, C.; Pecoraro, V. L., Rational De Novo Design of a Cu-Metalloenzyme for Superoxide Dismutation. *Chem.--Eur. J.* **2019,** *26*, 249-258.

13. *Fmoc Solid Phase Peptide Synthesis: A Practical Approach*. 2 ed.; Oxford University Press: New York, 2000.

14. Hendrich, M. P. *SpinCount*.

15. George, G. N.; Pickering, I. J. EXAFSPAK. http://ssrl.slac.stanford.edu/~george/exafspak/exafs.htm.

16. Rehr, J. J.; Kas, J. J.; Vila, F. D.; Prange, M. P.; Jorrissen, K., Recent developments in X-ray absorption spectroscopy. *Phys. Chem. Chem. Phys.* **2010,** *12* (21), 5503-5513.

17. Dimakis, N.; Bunker, G., Group-fitted ab initiosingle- and multiple-scattering EXAFS Debye-Waller factors. *Physical Review B* **2002,** *65* (20), 201103.

18. Weng, T. C.; Waldo, G. S.; Penner-Hahn, J. E., *Journal of Synchrotron Radiation* **2005,** *12*, 506-510.

19. Yu, F. De novo designed metallopeptides with a type 2 copper center : a structural and functional model for copper nitrite reductase by. University of Michigan, 2014.

20. Yu, F.; Penner-Hahn, J. E.; Pecoraro, V. L., De novo-designed metallopeptides with type 2 copper centers: modulation of reduction potentials and nitrite reductase activities. *J. Am. Chem. Soc.* **2013,** *135* (48), 18096-107.

21. Lindskog, S., Interaction of Cobalt (II)-Carbonic Anhydrase with Anions. *Biochemistry* **1966,** *5* (8), 2641-2646.

22. Avvaru, B. S.; Arenas, D. J.; Tu, C.; Tanner, D. B.; McKenna, R.; Silverman, D. N., Comparison of solution and crystal properties of Co(II)-substituted human carbonic anhydrase II. *Arch. Biochem. Biophys.* **2010,** *502* (1), 53-9.

23. Scarpellini, M.; Wu, A. J.; Kampf, J. W.; Pecoraro, V. L., Corroborative models of the cobalt(II) inhibited Fe/Mn superoxide dismutases. *Inorg. Chem.* **2005,** *44* (14), 5001-5010.

24. Vallee, B. L., In *Newer Trace Elements in Nutrition*, Mertz, W.; Cornatzer, W. E., Eds. Dekker: New York, 1971.

25. Maret, W.; Vallee, B. L., Cobalt as Probe and Label of Proteins. *Methods Enzymol.* **1993,** *226* (C), 52-71.

26. Vallee, B. L., Cobalt substituted zinc metalloenzymes. In *Met. Ions Biol. Syst.*, 1973; Vol. 40.

27. Vallee, B. L.; Rupley, J. A.; Coombs, T. L.; Neurath, H., The Role of Zinc in Carboxypeptidase. *J. Biol. Chem.* **1960,** *235* (1), 64-69.

28. Prenesti, E.; Daniele, P. G.; Prencipe, M.; Ostacoli, G., Spectrum–structure correlation for visible absorption spectra of copper(II) complexes in aqueous solution. *Polyhedron* **1999,** *18*, 3233–3241.

29. Strange, R. W.; Antonyuk, S. V.; Hough, M. A.; Doucette, P. A.; Valentine, J. S.; Hasnain, S. S., Variable metallation of human superoxide dismutase: atomic resolution crystal structures of Cu-Zn, Zn-Zn and as-isolated wild-type enzymes. *J. Mol. Biol.* **2006,** *356* (5), 1152-62.

30. Perry, J. J.; Shin, D. S.; Getzoff, E. D.; Tainer, J. A., The structural biochemistry of the superoxide dismutases. *Biochim. Biophys. Acta* **2010,** *1804* (2), 245-62.

31. Bannister, J. V.; Bannister, W. H.; Rotilio, G., Aspects of the Structure, Function, and Applications of Superoxide Dismutas. *Critical Reviews in Biochemistry* **1987,** *22* (2), 111-180.

32. Hart, P. J.; Balbirnie, M. M.; Ogihara, N. L.; M., N. A.; Weiss, M. S.; Valentine, J. S.; Eisenberg, D., A Structure-Based Mechanism for Copper-Zinc Superoxide Dismutase. *Biochemistry* **1999,** *38*, 2167-2178.

33. Miller, A. F., Superoxide dismutases: active sites that save, but a protein that kills. *Curr. Opin. Chem. Biol.* **2004,** *8* (2), 162-8.

34. Cardoso, R. M.; Silva, C. H.; Ulian de Araujo, A. P.; Tanaka, T.; Tanaka, M.; Garratt, R. C., Structure of the cytosolic Cu,Zn superoxide dismutase from Schistosoma mansoni. *Acta Crystallogr. D Biol. Crystallogr.* **2004,** *60* (Pt 9), 1569-78.

35. Solomon, E. I.; Heppner, D. E.; Johnston, E. M.; Ginsbach, J. W.; Cirera, J.; Qayyum, M.; Kieber-Emmons, M. T.; Kjaergaard, C. H.; Hadt, R. G.; Tian, L., Copper Active Sites in Biology. *Chem. Rev.* **2014,** *114*, 3659-3853.

36. Solomon, E. I.; Sundaram, U. M.; Machonkin, T. E., Multicopper Oxidases and Oxygenases. *Chem. Rev. (Washington, DC, U. S.)* **1996,** *96*, 2563−2605.

37. Tibell, L.; Aasa, R.; Marklund, S. L., Spectral and Physical Properties of Human Extracellular Superoxide Dismutase: A Comparison with CuZn Superoxide Dismutase. *Arch. Biochem. Biophys.* **1993,** *304* (2), 429-433.

38. Haberland, A.; Mader, K.; Stosser, R.; Schimke, I., Comparison of malondialdehyde and hydrogen peroxide modified CuZnSOD by EPR spectroscopy. *Agents Actions Suppl.* **1993,** *40*, 166-170.

39. Sarangi, R. Introduction to X-ray Absorption Near Edge Spectroscopy (XANES). https://www-ssrl.slac.stanford.edu/conferences/workshops/srxas2011/presentations/sarangi_xanes_2011.pdf.

40. Koebke, K. J.; Yu, F.; Van Stappen, C.; Pinter, T. B. J.; Deb, A.; Penner-Hahn, J. E.; Pecoraro, V. L., Methylated Histidines Alter Tautomeric Preferences that Influence the Rates of

Cu Nitrite Reductase Catalysis in Designed Peptides. *J. Am. Chem. Soc.* **2019,** *141* (19), 7765-7775.

41. Koebke, K. J.; Yu, F.; Salerno, E.; Van Stappen, C.; Tebo, A. G.; Penner-Hahn, J. E.; Pecoraro, V. L., Modifying the Steric Properties in the Second Coordination Sphere of Designed Peptides Leads to Enhancement of Nitrite Reductase Activity. *Angew. Chem. Int. Ed. Engl.* **2018**.

Chapter 4 Hydrolytic Catalysis Within Self-Assembling Asymmetric Scaffolds

Introduction

De novo protein design has been used to investigate metal binding environments of native proteins. Through step-wise inclusion of active site residues, one can imagine building, from scratch, a metalloenzyme with comparable activity to a native protein with a fundamental understanding of the properties leading to this activity. In the Pecoraro group, work has been focused on the construction of enzymes essential for human health that perform at diffusion limited rates. By focusing on enzymes of this caliber, we aim to elucidate every aspect of a protein that allows for maximum efficiency. This begins with construction of the first coordination sphere of the catalytic metal and expands to secondary sphere interactions.

One such enzyme is zinc carbonic anhydrase which catalyzes the interconversion of carbon dioxide and carbonate at diffusion limited rates (Equation 4-1). The primary coordination sphere of the zinc consists of three histidine residues and a solvent molecule in a pseudotetrahedral arrangement (Figure 4-1).[1] The histidine residues are coordinated via two epsilon and one delta nitrogen. The solvent molecule is further coordinated via hydrogen bonds to a threonine residue and additional solvent molecules in a water channel. This water channel provides a solvent exposed route for substrate and product to travel to and from the buried active site. The second coordination sphere threonine residue plays an important role not only by facilitating transport of solvent and protons through the water channel, but also serves as an acid/base catalyst to perturb the pK_a of the water bound to zinc.[2-4]

Equation 4-1 Reaction catalyzed by carbonic anhydrase

$$CO_2 + H_2O \rightleftharpoons H_2CO_3$$

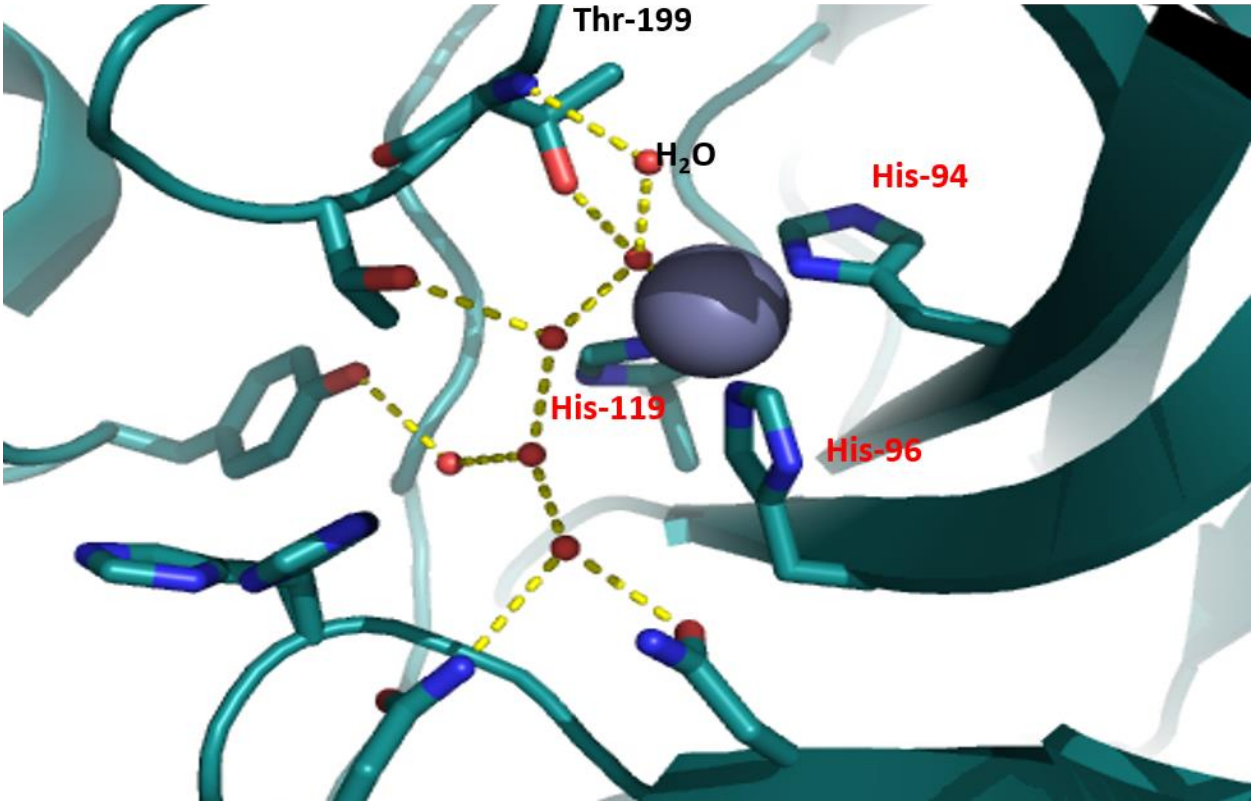

Figure 4-1 Active site of CA (PDB: 2CBA)[1]

The secondary sphere threonine residue (T199) was found to be essential to the efficiency of CA. A Thr to Ala mutation (T199A) was incorporated to remove the side chain hydrogen bonding interaction while minimally disrupting the sterics of the active site. The T199A mutation resulted in ~100 fold loss in activity and an increase in the pKa of the active site of about 2 pH units, from 6.8 to 8.5.[5-7] Thus, while this threonine does not play a direct role in the hydrolysis reaction, it does influence the active site to allow for a more conducive reaction environment.

These electrostatic interactions are required for optimal carbonic anhydrase activity. The mechanism of carbonic anhydrase may not require changing coordination number or environment of the metal center as many redox enzymes do. Some mechanisms propose that the zinc ion remains four-coordinate throughout the catalytic cycle and all substrate interactions are mediated by the zinc coordinated solvent molecule. Carbon dioxide enters the active site and hydrogen bonds to the backbone nitrogen of T199, an interaction that is not disrupted by T199 mutations (Figure 4-2). The first coordination sphere solvent molecule, as a deprotonated hydroxide, is then able to nucleophilically attack the carbon to form carbonate. Carbonate binds

very weakly to this site and dissociates quickly with a new water molecule coordinating the zinc. The rate limiting step of this reaction is actually the deprotonation of this new water by H64, which acts as a proton shuttle by flipping between active site and bulk solvent orientations. The ability of the water to attack CO_2, therefore, relies heavily upon the hydrogen bond to T199.

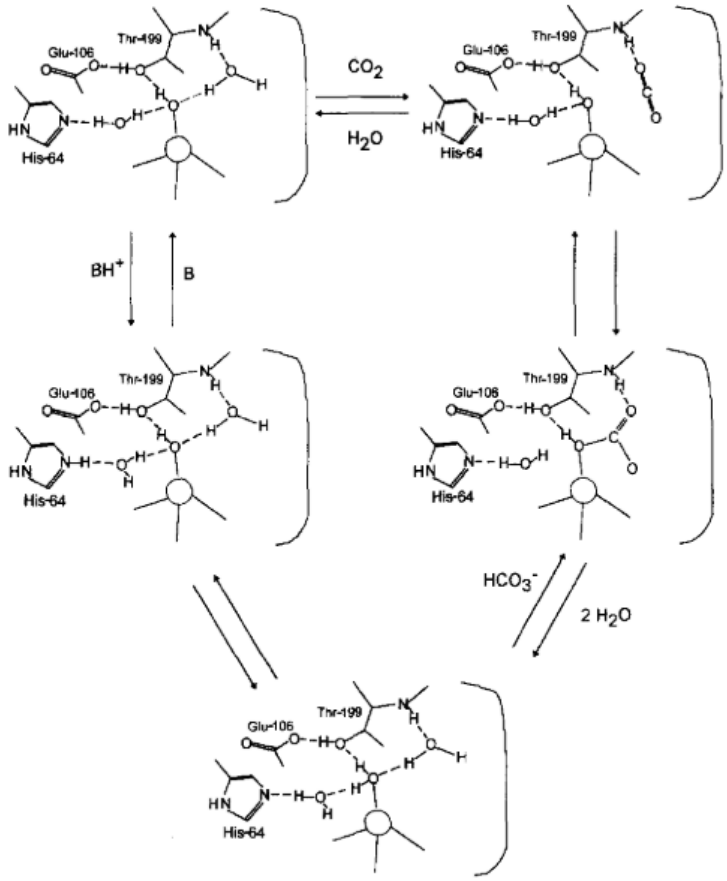

Figure 4-2 Proposed mechanism of CO_2 hydration by carbonic anhydrase in which the Zn(II) coordination number does not change[3]

An alternate mechanism proposes an increase in the Zn(II) coordination number. In this mechanism, the carbonate anion binds as a bidentate ligand before being displaced by a solvent molecule (Figure 4-3).[2] This mechanism is the same as the former in all other steps.

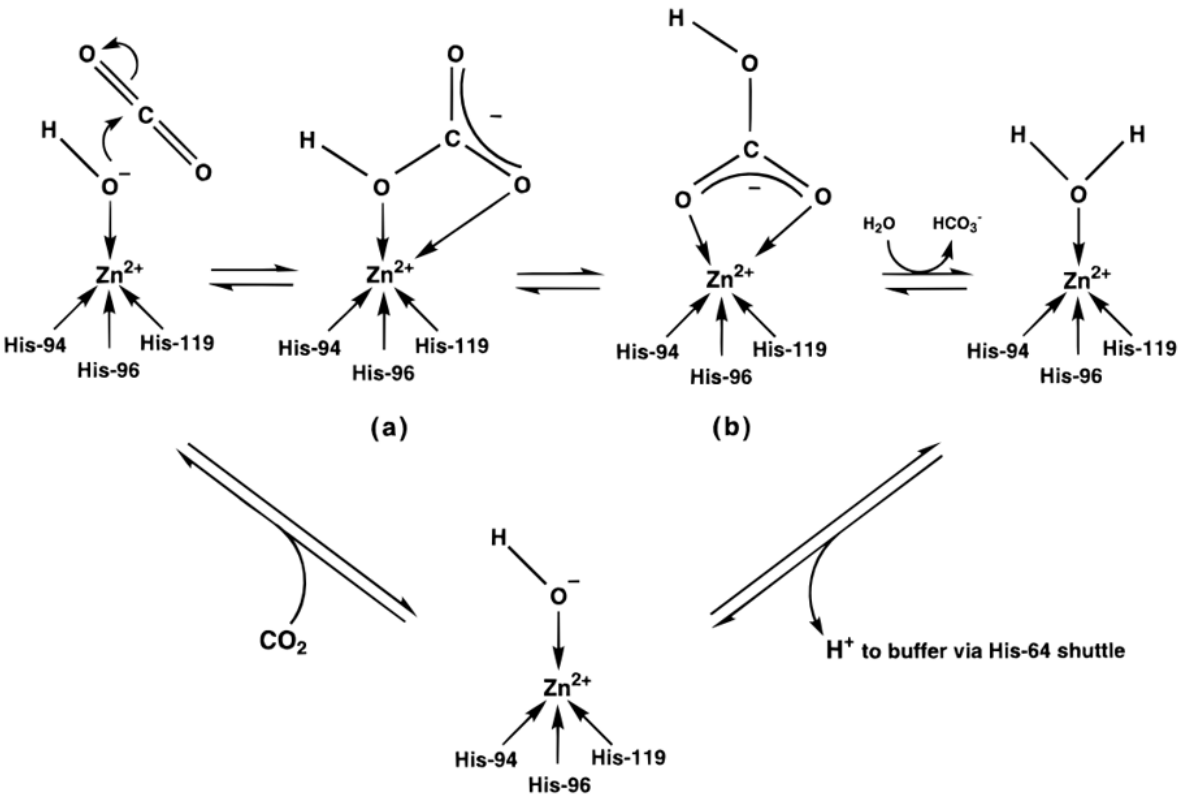

Figure 4-3 Proposed mechanism for CA in which the Zn(II) ion increases in coordination number.[2]

Further investigation into T199 has shown that catalysis does not rely on simply having a polar residue in that position, but that hydrogen bonding is necessary. As previously mentioned, replacement of T199 with alanine resulted in an increase in the pKa of the zinc bound hydroxide, leading to a loss in efficiency of ~100 fold. The Fierke and Christianson groups have investigated several more T199 mutations, including Cys, Asp, and Glu.[2, 8-9] Crystallographic and spectroscopic studies of these mutants showed that zinc remains four coordinate, but the fourth ligand is the T199 residue rather than a solvent molecule. This decreases the efficiency of the native enzyme by ~1000 fold for T199C and up to 3000 fold for T199E and T199D. Interestingly, T199H does not directly coordinate the zinc, but significant steric constraints result in an efficiency loss of ~5500 fold. Thus, direct coordination of a fourth protein ligand or steric hindrance of the active site precludes activity as the zinc can no longer coordinate the hydroxide for efficient catalysis.

Previous work in the Pecoraro lab has focused on the design and characterization of the primary coordination sphere of CA. Dr. Melissa Zastrow successfully constructed a $His_3(H_2O/OH^-)$ Zn(II) binding site in the TRI peptide. This site was located at the 23rd position,

the most C-terminal **a** site of the TRI peptide (Figure 4-4). To aid in stability, a Cys_3^a site was also included for Hg(II) binding.

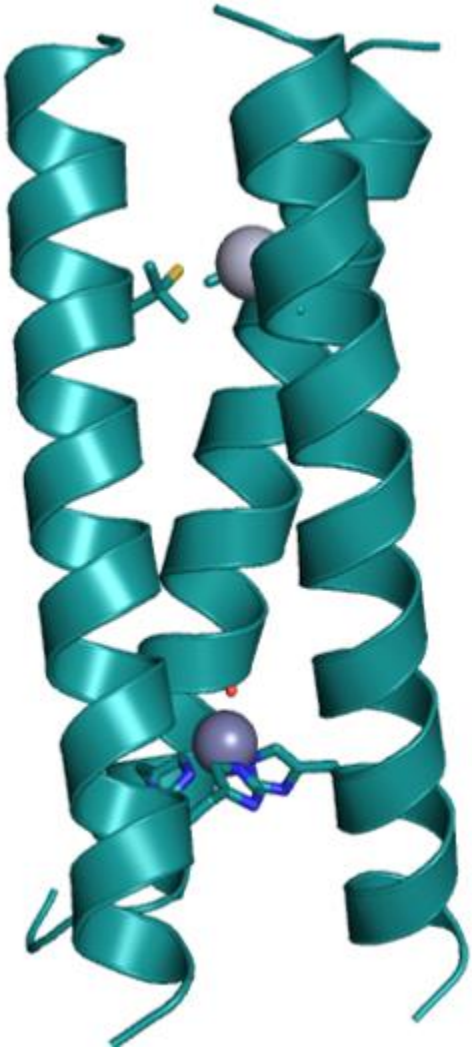

Figure 4-4 Crystal structure of TRI His_3^a with N-terminal Hg(II) site and C-terminal Zn(II) site (PDB: 3PBJ)[10]

To avoid confusion with the GR peptides described later in this work, this peptide will be described as TRI His_3^a. Zn(II) binds pseudotetrahedrally in this site with all histidines coordinated via the epsilon nitrogen, while Hg(II) binds in a trigonal planar environment created by three cysteine thiolates. Through a battery of assays, Dr. Zastrow concluded that the incorporation of the Cys_3^a site did not affect the His_3^a site, so it will not be discussed further in this work, although it should be noted that this observation suggested that a remote heavy metal bound to cysteines such as Pb(II) would similarly have no effect on catalysis.[11]

Zinc affinity was determined by zincon competitive titrations at both pH 7.5 and 9.0 with sub-mM affinity observed at both pH values. Kinetic analysis of CO_2 hydration found that this

construct is the best aqueous model of this reaction, with a rate of $1.8x10^5$ $M^{-1}s^{-1}$ at pH 9.5, only ~400 fold slower than the native enzyme. More robust studies of this active site were performed via an ester hydrolysis assay, which is a secondary function of the native enzyme. P-nitrophenyl acetate (pNPA) is hydrolytically cleaved to form p-nitrophenol (pNP) and acetate (Figure 4-5). At pH 9.5, a catalytic efficiency of 23.3 $M^{-1}s^{-1}$ was observed, with k_{cat}=$40x10^{-3}$ s^{-1} and k_M=1.7 mM.[10] Dr. Zastrow also investigated the effect of active site position on catalytic efficiency. Constructs with the His_3 site in an **a** layer towards the N-terminus (TRI L9H) and in an interior **d** layer (L19H) were studied. Interestingly, k_{cat} and k_M were individually affected by the change in position, but overall catalytic efficiency remained unchanged.[12]

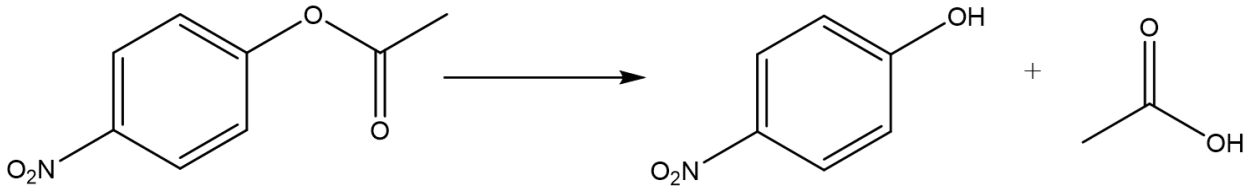

Figure 4-5 Cleavage of pNPA to pNP and acetate

This ester hydrolysis activity observed in these constructs was pH dependent, with a pK_a of 8.8 for the synthetic construct TRI His_3^a vs a pK_a of 6.8 for the native enzyme. As was discussed above, the removal of the hydrogen bond afforded by T199 resulted in a similar pK_a shift. The next step, therefore, is to introduce a hydrogen bonding residue to model interaction of T199 on the native enzyme. It was hypothesized that decreasing the active site pK_a of the TRI system would result in ~100 fold increase in activity as was observed in the native enzyme. Dr. Zastrow explored this possibility by introducing an Asp_3 layer in the **d** site adjacent to the His_3^a layer ($Asp_3^dHis_3^a$). There was no improvement to the catalytic efficiency with the introduction of 3 aspartate residues (24.2 $M^{-1}s^{-1}$). This may be due to undesired interactions of the aspartate residues rather than the intended hydrogen bonding interaction. Potential coordination environments for this system are discussed further in this work. This model was limited in that all potential hydrogen bonding residues had to be incorporated three-fold. With an asymmetric scaffold, however, one can introduce a hydrogen bonding residue whose side chain has a higher chance of coordinating in either the primary or secondary coordination sphere.

Dr. Virginia Cangelosi designed several models of CAII in the helical bundle protein α_3D. This protein is inherently asymmetric which allowed for the incorporation of only a single hydrogen bonding residue. The initial His_3 model did not perform as well as the TRI model

characterized by Dr. Zastrow, with a pK_a of 9.4 and catalytic efficiency of CO_2 hydration an order of magnitude lower than TRI His_3^a.[13] To improve upon this, serine and threonine residues were added at several different positions in proximity to the His_3 site, but no improvement in catalysis was observed. Thus, Dr. Catherine Mocny aimed to utilize an asymmetric TRI scaffold to achieve greater catalytic efficiency.

Dr. Mocny began work on this aim by incorporating Thr residues adjacent to a His_3 site. To accommodate both the Pb(II) site and the Zn(II) site, her work was done in the GR scaffold. The increased scaffold length over the TRI peptide allows for more leucine substitutions in the core of the 3SCC before significant decreases in stability are observed. The nomenclature for peptides described in this chapter follow the same format as in Chapter 3, listing only the mutations from the GR sequence at the transition metal site. Thus, formation of the $Glu_3^dHis_3^a$ homotrimer requires 3 equivalents of the Glu^dHis^a peptide listed in Table 4-1, which has only the Cys^d mutation at the Pb(II) binding site. The alternate homotrimer, His_3^a, is formed from 3 equivalents of the His^a strand, containing both the Ala^a and Cys^d mutations at the Pb(II) binding site. Heterotrimers containing intermediate numbers of Glu resides contain a mixture of these two strands to achieve the desired Glu stoichiometry. The fully selective heterotrimers are induced by the mixed Cys^d and Ala^aCys^d layers at the Pb(II) site from the Glu^dHis^a and His^a strands, respectively. Instances in which Cys^a based systems are used will be noted accordingly.

In order to model T199, Dr. Mocny incorporated a Thr residue in the 26th position, the **d** site N-terminally adjacent to the His^a site (Thr^dHis^a). At pH 9.5 no improvement to catalytic efficiency over Dr. Zastrow's construct was found for $Thr_1^dHis_3^a$ (20.6 $M^{-1}s^{-1}$) and a significant decrease was observed for $Thr_3^dHis_3^a$ (14.8 $M^{-1}s^{-1}$).[11, 14] Given the amphipathic nature of the 3SCC, it was hypothesized that the Thr residue did not achieve the desired rate enhancement since it was likely oriented with the hydroxyl group towards the helical interface and the methyl group in the hydrophobic core, preventing any interaction from occurring.

Heterotrimers containing an aspartate residue (Asp^dHis^a) were then investigated as this amino acid is structurally similar to threonine but contains only terminal oxygen residues so either side chain orientation should provide an oxygen to hydrogen bond the Zn(II)-coordinated solvent molecule. Again, no significant increase in catalytic efficiency was observed for $Asp_3^dHis_3^a$ (24.2 $M^{-1}s^{-1}$).[11] $D_1^dH_3^a$, however, also does not show a significant increase in catalytic efficiency (25.1 $M^{-1}s^{-1}$). Dr. Mocny proposed that, rather than coordinating as a desired

second coordination sphere residue, a chelate ring motif was instead formed. With only a single Asp residue, the Zn(II) was shifting out of the center of the 3SCC towards the strand with the Asp residue and coordinating only one or two His residues (Figure 4-6). These sites are more reminiscent of thermolysin (His_2Asp) or carboxypeptidase A (His_2Asp_1OH).[15-16]

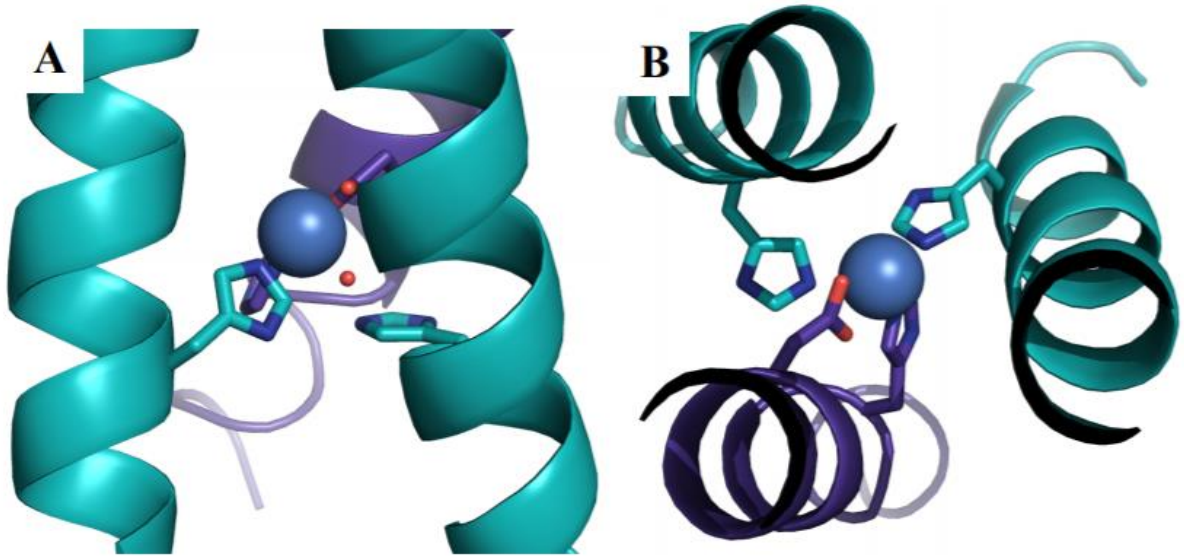

Figure 4-6 Side (a) and top down (b) Pymol models of a proposed His_2Asp_1OH binding environment posited by Dr. Mocny based on the structure 3PBJ. Figure taken from reference[14]

My work aimed to rectify this by lengthening the side chain of the carboxylate residue. The Asp residue was not providing a hydrogen bond, but was instead directly coordinating Zn(II), disrupting the His_3 binding environment. By utilizing a Glu residue instead of an Asp residue, it was hypothesized that the increased side chain length would preclude the formation of such a chelate motif. Thus, the Zn(II) would remain coordinated to three His residues in the center of the 3SCC and the Glu residue would be free to form a hydrogen bond with the Zn(II)-coordinated solvent molecule. The previous chapter described the Co(II) binding environment in these constructs as well as the coordination environment of Zn(II) as measured by X-ray absorption spectroscopy. The cobalt spectroscopy showed that the heterotrimers are likely 5-coordinate with a mix of His and oxygen ligands, while the homotrimer is most likely 6-coordinate with His and oxygen ligands. This proved to be an unfaithful probe of the Zn(II) coordination environment, which was 4-coordinate regardless of the number of carboxylates or the pH (7.5 or 9.5). To build on this analysis, Zn(II) affinities were determined and Michaelis-Menten kinetics of the pNPA ester hydrolysis assay are described. Previous chapters had an

emphasis on the design of heterotrimers and the following work highlights the use of these heterotrimers in catalysis.

*Table 4-1 List of peptide sequences discussed in this chapter with mutations at the lead site in **bold green** and mutations at the transition metal site in **bold red**.*

Peptide	Sequence
His[a]	Ac-G WKALEEK LKA**C**EEK **A**KALEEK LKALEEK **H**KALEEK G-NH_2
Asp[d]His[a]	Ac-G WKALEEK LKA**C**EEK LKALEEK LKA**D**EEK **H**KALEEK G-NH_2
Glu[d]His[a]	Ac-G WKALEEK LKA**C**EEK LKALEEK LKA**E**EEK **H**KALEEK G-NH_2
TRI His[a]	Ac-G WKALEEK LKA**C**EEK LKALEEK **H**KALEEK G-NH_2
TRI L19H	Ac-G WKALEEK LKALEEK LKA**H**EEK LKALEEK G-NH_2
TRI L9H	Ac-G WKALEEK **H**KALEEK LKALEEK LKALEEK G-NH_2
CS L9PenL23H	Ac-E WEALEKK **Pen**AALESK LQALEKK **H**EALEHG-NH_2
GRCS L16CL30H	Ac-E WEALEKK LAALESK **C**QALEKK LQALEKK **H**EALEHG-NH_2

Methods

Peptide synthesis and purification

Peptides were synthesized on a Biotage Initiator+ Alstra peptide synthesizer using Fmoc-rink amide-methylbenzhydrylamine (MBHA) resin. Standard deprotection and coupling protocols with HOBt/HBTU/DIEA were used.[17] Peptides were cleaved from the resin using trifluoroacetic acid, thioanisole, ethanedithiol, and anisole (90:5:3:2) for four hours, precipitated with cold ether, and redissolved in double distilled water. The crude peptide was then lyophilized to dryness. The peptide was purified using a Waters 600 HPLC with a reverse phase C-18 column. A linear gradient from 70% A (0.1% trifluoroacetic acid in double distilled water) 30% B (0.1 % trifluoroacetic acid, 10% double distilled water, 90% acetonitrile) to 20% A/80% B was utilized at a flow rate of 20 mL/min over 35 minutes. ESI-MS was used to confirm the mass of the pure peptide, which was then lyophilized to dryness.

Zn(II) Affinity

Zn(II) affinity was determined by competitive titration with the divalent metal chelator zincon (2- carboxy-2'-hydroxy-5'-(sulfoformazyl)benzene). Zn(II) forms a 1:1 species with zincon (Zi) with an apparent dissociation constant ($K_{d,app}$) of 2.1 x 10^{-6} M at pH 7.5 and 5.88 x 10^{-9} M at pH 9.5.[18] The zinc-zincon (ZnZi) complex has an absorption band at 620 nm with ε=16000 $M^{-1}cm^{-1}$ and the formation or dissolution of this complex was monitored by UV-visible spectroscopy. A lead-zincon complex has a maximum absorbance at 541 nm with an extinction coefficient of

23200 $M^{-1}cm^{-1}$ at pH 7.5 and was not observed in these experiments.[18] The formation of the ZnZi complex was performed by titrating a solution of Zi into a 1 cm pathlength quartz cuvette containing 20 μM trimer, 20 μM $Pb(NO_3)_2$, 10 μM $ZnSO_4$, 0.1 M Na_2SO_4, and 50 mM HEPES, pH 7.5 or CHES pH 9.5. The dissolution of the ZnZi complex was monitored by titration of lead-bound trimer into a 1 cm pathlength quartz cuvette containing 10 μM Zi, 5 μM $ZnSO_4$, 0.1 M Na_2SO_4, and 50 mM HEPES, pH 7.5 or CHES pH 9.5. Both the forward and reverse titrations should result in similar apparent binding constants, indicating an equilibrium has been reached during the titration.

The equilibrium can be expressed as follows:

Equation 4-2

$$Znpep_3Pb + Zi \rightleftharpoons pep_3Pb + ZnZi$$

The apparent dissociation of $ZnPep_3Pb$ can be expressed as:

Equation 4-3

$$K_{d,Znpep3Pb} = \frac{[Znpep_3Pb]}{[pep_3Pb][Zi]}$$

And the apparent dissociation of ZnZi can be expressed as:

Equation 4-4

$$K_{d,ZnZi} = \frac{[ZnZi]}{[Zn][Zi]}$$

These two expressions for the dissociation constants can be combined to form the following equation:

Equation 4-5

$$\frac{K_{d,Znpep3Pb}}{K_{d,ZnZi}} = \frac{[ZnZi][pep_3Pb]}{[Znpep_3Pb][Zi]}$$

The concentrations of each species can be determined via the following relations:

Equation 4-6

$$[pep_3Pb]_T = [pep_3Pb]_F + [Znpep_3Pb]$$

Equation 4-7

$$[Zi]_T = [Zi]_F + [ZnZi]$$

Equation 4-8

$$[Zn]_T = [ZnZi] + [Znpep_3Pb] + [Zn]_F$$

Where $[Zn]_F$ is approximated as 0 as the experimental setup should preclude free zinc in solution.

Rearrangement of these equations (5-7) can be done to substitute for all unknown variables in equation 4, which can then be rearranged to the following quadratic expression:

Equation 4-9

$$[ZnZi]^2\left(k_{d,Znpep3Pb} - k_{d,ZnZi}\right) + [ZnZi](k_{d,ZnZi}[Zn]_T - k_{d,ZnZi}[pep_3Pb]_T - k_{d,Znpep3Pb}[Zn]_T - k_{d,Znpep3Pb}[Zi]_T) + k_{d,Znpep3Pb}[Zn]_T[Zi]_T = 0$$

Where x is either [pep_3Pb] for the titration of peptide into ZnZi or [Zi] for the reverse titration.

Finally, the real solution of equation 8 is substituted into the following equation:

Equation 4-10

$$A_{620\,nm} = \varepsilon * b * [ZnZi]$$

Because all absorbance at 620 nm is attributed to the ZnZi species, the Beer-Lambert law can be applied to determine the concentration of ZnZi at each point in the equation, leaving the final unknown as the dissociation constant of $Znpep_3Pb$, which was fit using Origin.

pNPA esterase assay

The rate of ester hydrolysis was determined by monitoring the production of pNP at 348 nm the isosbestic point for p-nitrophenol and p-nitrophenolate (ε=5000 $M^{-1}cm^{-1}$) at room temperature. A fresh solution of pNPA was prepared daily by diluting a 0.1 M solution of pNPA in acetone to 4.5 mM with doubly distilled water while mixing vigorously. In a 0.1 cm pathlength cuvette, a solution containing 50 mM CHES, pH 9.5, 50 μM trimer, 50 μM $Pb(NO_3)_2$, and 10 μM $ZnSO_4$ was blanked. The excess of peptide was used to ensure that all Zn(II) was bound. Then pNPA was added to a final concentration between 0.06 and 3.5 mM and the change in absorbance was monitored for at least 15 minutes. Control reactions containing 40 μM trimer, 40 μM $Pb(NO_3)_2$, and 50 mM CHES pH 9.5 were similarly monitored which allowed for correction due to baseline spontaneous hydrolysis and hydrolysis due to free imidazole.

Initial rates for the reaction at each substrate concentration were determined from linear fits of plots of concentration of pNP versus time. These initial rates were then plotted as a function of substrate concentration and fit to the Michaelis-Menten equation (Equation 4-11) in GraphPad Prism 8.[19]

Equation 4-11 The Michaelis-Menten equation, where v_0 is the initial rate, V_{max} is the maximum rate at substrate saturation, [S] is substrate concentration, and K_M is the Michaelis constant, or the concentration of substrate at which v is ½ V_{max}

$$v_0 = \frac{V_{max}[S]}{K_M + [S]}$$

Results

Zn(II) Affinity at pH 7.5

The affinity for zinc to His_3^a, $Asp_x^dHis_3^a$, and $Glu_x^dHis_3^a$ peptides was determined by competitive titration with zincon, a zinc chelator at pH 7.5 ($K_d = 2.1x10^{-6}$ M).[18] Previously, the affinities of Asp peptides for Zinc were reported by Dr. Mocny at pH 9.0.[14] As the majority of structural data for both Zn(II) and Co(II) were collected at pH 7.5, affinities were determined at this pH. The His_3^a peptide had an affinity of 250 ± 130 nM at pH 7.5 (Figure 4-7). The affinity at pH 9.0 was 170 ± 100 nM, which is not statistically different (Table 4-2).

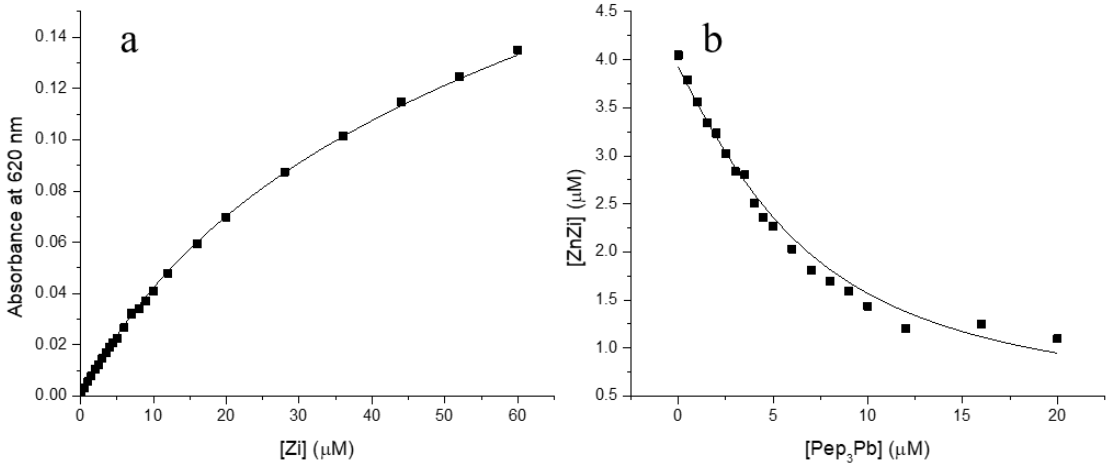

Figure 4-7 (a) Zincon and (b) Pep_3Pb titrations for Zn(II) affinity determination of His_3^a at pH 7.5. Solutions contained either (a) 20 μM Pep_3Pb and 10 μM ZnOAc or (b) 10 μM Zi and 5 μM ZnOAc in 50 mM HEPES pH 7.5.

The $Asp_x^dHis_3^a$ peptides bound Zn(II) with a K_d between 600 and 700 nM with no significant difference between the three. Nominally, $Asp_1^dHis_3^a$ (Figure 4-8) had the tightest Zn(II) affinity, $Asp_2^dHis_3^a$ (Figure 4-9) had the weakest affinity, and the $Asp_3^dHis_3^a$ homotrimer (Figure 4-10) had an intermediate affinity.

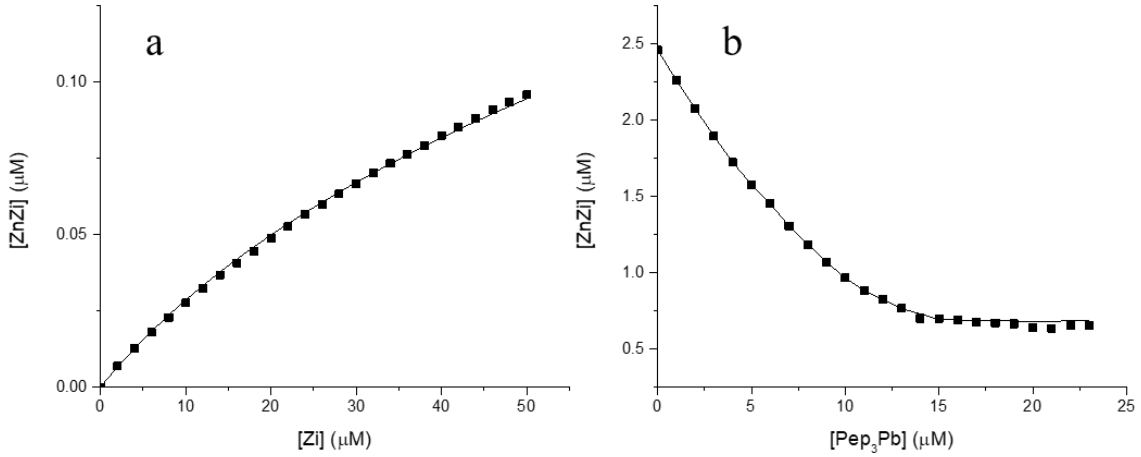

Figure 4-8 (a) Zincon and (b) Pep_3Pb titrations for Zn(II) affinity determination of $Asp_1^dHis_3^a$ at pH 7.5. Solutions contained either (a) 20 μM Pep_3Pb and 10 μM ZnOAc or (b) 10 μM Zi and 5 μM ZnOAc in 50 mM HEPES pH 7.5.

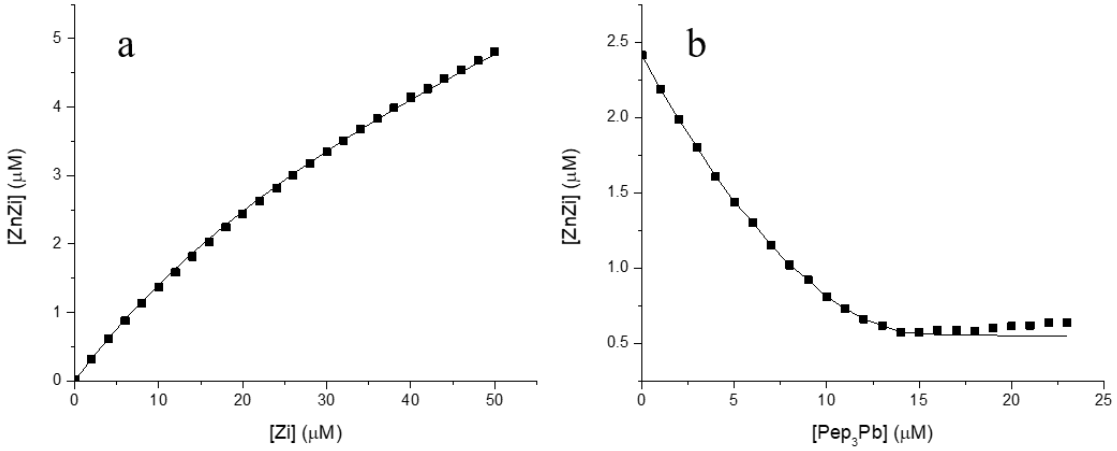

Figure 4-9 (a) Zincon and (b) Pep_3Pb titrations for Zn(II) affinity determination of $Asp_2^dHis_3^a$ at pH 7.5. Solutions contained either (a) 20 μM Pep_3Pb and 10 μM ZnOAc or (b) 10 μM Zi and 5 μM ZnOAc in 50 mM HEPES pH 7.5.

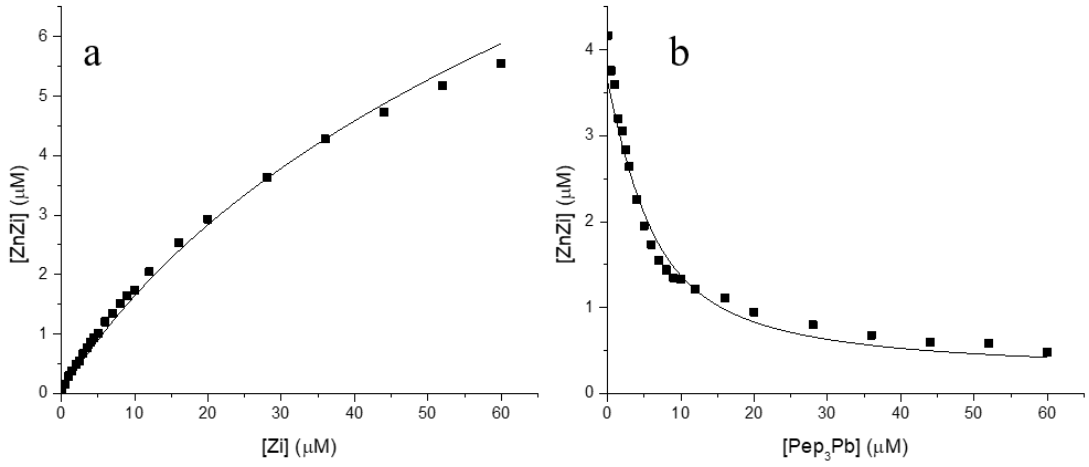

Figure 4-10 (a) Zincon and (b) Pep_3Pb titrations for Zn(II) affinity determination of $Asp_3{}^dHis_3{}^a$ at pH 7.5. Solutions contained either (a) 20 μM Pep_3Pb and 10 μM ZnOAc or (b) 10 μM Zi and 5 μM ZnOAc in 50 mM HEPES pH 7.5.

The Glu heterotrimers bound Zn(II) weaker than the Asp trimers with affinities of 730 ± 120 nM for $Glu_1{}^dHis_3{}^a$ (Figure 4-11) and 830 ± 80 nM for $Glu_2{}^dHis_3{}^a$ (Figure 4-12). The homotrimer, however, bound Zn(II) with a much tighter affinity of 300 ± 80 nM (Figure 4-13).

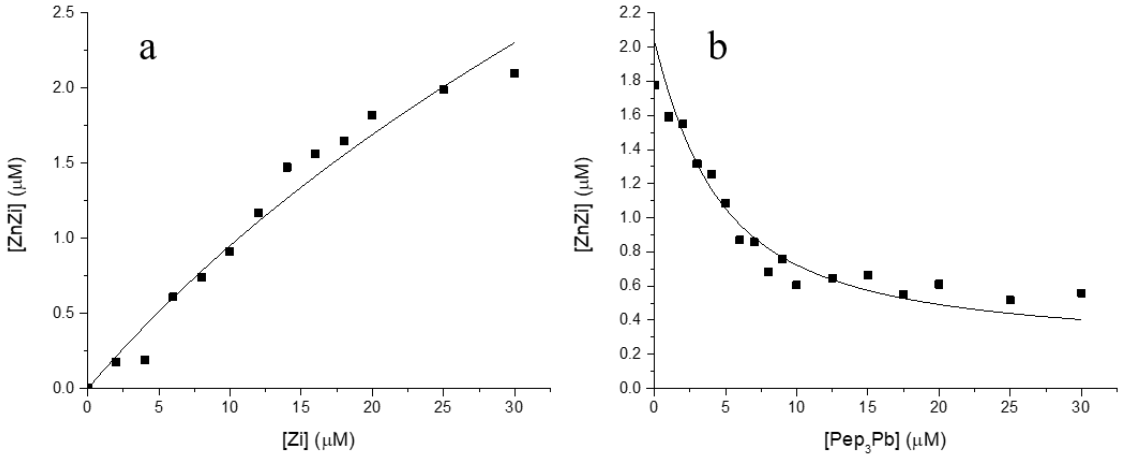

Figure 4-11 (a) Zincon and (b) Pep_3Pb titrations for Zn(II) affinity determination of $Glu_1{}^dHis_3{}^a$ at pH 7.5. Solutions contained either (a) 20 μM Pep_3Pb and 10 μM ZnOAc or (b) 10 μM Zi and 5 μM ZnOAc in 50 mM HEPES pH 7.5.

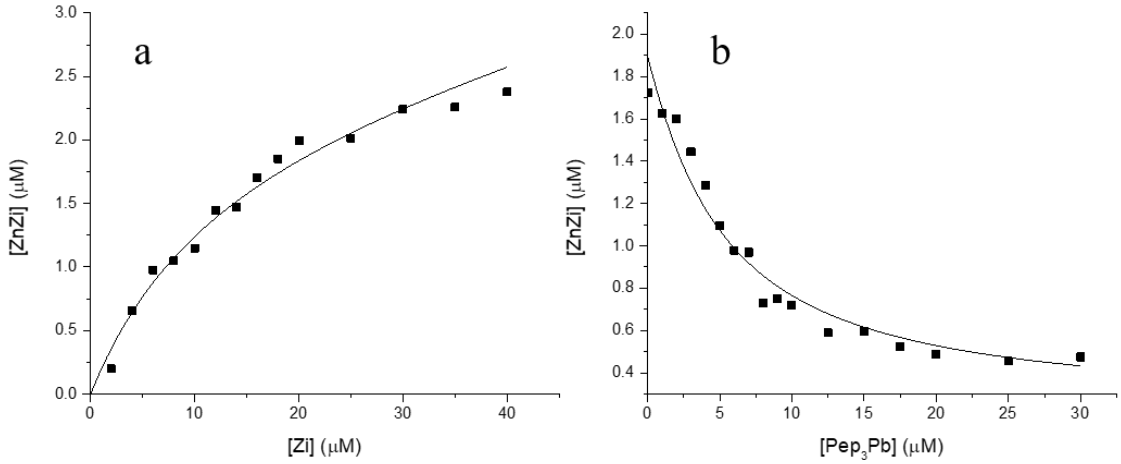

Figure 4-12 (a) Zincon and (b) Pep_3Pb titrations for Zn(II) affinity determination of $Glu_2{}^dHis_3{}^a$ at pH 7.5. Solutions contained either (a) 20 μM Pep_3Pb and 10 μM ZnOAc or (b) 10 μM Zi and 5 μM ZnOAc in 50 mM HEPES pH 7.5.

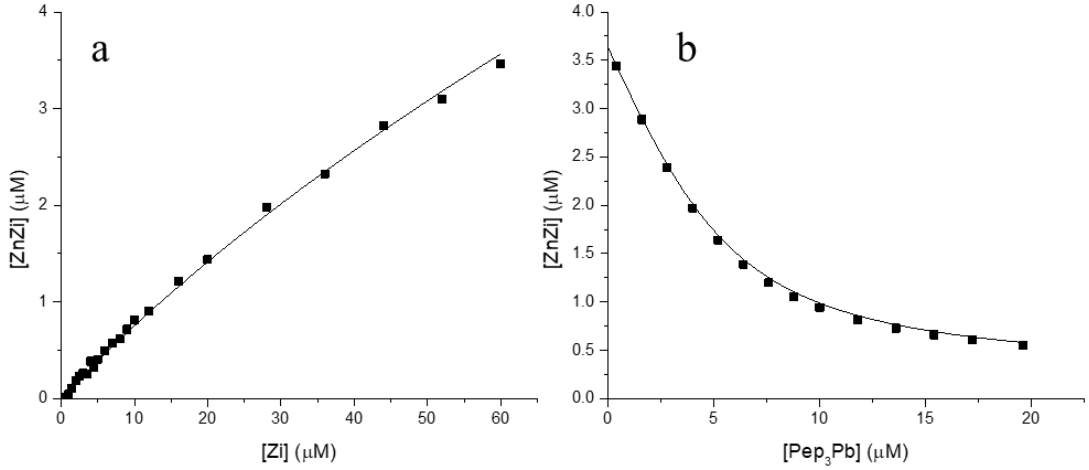

Figure 4-13 (a) Zincon and (b) Pep_3Pb titrations for Zn(II) affinity determination of $Glu_3{}^dHis_3{}^a$ at pH 7.5. Solutions contained either (a) 20 μM Pep_3Pb and 10 μM ZnOAc or (b) 10 μM Zi and 5 μM ZnOAc in 50 mM HEPES pH 7.5.

$His_3{}^a$ and $Glu_3{}^dHis_3{}^a$ do not have statistically different Zn(II) K_d values at pH 7.5, indicating a similar zinc ligand environment. $His_3{}^a$ also does not have a statistically different binding affinity between pH 7.5 and 9.0, so the binding environment is unaffected by pH across this range. The remaining peptides all have similar K_d values, indicating a similar ligand environment.

Zn(II) affinity at pH 9.5

In addition to affinity determinations at pH 7.5, the Zn(II) affinity of these peptides was also determined at pH 9.5 (Zi K_d = 5.88 x 10^{-9} M).[18] Dr. Zastrow determined the affinity of His_3^a and $Asp_3^dHis_3^a$ at pH 9.0, but affinity determinations were not done at pH 9.5 where kinetic analyses were done. At pH 9.5, the affinity of $Asp_3^dHis_3^a$ for Zn(II) is 9.3 ± 1.1 nM (Figure 4-14). This is slightly weaker than the affinity measured by Dr. Zastrow (3.1 ± 1.0 nM), but this may be due to the difference in pH. The $Asp_2^dHis_3^a$ heterotrimer also bound zinc more tightly at pH 9.5, with an affinity of 3.6 ± 0.5 nM (Figure 4-15). The other Asp heterotrimer, $Asp_1^dHis_3^a$, has an affinity of 5.8 ± 0.2 nM at pH 9.5 (Figure 4-16). At pH 7.5, there was no statistical difference in Zn(II) affinity for the $Asp_x^dHis_3^a$ peptides. At pH 9.5, however, the $Asp_2^dHis_3^a$ peptide has the tightest zinc affinity and the homotrimer $Asp_3^dHis_3^a$ has the weakest affinity.

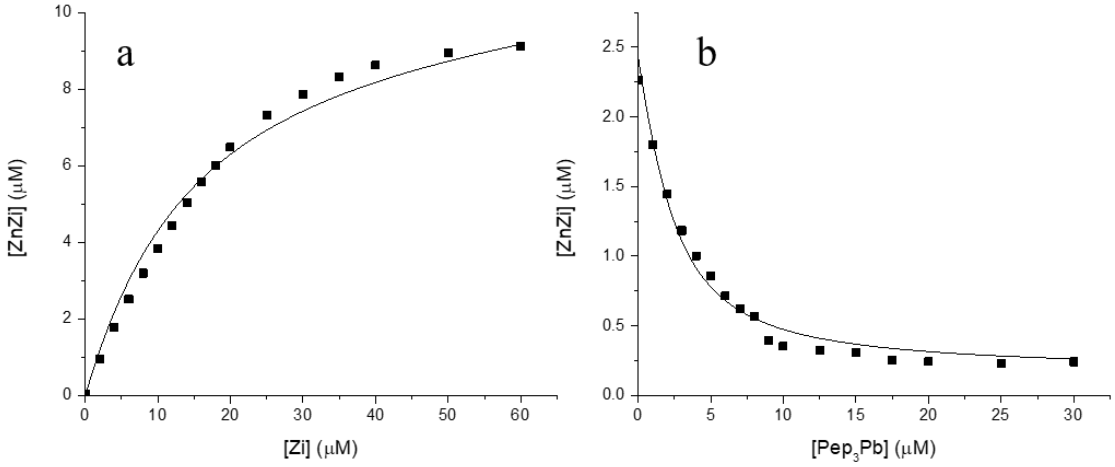

Figure 4-14 (a) Zincon and (b) Pep_3Pb titrations for Zn(II) affinity determination of $Asp_3^dHis_3^a$ at pH 9.5. Solutions contained either (a) 20 μM Pep_3Pb and 10 μM ZnOAc or (b) 10 μM Zi and 5 μM ZnOAc in 50 mM CHES pH 9.5.

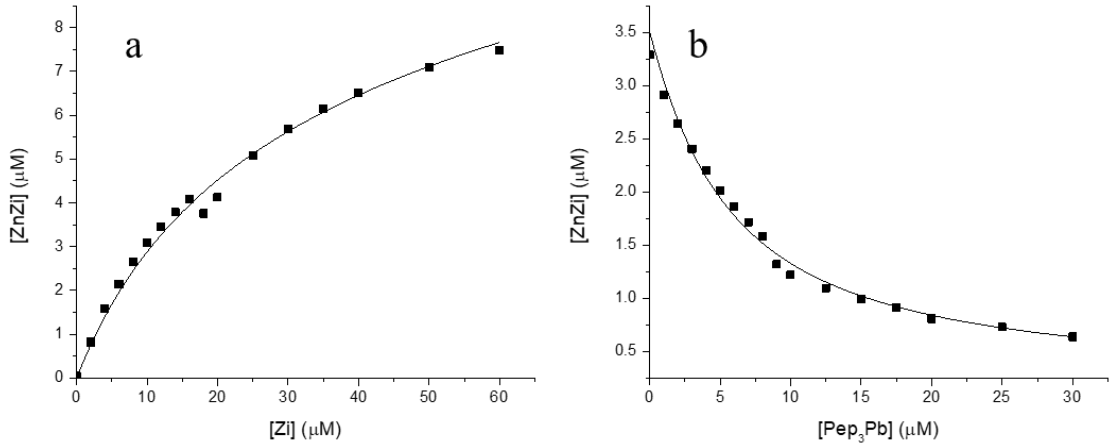

Figure 4-15 (a) Zincon and (b) Pep_3Pb titrations for Zn(II) affinity determination of $Asp_2{}^dHis_3{}^a$ at pH 9.5. Solutions contained either (a) 20 μM Pep_3Pb and 10 μM ZnOAc or (b) 10 μM Zi and 5 μM ZnOAc in 50 mM CHES pH 9.5.

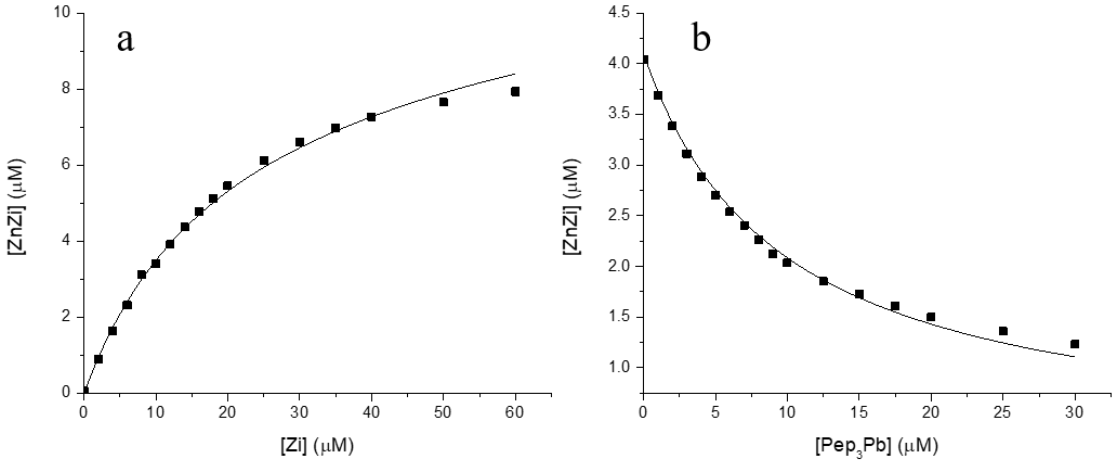

Figure 4-16 (a) Zincon and (b) Pep_3Pb titrations for Zn(II) affinity determination of $Asp_1{}^dHis_3{}^a$ at pH 9.5. Solutions contained either (a) 20 μM Pep_3Pb and 10 μM ZnOAc or (b) 10 μM Zi and 5 μM ZnOAc in 50 mM CHES pH 9.5.

Similarly, the Zn(II) affinity for Glu containing peptides was determined at pH 9.5. For the $Glu_3{}^dHis_3{}^a$ homotrimer, the zinc affinity increased by two orders of magnitude with increased pH to 2.4 ± 1.0 nM (Figure 4-17). The $Glu_2{}^dHis_3{}^a$ heterotrimer had a similar increase in affinity. At pH 9.5, the Zn(II) affinity increased to 7.5 ± 1.1 nM from 830 ± 80 nM at pH 7.5 (Figure 4-18). Lastly, the $Glu_1{}^dHis_3{}^a$ heterotrimer increased in affinity to 12.5 ± 5.2 nM (Figure 4-19). At both pH 7.5 and 9.5 the $Glu_3{}^dHis_3{}^a$ peptide has the tightest zinc affinity while the two

heterotrimers bind zinc up to 5 times weaker. There is no statistical difference in zinc affinity between the two heterotrimers.

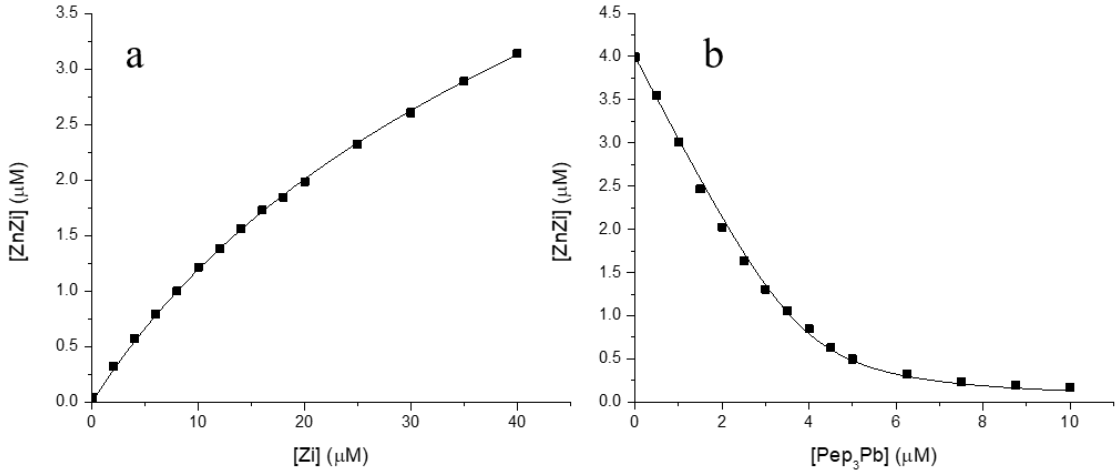

Figure 4-17 (a) Zincon and (b) Pep_3Pb titrations for Zn(II) affinity determination of $Glu_3{}^dHis_3{}^a$ at pH 9.5. Solutions contained either (a) 20 μM Pep_3Pb and 10 μM ZnOAc or (b) 10 μM Zi and 5 μM ZnOAc in 50 mM CHES pH 9.5.

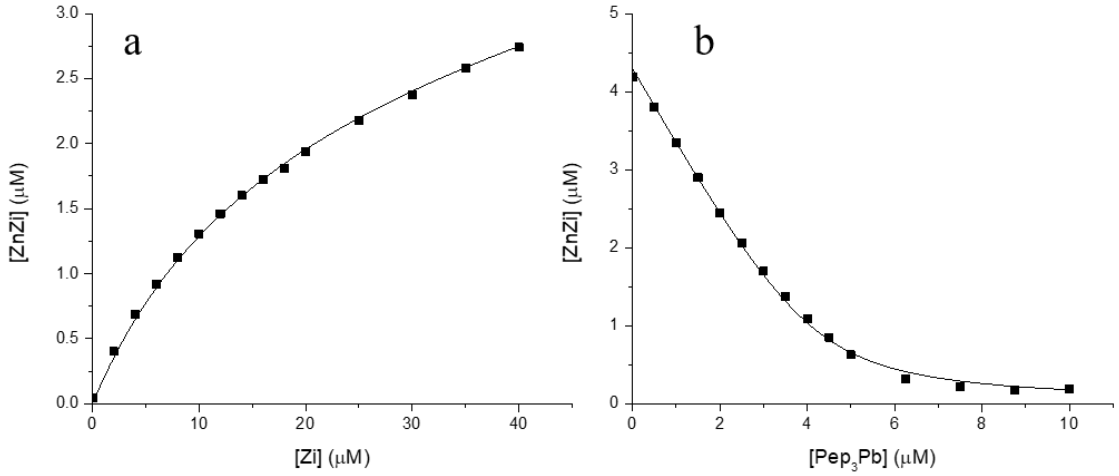

Figure 4-18 (a) Zincon and (b) Pep_3Pb titrations for Zn(II) affinity determination of $Glu_2{}^dHis_3{}^a$ at pH 9.5. Solutions contained either (a) 20 μM Pep_3Pb and 10 μM ZnOAc or (b) 10 μM Zi and 5 μM ZnOAc in 50 mM CHES pH 9.5.

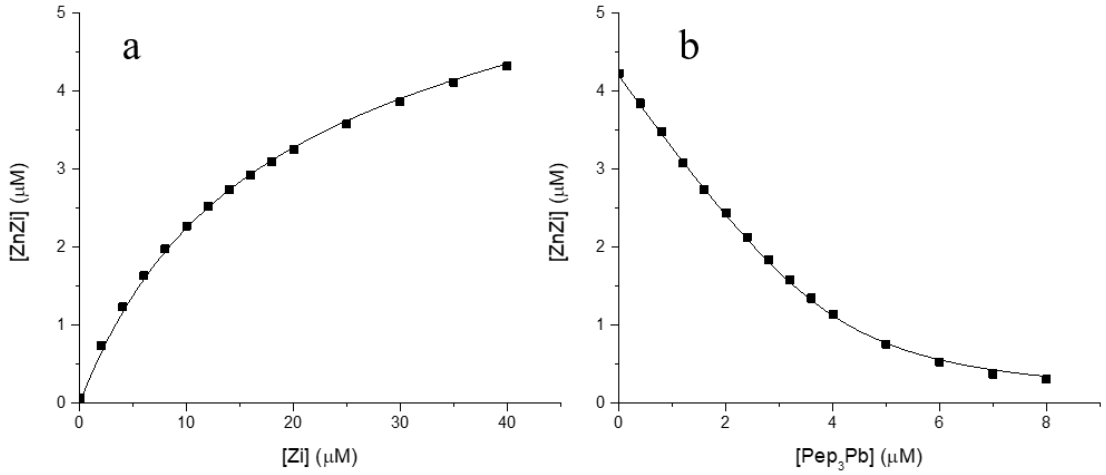

Figure 4-19 (a) Zincon and (b) Pep_3Pb titrations for Zn(II) affinity determination of $Glu_1{}^dHis_3{}^a$ at pH 9.5. Solutions contained either (a) 20 μM Pep_3Pb and 10 μM ZnOAc or (b) 10 μM Zi and 5 μM ZnOAc in 50 mM CHES pH 9.5.

Table 4-2 Zn(II) affinities at pH 7.5 (this work), 9.0 (determined by Dr. Zastrow[11] and Dr. Mocny[14]), and 9.5 (this work)

Peptide	K_d (nM) pH 7.5	K_d (nM) pH 9.0	K_d (nM) pH 9.5
$His_3{}^a$	260 ± 130	110 ± 50*	ND
$Asp_1{}^dHis_3{}^a$	600 ± 60	1100 ± 600$^+$	5.8 ± 0.3
$Asp_2{}^dHis_3{}^a$	700 ± 150	ND	3.6 ± 0.5
$Asp_3{}^dHis_3{}^a$	640 ± 160	2.3 ± 1.4*	9.3 ± 1.1
$Glu_1{}^dHis_3{}^a$	730 ± 120	ND	13 ± 5
$Glu_2{}^dHis_3{}^a$	830 ± 80	ND	7.5 ± 1.1
$Glu_3{}^dHis_3{}^a$	300 ± 80	ND	2.4 ± 1.0

*With Hg(II) bound at the $Cys_3{}^a$ site rather than Pb(II) determined by Dr. Zastrow

$^+$With Pb(II) bound at the $Cys_3{}^a$ site determined by Dr. Mocny

pNPA esterase activity

The activity of $Glu_x{}^dHis_3{}^a$ peptides was determined at pH 9.5 via the colorimetric hydrolysis of pNPA as esterase activity is a secondary function of carbonic anhydrase. The goal of this work is to determine how asymmetry in a transition metal site affects catalysis. The least efficient peptide was $Glu_1{}^dHis_3{}^a$, with a catalytic efficiency of 11.4 ± 0.1 $M^{-1}s^{-1}$ (

Table 4-3, Figure 4-20). This low efficiency is due to the slower k_{cat} of 0.008 ± 0.002 s^{-1}.

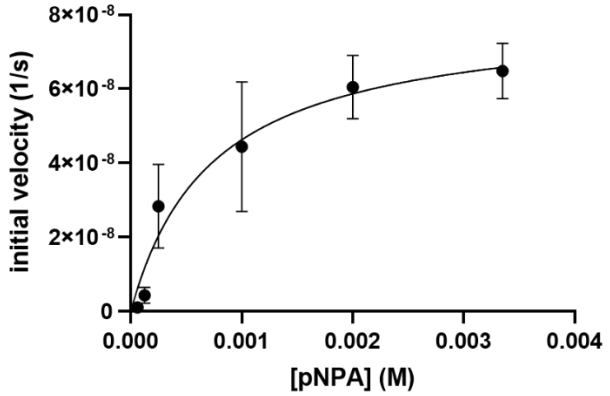

Figure 4-20 Michaelis-Menten curve (average ± S.D.) for pNPA hydrolysis by $Glu_1^dHis_3^a$ at pH 9.5. Solutions contained 50 μM Pep_3Pb and 10 μM ZnOAc (experimental) or 40 μM Pep_3Pb (control) in 50 mM CHES pH 9.5.

The other heterotrimer, $Glu_2^dHis_3^a$, had a similar K_M to $Glu_1^dHis_3^a$ but a significantly faster k_{cat} (0.013 ± 0.001 s^{-1}). This resulted in an efficiency of 22 ± 1 $M^{-1}s^{-1}$ (Figure 4-21). This is within error of the efficiency of TRI His_3^a determined by Dr. Zastrow (23.5 ± 1.9 $M^{-1}s^{-1}$).[10]

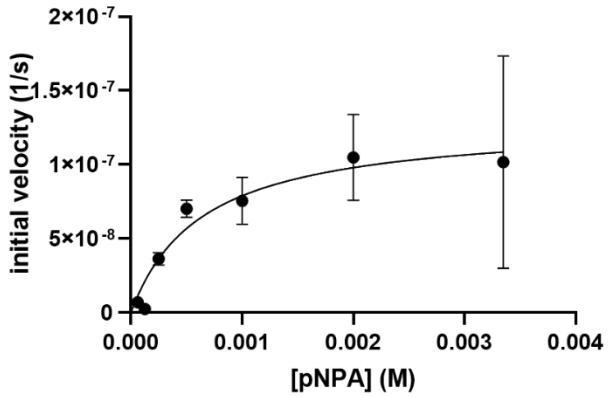

Figure 4-21 Michaelis-Menten curve (average ± S.D.) for pNPA hydrolysis by $Glu_2^dHis_3^a$ at pH 9.5. Solutions contained 50 μM Pep_3Pb and 10 μM ZnOAc (experimental) or 40 μM Pep_3Pb (control) in 50 mM CHES pH 9.5.

The homotrimer $Glu_3^dHis_3^a$ had both the fastest k_{cat} (0.021 ± 0.004 s^{-1}) and the highest K_M (1.1 ± 0.4 mM). This resulted in an intermediate efficiency of 18.7 ± 0.7 $M^{-1}s^{-1}$ (Figure 4-22).

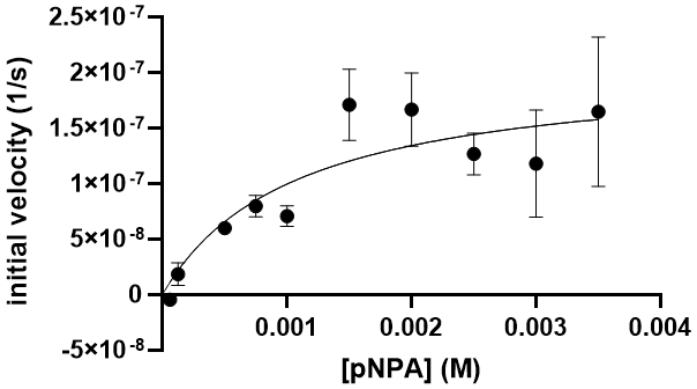

Figure 4-22 Michaelis-Menten curve (average ± S.D.) for pNPA hydrolysis by $Glu_3{}^dHis_3{}^a$ at pH 9.5. Solutions contained 50 μM Pep_3Pb and 10 μM ZnOAc (experimental) or 40 μM Pep_3Pb (control) in 50 mM CHES pH 9.5.

The homotrimeric $His_3{}^a$ peptide was also examined as discrepancies were observed between Drs. Zastrow and Mocny. In this work, a catalytic efficiency of 14.7 ± 0.5 $M^{-1}s^{-1}$ was observed, which is lower than that measured previously (Figure 4-23). It should be noted that this work included higher concentrations of substrate in Michaelis-Menten calculations.

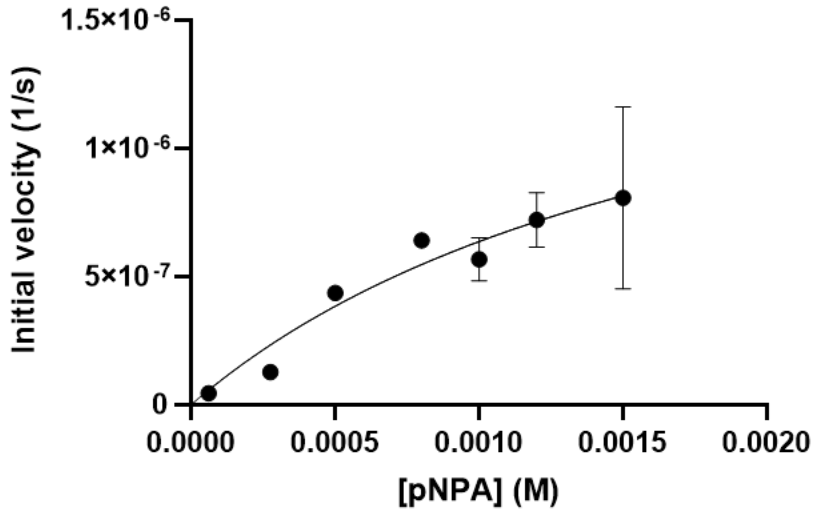

Figure 4-23 Michaelis-Menten curve (average ± S.D.) for pNPA hydrolysis by $His_3{}^a$ at pH 9.5. Solutions contained 50 μM Pep_3Pb and 10 μM ZnOAc (experimental) or 40 μM Pep_3Pb (control) in 50 mM CHES pH 9.5. Note that errors are too small on lower [pNPA] points for error bars to be visible.

The Asp measurements performed by Dr. Mocny were also repeated with much higher substrate concentrations for a more accurate determination of K_M. For the $Asp_1{}^dHis_3{}^a$

heterotrimer, the k_{cat} was comparable but the K_M was significantly higher, resulting in a decreased efficiency of 20.0 ± 0.7 $M^{-1}s^{-1}$ (Figure 4-24).

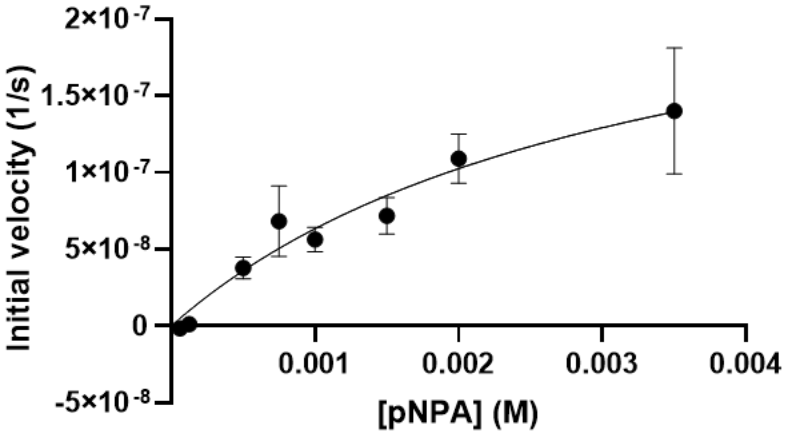

Figure 4-24 Michaelis-Menten curve (average ± S.D.) for pNPA hydrolysis by $Asp_1{}^dHis_3{}^a$ at pH 9.5 Solutions contained 50 μM Pep_3Pb and 10 μM ZnOAc (experimental) or 40 μM Pep_3Pb (control) in 50 mM CHES pH 9.5.

The $Asp_3{}^dHis_3{}^a$ homotrimer had elevated k_{cat} and K_M compared to the data acquired by Dr. Mocny. This resulted in an equivalent efficiency of 23.0 ± 0.8 $M^{-1}s^{-1}$ (Figure 4-25).

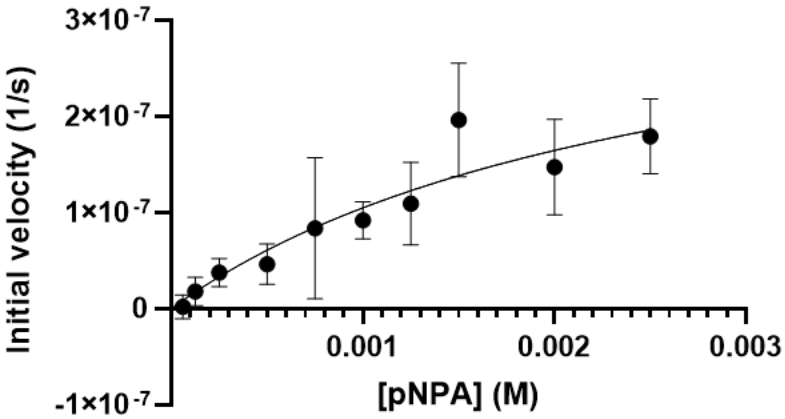

Figure 4-25 Michaelis-Menten curve (average ± S.D.) for pNPA hydrolysis by $Asp_3{}^dHis_3{}^a$ at pH 9.5 Solutions contained 50 μM Pep_3Pb and 10 μM ZnOAc (experimental) or 40 μM Pep_3Pb (control) in 50 mM CHES pH 9.5.

Table 4-3 Kinetic parameters for all peptides at pH 9.5 All peptides are GR length unless otherwise noted.

Peptide	k_{cat} (s^{-1})	K_M (mM)	k_{cat}/K_M ($M^{-1}s^{-1}$)
TRI His_3^a*	0.040 ± 0.012	1.5 ± 0.5	23.3 ± 0.3
$His_3^{a\#}$	0.011 ± 0.001	0.5 ± 0.1	23.5 ± 1.9
His_3^a*	0.064 ± 0.007	3.5 ± 0.5$^+$	18.5 ± 0.6
His_3^a	0.019 ± 0.004	1.3 ± 0.7	14.7 ± 0.5
$Glu_1^dHis_3^a$	0.008 ± 0.002	0.7 ± 0.4	11.4 ± 0.2
$Glu_2^dHis_3^a$	0.013 ± 0.001	0.6 ± 0.2	22 ± 1
$Glu_3^dHis_3^a$	0.021 ± 0.004	1.1 ± 0.4	18.7 ± 0.7
$Asp_1^dHis_3^a$	0.026 ± 0.005	1.3 ± 0.4	20 ± 0.7
$Asp_1^dHis_3^{a\#}$	0.021 ± 0.003	0.8 ± 0.2	25.1 ± 2.5
$Asp_3^dHis_3^a$	0.038 ± 0.0094	1.7 ± 0.1	23 ± 0.8
$Asp_3^dHis_3^a$*	0.024 ± 0.004	1.0 ± 2.0$^+$	24.2 ± 2.5
Average His_3^a	0.015	1.5	18.9
Average $Asp_1^dHis_3^a$	0.023	1.1	22.6
Average $Asp_3^dHis_3^a$	0.031	1.4	23.6

*With Hg(II) bound to a Cys_3^a site from Dr. Zastrow[11]
#With Pb(II) bound to an $Ala_2^dCys_3^a$ site from Dr. Mocny[14]
+K_M values are likely an underdetermination due to the range of substrates measured

Discussion

This work aimed to introduce a second coordination sphere hydrogen bonding residue to the Zn(II)His_3^a site described by Dr. Zastrow to model native CAII more accurately. The native enzyme active site consists of Zn(II) bound to three His residues and a solvent molecule.[2] This solvent molecule is also hydrogen bonded to a key residue, T199, that has been shown to mediate the pK_a of the active site. Loss of this hydrogen bonding residue increases the pKa ~2 pH units and decreases the efficiency of the enzyme by a factor of ~100.[6-7, 20] Dr. Mocny previously attempted to model this interaction with both Thr and Asp residues with limited success. It was hypothesized that the Thr residue was oriented such that the hydroxy group was pointed to the helical interface while the methyl group was positioned in the hydrophobic core of the trimer. This orientation prevented a potential hydrogen bond from forming between the Zn(II) coordinated solvent molecule and the Thr residue. To prevent this, Dr. Mocny then tried replacing the Thr with Asp. Instead of generating a hydrogen bond, it was hypothesized that a His_2Asp chelate motif was generated. My work, therefore, has focused on using Glu instead of Asp to increase the length of the sidechain. We hypothesized that by increasing the sidechain

length the Zn(II) could stay in the center of the 3SCC and retain the desired His_3 coordination instead of forming a chelate ring.

In the previous chapter, structural characterization of Zn(II) bound to $Glu_x^dHis_3^a$ peptides was performed at both pH 7.5 and 9.5. These XAS experiments showed that Zn(II) is four coordinate regardless of pH or number of Glu residues present. Equally good fits were observed for both His_3O and His_2O_2 models. By measuring the Zn(II) affinity for these peptides, I aimed to determine if an affinity difference could distinguish between these two possible coordination environments.

Affinity determinations were done at pH 7.5 for comparison to Zn(II) XAS and Co(II) spectroscopy collected at this pH. Zn(II) bound tightest to His_3^a and $Glu_3^dHis_3^a$. There was no statistical difference in Zn(II) affinity for the $Asp_x^dHis_3^a$ peptides or Glu heterotrimers. Based on crystal structures, the Zn(II) coordination environment of His_3^a is three histidine residues and a solvent molecule. It is likely, therefore, that $Glu_3^dHis_3^a$ has a similar Zn(II) coordination environment. Without a crystal structure for this peptide, I instead modeled the Glu mutation in Pymol based on the structure of GRCS L2WL16CL30H, a His_3^a peptide. The only model that prevented significant steric strain between the Glu residues and the Zn(II) ion was an orientation in which all Glu residues were oriented towards the helical interface (Figure 4-26). This orientation prevented direct interaction of Glu residues with the Zn(II) or His residues, generating the same Zn(II)His_3OH coordination environment as in His_3^a. Of course, it is also difficult to predict the charge of these residues without a crystal structure. It is possible that in the presence of multiple carboxylate groups and in the hydrophobic core that the Glu side chains are protonated. This protonation would prevent the desired carboxylate-water hydrogen bond, resulting in similar kinetic parameters to His_3^a. Thus, a crystal structure of this system is necessary to determine if the similar kinetic parameters are due to deprotonated Glu residues repelling each other and orienting along the helical interface as shown below, protonated Glu residues that cannot form the desired second sphere interactions, or a mix of protonation states that coincidently result in similar catalytic efficiency to His_3^a. I have collected data on a $Glu_3^dHis_3^a$ peptide but have not been able to solve the structure due to COVID restrictions.

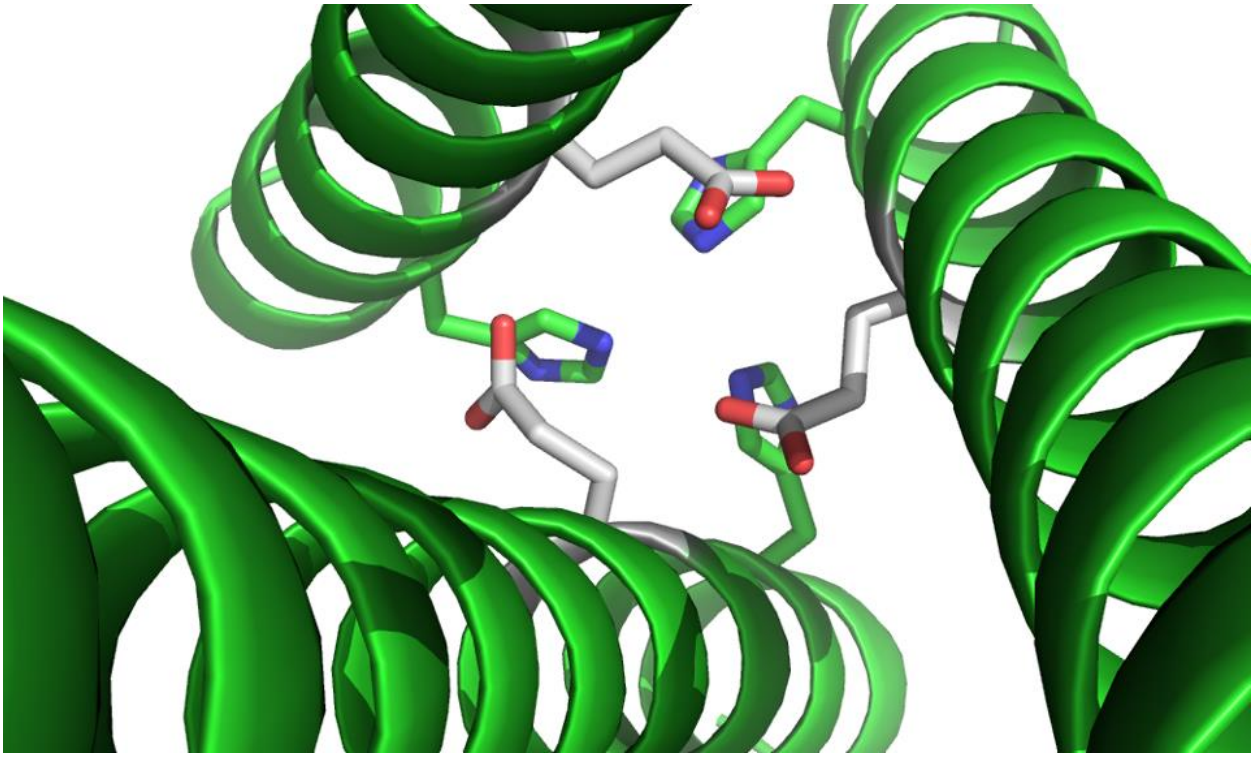

Figure 4-26 Pymol model of $Glu_3^dHis_3^a$ based on the structure of His_3^a (PDB: 5KB0)[21]

The remaining peptides, however, all had Zn(II) affinities 2-3 times weaker than the His_3^a peptide at pH 7.5. All peptides however, have the residues necessary to bind zinc in the same manner as His_3^a. This coordination would result in a tighter affinity than what was observed, so a structural difference must account for this. Dr. Mocny previously described a likely chelate ring formed with Asp and His residues in the Asp containing heterotrimers.[14] In the $Asp_1^dHis_3^a$ heterotrimer, she modeled an interaction in which the Zn(II) is coordinated by 2 His and 1 Asp residue. This coordination is certainly possible, but is unlikely given the lower Zn(II) affinity. As the His_3 coordination environment is possible and binds Zn(II) more tightly than the proposed His_2Asp coordination, that should be the preferred coordination environment for all peptides. There are two instances in which this is not possible: (i) the carboxylate directly coordinates a His residue, preventing Zn(II) from coordinating or (ii) the proximity of the chelate motif formation grants very high zinc affinity for the chelate to form and much weaker affinity for the second His to coordinate, averaging a lower affinity than the His_3 model. If the latter case were true, one would expect this chelate motif to form in the $Glu_3^dHis_3^a$ peptide, displacing the other residues to form this high affinity scaffold. As this is not observed, only the first case will be considered.

In this instance, a His residue is coordinated, not by Zn(II), but by a carboxylate residue. Pymol models based on the structure of **CS** L9PenL23H (a His_3^a peptide) were generated to determine possible side chain orientations. For both $Glu_1^dHis_3^a$ and $Glu_2^dHis_3^a$, the conformation with the least amount of strain had one glutamate residue oriented in the core of the 3SCC. In this orientation, the distance between the Glu-O- and His-NH is 2.4 Å (Figure 4-27With this configuration, the Zn(II) can reorient to coordinate the remaining two His residues and two solvent molecules to generate a 4-coordinate Zn(II).

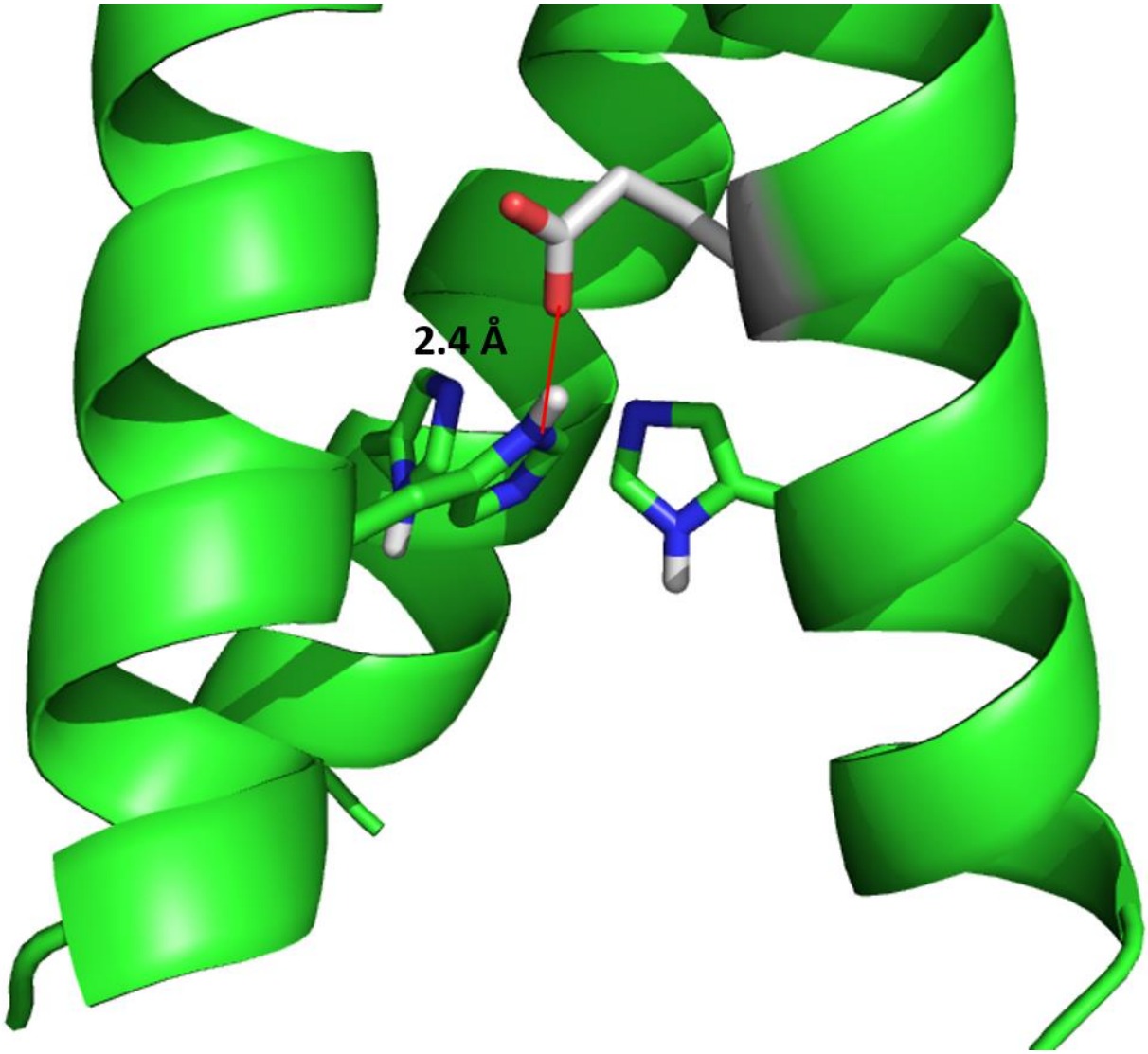

Figure 4-27 Side view of a model of $Glu_1^dHis_3^a$ based on the structure 3PBJ

The Zn(II) ion in this model likely doesn't coordinate in the center of the 3SCC because of the Glu residue, but instead closer to the helical interface between the two His containing strands (Figure 4-28). The coordination sphere of the Zn(II) is completed with two solvent

molecules in addition to the two His residues because the third His residue is involved in a hydrogen bond with the Glu residue.

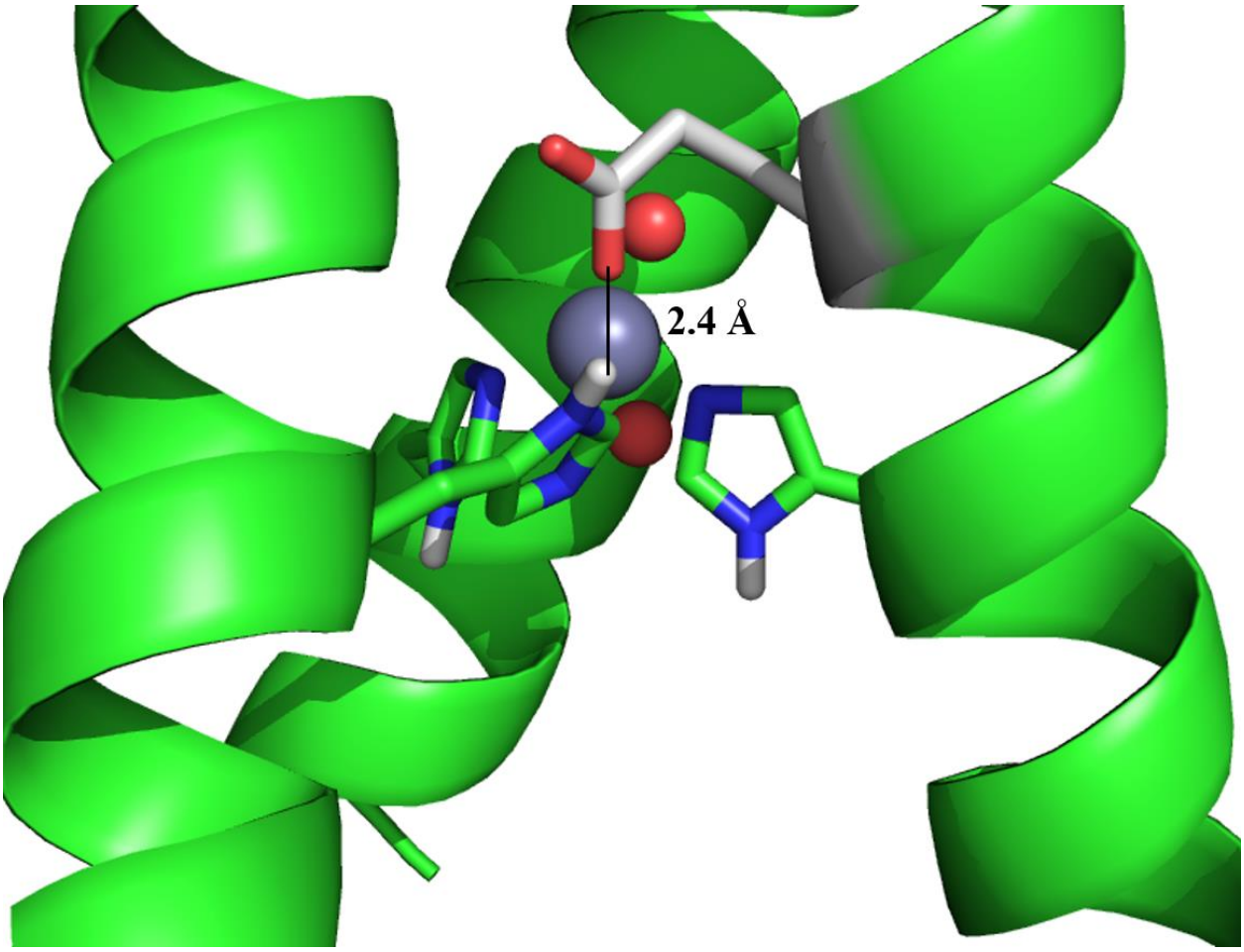

Figure 4-28 Side view of a Pymol model of $Glu_1{}^dHis_3{}^a$ with Zn(II) shown as a grey sphere and coordinated water as red spheres based on the structure 3PBJ

With 2 Glu residues, a similar coordination environment is formed. There is too much steric strain for both Glu side chains to orient towards the His_3 site. The second Glu, therefore, may orient towards the helical interface as with $Glu_3{}^dHis_3{}^a$ or towards the N-termini of the 3SCC. With the second Glu pointed towards the N-termini, the Zn(II) can shift from the center of the 3SCC as is seen with $His_3{}^a$ towards the two helices with available binding sites (Figure 4-29). Similar coordination environments are possible with the $Asp_x{}^dHis_3{}^a$ peptides.

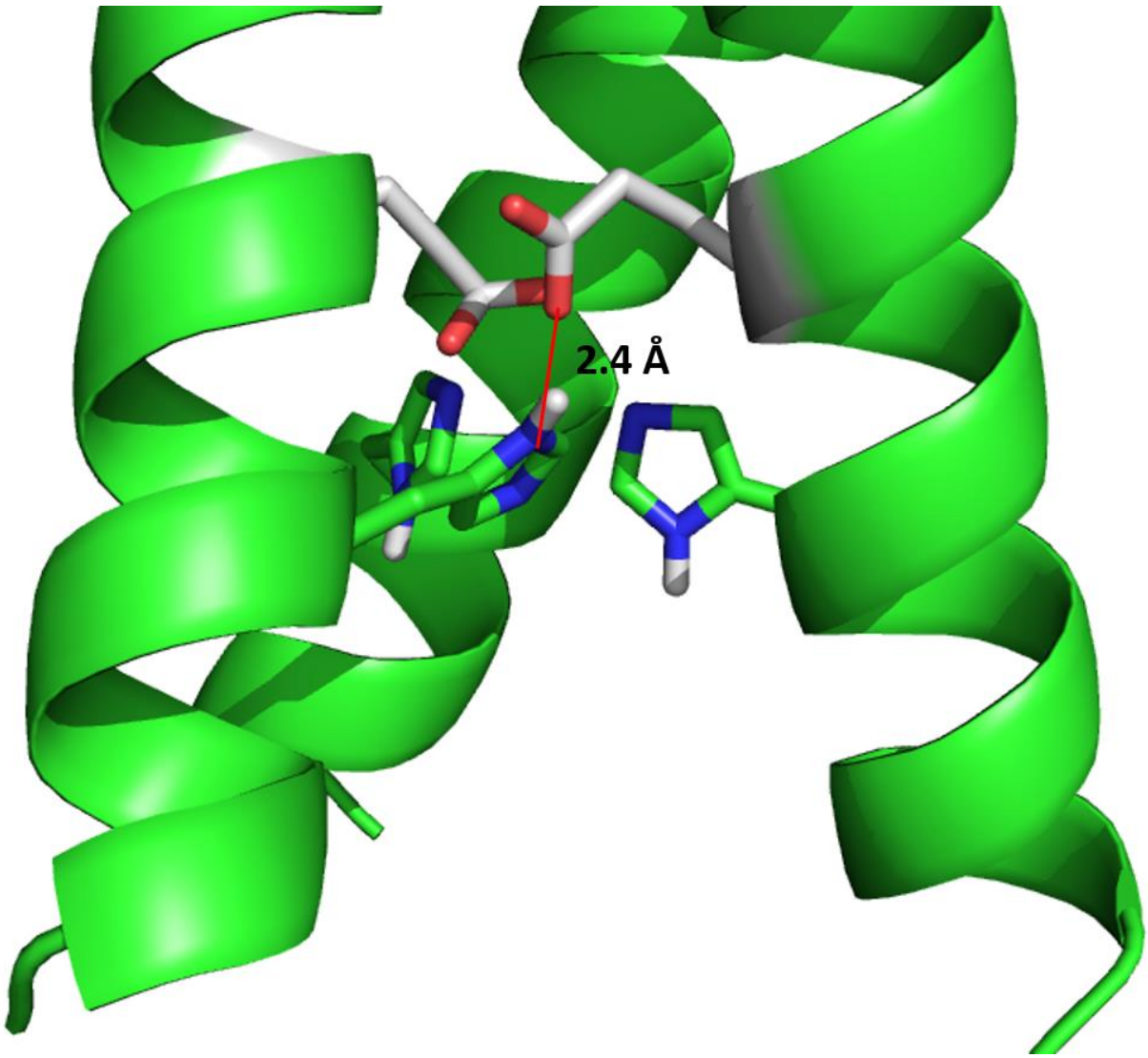

Figure 4-29 Side view of a Pymol model of $Glu_2^dHis_3^a$ with a potential hydrogen bonding interaction in red. Note that this bond is between the Glu-O- and the His delta nitrogen. Based on the structure 3PBJ

Again, the introduction of Zn(II) to this binding site likely results in the zinc orienting along a helical interface (Figure 4-30). This orientation is still possible because the second Glu residue likely orients along this interface as well rather than pointing towards the interior of the 3SCC to sterically hinder Zn(II) coordination. This shift of the coordinated metal to the helical interface has been observed with copper in Dr. Karl Koebke's work on *de novo* designed cupredoxins. In these systems, a surface Glu residue was found to coordinate the copper ion, contributing to unique spectroscopic properties.[22]

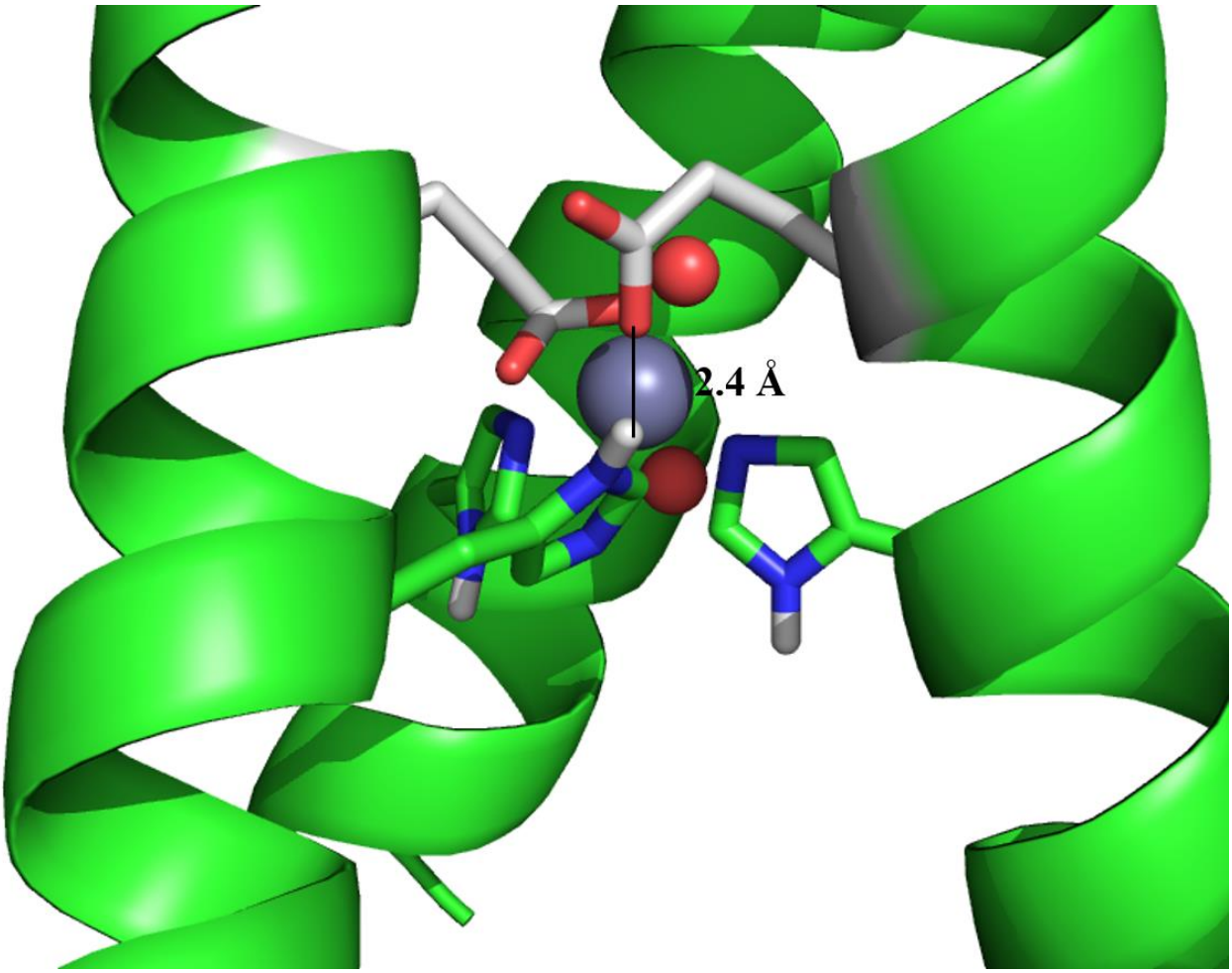

Figure 4-30 Side view of a Pymol model of $Glu_2^dHis_3^a$ with Zn(II) shown as a grey sphere and coordinated water as red spheres based on the structure 3PBJ

As discussed in Chapter 3, Co(II) was shown to be an unfaithful probe of Zn(II) coordination. Both UV-visible and XAS data showed that $Glu_3^dHis_3^a$ coordinates Co(II) as a predominantly 6-coordinate complex and the Glu heterotrimers as 5-coordinate complexes. This shows that the carboxy-His interactions modeled here are not particularly strong. Zn(II) prefers a 4-coordinate geometry as a d_{10} ion and can easily reorient within this binding site to form an alternate 4-coordinate complex than the desired N_3OH. Co(II), however, can form higher coordinate complexes and may be able to disrupt the side chain interactions to coordinate 3 His residues and additional oxygen ligands. Alternately, Co(II) may bind in the same manner as Zn(II), but with additional solvent molecules to complete the 5- or 6-coordinate structure. A crystal structure with Co(II) or more thorough computational analysis of this site is necessary to determine the exact Co(II) environment.

At pH 9.5, the Zn(II) affinity increases in all peptides described herein. This is consistent with work done by Dr. Zastrow in TRI length peptides. The trend in affinities among $Glu_x{}^dHis_3{}^a$ peptides is consistent with that observed at pH 7.5, in which the homotrimer binds Zn(II) with the highest affinity. The Asp peptide data is less clear, with the homotrimer having the weakest affinity at pH 9.5. If, however, the affinity at pH 9.0 determined by Dr. Zastrow is considered in addition to the data at pH 9.5, there is no significant difference between the three Asp peptides. It is likely that the μM affinity reported by Dr. Mocny for $Asp_1{}^dHis_3{}^a$ is actually nM affinity at pH 9.0 based on an estimation of her data. This is consistent with her report of a competitive titration. Zincon, the zinc chelator, has nM affinity in basic conditions and would not be a good competitor for Zn(II) if the peptide affinity was 3 orders of magnitude weaker. If this is true, the data for $Asp_1{}^dHis_3{}^a$ is consistent between what was reported by Dr. Mocny at pH 9.0 and this report at pH 9.5.

This increase in affinity with an increase in pH is due to a pH dependent change in the Zn(II) coordination environment. Based only on the literature values of amino acid pK_a's, one would assume that the carboxylate and histidine sidechains are deprotonated by pH 7.5. This, however, fails to account for the influence of the local protein environment on these pK_a's. The carboxylate side chains are likely always deprotonated because the pK_a of that sidechain is quite acidic. The histidine, however, has a pK_a of ~6 that may be slightly elevated in the interior of the 3SCC. This elevated pK_a would allow for hydrogen bonding between the proton on the delta nitrogen and the carboxylate residue. In basic solution, however, this proton is lost and the histidine cannot form this hydrogen bond. This would create similar binding environments for all the described peptides, resulting in similar affinities at pH 9.5.

Ultimately, the goal of this work was to determine how the kinetics of ester hydrolysis would be affected by the introduction of Glu residues. The TRI $His_3{}^a$ model reported by Dr. Zastrow is currently the most efficient model of CA for native reaction and is the most efficient 3SCC in performing ester hydrolysis (k_{cat}/K_M 23.3 ± 0.3 $M^{-1}s^{-1}$). When Dr. Zastrow increased the length of the peptide to the GR scaffold, the efficiency decreased to 18.5 ± 0.6 $M^{-1}s^{-1}$. The $His_3{}^a$ experiment was repeated in this work with data points at higher substrate concentrations, resulting in an efficiency of 14.7 ± 0.5 $M^{-1}s^{-1}$. This is due to differences in both k_{cat} and K_M. The k_{cat} reported in this work is similar to that reported by Dr. Mocny for a $His_3{}^a$ peptide but is about 4-fold less than the value reported by Dr. Zastrow. The K_M is also much lower, but is within the

range of measure substrate values, unlike the previously reported K_M. This K_M is within error of the TRI His_3^a peptide, thought the k_{cat} is half the value reported for TRI His_3^a, giving an overall efficiency about half of this peptide. On average, the GR constructs had a decreased overall catalytic efficiency of 18.9 $M^{-1}s^{-1}$ as compared to the TRI peptide.

The k_{cat} and K_M for His_3^a reported herein are equivalent to those for $Glu_3^dHis_3^a$, though the overall efficiency is better due to slight variations in these measurements (18.7 ± 0.7 $M^{-1}s^{-1}$). Based on the XAS and Zn(II) affinity data discussed previously, this is consistent with the hypothesized Zn(II) environment of His_3OH.

The Glu containing heterotrimers are a much different story. $Glu_1^dHis_3^a$ is the least efficient model described here, with an efficiency of 11.4 ± 0.2 $M^{-1}s^{-1}$, while $Glu_2^dHis_3^a$ is the most efficient at 22 ± 1 $M^{-1}s^{-1}$. These two heterotrimers have equivalent K_M values, but $Glu_2^dHis_3^a$ has twice the k_{cat}, resulting in twice the efficiency. Based on affinity determinations and XAS structural characterization, these two trimers have the same Zn(II) coordination environment. In native CAII, the most efficient CA analog, the rate limiting step is the rate that protons can be shuttled to the active site via a key His residue. It was found that decreasing the bulk of a hydrophobic residue (Phe) adjacent to the active site of CAIII, the least efficient isoform of CA, increased the efficiency by up to 140-fold.[23] Increases in efficiency were seen both with smaller hydrophobic and with hydrophilic residues, with the most efficient mutant containing an Asp at this site. They hypothesized that this increase in efficiency was due to increased solvent access adjacent to the active site to allow for more efficient proton transfer, primarily effecting k_{cat} rather than K_M.

The $Glu_1^dHis_3^a$ system does not contain any possible proton shuttles. The addition of a second Glu residue, however, may allow for easier transfer of protons to the active site from the bulk solvent. As described above, the first Glu residue coordinate a His residue but the second Glu residue does not coordinate anything. This residue, therefore, may adopt multiple conformations to transfer protons between the Zn(II) coordinated solvent molecule and the exterior bulk solvent. These effects would increase k_{cat} for $Glu_2^dHis_3^a$ but not $Glu_1^dHis_3^a$ or $Glu_3^dHis_3^a$.

This trend holds true for the Asp system. The homotrimer is more efficient than the $Asp_1^dHis_3^a$ heterotrimer, with both a lower k_{cat} and higher K_M. The increases in K_M reported herein as compared to the values determined by Dr. Mocny are due to an increase in range of

substrate concentration to give a more accurate K_M determination. This data was essential for the determination of the $Asp_3{}^dHis_3{}^a$ parameters as the previous error was twice the reported value and V_{max} was not well defined. Thus, only the trends observed in this work will be considered. In the case of the Asp system, the catalytic efficiency differences are not as drastic because there is not as large of a discrepancy between each kinetic parameter. This work also shows that increasing the length of the side chain significantly lowers k_{cat}. This may again be due to the proton shuttle. With a smaller side chain there are fewer steric constraints to allow for more efficient conformational changes.

Conclusion

In this chapter I have described the Zn(II) affinity of both homo- and heterotrimers as well as determination of the Zn(II) coordination environment. Zn(II) affinity determinations in the $Glu_x{}^dHis_3{}^a$ systems were performed and, considered with XAS results, were used to determine possible Zn(II) ligands. The $Glu_3{}^dHis_3{}^a$ homotrimer binds Zn(II) as tightly as $His_3{}^a$, while the heterotrimers bind Zn(II) more weakly. It is likely, therefore, that $Glu_3{}^dHis_3{}^a$ coordinates Zn(II) similarly to $His_3{}^a$. Pymol models of this construct show that the structure with the least steric strain places all three Glu residues at the helical interface with no Zn(II) interactions. The heterotrimers, however, were best modeled with one Glu residue coordinating a His residue, forcing the Zn(II) to coordinate only 2 His residues. This coordination sphere is completed with 2 oxygen ligands, likely from solvent.

None of the peptides characterized in this work increased the efficiency of ester hydrolysis above what was observed by Dr. Zastrow in TRI $His_3{}^a$. At best, the $Glu_2{}^dHis_3{}^a$ heterotrimer was almost as good as the best system. This work highlights the complexity of introducing second sphere interactions in designed systems. Based on all characterization of the $Glu_x{}^dHis_3{}^a$ systems, the Glu residues were not able to form a second sphere hydrogen bond with the Zn(II) bound solvent molecule. Instead, in the case of the homotrimer, no effect was seen and, in the case of the heterotrimers, the first Glu residue disrupted the desired His_3 coordination by instead coordinating a His residue. The most significant mutation was the introduction of a second Glu residue to provide a proton shuttle to the active site from the exterior solvent. Further work through X-ray crystallography needs to be performed to determine if this coordination environment is accurate.

Ultimately, this work shows the complexity of protein design in incorporating second sphere interactions. This work has shown that Glu residues do affect catalysis, though our current understanding of the structure/function relationship was inadequate to predict how catalysis was affected. In these cases, the desired second sphere residue was placed too close to the primary coordination sphere which allowed for undesired interactions. The distance between the His residues and potential hydrogen bonding residues must be increased to form a hydrogen bond. This may be accomplished by placing the hydrogen bonding reside a full heptad above the His_3 layer. To allow for an interaction, the Leu residue between these sites must be mutated to a smaller hydrophobe. An alanine residue would provide the space necessary for a hydrogen bond to bridge between layers, but the hydrophobic and helix inducing properties will afford the most stability if a bulkier hydrophobe cannot be used.

If alternate activities are explored, the bulk of the Leu hydrophobe also prevents charged residues from orienting within the helical core. As was shown with $Glu_2^dHis_3^a$, the second glutamate residue sidechain cannot point towards the center of the coiled coil both because of the charge repulsion from the first Glu, but also because of steric strain due to the Leu residue. An additional element of negative design is needed to remove this barrier to carboxylate coordination. This hydrophobic core is necessary for the stability of the coiled coil, but Ala is hydrophobic and helix inducing, presenting the best natural amino acid for this role.

This work also does not consider if the introduction of Glu residues decrease the pK_a of the active site. In the native enzyme, the second sphere Thr residue mediates the pK_a of the active site at pH 6.8, rather than at 8.5 in its absence. While these results do not support the formation of a hydrogen bond to provide this mediation, it is possible that the perturbations of the His_3^a site afforded by Glu residues has still affected the pK_a of the active site. To determine this, Michaelis-Menten kinetics must be performed under neutral and mildly basic conditions. This may show that, while the desired effect was not achieved at pH 9.5, $Glu_x^dHis_3^a$ peptides may be more efficient at a lower pH.

References

1. Hakansson, K.; Carlsson, M.; Svensson, L. A.; Liljas, A., Structure of Native and Apo Carbonic Anhydrase II and Structure of Some of Its Anion-Ligand Complexes. *J. Mol. Biol.* **1992,** *227*, 1192-1204.

2. Christianson, D. W.; Fierke, C. A., Carbonic Anhydrase: Evolution of the Zinc Binding Site by Nature and by Design. *Acc. Chem. Res.* **1996,** *29*, 331-339.

3. Lindskog, S., Structure and Mechanism of Carbonic Anhydrase. *Pharmacol. Ther.* **1997,** *74* (1), 1-20.

4. Maren, T. H., Carbonic Anhydrase: Chemistry, Physiology, and Inhibition. *Physiol. Rev.* **1967,** *47*, 597-781.

5. Kiefer, L. L.; Paterno, S. A.; Fierke, C. A., Hydrogen Bond Network in the Metal Binding Site of Carbonic Anhydrase Enhances Zinc Affinity and Catalytic Efficiency. *J. Am. Chem. Soc.* **1995,** *117* (26), 6831-6837.

6. Liang, Z.; Xue, Y.; Behravan, G.; Jonsson, B.-H.; Lindskog, S., Importance of the conserved active-site residues Try7, Glu106 and Thr199 for the catalytic function of human carbonic anhydrase II. *Eur. J. Biochem.* **1993,** *211* (3), 821-827.

7. Xue, Y.; Liljas, A.; Jonsson, B.; Lindskog, S., Structural analysis of the zinc hydroxide-Thr-199-Glu-106 hydrogen-bond network in human carbonic anhydrase II. *Proteins* **1993,** *17* (1), 93-106.

8. Ippolito, J. A.; Christianson, D. W., Structure of an Engineered His3Cys Zinc Binding Site in Human Carbonic Anhydrase II. *Biochemistry* **1993,** *32*, 9901-9905.

9. Kiefer, L. L.; Krebs, J. F.; Paterno, S. A.; Fierke, C. A., Engineering a Cysteine Ligand into the Zinc Binding Site of Human Carbonic Anhydrase II. *Biochemistry* **1993,** *32*, 9896-9900.

10. Zastrow, M. L.; Peacock, A. F.; Stuckey, J. A.; Pecoraro, V. L., Hydrolytic catalysis and structural stabilization in a designed metalloprotein. *Nat. Chem.* **2011,** *4* (2), 118-23.

11. Zastrow, M. L. De novo designed metalloenzymes: structural stabilization and hydrolytic catalysis in a family of α-helical coiled coils. 2013.

12. Zastrow, M. L.; Pecoraro, V. L., Influence of active site location on catalytic activity in de novo-designed zinc metalloenzymes. *J. Am. Chem. Soc.* **2013,** *135* (15), 5895-903.

13. Cangelosi, V. M.; Deb, A.; Penner-Hahn, J. E.; Pecoraro, V. L., A De Novo Designed Metalloenzyme for the Hydration of CO2. *Angewandte Chemie International Edition* **2014,** *53* (30), 7900-7903.

14. Mocny, C. S. Ph.D. Dissertation, Examining the metal selectivity of thiol rich de novo designed peptides as a strategy to make asymmetric alpha- helical protein assemblies. 2016.

15. Holland, D. R.; Hausrath, A. C.; Juers, D.; Matthews, B. W., Structural-Analysis of Zinc Substitutions in the Active-Site of Thermolysin. *Protein Sci.* **1995,** *4* (10), 1955-1965.

16. Greenblatt, H. M.; Feinberg, H.; Tucker, P. A.; Shoham, G., Carboxypeptidase A: Native, zinc-removed and mercury-replaced forms. *Acta Crystallographica Section D: Biological Crystallography* **1998,** *54* (3), 289-305.

17. *Fmoc Solid Phase Peptide Synthesis: A Practical Approach*. 2 ed.; Oxford University Press: New York, 2000.

18. Kocyla, A.; Pomorski, A.; Krezel, A., Molar absorption coefficients and stability constants of Zincon metal complexes for determination of metal ions and bioinorganic applications. *J. Inorg. Biochem.* **2017,** *176*, 53-65.

19. *GraphPad Prism version 8.4.2.679 for Windows, GraphPad Software, San Diego, California USA, www.graphpad.com*.

20. Krebs, J. F.; Ippolito, J. A.; Christianson, D. W.; Fierke, C. A., Structural and Functional Importance of a Conserved Hydrogen Bond Network in Human Carbonic Anhydrase II. *The Journal of Biological Chemistry* **1993,** *268* (36), 27458-27466.

21. Ruckthong, L.; Zastrow, M. L.; Stuckey, J. A.; Pecoraro, V. L., A Crystallographic Examination of Predisposition versus Preorganization in de Novo Designed Metalloproteins. *J. Am. Chem. Soc.* **2016,** *138* (36).

22. Koebke, K. J.; Ruckthong, L.; Meagher, J. L.; Mathieu, E.; Harland, J.; Deb, A.; Lehnert, N.; Policar, C.; Tard, C.; Penner-Hahn, J. E.; Stuckey, J. A.; Pecoraro, V. L., Clarifying the Copper Coordination Environment in a de Novo Designed Red Copper Protein. *Inorg. Chem.* **2018,** *57* (19), 12291-12302.

23. LoGrasso, P. V.; Tu, C.; Chen, X.; Taoka, S.; Laipis, P. J.; Silverman, D. N., Influence of Amino Acid Replacement at Position 198 on Catalytic Properties of Zinc-Bound Water in Human Carbonic Anhydrase III. *Biochemistry* **1993,** *32*, 5786-5791.

Chapter 5 Redox Catalysis Within Self-Assembling Asymmetric Peptide Scaffolds

Introduction

In addition to the hydrolytic catalysis discussed in Chapter 4, *de novo* designed enzymes have also been used to investigate redox catalysis within native protein systems. In this chapter, I will focus on the characterization of a copper redox enzyme, copper only superoxide dismutase (Cu-only SOD). SODs catalyze the dismutation of superoxide to molecular oxygen and peroxide at diffusion limited rates (Equation 5-1).[1] These reactions are catalyzed by several different transition metals, yielding Ni SODs, Fe/Mn SODs, Cu,Zn SODs, and Cu-only SODs. The Fe/Mn, Cu,Zn, and Cu-only SOD families all contain active sites rich in nitrogen and oxygen ligands. The active site of Ni SODs, however, contains Cys residues and N ligands from His and peptide backbones and will not be discussed further in this work.[2-3] The other three classes of SODs contain histidine (Cu,Zn and Cu-only)[4-7] or histidine and aspartate (Fe/Mn)[8-10] ligands and variations of these sites are explored herein using the His_3 site previously characterized extensively for Cu(I) and Cu(II) at pH 5.9 in our 3SCCs.

Equation 5-1 Half reactions catalyzed by SODs where M is the catalytic metal

$$O_2^{\cdot -} + M^n \rightarrow O_2^{2-} + M^{n+1}$$

$$O_2^{\cdot -} + M^{n+1} \rightarrow O_2 + M^n$$

Cu,Zn SODs contain a catalytic copper bound to His residues, one of which bridges to a structural zinc site. A recently discovered Cu-only SOD contains the same copper site, but lacks the structural zinc site. In both cases, the catalytic copper cycles between the Cu(II) and Cu(I) oxidation states at diffusion limited rates with an accompanying change in coordination number and geometry. As shown in Figure 5-1 with Cu-only SOD, the Cu(I) state binds to three His residues in a trigonal planar geometry.[4-5, 7, 11-12] The Cu(II) state coordinates an additional His residue due to a structural change in the enzyme that brings this residue in close proximity only in this oxidized state. This copper site is solvent exposed, unlike in Cu,Zn SOD which has a buried active site with the canonical positively charged tunnel to facilitate superoxide binding. The fourth His residue that coordinates in the Cu(II) bound form is the “bridging histidine”. This residue always coordinates the Zn(II) ion in the structural center and, in the oxidized state, shifts

to coordinate Cu(II) as well.[13] Thus, the primary coordination sphere of the Cu-only and Cu,Zn sites are identical, but the second coordination sphere for the solvent exposed Cu-only SOD is less controlled than in the buried active site of Cu,Zn SOD.

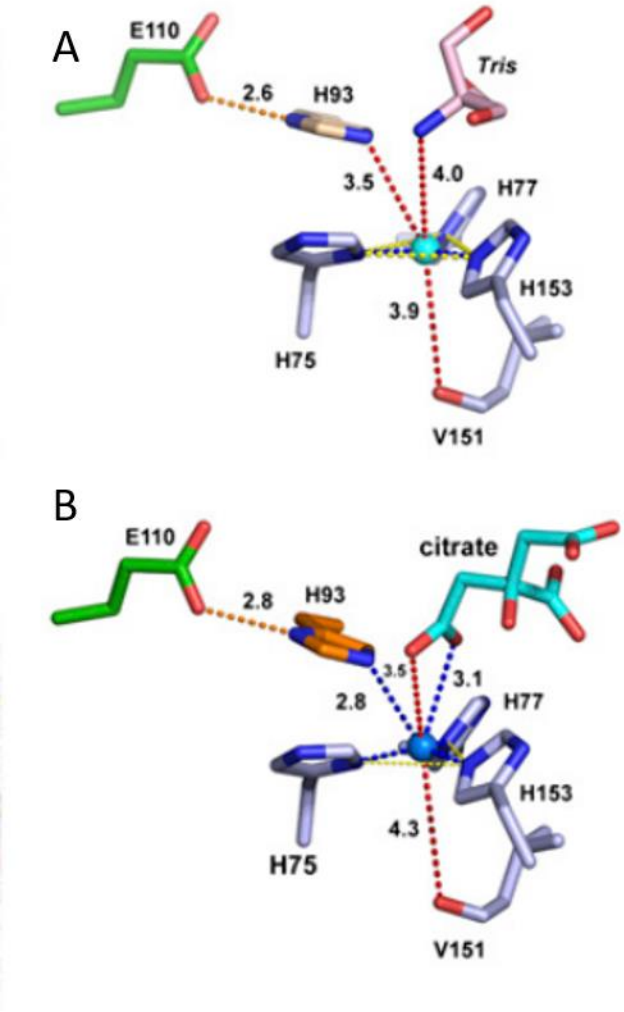

Figure 5-1 Structure of Cu(I) (a) and Cu(II) (b) coordinated Cu-only SOD[7]

The other class of SODs considered in this work is the Fe/Mn SOD family. Fe/Mn SODs bind either iron or manganese in a conserved active site. Most of these enzymes have high metal selectivity for catalysis, though a small subset, deemed cambialistic SODs, can function with either iron or manganese. This active site is trigonal bipyramidal with an equatorial plane of one aspartate and two histidine residues and histidine and solvent axial ligands. Unlike with Cu,Zn and Cu-only SODs, the protein environment does not change depending on the metal oxidation state, though there is debate if the reactions occur through inner or outer sphere mechanisms.

The mechanism of Cu,Zn SOD has been probed extensively through structural and kinetic studies. The reduction of superoxide by Cu(I) occurs through an outer sphere electron transfer. A crystal structure of Cu(I) with molecular oxygen showed that the copper was displaced from the His_3 trigonal plane and was instead square pyramidal, though with a mix of copper density suggesting multiple binding positions.[11] The Cu(II) crystals with azide, however, showed a square pyramidal structure with an azide ligand, suggesting an inner spere mechanism for the oxidation of superoxide.[11] The goal of this work is to design a *de novo* peptide that is capable of performing both the oxidation and reduction of superoxide with a catalytic copper ion that contains these binding environments.

We have previously designed several SOD environments in the GRα_3D peptide scaffold with a catalytic copper. Two designs contained only His ligands, either 3 His or 4 His, as models of the Cu(I) and Cu(II) binding sites, respectively. Two more constructs contained three histidine residues and a fourth aspartate residue, one in which the Asp replaced the axial His ligand and one meant to model the Fe/Mn SOD active site with an equatorial Asp residue (Figure 5-2). This work found that the His_3 model was the most efficient SOD (k_{McF}= 3.0 x 10^6 $M^{-1}s^{-1}$) of the four models.[14] There was not, however, a trend between redox potential, metal affinity, or EPR and XAS features that correlated with the observed activities.

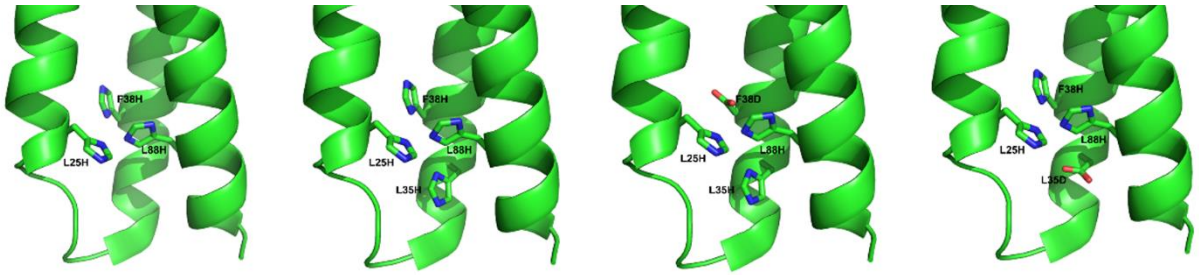

Figure 5-2 Pymol models of H3, H4, H2DH, and H3D (from left to right) based on the structure of GRα_3D (PDB 6DS9)

To improve upon these models, I aimed to make similar copper binding sites in an asymmetric 3SCC. Previous work with carbonic anhydrase has shown an increase in activity in 3SCC scaffolds over 3HB scaffolds.[15] This could be due to several reasons: stability of the coiled coil and the orientation of the His_3 plane relative to the coiled coil. The 3SCC constructs are more stable than the 3HB constructs as evidenced through thermal denaturation. α_3D peptides thermally denature at ~80°C while 3SCC peptides cannot be fully thermally denatured in aqueous solution.[16] The His_3 plane within 3HB is also not equivalent to the plane found within

the 3SCC peptides because the helical bundle is antiparallel. As the spacing between **a** and **d** residues and **d** and **a** residues of the following heptad are not equal, a His_3 plane perpendicular to the helical axis is unlikely to form. The 3SCC scaffolds, however, have layers of **a** or **d** residues that allow for the formation of a His_3 plane perpendicular to the helical axis. The Cu(II) geometry required for SOD activity may be better suited in the 3SCC than the 3HB as the center of the 3SCC may allow for axial ligand coordination unlike the 3HB.

This work, therefore, aims to improve upon our work with Cu-only SODs in GRα_3D by taking advantage of the design aspects of the GR scaffold that could contribute to increased activity. GRα_3D was an excellent scaffold to begin investigations of Cu-only SOD with an asymmetric scaffold, but the GR scaffold presents significant advantages that will allow for increased understanding of the structure-function relationship. These constructs utilize the previously described His_3^a environment with additional His or carboxylate ligands as models of Cu-only and Fe/Mn SOD active sites, respectively. A full list of sequences is provided in

Table 5-1. In addition, this work explores the effect of His placement in **a** and **d** positions on catalysis. The ability to explore **a** vs **d** layers as well as mixed **a** and **d** layers is unique to a parallel coiled coil and, as described in Chapter 2, can have drastic effects on metal coordination. This work will allow for the investigation of catalysis with respect to heptad placement. The increased stability of the GR scaffold over GRα_3D also allows for the introduction of metal binding residues to the core of the CC without a significant loss in scaffold stability.

*Table 5-1 List of peptide sequences with transition metal binding residues in **bold red** and lead binding residues in **bold green**. All GR sequences have an N-terminal acetyl and C-terminal amide. Note that the Ala mutation is shown for both His^a and His^d, though in $His_x^dHis_{3-x}^a$ peptides only one strand contains the Ala residue.*

Peptide	Sequence
His^a	G WKALEEK LKA**C**EEK **A**KALEEK LKALEEK **H**KALEEK G
His^d	G WKALEEK LKA**C**EEK **A**KALEEK LKA**H**EEK LKALEEK G
Asp^dHis^a	G WKALEEK LKA**C**EEK LKALEEK LKA**D**EEK **H**KALEEK G
His^dAsp^a	G WKALEEK LKA**C**EEK LKALEEK LKA**H**EEK **D**KALEEK G
Glu^dHis^a	G WKALEEK LKA**C**EEK LKALEEK LKA**E**EEK **H**KALEEK G
His^aHis^d	G WKALEEK LKA**C**EEK LKALEEK LKA**H**EEK **H**KALEEK G
GRα_3D H3	MGSWAEFKQRLAAIKTRLAAIKSR**H**DALGGS EAELAA**H**EKEIAAFESEIAAFESELQAYKGKG NPEVEALRKEAAAIRDEAAAIRDE**H**QAYRLNGSGA
GRα_3D H4	MGSWAEFKQRLAAIKTRLAAIKSR**H**DALGGS EAE**H**AA**H**EKEIAAFESEIAAFESELQAYKGKG NPEVEALRKEAAAIRDEAAAIRDE**H**QAYRLNGSGA
GRα_3D H2DH	MGSWAEFKQRLAAIKTRLAAIKSR**H**DALGGS EAE**H**AA**D**EKEIAAFESEIAAFESELQAYKGKG NPEVEALRKEAAAIRDEAAAIRDE**H**QAYRLNGSGA
GRα_3D H3D	MGSWAEFKQRLAAIKTRLAAIKSR**H**DALGGS EAE**D**AA**H**EKEIAAFESEIAAFESELQAYKGKG NPEVEALRKEAAAIRDEAAAIRDE**H**QAYRLNGSGA
GRCS L16CL30H	E WEALEKK LAALESK **C**QALEKK LQALEKK **H**EALEHG

Methods

Peptide synthesis and purification

Peptides were synthesized on a Biotage Initiator+ Alstra peptide synthesizer using Fmoc-rink amide-methylbenzhydrylamine (MBHA) resin. Standard deprotection and coupling protocols with HOBt/HBTU/DIEA were used.[17] Peptides were cleaved from the resin using trifluoroacetic acid, thioanisole, ethanedithiol, and anisole (90:5:3:2) for four hours, precipitated with cold ether, and redissolved in double distilled water. The crude peptide was then lyophilized to dryness. The peptide was purified using a Waters 600 HPLC with a reverse phase C-18 column. A linear gradient from 70% A (0.1% trifluoroacetic acid in double distilled water) 30% B (0.1 % trifluoroacetic acid, 10% double distilled water, 90% acetonitrile) to 20% A/80% B was utilized at a flow rate of 20 mL/min over 35 minutes. ESI-MS was used to confirm the mass of the pure peptide, which was then lyophilized to dryness.

Cu(I) Affinity

Cu(I) affinity was determined by competitive titration with the Cu(I) chelator bathocuproine disulfonate (BCS) under anaerobic conditions. BCS binds Cu(I) forming the colored $Cu(BCS)_2$ complex with λ_{max}=483 nm, ε_{483}=13,300 $M^{-1}cm^{-1}$, and log β_2=19.9 at pH 7.5.[18] A solution containing 80 μM peptide trimer as determined by Trp absorbance at 280 nm (ε_{280}=5500 $M^{-1}cm^{-1}$), 80 μM $Pb(NO_3)_2$, and 50 mM HEPES, pH 7.5 was scanned from 700 nm to 200 nm. An aliquot of 40 μM tetrakis(acetonitrile)copper(I)hexafluorophosphate was added and scanned from 700 nm to 200 nm to ensure that the Pb-S_3 LMCT absorbance at ~340 nm was unperturbed by the addition of Cu(I). A titration with 10 μM aliquots of BCS was performed to a final concentration of 200-300 μM.

Cu(II) Affinity

Cu(II) affinity was determined by Cu(II) quenching of Trp fluorescence at 350 nm. A solution containing 500-800 nM peptide trimer in 50 mM HEPES pH 7.5 was titrated with a solution of 936 μM $CuCl_2$ with 10 minutes of stirring between each addition. Only homotrimeric peptides with no Cys_3 site were considered for these experiments as the addition of $Pb(NO_3)_2$ also quenches Trp fluorescence. The Pb-S_3 quenching reduced the Trp fluorescence to such an extent that Cu(II)(N/O) quenching could not accurately be determined. The Cu(II) dissociation constant was determined by fitting the fluorescence intensity at 350 nm to Equation 5-2.

Equation 5-2 Fluorescence intensity fitting where I_F is final intensity reported as a percent (i.e. I_0=100)

$$I = \left(\frac{I_F - 100}{2[pep_3]}\right)\Big(([Cu(II)] + [pep_3] + K_d) - \sqrt{([Cu(II)] + [pep_3] + K_d])^2 - 4[pep_3][Cu(II)]}\Big) + 100$$

Cu(I/II) Reduction potential

The reduction potential for peptides was calculating from the experimentally determined Cu(I) and Cu(II) affinities. The ratio of dissociation constants can be related via the Nernst Equation (Equation 5-3). A reduction potential of 159 mV vs NHE was used for aqueous copper.[19-20]

Equation 5-3 Nernst equation

$$E^0_{CuPep3} = E^0_{Cu,aq} - \frac{2.303RT}{nF} log \frac{K_{d(Cu(I)Pep3)}}{K_{d(Cu(II)Pep3)}}$$

Fridovich assay

A buffer containing 200 μM xanthine in 50 mM HEPES, pH 7.5 was prepared by refluxing at 80°C for 3 hours. After cooling, 100 μM sodium 2,3-bis-(2-methoxy-4-nitro-5-sulfophenyl)-2*H*-tetrazolium-5-carboxanilide (XTT) was added. The production of superoxide was generated *in situ* by the addition of xanthine oxidase (XO) from a 20 mg/mL stock solution. The rate of XTT decomposition was monitored by the formation of formazan at 470 nm. The amount of XO added was adjusted to get a rate of formazan production such that the slope was between 0.25 and 0.30 to ensure linearity of product formation. The rate of formazan production was determined for 90 seconds, an aliquot of Pep_3PbCu (containing 1 equivalent of $Pb(NO_3)_2$ and 0.2 equivalents of $CuCl_2$ per trimer) was added and mixed, and the rate of formazan production was determined for a further 90 seconds (Figure 5-3).

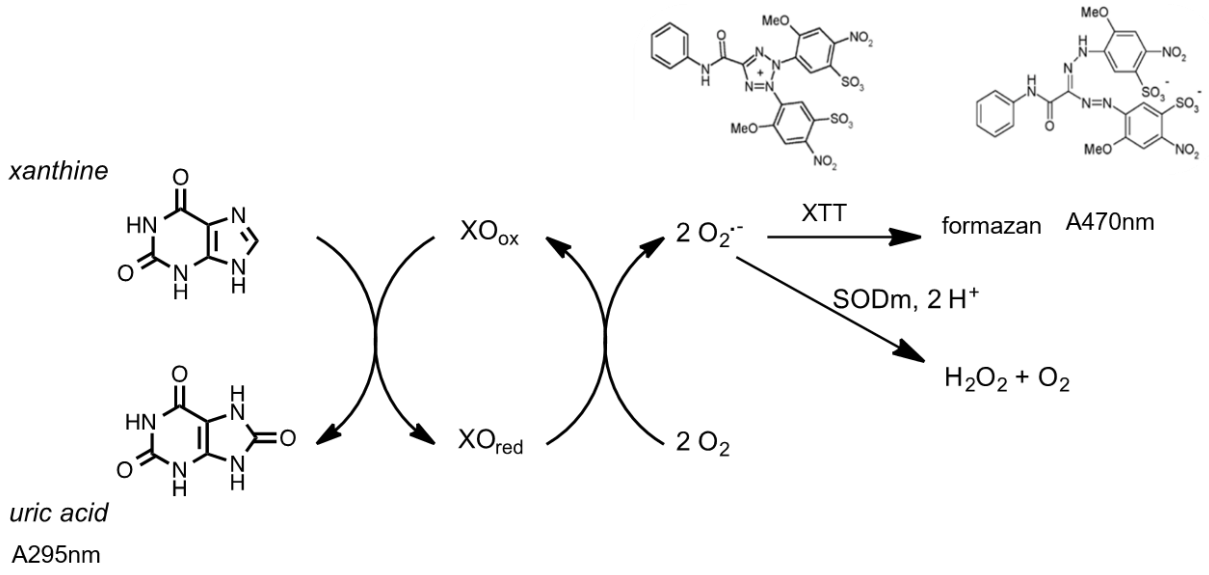

Figure 5-3 Schematic of Fridovich assay

The IC_{50} was determined from the inhibition of formazan production with increasing concentrations of Pep_3PbCu. The IC_{50} was used to calculate the rate for the McCord-Fridovich assay (k_{McF}) where k_{XTT}= 8.6 x 10^4 $M^{-1}s^{-1}$ (Equation 5-4).[21]

Equation 5-4 Determination of k_{McF} from experimentally determined IC_{50} value

$$k_{McF} = \frac{k_{XTT}[XTT]}{IC_{50}}$$

Several controls were performed to ensure that the addition of Pep_3PbCu did not disrupt the *in situ* generation of superoxide or quench the absorbance of formazan. The absorbance of uric

acid, a byproduct of xanthine oxidase, was monitored at 295 nm both before and after the addition of Pep_3PbCu. For all trimers discussed herein no significant difference in uric acid formation was observed in the absence and presence of trimer. Free copper and some proteins can also quench the absorbance of formazan. To determine if this occurred in solution, the production of formazan from XTT was allowed to go to completion as monitored by absorbance at 470 nm. An aliquot of Pep_3PbCu was added at the highest concentration used during the kinetic assay and the absorbance at 470 nm was monitored. No significant change to this absorbance was observed under these conditions.

Results

Cu(I) Affinity

The Cu(I) K_d for each homotrimeric and heterotrimer construct was determined by competitive titration with bathocuperine sulfonate (BCS) at pH 7.5. Of the four His_3 models, His_3^a had the weakest Cu(I) affinity (Figure 5-4) and His_3^d the tightest (Figure 5-5) with the heterotrimers at intermediate affinities (Figure 5-6 and Figure 5-7). All affinities are listed in Table 5-2.

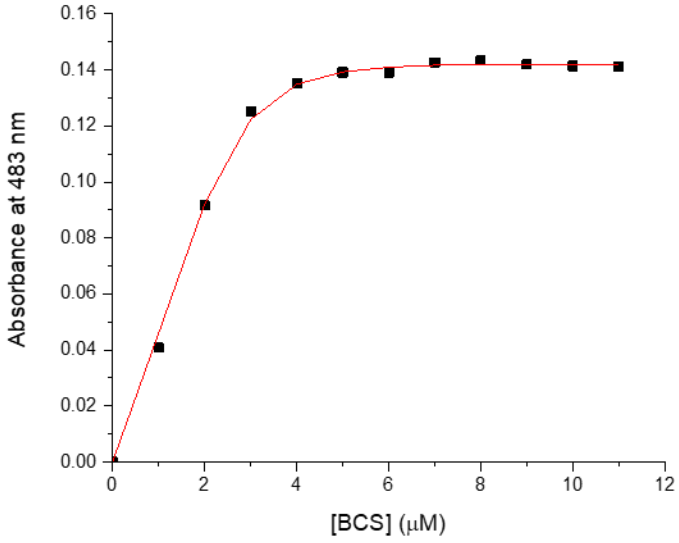

Figure 5-4 BCS titration for His_3^a with 80 μM Pep_3Pb and 40 μM Cu(I) in 50 mM HEPES pH 7.5

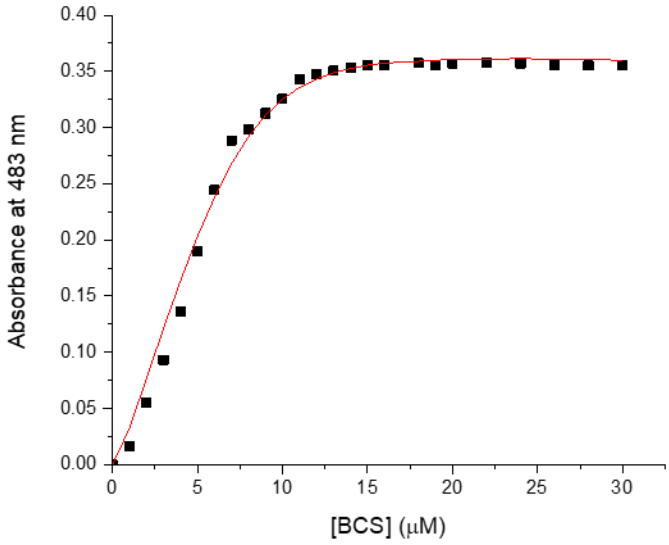

Figure 5-5 BCS titration for His_3^d with 80 μM Pep_3Pb and 40 μM Cu(I) in 50 mM HEPES pH 7.5

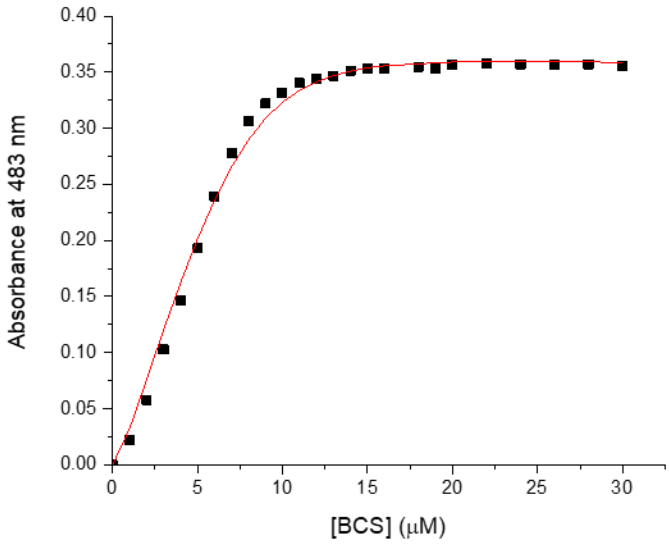

Figure 5-6 BCS titration for $His_1^dHis_2^a$ with 80 μM Pep_3Pb and 40 μM Cu(I) in 50 mM HEPES pH 7.5

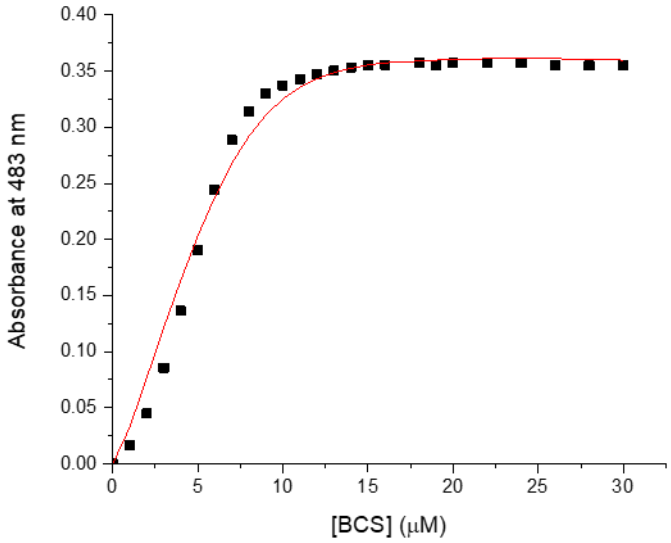

Figure 5-7 BCS titration for $His_2{}^dHis_1{}^a$ with 80 μM Pep_3Pb and 40 μM Cu(I) in 50 mM HEPES pH 7.5

The Cu(I) affinity of $His_1{}^dHis_3{}^a$ was comparable to $His_3{}^a$ (Figure 5-8), while $His_3{}^dHis_1{}^a$ bound Cu(I) an order of magnitude weaker (Figure 5-9). This is notable as it is three orders of magnitude weaker than just 3 His residues in the **d** site.

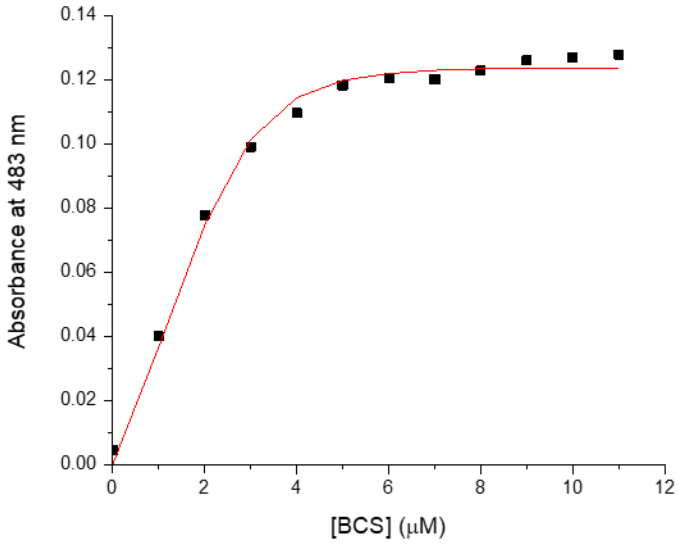

Figure 5-8 BCS titration for $His_1{}^dHis_3{}^a$ with 80 μM Pep_3Pb and 40 μM Cu(I) in 50 mM HEPES pH 7.5

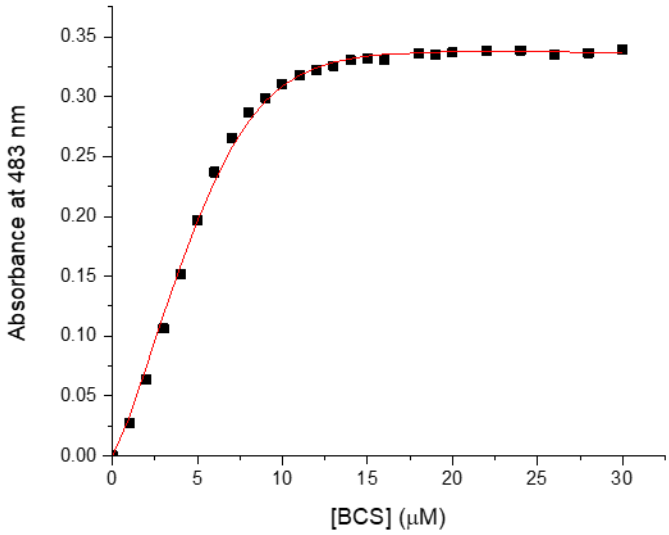

Figure 5-9 BCS titration for $His_3{}^dHis_1{}^a$ with 80 μM Pep_3Pb and 40 μM Cu(I) in 50 mM HEPES pH 7.5Of the Asp containing peptides, $Asp_1{}^dHis_3{}^a$ and $His_2{}^dAsp_1{}^dHis_1{}^a$ had weaker Cu(I) affinity than did $Asp_2{}^dHis_3{}^a$ and $Asp_3{}^dHis_3{}^a$ (Figure 5-10-Figure 5-13).

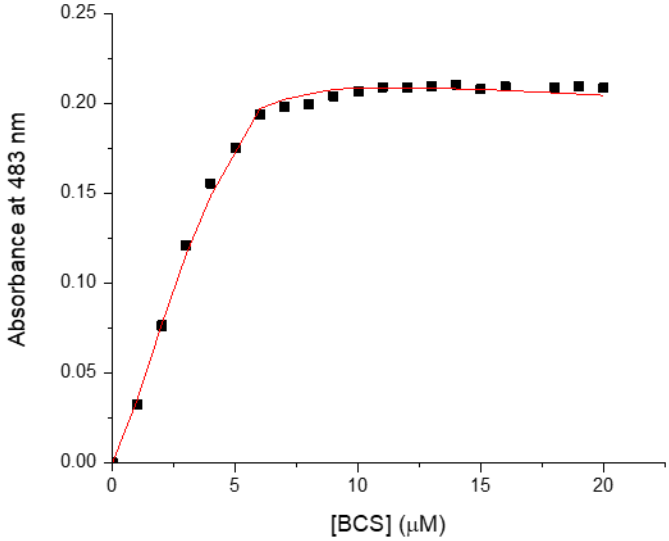

Figure 5-10 BCS titration for $Asp_1{}^dHis_3{}^a$ with 80 μM Pep_3Pb and 40 μM Cu(I) in 50 mM HEPES pH 7.5

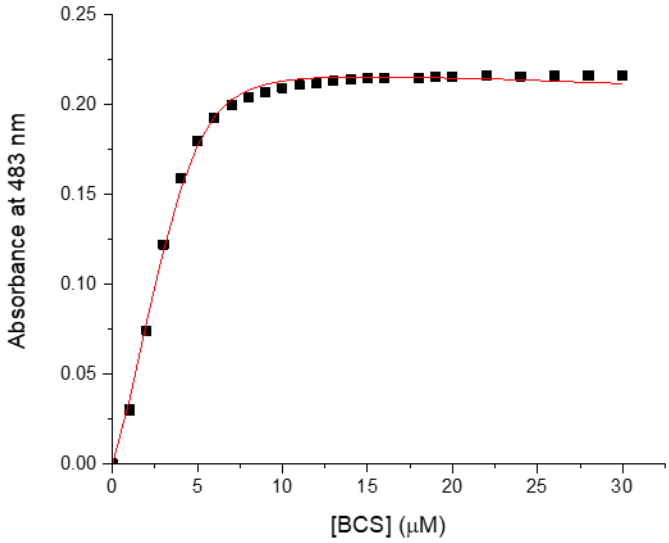

Figure 5-11 BCS titration for $Asp_2^dHis_3^a$ with 80 μM Pep_3Pb and 40 μM Cu(I) in 50 mM HEPES pH 7.5

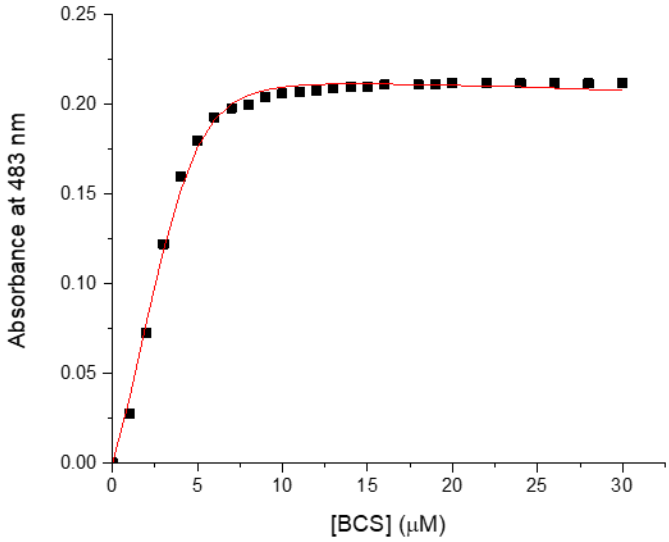

Figure 5-12 BCS titration for $Asp_3^dHis_3^a$ with 80 μM Pep_3Pb and 40 μM Cu(I) in 50 mM HEPES pH 7.5

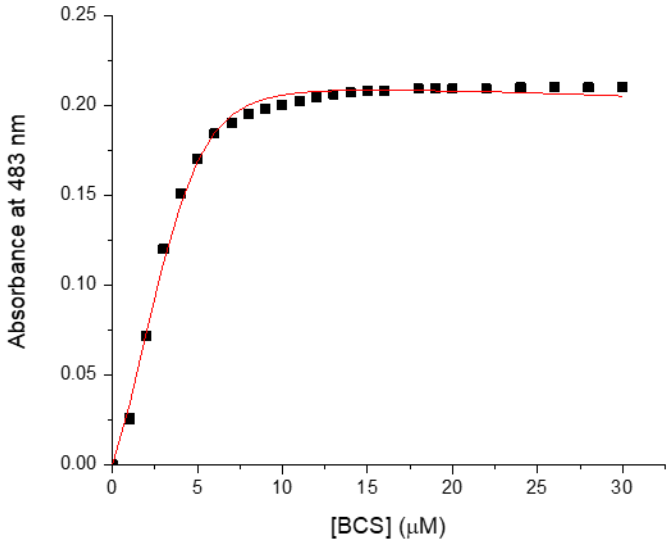

Figure 5-13 BCS titration for $His_2{}^dAsp_1{}^dHis_1{}^a$ with 80 μM Pep_3Pb and 40 μM Cu(I) in 50 mM HEPES pH 7.5

Similar to the Asp containing peptides, $Glu_1{}^dHis_3{}^a$ had the weakest Cu(I) affinity while $Glu_2{}^dHis_3{}^a$ and $Glu_3{}^dHis_3{}^a$ had similar higher Cu(I) affinities (Figure 5-14-Figure 5-16).

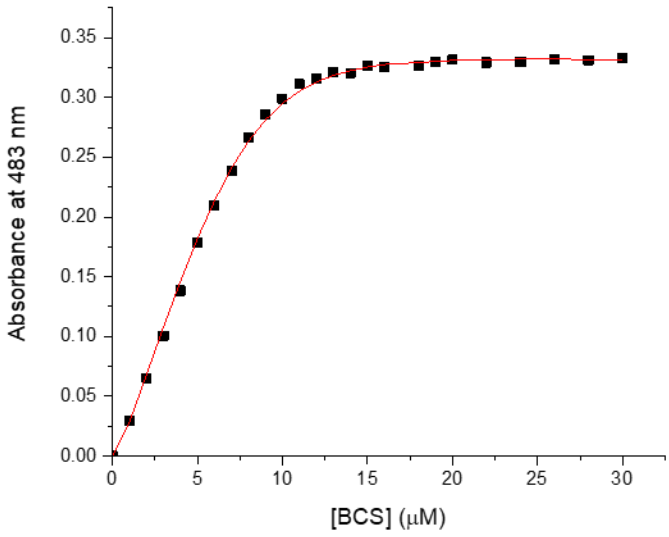

Figure 5-14 BCS titration for $Glu_1{}^dHis_3{}^a$ with 80 μM Pep_3Pb and 40 μM Cu(I) in 50 mM HEPES pH 7.5

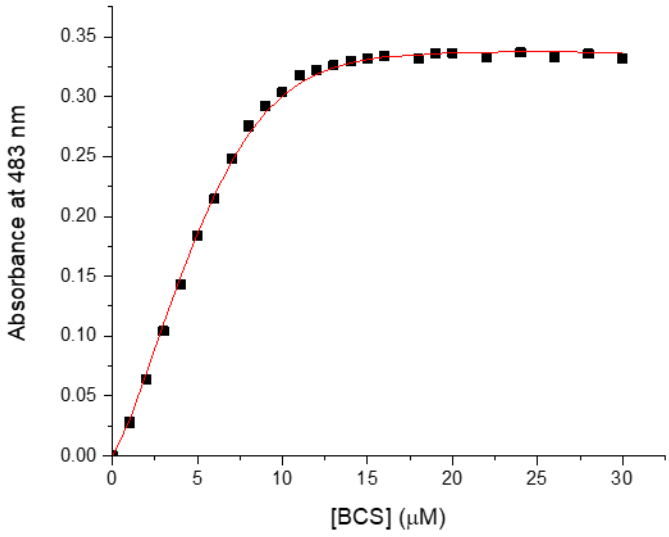

Figure 5-15 BCS titration for $Glu_2^dHis_3^a$ with 80 μM Pep_3Pb and 40 μM Cu(I) in 50 mM HEPES pH 7.5

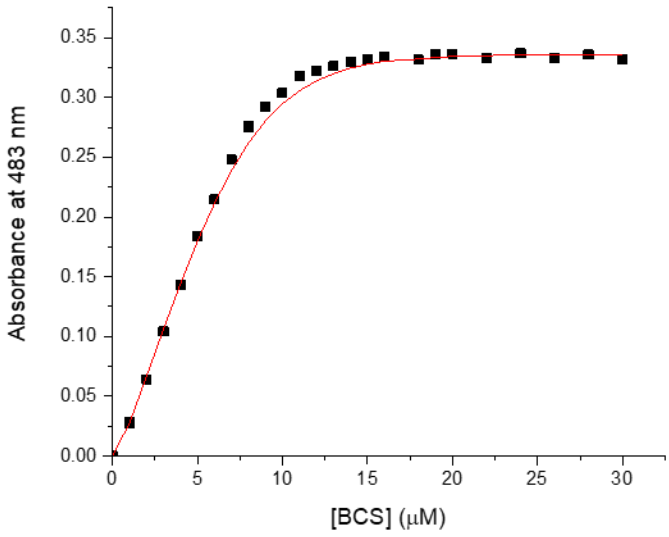

Figure 5-16 BCS titration for $Glu_3^dHis_3^a$ with 80 μM Pep_3Pb and 40 μM Cu(I) in 50 mM HEPES pH 7.5

Cu(II) Affinity

The Cu(II) K_d for each homotrimeric construct was determined at pH 7.5 via tryptophan fluorescence quenching. As described in the methods section, the Cu(II) affinity of heterotrimeric peptides could not be determined by this method due to interference from the Pb(II) ion. It was determined that His_3^a had the tightest Cu(II) affinity while His_3^d had the

weakest with the two carboxylate containing homotrimers at intermediate affinities (Figure 5-17-Figure 5-20).

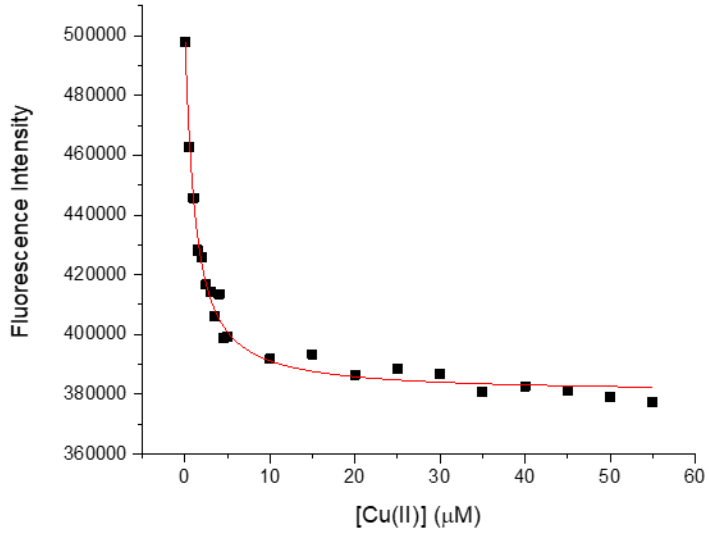

Figure 5-17 Fluorescence quenching of Trp residue as a function of Cu(II) binding for His_3^a at pH 7.5

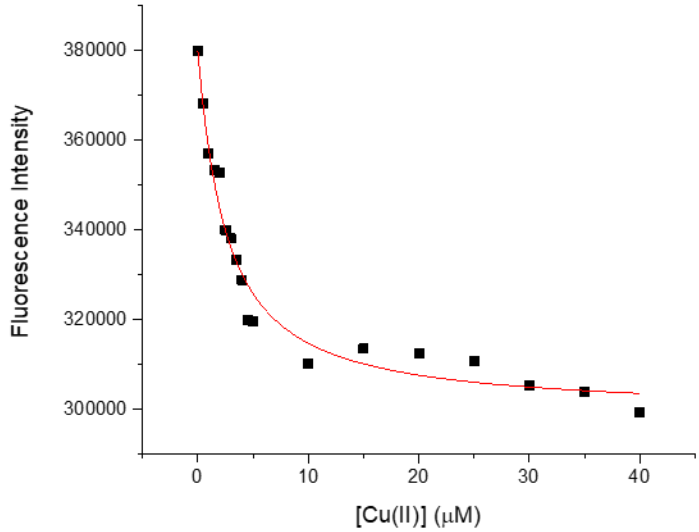

Figure 5-18 Fluorescence quenching of Trp residue as a function of Cu(II) binding for His_3^d at pH 7.5

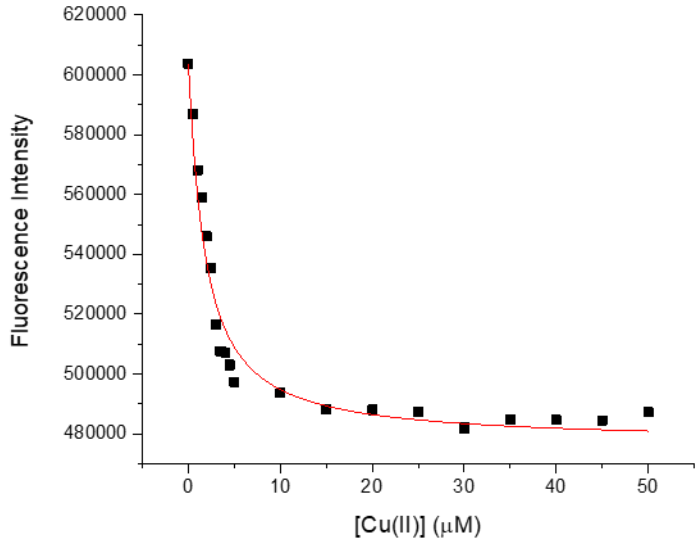

Figure 5-19 Fluorescence quenching of Trp residue as a function of Cu(II) binding for $Asp_3^dHis_3^a$ at pH 7.5

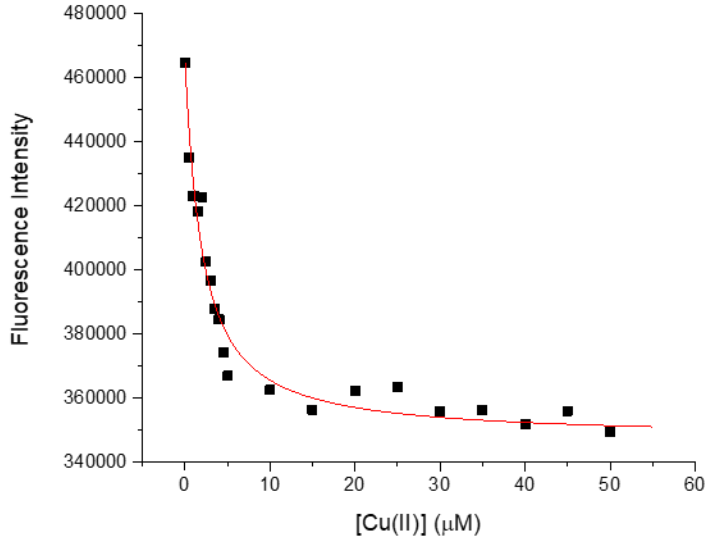

Figure 5-20 Fluorescence quenching of Trp residue as a function of Cu(II) binding for $Glu_3^dHis_3^a$ at pH 7.5

Copper reduction potential

The copper redox potential at pH 7.5 was calculated for each homotrimeric construct using the Cu(I) and Cu(II) affinities.

Table 5-2 Experimentally determined Cu(I) and Cu(II) affinities and calculated redox potentials at pH 7.5

Peptide	Cu(I) K_d (fM)	Cu(II) K_d (nM)	Redox potential (mV vs. NHE)
His_3^a	2.2 ± 0.1	6.6 ± 0.3	541 ± 54
$His_1^dHis_2^a$	0.14 ± 0.07	ND	
$His_2^dHis_1^a$	0.211 ± 0.02	ND	
His_3^d	0.0018 ± 0.0001	21 ± 5	695 ± 75
$His_1^dHis_3^a$	1.3 ± 0.3	ND	
$His_3^dHis_1^a$	19.3 ± 0.2	ND	
$Asp_1^dHis_3^a$	1.07 ± 0.02	ND	
$Asp_2^dHis_3^a$	0.64 ± 0.06	ND	
$Asp_3^dHis_3^a$	0.41 ± 0.01	15 ± 7	606 ± 59
$His_2^dAsp_1^dHis_1^a$	6.9 ± 0.5	ND	
$Glu_1^dHis_3^a$	5.4 ± 0.2	ND	
$Glu_2^dHis_3^a$	2.41 ± 0.02	ND	
$Glu_3^dHis_3^a$	2.2 ± 0.2	14 ± 4	561 ± 55

Cu(I)/(II) SOD activity

The activity of each construct was determined via the Fridovich assay. All controls were performed as described in the methods section. With only three His residues, the rate increased by a factor of ~7.5 with an incremental change from His_3^a to His_3 with mixed **a** and **d** residues to His_3^d (

Table 5-3). The His_4 models had rates between that of His_3^a and His_3^d, though with error values too large to determine the true values. This error was due to inconsistencies between trials, though the error on IC_{50} determination was low for each trial.

The addition of aspartate residues to His_3^a improved the rate, with $Asp_3^dHis_3^a$ and $Asp_2^dHis_3^a$ twice as good as His_3^a. $Asp_1^dHis_3^a$ (analogous to H3D in GRα_3D) was ~4.5x better than His_3^a. With layers of mixed His and Asp residues with no improvement was seen over His_3^a for $His_1^dAsp_1^aHis_2^a$ while a 10x improvement was seen for $His_2^dAsp_1^dHis_1^a$. If, however, the His_3^d plane is maintained and aspartate residues are instead added in the **a** layer, no improvement over His_3^d is observed.

$Glu_x^dHis_3^a$ trimers were also investigated. All had intermediate rates between His_3^a and His_3^d, but the error on IC_{50} determination was too high to accurately determine these rates.

Table 5-3 Cu-only SOD activity at pH 7.5

Peptide	IC_{50} (nM)	k_{McF} (10^7 $M^{-1}s^{-1}$)
His_3^a	1300 ± 400	0.67 ± 0.16
$His_1^dHis_2^a$	242 ± 8	3.56 ± 0.12
$His_2^dHis_1^a$	210 ± 30	4.07 ± 0.47
His_3^d	190 ± 30	4.51 ± 0.67
$His_1^dHis_3^a$	270 ± 480*	3.2 ± 2.05*
$His_3^dHis_1^a$	210 ± 170*	4.16 ± 1.89*
$Asp_1^dHis_3^a$	320 ± 70	2.7 ± 0.5
$Asp_2^dHis_3^a$	600 ± 100	1.4 ± 0.2
$Asp_3^dHis_3^a$	700 ± 200	1.2 ± 0.3
$His_2^dAsp_1^dHis_1^a$	140 ± 50	6.21 ± 1.67
$Glu_1^dHis_3^a$	250 ± 80*	3.39 ± 0.78*
$Glu_2^dHis_3^a$	300 ± 600*	2.5 ± 1.54*
$Glu_3^dHis_3^a$	180 ± 70*	4.88 ± 1.38*
$His_3^dAsp_1^a$	400 ± 200	2.25 ± 0.74
$His_3^dAsp_3^a$	600 ± 200	1.56 ± 0.42
$His_1^dAsp_1^aHis_2^a$	1700 ± 700	0.50 ± 0.15

*Significant error in determining IC_{50} due to high error between trials for H_4 constructs or within trials for $Glu_x^dHis_3^a$ constructs

Discussion

This work aimed to design and characterize a copper binding environment with an asymmetric first coordination sphere as a model of Cu-only SOD. The active site of Cu-only SOD consists of three His residues in the Cu(I) bound form, while in the Cu(II) bound form a fourth His residue is shifted to only 2.8 Å from the Cu(II) ion.[7] This work aimed to characterize His_3 and His_4 active sites using His residues in both **a** and **d** layers. In addition, active sites containing Asp and Glu residues were also investigated. These better approximate the active site of Fe/Mn SODs, containing a His_3Asp ligand environment in which the equatorial plane is composed of two His and one Asp residue. Previous work with related constructs in the GRα_3D scaffold showed that a simple His_3 model was the most efficient SOD, though was still within error of two His_3Asp models. One of these models contained the same equatorial plane as Fe/Mn SOD and the other had an equatorial plane of 3 His residues with an axial Asp residue. These models are not directly comparable structurally to the GR trimers described in this chapter because, as outlined above, the 3HB does not have planes of **a** or **d** residues directly perpendicular to the helical axis since it is antiparallel.

The work described in this chapter built upon the previously described His_3^a model that has been utilized for Zn(II) hydrolytic chemistry as described in Chapter 4 as well as Cu(I/II)

redox chemistry as a study of Cu NiR. The present work also aimed to determine the effect of **a** and **d** His residues on catalysis by investigating both His_3^d and constructs with His in both **a** and **d** layers. It was found that Cu(II) bound more tightly to His_3^a, while Cu(I) bound more tightly to His_3^d with the heterotrimers of intermediate Cu(I) affinity. As a consequence, His_3^d has a more positive redox potential than His_3^a and the intermediate Cu(I) affinities for the heterotrimers suggest intermediate redox potentials. Interestingly, the activities of these constructs trend inversely with redox potential. The ideal redox potential for SODs was determined to be 360 mV vs NHE, which is halfway between the oxidation and reduction of superoxide. All constructs described herein fall within this range, but the more efficient models have redox potentials further from this optimal value.

There are not significant differences in structure between the His_3 constructs as determined by EPR and XAS to account for these differences in affinity and activity. Models of both the Cu(I) and Cu(II) active sites for His^a containing constructs were constructed in Pymol based on the structure of GRCS L16CL30H (PDB: 5KB0). The Cu(I) environment is 3- or 4-coordinate based on XAS analysis, or more likely a mix of these coordination environments. A trigonal planar Cu(I) His_3 environment is shown in Figure 5-21 with bond distances of ~2.02 Å. In the Cu(II) bound form, the coordination number increases with an axial Cu(II) EPR environment. As such, the oxidized species may have the same His coordination environment but with axial solvent ligands, increasing the coordination number to 5 (Figure 5-22).

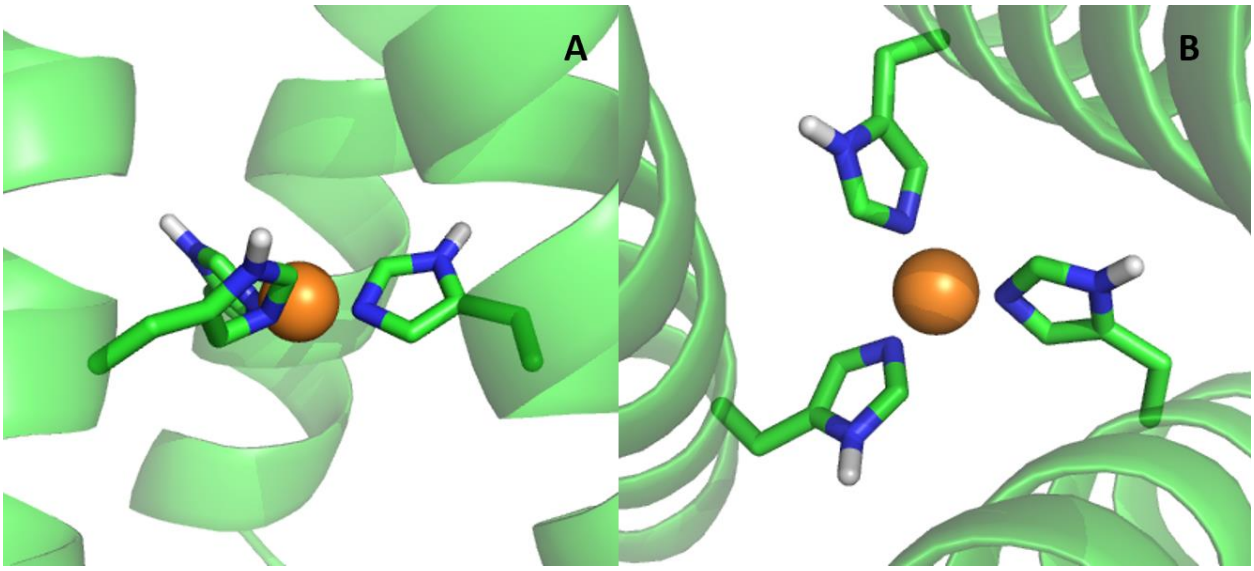

Figure 5-21 Pymol models of Cu(I) bound His_3^a with side view (a) and top down view (b) based on the structure 5KB0

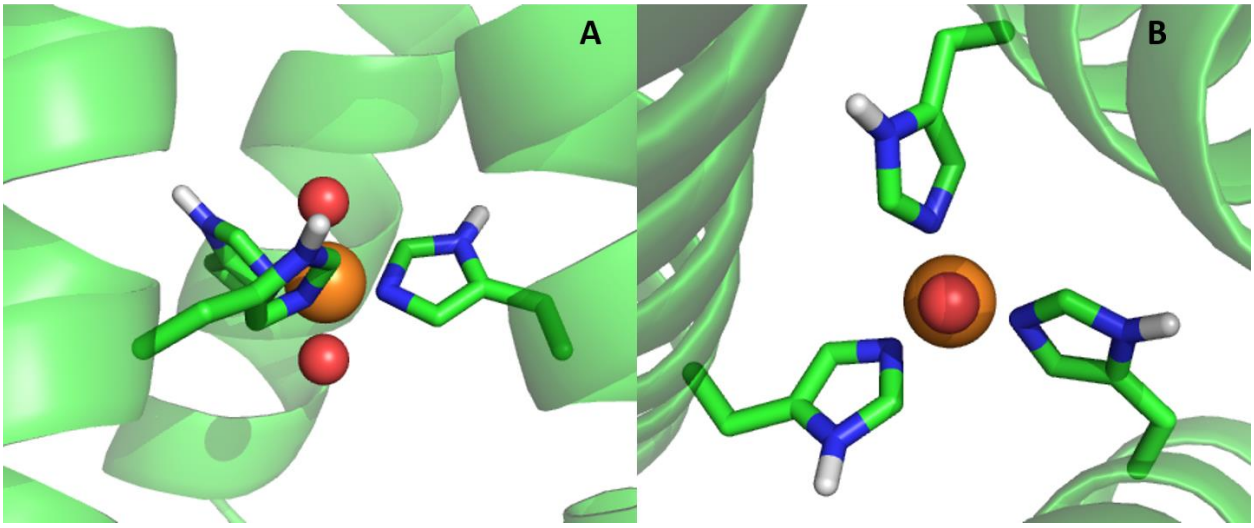

Figure 5-22 Pymol models of Cu(II) bound His_3^a with side view (a) and top down view (b) based on the structure 5KB0

With a mix of **a** and **d** His residues, the His_3 plane is shifted to span the two layers. A Pymol model of $His_1^dHis_2^a$ was generated based on the structure 5KB0. In the Cu(I) bound state, the copper ion has a similar His_3 environment to His_3^a (Figure 5-23). In the Cu(II) bound form, this His_3 environment is maintained, but additional solvent molecules may coordinate as both axial and equatorial ligands (Figure 5-24) or possibly still as axial ligands. The difference in rates for the His_3 heterotrimers may be due to the structure of these systems as the Cu(I) environment is slightly more stabilized than His_3^a and solvation necessary for the Cu(II) environment may be less energetically intensive as it is closer to the helical interface than for the His_3^a homotrimer.

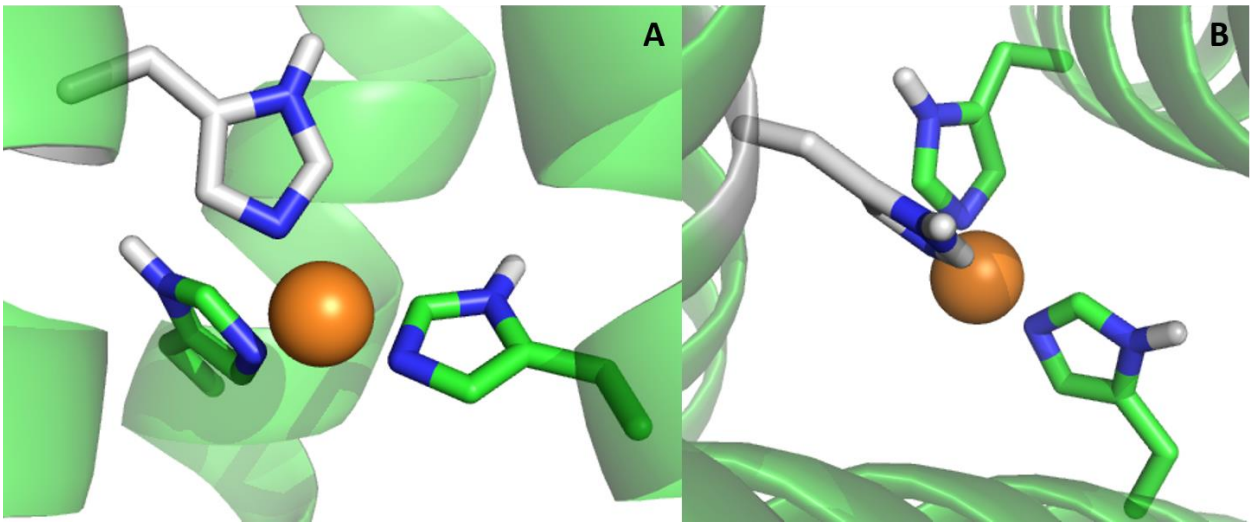

Figure 5-23 Pymol models of Cu(I) bound $His_1^dHis_2^a$ with side view (a) and top down view (b) based on the structure 5KB0

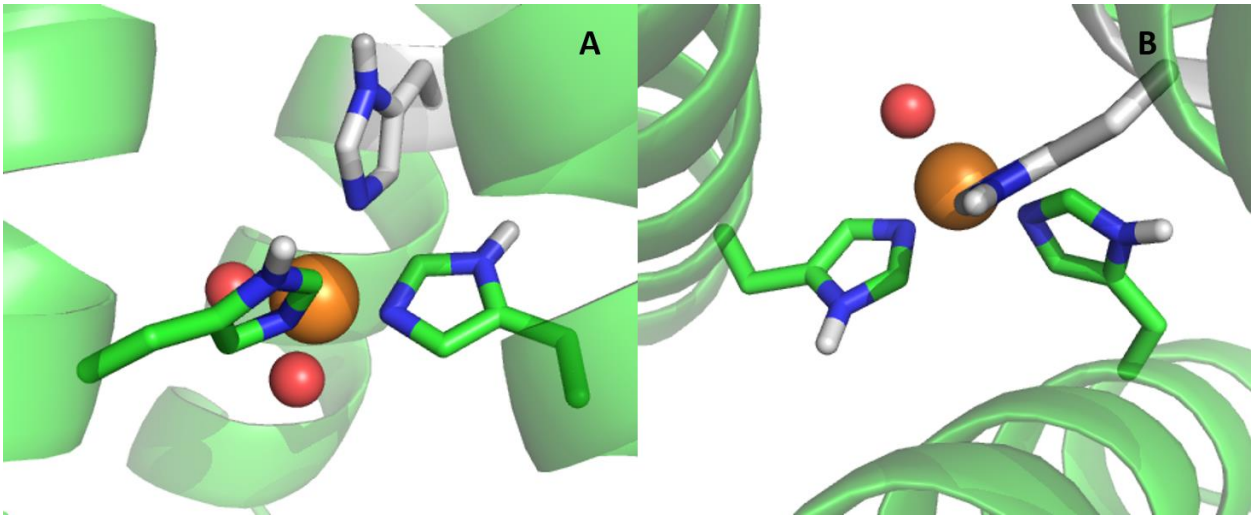

Figure 5-24 Pymol models of Cu(II) bound $His_1^dHis_2^a$ with side view (a) and top down view (b) based on the structure 5KB0

The His_3^d homotrimer stabilizes the Cu(I) environment over the Cu(II) environment as compared to His_3^a. This results in a more positive reduction potential, further from the ideal potential for the dismutation of superoxide. A Pymol model of this site was not generated as the addition of His residues is known to increase the interhelical distances.[22] It seems likely that the Cu(I) and Cu(II) coordination environments are similar to His_3^a based on all spectroscopic characterizations described in Chapter 3. The difference in activity may be attributed to different nitrogen coordination (delta vs. epsilon) or due to the relative destabilization of the Cu(II) environment. The **d** layer is further removed from the frayed C-termini of the 3SCC, which may induce a larger energetic barrier to solvate this site in the Cu(II) bound form. Ultimately, a crystal structure of this site is needed to determine this.

This difference may also be due to the relative stabilization of Cu(II) vs. Cu(I) bound forms in the His_3 systems and the thermodynamics of their interconversion. If the rate limiting step for this reaction is the reduction of superoxide by Cu(I) to return to the Cu(II) state, the difference between His_3^a and His_3^d may be due to the rearrangement necessary to solvate and desolvate the catalytic copper. The fraying of the 3SCC at the C-terminus allows for easy solvation below the His_3^a plane, stabilizing the Cu(II) bound form more than Cu(II)-His_3^d. The **d** site is closer to the midpoint of the 3SCC than His_3^a, possibly resulting in a larger energetic barrier to the solvation of the His_3^d site within the hydrophobic core. This thermodynamic barrier may, therefore, result in faster conversion of His_3^d from Cu(II) to Cu(I) relative to His_3^a and slower conversion of Cu(I) to Cu(II). Once this species is solvated, however, substrate binding is

facilitated by this polar environment, contributing to fast rates of superoxide reduction by Cu(I). Again, crystal structures of both Cu(I) and Cu(II) coordinated His_3^a and His_3^d as well as computational studies to determine stability of these complexes would aid in this determination.

This work presents an interesting contrast to the work done by Dr. Melissa Zastrow with Zn(II) coordinated TRI His_3^a and TRI His_3^d as a study of CA activity. She found that there was no difference in catalytic efficiency between the **a** and **d** sites for this reaction.[23] Throughout this thesis, I have described the significance of altered metal coordination environments in **a** and **d** sites for heterotrimer selectivity with Pb(II) and for SOD activity with Cu(I/II), but this work shows that the preferred metal coordination environment and the type of chemistry performed is also important when considering heptad placement. Zn(II) is likely 4-coordinate tetrahedral, regardless of the available ligands within these 3SCCS while Pb(II) is trigonal pyramidal and copper cycles between 3- and 5-coordinate depending on the oxidation state and ligand environment. Mechanisms for CA activity also suggest that the reaction may be catalyzed without a change in Zn(II) coordination number, while the redox reaction catalyzed by Cu-only SOD requires a change in coordination number.[24] The static nature of the Zn(II) ion, therefore, is less influenced by the surrounding protein environment than copper. As this work serves to probe the structure function relationship, particularly with regard heptad placement, these results show that one must consider both the ligand environment and the metal geometry when designing an active site.

The His_4 models have rates of superoxide dismutation that are intermediate between the His_3^a and His_3^d models, though with very large errors due to inconsistencies between trials. All experimental conditions were maintained between trials, suggesting an inconsistency in copper coordination within the 3SCC rather than an inconsistency in the assay itself. While one cannot make any definitive conclusions based on these results, this work does suggest that the inclusion of more His^d residues does not necessarily indicate an increase in rate as shown in the His_4 constructs. The Cu(I) pre-edge feature is significantly less intense for both $His_3^dHis_1^a$ and $His_1^dHis_3^a$ than for either His_3^a or His_3^d, so these species may have a higher proportion of 4-coordinate copper in the reduced form. Both His_4 species also have a much less stable Cu(I) binding affinity than the His_3 homotrimers. It is possible, therefore, that there are several different Cu(I) binding environments consisting of both His_3 and His_4 environments, leading to a large error in rate determination. This is reflected in the Cu(I) affinity of $His_3^dHis_1^a$, which is

three orders of magnitude weaker than His_3^d. If only a single His_3 species were present in this system, one would expect the affinity to be at least as tight as His_3^d as those ligands are available for Cu(I) binding. Instead, either a loss of stability in the His^dHis^a strand or the presence of a second, 4-coordinate Cu(I) environment must be considered to explain this decrease in affinity.

The addition of Asp residues improved upon the His_3^a site, but not upon the His_3^d site. $Asp_3^dHis_3^a$ was twice as fast as the His_3^a homotrimer with a redox potential that is ~60 mV more positive. The spectroscopic properties of these two homotrimers were not significantly different, but the addition of negatively charged residues in close proximity to the active site may allow for solvation of the Cu(II) bound form with a lower energy barrier than in His_3^a in which the neighboring residues are all hydrophobic leucine. Pymol models of $Asp_3^dHis_3^a$ system show that the Cu(I) environment is likely very similar to the Cu(I) environment of His_3^a (Figure 5-25). The Cu(II) environment is also very similar, with axial solvent molecules. The Asp carboxylate may be able to form a hydrogen bond with a solvent molecule, but cannot directly coordinate the copper and still maintain the Cu(II)His_3 plane (Figure 5-26). Note that the Asp-His distance is too great for a hydrogen bond to occur between these residues.

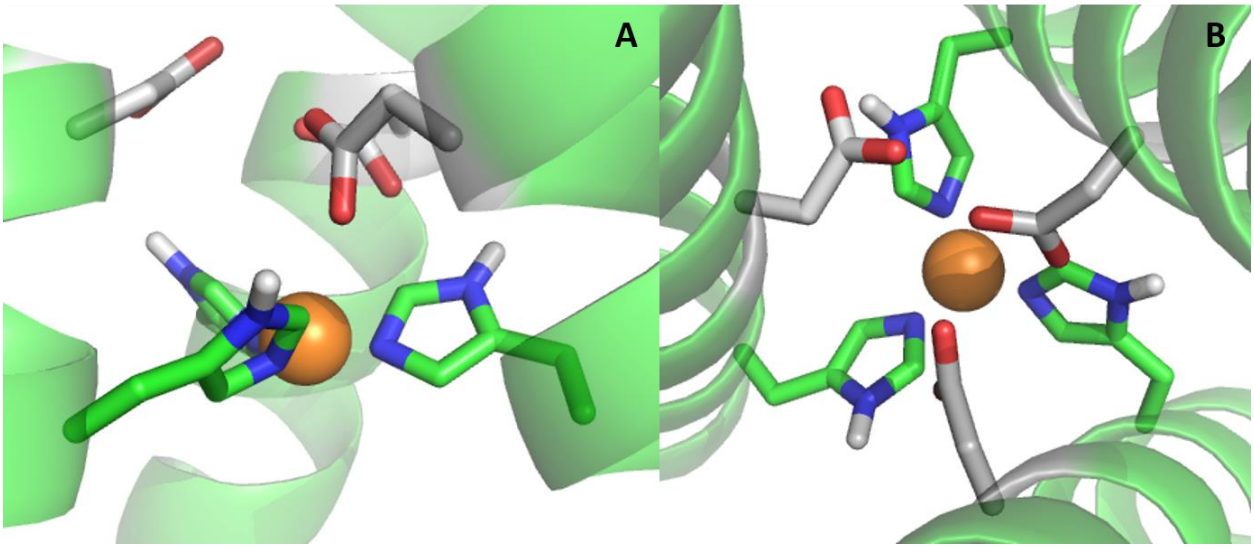

Figure 5-25 Pymol models of Cu(I) bound $Asp_3^dHis_3^a$ with side view (a) and top down view (b) based on the structure 5KB0

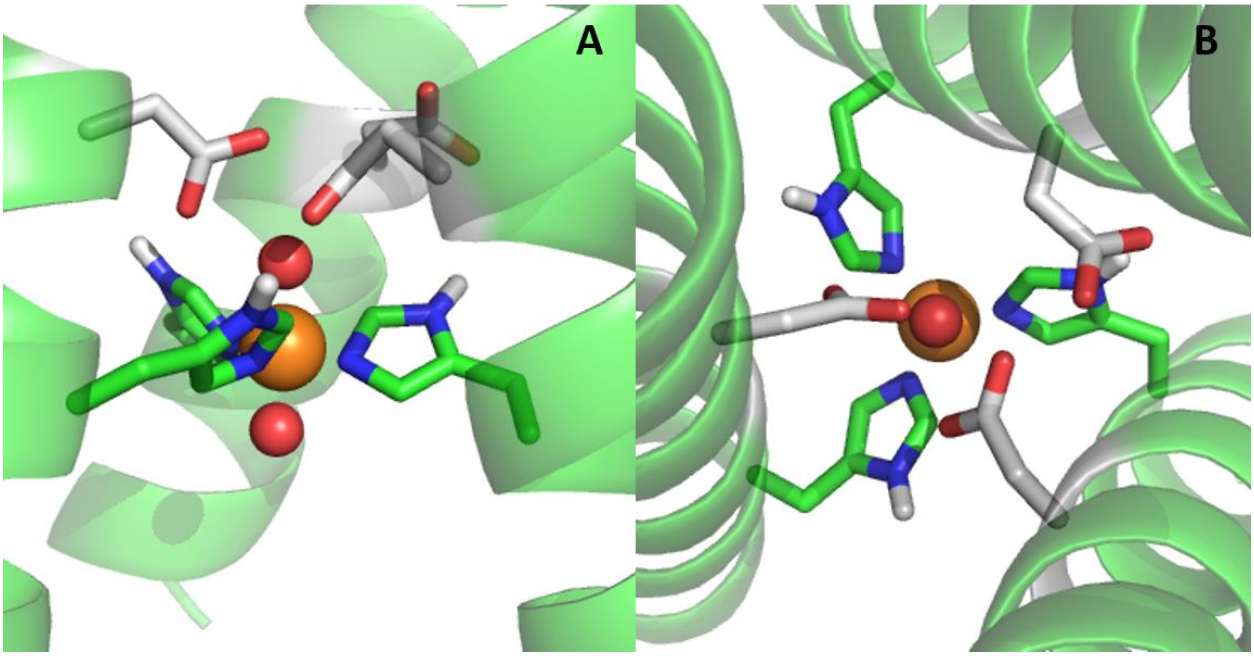

Figure 5-26 Pymol models of Cu(II) bound $Asp_3^dHis_3^a$ with side view (a) and top down view (b) based on the structure 5KB0

$Asp_2^dHis_3^a$ is spectroscopically and kinetically similar to $Asp_3^dHis_3^a$. $Asp_1^dHis_3^a$, however, is twice as fast as $Asp_3^dHis_3^a$. This construct also more weakly stabilizes the Cu(I) environment than $Asp_3^dHis_3^a$. The Cu(I) environment is largely unchanged from the previously discussed constructs (Figure 5-27). The Cu(II) environment may be more strongly favored as the polar solvent molecule is not in close proximity to as many carboxylate residues (Figure 5-28). By more strongly stabilizing the Cu(II) environment, this may shift the redox potential closer to the ideal value for SODs.

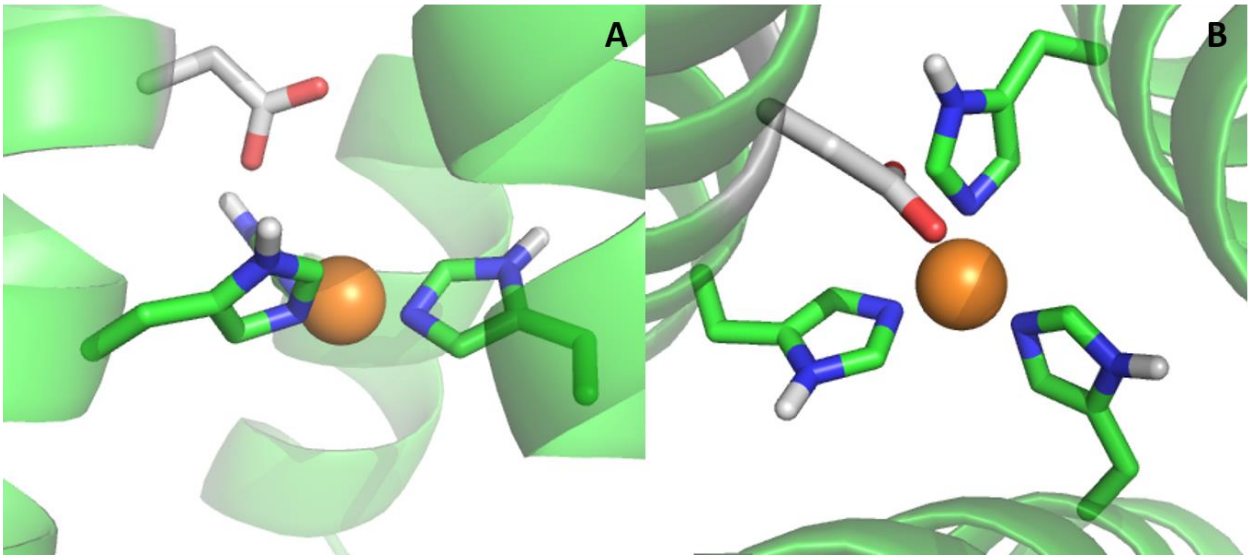

Figure 5-27 Pymol models of Cu(I) bound $Asp_1{}^dHis_3{}^a$ with side view (a) and top down view (b) based on the structure 5KB0

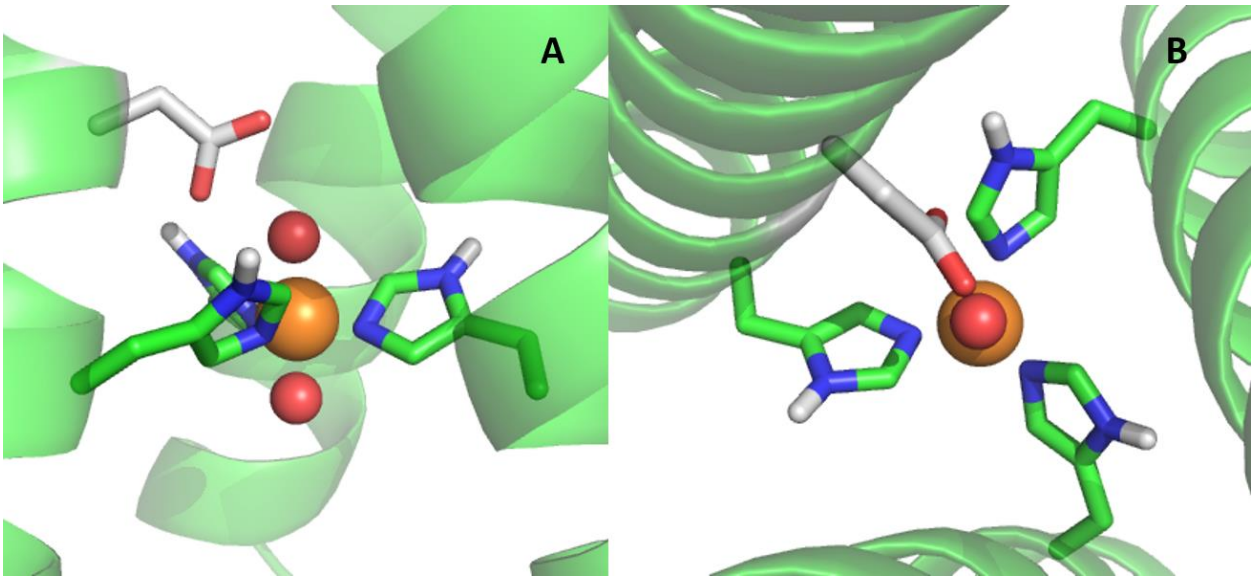

Figure 5-28 Pymol models of Cu(II) bound $Asp_1{}^dHis_3{}^a$ with side view (a) and top down view (b) based on the structure 5KB0

Interestingly, the addition of Asp residues below the $His_3{}^d$ plane did not have the same effect. Neither $His_3{}^dAsp_1{}^a$ or $His_3{}^dAsp_3{}^a$ were better at catalyzing the dismutation of superoxide than $His_3{}^d$ alone. As such, further spectroscopic characterization of these peptides was not done. It is possible that these Asp residues further increased the reduction potential above $His_3{}^d$ to a less suitable range for SOD activity. Copper affinities will need to be collected to determine the accuracy of this claim. Ultimately, these results enforce the finding that **a** and **d** residues are not equivalent in catalysis, and likely in metal coordination environments. This work has also not

considered the effect of metal binding residues in the **a** site above (N-terminal to) the **d** site. Studies by Dr. Karl Koebke with Cu NiR in TRI His_3^a showed that copper catalysis was affected by mutations in the **d** site both above and below (C-terminal to) the **a** site. The rate enhancement was ~75 fold for both $Asp_3^dHis_3^a$ and $His_3^aAsp_3^d$, though $His_3^aAsp_3^d$ was slightly better. As described in Chapter 3, the same is not true for Co(II) coordination, likely because the Co(II) sits above the His_3^a plane, while Cu(I) may be in the His_3^a plane. Thus, in the case of copper coordination, future studies should consider the introduction of metal binding residues above His_3^d to enhance catalysis. The work done by Dr. Koebke also explored the effect of methylated His residues on NiR catalysis and found that delta-methyl His enhanced the rate by a factor of 2.3 while epsilon methyl His enhanced the rate 300-fold. This work suggests that the difference in rate between His_3^d and His_3^a may be due to nitrogen coordination. The crystallographic studies performed by Dr. Leela Ruckthong on Cys residues in **a** and **d** sites (discussed in Chapter 2) found that the heptad position dictated Cys side chain angle. The same is likely true for His residues. X-ray crystallography of His_3^a showed epsilon nitrogen coordination to Zn(II).[25] A crystal structure of His_3^d may indeed show that the His side chain orients differently within the coiled coil, affording delta nitrogen coordination.

The final Asp containing systems that were investigated contained His_2Asp planes with an additional His residue, which is reminiscent of Fe/Mn SOD active sites. This work showcases the underlying theme of my work that **a** and **d** residues are not equivalent when considering metal binding (whether Pb(II) or a transition ion). $His_1^dAsp_1^aHis_2^a$ was the slowest of all constructs described herein. $His_2^dAsp_1^dHis_1^a$, which presents an identical stoichiometric environment in which the **a** and **d** layers are switched, was the fastest of all constructs described herein. No spectroscopic characterization was performed on $His_1^dAsp_1^aHis_2^a$ because the rate was so slow relative to all other constructs. $His_2^dAsp_1^dHis_1^a$ did not have any spectroscopic features that were unique and had a Cu(I) binding affinity intermediate between His_3^a and His_3^d. This suggests that the Cu(II) affinity may also be intermediate so the redox potential would be less positive than the more active His_3^d, but still not approaching the ideal 360 mV. Instead, a structural feature may account for these differences in rate. If the His_3^d peptide does have a different nitrogen coordination to His_3^a it is possible that a primary Cu(I) coordination environment of His_2Asp is beneficial and the barrier to an increased coordination number in the Cu(II) bound state is

relatively low. Ultimately, X-ray crystallographic data would be needed to address this hypothesis.

The final constructs considered in this work were glutamate containing trimers. The $Glu_3^dHis_3^a$ homotrimer had a similar redox potential to $Asp_3^dHis_3^a$ though it was about twice as active. All three Glu containing trimers had large errors in rate determination due to error in determining the IC_{50} value in each trial. As such, there is no significant difference in rate between the three trimers. A Pymol model of $Glu_1^dHis_3^a$ based on the structure of 5KB0 was generated to elucidate the features responsible for these rates. The Cu(I) bound form is like that of all other previously described systems, but the Glu residue is able to hydrogen bond to the His residue on an adjacent strand at 2.4 Å (Figure 5-29). This does not preclude Cu(I) coordination as the copper is within the His_3 plane. The Cu(II) bound form can maintain this hydrogen bond, as is depicted in Figure 5-30 or the Glu may be able to directly coordinate the Cu(II). A similar environment is expected for $Glu_2^dHis_3^a$ and $Glu_3^dHis_3^a$. The ability of the Glu to either hydrogen bond with a His residue or to coordinate Cu(II) may account for some variability in rate. The XAS data of $Glu_3^dHis_3^a$ also suggests that Pb(II) and Cu(I) are able to coordinate to either the sulfur site or the carboxylate site, which results in a lower relative CuN/O concentration than expected. This work has not explored the kinetics of copper in a Cys_3 environment to determine if this is a further compounding variable.

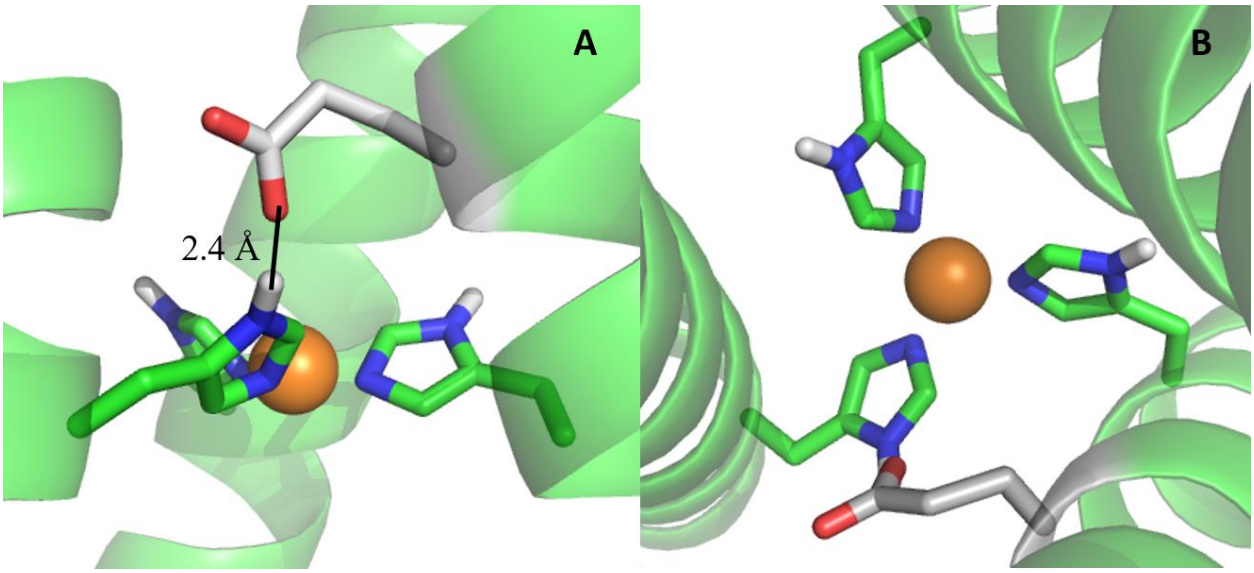

Figure 5-29 Pymol models of Cu(I) bound $Glu_1^dHis_3^a$ with side view (a) and top down view (b) based on the structure 5KB0

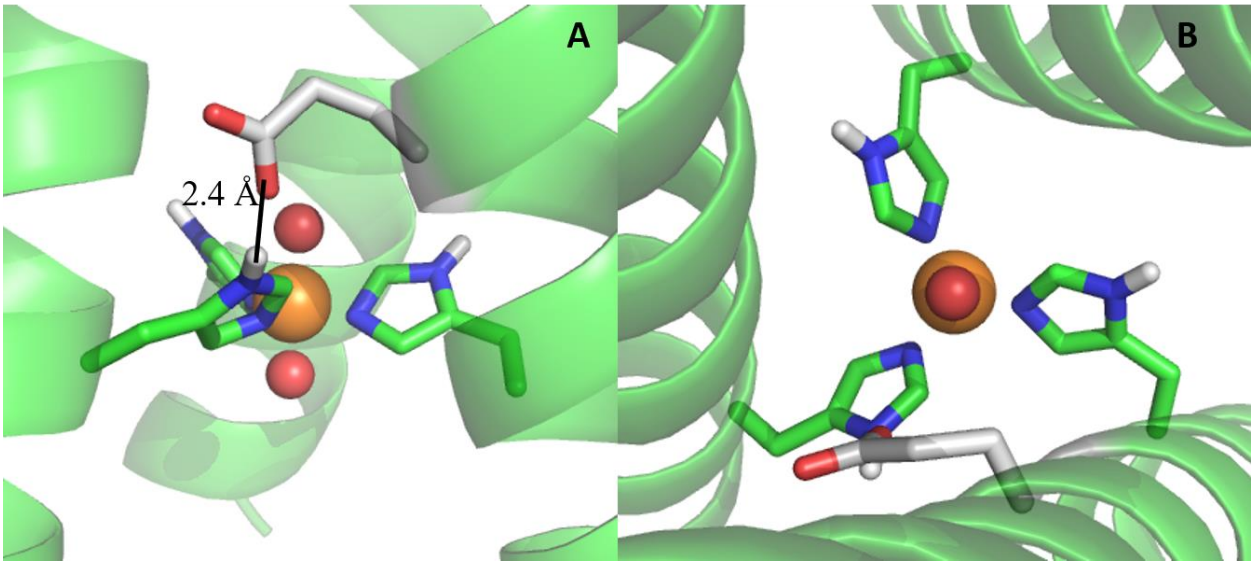

Figure 5-30 Pymol models of Cu(II) bound $Glu_1{}^dHis_3{}^a$ with side view (a) and top down view (b) based on the structure 5KB0

Conclusion

This work has investigated the role of histidine and carboxylate residues and their position (**a** vs. **d** site) on SOD activity. This built upon the previously characterized $His_3{}^a$ site to include His^d residues and carboxylate residues in both **a** and **d** positions. Ultimately, this work showed that an increase in His^d residues correlated with an increase in SOD activity despite shifting the potential further from the theoretical ideal. $His_3{}^d$ was ~7.5x faster than $His_3{}^a$, with $His_1{}^dHis_2{}^a$ and $His_2{}^dHis_1{}^a$ at intermediate rates. His_4 models did not follow this correlation due to likely disorder in the copper binding environment and decreased stability of the His^dHis^a strand. Similarly, Glu containing peptides were likely too disordered to give reliable kinetic results.

The His_3 peptides were all spectroscopically similar with both coordinated Cu(I) and Cu(II), but $His_3{}^d$ has a reduction potential ~150 mV more positive than $His_3{}^a$. This more positive potential is further from the midpoint of the oxidation and reduction of superoxide, but the enhanced kinetics may be due to a faster interconversion of the Cu(II) and Cu(I) states in the **d** site. This site is less solvent exposed as it is closer to the center of the 3SCC, so may desolvate to the Cu(I) form faster than $His_3{}^a$. With intermediate rates, the $His_3{}^a$ heterotrimers may also have intermediate rates of solvation. Structures of both Cu(I) and Cu(II) bound $His_3{}^d$ and $His_3{}^a$ are necessary to determine the coordination environment and may be used to computationally determine the energy barriers for their interconversion.

The addition of Asp residues also increased the rate over His_3^a but not over His_3^d. For an Asp residue to improve upon His_3^d, it must be in a **d** site with the third His in an **a** position ($His_2^dAsp_1^dHis_1^a$). This construct is the best designed Cu-only SOD to date but more closely resembles the active site of Fe/Mn SODs. This may be due to structural factors or because the redox potential for other Asp containing His_3^d peptides is too positive to catalyze this reaction. To determine the underlaying factor contributing to this rate increase both a redox potential and a structure of His_3^d and Asp containing heterotrimers would be needed.

This work shows the importance of residue position on catalysis despite minimal differences in spectroscopy. Based on results with **a** and **d** Cys residue orientation, this may be due to differences in His orientation, allowing for preferential delta or epsilon nitrogen coordination depending on heptad position. Work with TRI His_3^a showed ~300x rate enhancement for NiR activity with delta nitrogen coordination over His_3^a and epsilon nitrogen coordination. Thus, it is likely that this rate enhancement is due to an increase in delta nitrogen coordination, which would not have significant spectroscopic differences using the techniques discussed herein. This work will require crystallographic data of the His_3^d construct to determine the structural factors contributing to this difference.

This work is particularly interesting in the context of all the work previously done in the Pecoraro group for CA activity, which showed no difference in catalytic efficiency for His_3^a and His_3^d sites with Zn(II). This shows that one must consider the metal, its coordination environment, and the desired activity when determining heptad placement for active sites. As discussed in Chapter 4, Zn(II) remains 4-coordinate regardless of the ligand environment, while copper undergoes a coordination number change throughout the catalytic cycle, requiring different flexibilities within the protein scaffold. The copper ion requires changing solvation as well as ligand orientation which is better accommodated in His_3^d than His_3^a, requirements that need not be considered for Zn(II) hydrolytic activity. Thus, this work has shown the importance of **a** vs **d** site ligand placement and also the differences in successful catalysis depending on the type of chemistry being performed.

References

1. McCord, J. M.; Fridovich, I., Superoxide Dismutase: An enzymatic function for erythrocuprein (hemocuprein). *The Journal of Biological Chemistry* **1969,** *244* (22), 6049-6055.

2. Barondeau, D. P.; Kassmann, C. J.; Bruns, C. K.; Tainer, J. A.; Getzoff, E. D., Nickel Superoxide Dismutase Structure and Mechanism. *Biochemistry* **2004,** *43*, 8038-8047.

3. Wuerges, J.; Lee, J.-W.; Yim, Y.-I.; Yim, H.-S.; Kang, S.-O.; Carugo, K. D., Crystal structure of nickel-containing superoxide dismutase reveals another type of active site. *Proceedings of the National Academy of Sciences* **2004,** *101* (23), 8569–8574.

4. Tainer, J. A.; Hallewell, R. A.; Parge, H. E., Atomic structures of wild-type and thermostable mutant recombinant human Cu,Zn superoxide dismutase. *Proceedings of the National Academy of Sciences* **1992,** *89*, 6109-6113.

5. Tainer, J. A.; Getzoff, E. D.; Beem, K. M.; Richardson, J. S.; Richardson, D. C., Determination and Analysis of the 2 A Structure of Copper, Zinc Superoxide Dismutase. *J. Mol. Biol.* **1982,** *160*, 181-217.

6. Banci, L.; Bertini, I.; Cramaro, F.; Del Conte, R.; Viezzoli, M. S., The solution structure of reduced dimeric copper zinc superoxide dismutase. The structural effects of dimerization. *Eur. J. Biochem.* **2002,** *269* (7), 1905-15.

7. Gleason, J. E.; Galaleldeen, A.; Peterson, R. L.; Taylor, A. B.; Holloway, S. P.; Waninger-Saroni, J.; Cormack, B. P.; Cabelli, D. E.; Hart, P. J.; Culotta, V. C., Candida albicans SOD5 represents the prototype of an unprecedented class of Cu-only superoxide dismutases required for pathogen defense. *Proc. Natl. Acad. Sci. U. S. A.* **2014,** *111* (16), 5866-5871.

8. Kardinahl, S.; Anemuller, S.; Schafer, G., The hyper-thermostable Fe-superoxide dismutase from the archaeon Acidianus ambivalens: Characterization, recombinant expression, crystallization and effects of metal exchange. *Biol. Chem.* **2000,** *381* (11), 1089-1101.

9. Kerfeld, C. A.; Yoshida, S.; Tran, K. T.; Yeates, T. O.; Cascio, D.; Bottin, H.; Berthomieu, C.; Sugiura, M.; Boussac, A., The 1.6 Å resolution structure of Fe-superoxide dismutase from the thermophilic cyanobacterium Thermosynechococcus elongatus. *J. Biol. Inorg. Chem.* **2003,** *8* (7), 707-714.

10. Yu, J.; Yu, X.; Liu, J., A thermostable manganese-containing superoxide dismutase from pathogenChlamydia pneumoniae. *FEBS Lett.* **2004,** *562* (1-3), 22-26.

11. Hart, P. J.; Balbirnie, M. M.; Ogihara, N. L.; M., N. A.; Weiss, M. S.; Valentine, J. S.; Eisenberg, D., A Structure-Based Mechanism for Copper-Zinc Superoxide Dismutase. *Biochemistry* **1999,** *38*, 2167-2178.

12. Peterson, R. L.; Galaleldeen, A.; Villarreal, J.; Taylor, A. B.; Cabelli, D. E.; Hart, P. J.; Culotta, V. C., The Phylogeny and Active Site Design of Eukaryotic Copper-only Superoxide Dismutases. *J. Biol. Chem.* **2016,** *291* (40), 20911-20923.

13. Perry, J. J.; Shin, D. S.; Getzoff, E. D.; Tainer, J. A., The structural biochemistry of the superoxide dismutases. *Biochim. Biophys. Acta* **2010,** *1804* (2), 245-62.

14. Mathieu, E.; Tolbert, A. E.; Koebke, K. J.; Tard, C.; Iranzo, O.; Penner-Hahn, J.; Policar, C.; Pecoraro, V. L., Rational De Novo Design of a Cu-Metalloenzyme for Superoxide Dismutation. *Chem.--Eur. J.* **2019,** *26*, 249-258.

15. Cangelosi, V. M.; Deb, A.; Penner-Hahn, J. E.; Pecoraro, V. L., A de novo designed metalloenzyme for the hydration of CO2. *Angewandte Chemie - International Edition* **2014,** *53* (30), 7900-7903.

16. Walsh, S. T. R.; Cheng, H.; Bryson, J. W.; Roder, H.; DeGrado, W. F., Solution structure and dynamics of a de novo designed three-helix bundle protein. *Proc. Natl. Acad. Sci. U. S. A.* **1999,** *96* (10), 5486-5491.

17. *Fmoc Solid Phase Peptide Synthesis: A Practical Approach*. 2 ed.; Oxford University Press: New York, 2000.

18. Xiao, Z.; Brose, J.; Schimo, S.; Ackland, S. M.; La Fontaine, S.; Wedd, A. G., Unification of the copper(I) binding affinities of the metallo-chaperones Atx1, Atox1, and related proteins: detection probes and affinity standards. *The Journal of biological chemistry* **2011,** *286* (13), 11047-55.

19. Atkins, P.; Overton, T.; Rourke, J.; Weller, M.; Armstrong, F.; Hagerman, M., *Inorganic Chemistry*. Fifth Edition ed.; Oxford University Press, W. H. Freeman and Company: New York, 2010.

20. Tegoni, M.; Yu, F.; Bersellini, M.; Penner-Hahn, J. E.; Pecoraro, V. L., Designing a functional type 2 copper center that has nitrite reductase activity within α-helical coiled coils. *Proceedings of the National Academy of Sciences* **2012,** *109* (52), 1-6.

21. Policar, C., In *Redox Active Therapeutics*, Reboucas, J. S.; Batinic-Haberle, I.; Spasojevic, I.; Warner, D. S.; St. Clair, D., Eds. Springer: 2016; pp 125-164.

22. Ruckthong, L. Crystallographic comparison of tris-thiolate sites in designed proteins to control metal geometries. University of Michigan, Ann Arbor, MI, 2016.

23. Zastrow, M. L.; Pecoraro, V. L., Influence of active site location on catalytic activity in de novo-designed zinc metalloenzymes. *J. Am. Chem. Soc.* **2013,** *135* (15), 5895-903.

24. Lindskog, S., Structure and Mechanism of Carbonic Anhydrase. *Pharmacol. Ther.* **1997,** *74* (1), 1-20.

25. Zastrow, M. L.; Peacock, A. F.; Stuckey, J. A.; Pecoraro, V. L., Hydrolytic catalysis and structural stabilization in a designed metalloprotein. *Nat. Chem.* **2011,** *4* (2), 118-23.

Chapter 6 Future Directions

One of the biggest problems in biology is the question of the relationship between protein structure and function. There are two main areas of research within the protein biochemistry community meant to elucidate this relationship: *de novo* protein design and protein redesign. *De novo* design investigates this relationship by building, from first principles, protein structures in order to determine the aspects that contribute to function. Protein redesign utilizes native proteins with additional mutations to increase or change functionality. The work discussed herein has all focused on the *de novo* design of metalloproteins that are capable of performing both hydrolytic and redox catalysis. The Pecoraro lab has previously had great success in this field using a simple alpha-helical coiled-coil scaffold. This work has included the design of the best aqueous model of zinc carbonic anhydrase using a His_3 binding site.[1] This His_3 binding site also successfully performs redox catalysis with a coordinated copper ion as a model of nitrite reductase.[2] All this work, however, has been limited by the symmetry of the 3SCC scaffold. This scaffold is inherently three-fold symmetric and cannot incorporate a single mutation to either the first or second metal coordination spheres, though such asymmetry is commonplace in native systems. My work has focused on incorporating this asymmetry to improve upon previous three-fold symmetric models and to expand the scope of activities explored.

Asymmetric scaffold design

In order to do this work, I began by describing the first fully selective, self-assembling, heterotrimeric 3SCC. A previous graduate student, Dr. Catherine Mocny, successfully characterized the first self-assembling, asymmetric 3SCCs using only a Cys^a binding site, Pb(II), and an adjacent **d** layer of mixed Leu and Ala residues (see Table 6-1 for a list of sequences). The Leu residues provide stability via hydrophobic packing within the core of the 3SCC, while the Ala residues provide stability because the smaller residue allows space for water to hydrogen bond to the Cys sulfur atom. These asymmetric scaffolds could then incorporate a transition metal for catalysis at a distant binding site. This was groundbreaking work in the field of protein design, but still left room for improvement as this design is unable to achieve full selectivity with

both A_2B- and AB_2-type heterotrimers. This distinction is necessary as the total number of allowed mutations in each strand is limited to maintain stability. The fully selective heterotrimer contained 2 Ala^dCys^a strands and 1 Cys^a strand at the Pb(II) binding site as well as a distant His_3^a site for transition metal binding. Thus, only a single additional residue could be incorporated on the Cys^a strand to maintain stability of the trimer, limiting the asymmetric studies to X_1H_3 sites, where X is any residue.

*Table 6-1 Peptide sequences discussed in this chapter with mutations in at the lead binding site in **bold green** and mutations at the transition metal binding site in **bold red***

Peptide	Sequence
Cys^a	Ac-G WKALEEK LKALEEK **C**KALEEK LKALEEK LKALEEK G-NH_2
Ala^dCys^a	Ac-G WKALEEK LKA**A**EEK **C**KALEEK LKALEEK LKALEEK G-NH_2
Cys^d	Ac-G WKALEEK LKA**C**EEK LKALEEK LKALEEK LKALEEK G-NH_2
Cys^dAla^a	Ac-G WKALEEK LKA**C**EEK **A**KALEEK LKALEEK LKALEEK G-NH_2
His^a	Ac-G WKALEEK LKA**C**EEK **A**KALEEK LKALEEK **H**KALEEK G-NH_2
His^d	Ac-G WKALEEK LKA**C**EEK **A**KALEEK LKA**H**EEK LKALEEK G-NH_2
Asp^dHis^a	Ac-G WKALEEK LKA**C**EEK LKALEEK LKA**D**EEK **H**KALEEK G-NH_2
Glu^dHis^a	Ac-G WKALEEK LKA**C**EEK LKALEEK LKA**E**EEK **H**KALEEK G-NH_2
Ile^dHis^a	Ac-G WKALEEK LKA**A**EEK **C**KALEEK LK**I**EEK **H**KALEEK G-NH_2
Phe^dHis^a	Ac-G WKALEEK LKA**A**EEK **C**KALEEK LK**F**EEK **H**KALEEK G-NH_2

In chapter 2 I described a similar system to generate heterotrimers, but with Cys^d residues instead of Cys^a residues. This modification exploited the different orientation of **a** and **d** residues because, though they are both interior positions within the 3SCC, these layers are not directly in line with one another. Cys^d heterotrimers are fully selective for both A_2B and AB_2 heterotrimers, allowing for further control of the distant asymmetric transition metal binding site. Further work in both the Cys^a and Cys^d based heterotrimers showed that similar selectivity is maintained at another interior heptad. This allows for further control of the transition metal site as it can be moved within the 3SCC to exploit differences in catalytic properties at different positions[3] by moving the location of the Pb(II) binding site.

The differences in heterotrimer selectivity were investigated through both crystallographic and computational methods. X-ray crystallography of homotrimeric peptides showed that the selectivity differences of Cys^a and Cys^d peptides was likely due to the organization of the water molecules in $Ala_3^dCys_3^a$ and $Cys_3^dAla_3^a$. In $Ala_3^dCys_3^a$, the water molecules were oriented along the helical interface allowing for hydrogen bonding to both adjacent Cys residues. In $Cys_3^dAla_3^a$, however, the solvent molecules align closer to the helical

core, directly below (C-terminal to) each Cys residue, allowing for coordination to only a single Cys residue. Computational studies supported this work, finding that the most stable trimer is the 2 Ala:1 Leu heterotrimer for both Cys^a and Cys^d systems. The Cys^d systems, however, had a larger energy gap between the two heterotrimers than Cys^a systems, contributing to the selectivity of both A_2B and AB_2 heterotrimers. Thus, this work has shown that fully selective, self-assembling asymmetric 3SCCs can be achieved using only a Cys^d layer, Pb(II), and an adjacent layer of mixed Ala and Leu residues.

There remains a great deal of work that can be done to advance our understanding of Pb(II) binding to these sites and to the formation of heterotrimers. First, it remains to be determined why the pK_a of Pb(II) binding to GR Cys^d systems is significantly more acidic than all previously described systems. Work described in Chapter 2 showed that the pH dependence of lead binding is not due to solely to the deprotonation of Cys residues in 3SCCs, but is instead occurring simultaneously to the formation of 3SCCs from 2SCCs. pH dependent analytical ultracentrifugation could be performed to determine the exact pH profile of this 2SCC to 3SCC shift as the previously determined pK_a of 4.5 may be inaccurate for these systems since the 3SCCs described herein do not show formation of $Pb(II)S_3$ until pH ~5.5.[4]

The formation of heterotrimers has also been shown to be metal dependent. Dr. Mocny showed that trigonal planar Hg(II) does not afford selective heterotrimer formation.[5] It was also hypothesized that Cd(II), that can form 3- to 5-coordinate complexes, would be unsuitable for heterotrimer formation. As we now know that the solvation of the Pb(II) environment is key for stability and selectivity of the heterotrimers, a coordination environment that cannot be controlled will likely not lead to heterotrimer formation. It remains undetermined, however, if any trigonal pyramidal metal ion will template selective heterotrimers. As(III) also complexes Cys_3 in a trigonal pyramid, but has not been investigated for this purpose. A 3+ cation instead of the characterized 2+ cation will more strongly polarize the metal-Cys bond. A more strongly polarized Cys-S will form a more stable hydrogen bond, though it is difficult to say if a stronger hydrogen bond will aid in or preclude heterotrimer formation. As(III) is also significantly smaller than Pb(II) which may change the stability of the Cys_3^d homotrimer. Thus, heterotrimers may be scaffolded with As(III), though the relative stabilities of the heterotrimers may be different than Pb(II) scaffolded heterotrimers. Of course, the hope would be that the enhanced hydrogen bonding could allow high selectivity for Cys_3^a peptides as now found for Cys_3^d peptides.

This would allow for more flexibility in uses for heterotrimers as Dr. Mocny described Pb(II)-catalyzed pNPA hydrolysis in Cys^a systems.[5] Such non-innocence is not observed in Cys^d systems, likely due to the altered Cys ligand orientation and solvent networks which either prevent substrate access or alter polarizability. As(III)-coordinated 3SCCs have also successfully been interrogated by MALDI-TOF MS, which are the only 3SCCs the Pecoraro group has been able to characterize by mass spectrometry.[6-7] MS characterization of heterotrimers would further solidify the work described herein. As(III), however, has a spin 3/2 nucleus with only a 600 ppm chemical shift range which may make detection of heterotrimers by NMR more difficult if the species have similar chemical shift values.[8] As(III) also binds to Cys_3 sites much slower than Pb(II) does which would limit the use of these trimers to only instances in with Pb(II) was not suitable (Pb(II) hydrolysis, lower pH range).

Zn(II) hydrolytic catalysis

In Chapters 3 and 4 of this work I described the spectroscopic and catalytic properties of $Glu_x^dHis_3^a$ heterotrimers with Co(II) and Zn(II) as a model of carbonic anhydrase. Co(II) was used as a spectroscopic probe for Zn(II), which is a d^{10} ion. UV-visible and X-ray absorption spectroscopies found that Co(II) bound to homotrimeric His_3^a and $Glu_3^dHis_3^a$ was 6-coordinate, though with a less symmetric environment in the $Glu_3^dHis_3^a$ construct than the His_3^a construct. Heterotrimeric $Glu_1^dHis_3^a$ and $Glu_2^dHis_3^a$ were more likely 5-coordinate based on XAS fits and the extinction coefficient of the visible d-d transition. Thus, a transition metal in an asymmetric ligand environment did indeed bind asymmetrically, which is consistent with work done by Dr. Catherine Mocny on $Asp_x^dHis_3^a$ peptides. All of this characterization was done at pH 7.5

The Co(II) coordinated heterotrimers were not, however, investigated as catalysts for ester hydrolysis. Dr. Melissa Zastrow found that at high pH Co(II) was as active as Zn(II) in catalyzing this reaction with the TRI His_3^a construct.[9] At pH 7.5, as with His_3^a characterized in Chapter 3, the Co(II) d-d transition was consistent with a 6-coordinate species. In basic conditions, the transition was less symmetric which correlates with a 5-coordinate complex (Figure 6-1). It was hypothesized that this spectroscopic change was due to the deprotonation of coordinated solvent molecules, but more recent work with 5-coordinate heterotrimeric species instead indicates that a change in coordination number may be occurring. This activity was not observed at lower pH, indicating the need for a lower coordination number for efficient catalysis. It is, therefore, worth investigating if this activity is observed in heterotrimers at neutral pH

where 5-coordinate Co(II) is observed. A pH profile of Co(II) coordinated heterotrimers is necessary to determine the pK_a for this system in comparison to TRI His_3^a. While Co(II) is not a faithful probe for Zn(II) in these constructs, it nevertheless presents an interesting opportunity to explore the effects of an asymmetric ligand environment on transition metal catalysis.

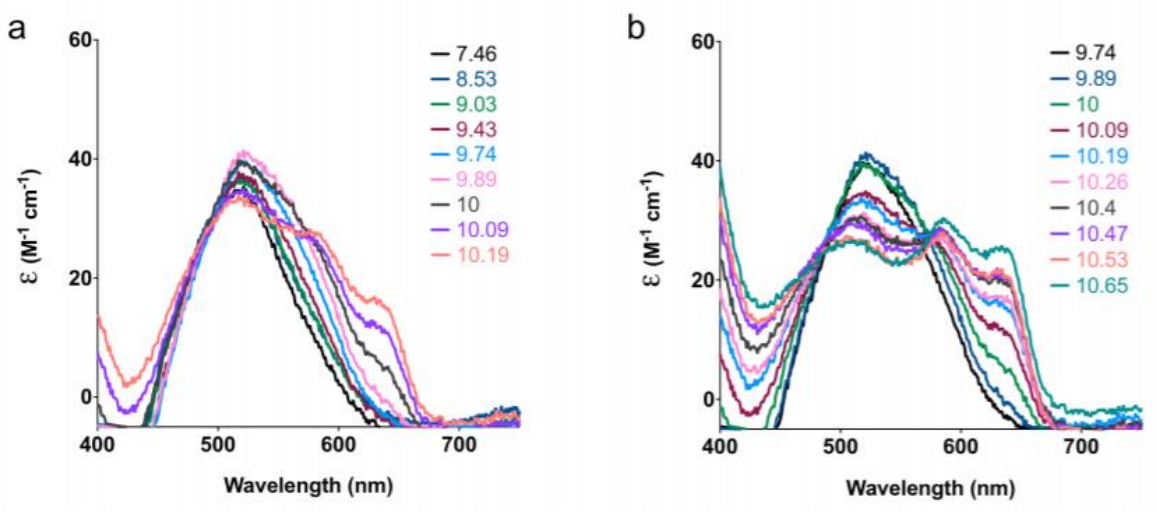

Figure 6-1 Co(II) d-d transition of TRI His_3^a as a function of pH with 0.23 mM $CoSO_4$ and 0.47 mM TRI His_3^a with (a) selected neutral and basic pH measurements and (b) basic pH measurements. Figure from Dr. Melissa Zastrow.[9]

Zn(II) was found to remain 4-coordinate regardless of the ligand environment or pH (7.5 or 9.5). Esterase activity was not enhanced above what was observed by Dr. Zastrow with TRI His_3^a at pH 9.5, likely because the glutamate residues were hydrogen bonding with histidine instead of forming a second coordination sphere interaction as was intended. The carboxylate ligand was intended to form a hydrogen bond with the Zn(II) coordinated solvent molecule as such a hydrogen bond in the native enzyme decreased the active site pKa by ~2 pH units and increased the activity ~100 fold. Thus, while Zn(II) catalysis was not enhanced in heterotrimeric constructs at pH 9.5, the effect of a single carboxylate residue on the active site pKa was not determined. It remains to be determined if higher activity is seen in neutral or less basic solution.

Structural characterization of the $Glu_3^dHis_3^a$ site also remains to be done. The Pecoraro group has solved crystal structures of both Zn(II)His_3OH and Zn(II)His_3Cl, but no structures have been determined for carboxylate containing 3SCCs. I have collected data on a crystal of $Glu_3^dHis_3^a$ but have been unable to solve it due to COVID restrictions. This structure (or a structure of $Asp_3^dHis_3^a$) would allow for more complete analysis of the reported kinetic results. Structures with His substitutions have shown an increase in interhelical distance over wild type

sequences but it is unknown if carboxylate residues have any effect on interstrand distances. It also must be determined if hydrogen bonding or direct coordination is possible in these systems. All structural analyses proposed in Chapter 4 are consistent with current data, but would best be described from a crystallographic data set containing carboxylate ligands.

These systems are also being investigated as catalysts for a wider scope of reactivity than the hydrolysis work described herein. A collaboration with the research group of Dr. Amy Barrios at the University of Utah is underway to determine alternate functionalities for these Zn(II) systems via high throughput screening. Through the use of fluorogenic probes, Dr. Barrios is able to identify enzymes capable of performing peptidase, sulfatase, esterase, phosphatase, and galactosidase reactions (Figure 6-2). So far, her group has identified sulfatase, esterase, and peptidase activities in His_3^a. The esterase activity reported for His_3^a agrees well with previously reported values. At 37°C, Dr. Barrios reported a catalytic efficiency of 2.8 $M^{-1}s^{-1}$ for the MU-ester substrate shown in Figure 6-2. With the elevated temperature, this increase in activity is expected over previously reported values at 25°C. A continuation of this work with heterotrimeric peptides will undoubtedly identify alternate reactivities to the esterase work described herein. As discussed in Chapter 4, the addition of carboxylate residues did not afford the intended second coordination sphere hydrogen bonding residue while maintaining the Zn(II)His_3(OH/H_2O) catalytic center. The Zn(II) is more likely coordinated to 2 His residues and 2 solvent molecules, generating an active site more similar to peptidases such as thermolysin ($His_2Carboxy(H2O)_2$) or carboxypeptidase ($His_2CarboxyH_2O$).[10-11] This project will continue to identify alternate activities of heterotrimeric peptides to advance our understanding of the structure/function relationship.

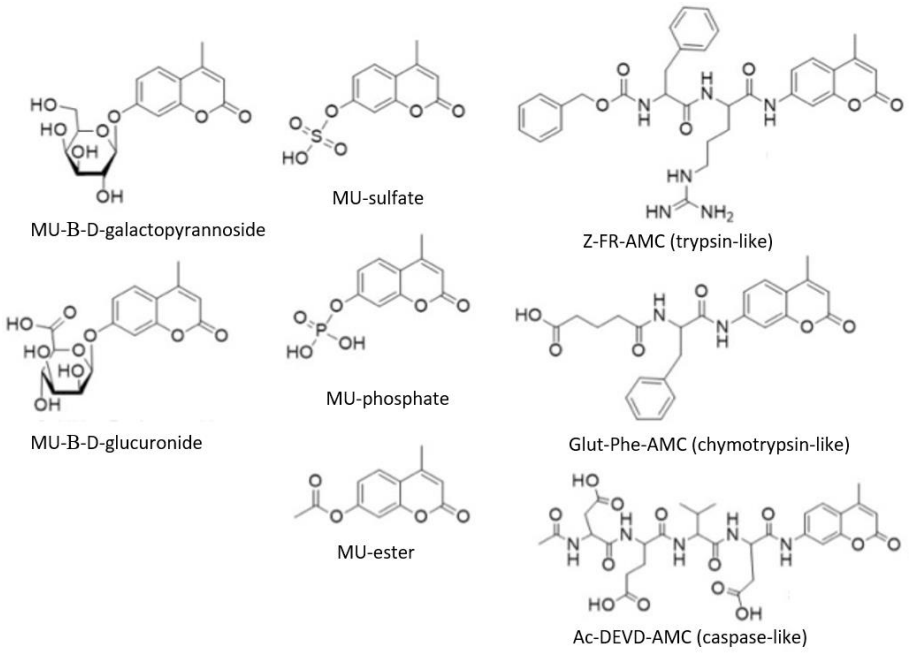

Figure 6-2 Fluorogenic substrate panel for high throughput screening developed by Dr. Amy Barrios[12]

Cu(I/II) superoxide dismutase activity

In addition to the previously described hydrolytic work, I also designed and characterized the best models of Cu-only SODs. This work found that His^{d} sites were significantly better than His^{a} sites for performing this reaction, despite the fact that the reduction potential is less ideal. The addition of Asp residues to the His_3^{a} peptides improves upon catalytic activity, but the same is not seen for His_3^{d} peptides. The only Asp containing peptide that improved upon the His_3^{d} construct is $His_2^{d}Asp_1^{d}His_1^{a}$. Cu(II) affinities and redox potentials for heterotrimeric constructs are needed to determine if these peptides are within the range necessary for the dismutation of superoxide.

In addition to the redox potentials, crystal structures of copper bound 3SCCs are necessary for future studies. Dr. Fangting Yu was able to grow a crystal of $Cu(II)His_3^{a}$, but was unable to collect data without photoreduction. With advances to crystallographic data acquisition, it may be possible to collect data on Cu(II) coordinated peptides. Cu(I) structures may also be obtained by growing and harvesting crystals in an anaerobic environment. This is necessary to advance our understanding of the copper binding environment with both oxidation states to identify changes in ligand type, number, and distance. Any structure obtained with carboxylate residues would afford additional understanding of how such residues affect copper coordination and 3SCC structure. Additionally, a structure with His^{d} residues would also greatly

advance our understanding of these systems because, as discussed in Chapter 5, it is likely a structural difference between His^{d} and His^{a} residues affords increased activity. Work by Dr. Leela Ruckthong has shown that the interstrand distance of the 3SCC is increased with the substitution of Leu residues for His residues in the **a** site, but the extent of this is not yet known for the **d** site so we are unable to generate any models for this environment without an accurate structure.[13]

As the most active construct is more similar to Fe/Mn SOD active sites than to Cu-only or Cu,Zn SOD active sites, I also began to investigate Mn coordination in these peptides. Mn(II) binds to $Asp_1{}^{d}His_3{}^{a}$ as determined by EPR (Figure 6-3). The spectrum below is similar to a Mn SOD EPR spectrum reported by Whittaker and Whittaker with a positive peak at ~1000G and a negative peak ~4000G (Figure 6-4), though the Mn(II) concentration in the figure below is too high to fully resolve these features. Free Mn(II) ($Mn(II)(H_2O)_6$) is expected to have a single peak at ~3000G with 6-line hyperfine splitting.[14] At lower concentration, the spectrum is better resolved below 7500 G, but a large peak between 10000 and 12500 G is also present that is not found in the native system (Figure 6-5). It is possible that this environment is highly asymmetric or that there may be multiple Mn(II) species contributing to the signal. The activity of manganese in these peptides would provide an interesting study into the structure/function relationship of both Cu-only and Fe/Mn SODS. This project would address the question of metal selectivity as a function of evolution and metal ion availability or as a necessity for activity in each SOD family.

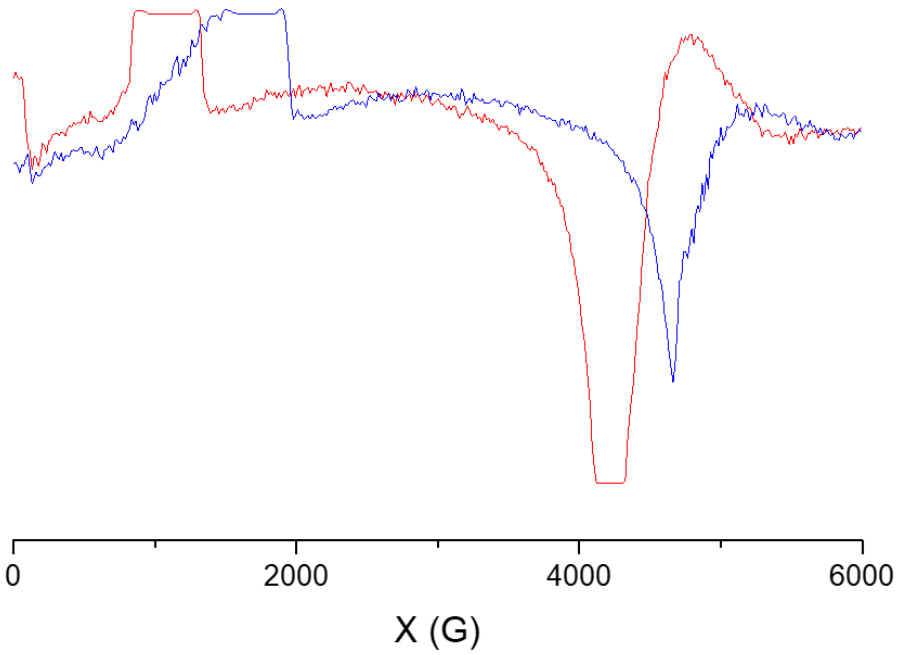

Figure 6-3 X-band Mn(II) EPR of $Asp_1^dHis_3^a$ (blue) and $Asp_3^dHis_3^a$ (red) with 200 μM 3SCC, 200 μM $Pb(NO_3)_2$, and 50 μM $MnCl_2$ in 50 mM HEPES pH 7.5. Microwave frequency 9.46 GHz, microwave power 1 mW, modulation amplitude 10 G. Note that samples were too concentrated to allow for resolution of peaks at 1000 and 4000 G.

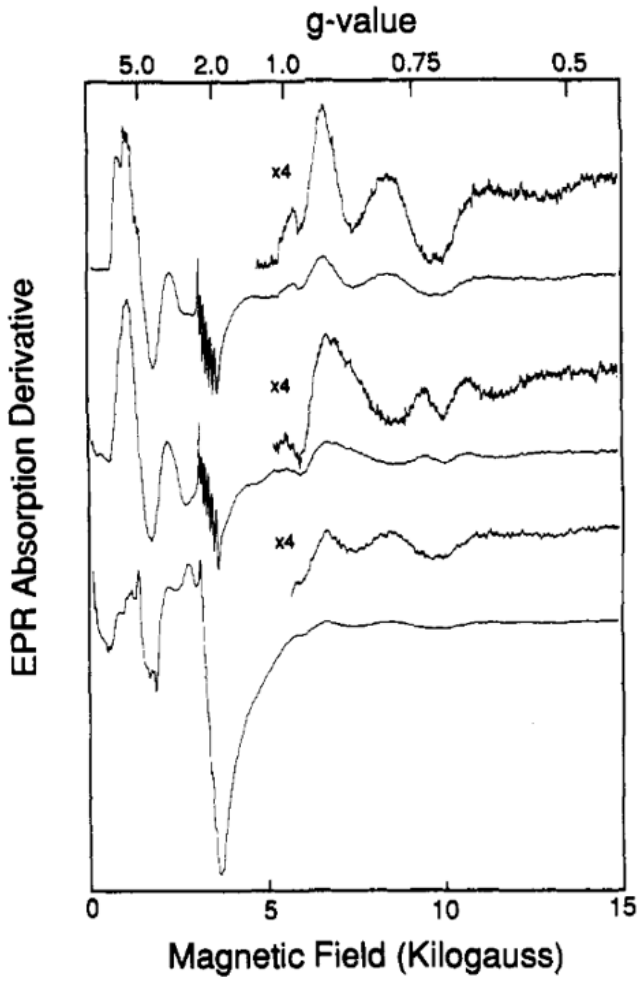

Figure 6-4 Mn(II) EPR of (top) anaerobic superoxide dismutase with dithionite, (middle) superoxide dismutase with 1 M KF, and (bottom) superoxide dismutase with 1 M KN_3 at 5K with 9.46 GHz microwave frequency, 1 mW microwave power, 10 G modulation amplitude and ~3 mM protein active sites[14]

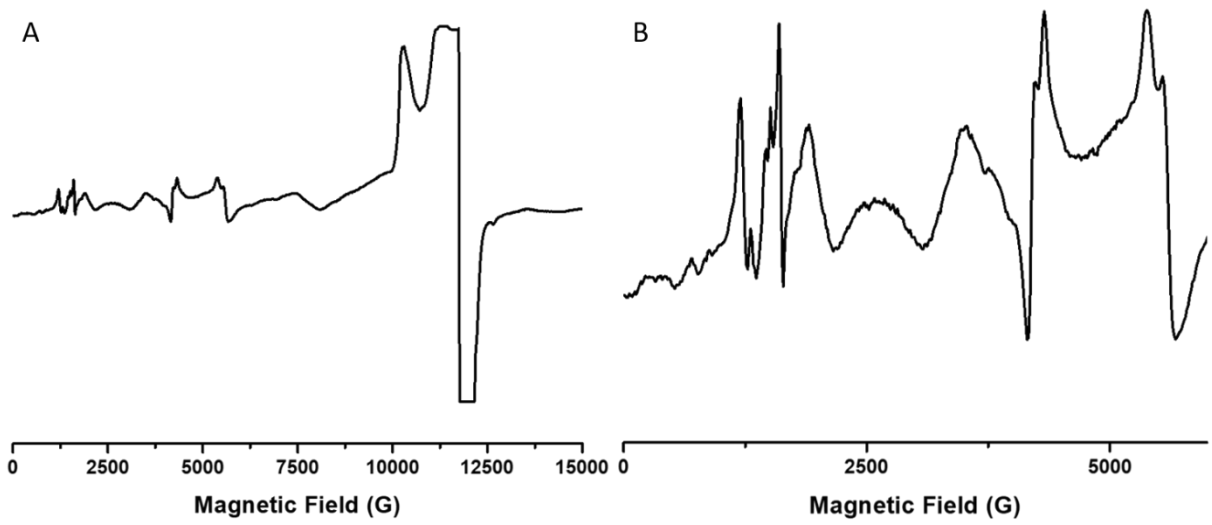

Figure 6-5 X-band Mn(II) EPR of $Asp_1{}^dHis_3{}^a$ from 0 to 15000 G (A) and 0 to 7500 G (B) with 100 μM 3SCC, 100 μM $Pb(NO_3)_2$, and 25 μM $MnCl_2$ in 30 mM Potassium Phosphate pH 7.5. Microwave frequency 9.46 GHz, microwave power 1 mW, modulation amplitude 10 G. Data collected by Winston Pitts.

General asymmetric catalysis

The largest and most interesting protein design problem remaining from this work is the need to generate a single metal coordination environment within an asymmetric peptide scaffold. This work has shown that a fully selective, self-assembling, asymmetric 3SCC can impart an asymmetric transition metal environment. These peptides do not however, enforce only a single coordination environment as determined by XAS, EPR, and UV-visible spectroscopies. This is true for Co(II) and Zn(II) characterization of $Asp_x{}^dHis_3{}^a$ and $Glu_x{}^dHis_3{}^a$ peptides as hydrolytic catalysts and Cu(I/II) coordinated $His_x{}^dHis_{3-x}{}^a$ and mixed Carboxy/His peptides as redox catalysts. Asp residues do not afford better control than Glu residues nor do His^d residues over His^a residues. Without a single coordination environment at the catalytic metal site, one cannot determine if catalysis is due to only a single conformer, reducing the reported efficiencies, or a mixture of conformers, further convoluting the results. Thus, a high level of control over the primary and secondary metal coordination spheres is necessary to advance this work because without full selectivity one cannot determine if activity comes from only a single species or the mixture of species.

This selectivity may be afforded by negative design. The only hydrophobes investigated in this system are Leu residues as these are known to form 3SCCs instead of 2SCCs or 4SCCs.[15-

[16] The Leu residue(s) adjacent to the transition metal binding site may allow for too much flexibility in side chain orientation and metal solvation. Isoleucine in place of these leucine residues ($Ile^{d}His^{a}$) would likely not negatively impact the stability, but the increased bulk at the center of the 3SCC may prevent multiple side chain conformations. Phenylalanine may also achieve this end ($Phe^{d}His^{a}$), though with a cost incurred to stability with such a bulky core residue.

One could also consider the position of the transition metal site within the 3SCC. This work has only investigated the most C-terminal **a** site and the **d** site in the previous heptad for transition metal binding. It is possible that by positioning this site further towards the interior of the trimer, the solvation of the transition metal may be affected. Dr. Zastrow showed that overall catalytic efficiency of $Zn(II)His_3$ CA activity remained unchanged throughout the 3SCC, but did not determine the structural mechanism that affect k_{cat} and K_M.[3] These structural differences may be sufficient to enforce a single transition metal coordination environment.

In summary, this thesis has described the first fully selective, self-assembling, asymmetric *de novo* 3SCC and its use as a scaffold for both hydrolytic and redox catalysis. This asymmetric scaffold design presents a significant advancement in the field of protein design as it requires only a single heptad of the scaffold to induce asymmetry allowing for the incorporation of a second, distant transition metal binding site. This transition metal binding site can be used to investigate both hydrolytic and redox catalysis with asymmetric primary or secondary coordination spheres without perturbing the $Pb(II)Cys_3$ site used to scaffold the trimer. This achievement allows for the characterization of catalytic centers that more closely model the asymmetric sites found in native enzymes, furthering our study of the structure/function relationship of these systems. To extend these achievements, future students should consider improvements of this scaffold design to preclude multiple transition metal binding ligand environments within a single heterotrimer through the incorporation of bulkier hydrophobes to prevent multiple side chain conformations. This will allow for more accurate studies of the enzymes described herein as well as a wealth of new reactivities to explore.

References

1. Zastrow, M. L.; Peacock, A. F.; Stuckey, J. A.; Pecoraro, V. L., Hydrolytic catalysis and structural stabilization in a designed metalloprotein. *Nat. Chem.* **2011,** *4* (2), 118-23.

2. Yu, F.; Penner-Hahn, J. E.; Pecoraro, V. L., De novo-designed metallopeptides with type 2 copper centers: modulation of reduction potentials and nitrite reductase activities. *J. Am. Chem. Soc.* **2013,** *135* (48), 18096-107.

3. Zastrow, M. L.; Pecoraro, V. L., Influence of active site location on catalytic activity in de novo-designed zinc metalloenzymes. *J. Am. Chem. Soc.* **2013,** *135* (15), 5895-903.

4. Peacock, A. F. A.; Iranzo, O.; Pecoraro, V. L., Harnessing natures ability to control metal ion coordination geometry using de novo designed peptides. *Dalton Trans.* **2009,** *9226* (13), 2271-80.

5. Mocny, C. S. Ph.D. Dissertation, Examining the metal selectivity of thiol rich de novo designed peptides as a strategy to make asymmetric alpha- helical protein assemblies. 2016.

6. Zampella, G.; Neupane, K. P.; De Gioia, L.; Pecoraro, V. L., The importance of stereochemically active lone pairs for influencing Pb(II) and As(III) protein binding. *Chemistry* **2012,** *18* (7), 2040-50.

7. Farrer, B. T.; McClure, C. P.; Penner-Hahn, J. E.; Pecoraro, V. L., Arsenic(III) - Cysteine interactions stabilize three-helix bundles in aqueous solution. *Inorg. Chem.* **2000,** *39* (24), 5422-5423.

8. Balimann, G.; Pregosin, P. S., Arsenic-75 Nuclear Magnetic Resonance. A Study of Some Arsenic Salts. *J. Magn. Reson.* **1977,** *26*, 283-289.

9. Zastrow, M. L. De novo designed metalloenzymes: structural stabilization and hydrolytic catalysis in a family of α-helical coiled coils. 2013.

10. Greenblatt, H. M.; Feinberg, H.; Tucker, P. A.; Shoham, G., Carboxypeptidase A: Native, zinc-removed and mercury-replaced forms. *Acta Crystallographica Section D: Biological Crystallography* **1998,** *54* (3), 289-305.

11. Holland, D. R.; Hausrath, A. C.; Juers, D.; Matthews, B. W., Structural-Analysis of Zinc Substitutions in the Active-Site of Thermolysin. *Protein Sci.* **1995,** *4* (10), 1955-1965.

12. McCullough, B. S.; Barrios, A. M., Fluorogenic probes for imaging cellular phosphatase activity. *Curr. Opin. Chem. Biol.* **2020,** *57*, 34-40.

13. Ruckthong, L. Crystallographic comparison of tris-thiolate sites in designed proteins to control metal geometries. University of Michigan, Ann Arbor, MI, 2016.

14. Whittaker, J. W.; Whittaker, M. M., Active site spectral studies on manganese superoxide dismutase. *J. Am. Chem. Soc.* **1991,** *113* (15), 5528-5540.

15. Gonzalez, L. J.; Brown, R. A.; Richardson, D.; Alber, T., Crystal structures of a single coiled-coil peptide in two oligomeric states reveal the basis for structural polymorphism. *Nat. Struct. Biol.* **1996,** *3* (12), 1002-1010.

16. Harbury, P. B.; Zhang, T.; Kim, P. S.; Alber, T., A Switch Between Two-, Three-, and Four-Stranded Coiled Coils in GCN4 Leucine Zipper Mutants. *Science* **1993,** *262* (5138), 1401-1407.

Appendix A Table of Peptide Sequences

*Table A-1 All peptide sequences discussed in this work with Pb(II) sites in **bold green** and transition metal sites in **bold red***

Peptide Name	Abbreviation	Sequence
Coil Ser		Ac E WEALEKK LAALESK LQALEKK LEALEHG NH_2
TRI		Ac G LKALEEK LKALEEK LKALEEK LKALEEK G NH_2
Grand (GR)		Ac G LKALEEK LKALEEK LKALEEK LKALEEK LKALEEK G NH_2
Baby L9C		Ac-G WKALEEK **C**KALEEK LKALEEK G-NH_2
TRI L2WL16C	TRI Cys^a	Ac G WKALEEK LKALEEK **C**KALEEK LKALEEK G NH_2
TRI L2WL12C	TRI Cys^d	Ac G WKALEEK LKA**C**EEK LKALEEK LKALEEK G NH_2
TRI L2WL19C	TRI $19Cys^d$	Ac G WKALEEK LKALEEK LKA**C**EEK LKALEEK G NH_2
TRI L9CL23H		Ac G WKALEEK **C**KALEEK LKALEEK **H**KALEEK G NH_2
GR L2WL16C	Cys^a	Ac G WKALEEK LKALEEK **C**KALEEK LKALEEK LKALEEK G NH_2
GR L2WL12AL16C	Ala^dCys^a	Ac G WKALEEK LKA**A**EEK **C**KALEEK LKALEEK LKALEEK G NH_2
GR L2WL12C	Cys^d	Ac-G WKALEEK LKA**C**EEK LKALEEK LKALEEK LKALEEK G-NH_2
GR L2WL12CL16A	Cys^dAla^a	Ac-G WKALEEK LKA**C**EEK **A**KALEEK LKALEEK LKALEEK G-NH_2
GR L2WL23C	$23Cys^a$	Ac-G WKALEEK LKALEEK LKALEEK **C**KALEEK LKALEEK G-NH_2
GR L2W19AL23C	Ala^d23Cys^a	Ac-G WKALEEK LKALEEK LKA**A**EEK **C**KALEEK LKALEEK G-NH_2
GR L2WL19C	$19Cys^d$	Ac-G WKALEEK LKALEEK LKA**C**EEK LKALEEK LKALEEK G-NH_2
GR L2WL19CL23A	$19Cys^dAla^a$	Ac-G WKALEEK LKALEEK LKA**C**EEK **A**KALEEK LKALEEK G-NH_2
GR L2WL30C	$30Cys^a$	Ac-G WKALEEK LKALEEK LKALEEK LKALEEK **C**KALEEK G-NH_2
TRI L9CL23H		Ac-G WKALEEK **C**KALEEK LKALEEK **H**KALEEK G-NH_2
TRI L19H		Ac-G WKALEEK LKALEEK LKA**H**EEK LKALEEK G-NH_2
TRI L9H		Ac-G WKALEEK **H**KALEEK LKALEEK LKALEEK G-NH_2
TRI L2WL23H	TRI His^a	Ac-G WKALEEK LKALEEK LKALEEK **H**KALEEK G-NH_2
GR L2WL12CL16AL30H	His^a	Ac-G WKALEEK LKA**C**EEK **A**KALEEK LKALEEK **H**KALEEK G-NH_2
GR L2WL12CL26DL30H	Asp^dHis^a	Ac-G WKALEEK LKA**C**EEK LKALEEK LKA**D**EEK **H**KALEEK G-NH_2
GR L2WL12CL26EL30H	Glu^dHis^a	Ac-G WKALEEK LKA**C**EEK LKALEEK LKA**E**EEK **H**KALEEK G-NH_2
GR L2WL12CL16AL26H	His^d	Ac-G WKALEEK LKA**C**EEK **A**KALEEK LKA**H**EEK LKALEEK G-NH_2
GR L2WL12CL26HL30H	His^dHis^a	Ac-G WKALEEK LKA**C**EEK LKALEEK LKA**H**EEK **H**KALEEK G-NH_2
GR L2WL12CL30HL33E	His^aGlu^d	Ac-G WKALEEK LKALEEK **C**KALEEK LKALEEK **H**KA**E**EEK G-NH_2
GR L2WL12CL30HL33D	His^aAsp^d	Ac-G WKALEEK LKALEEK **C**KALEEK LKALEEK **H**KA**D**EEK G-NH_2

GR L2WL12CL26IL30H	Ile^{d}His^{a}	Ac-G WKALEEK LKA**A**EEK **C**KALEEK LK**I**EEK **H**KALEEK G-NH_2
GR L2WL12CL26FL30H	Phe^{d}His^{a}	Ac-G WKALEEK LKA**A**EEK **C**KALEEK LK**F**EEK **H**KALEEK G-NH_2
CS L9PenL23H		Ac-E WEALEKK **Pen**AALESK LQALEKK **H**EALEHG-NH_2
GRCS L16CL30H		Ac-E WEALEKK LAALESK **C**QALEKK LQALEKK **H**EALEHG-NH_2
α_3D		MGSWAEFKQRLAAIKTRLQALGG SEAELAAFEKEIAAFESELQAYKGKGNPE VEALRKEAAAIRDELQAYRVNGSGA
α_3D H3		MGSWAEFKQRLAAIKTR**H**QALGG SEAE**H**AAFEKEIAAFESELQAYKGKGNPE VEALRKEAAAIRDE**H**QAYRVNGSGA
GRα_3D		MGSWAEFKQRLAAIKTRLAAIKSRLDALGGS-EAELAAFEKEIAAFESEIAAFESELQAYKGKG-NPEVEALRKEAAAIRDEAAAIRDELQAYRLNGSGA
GRα_3D H3		MGSWAEFKQRLAAIKTRLAAIKSR**H**DALGGS-EAELAA**H**EKEIAAFESEIAAFESELQAYKGKG-NPEVEALRKEAAAIRDEAAAIRDE**H**QAYRLNGSGA
GRα_3D H4		MGSWAEFKQRLAAIKTRLAAIKSR**H**DALGGS-EAE**H**AA**H**EKEIAAFESEIAAFESELQAYKGKG-NPEVEALRKEAAAIRDEAAAIRDE**H**QAYRLNGSGA
GRα_3D H3D		MGSWAEFKQRLAAIKTRLAAIKSR**H**DALGGS-EAE**D**AA**H**EKEIAAFESEIAAFESELQAYKGKG-NPEVEALRKEAAAIRDEAAAIRDE**H**QAYRLNGSGA
GRα_3D H2DH		MGSWAEFKQRLAAIKTRLAAIKSR**H**DALGGS-EAE**H**AA**D**EKEIAAFESEIAAFESELQAYKGKG-NPEVEALRKEAAAIRDEAAAIRDE**H**QAYRLNGSGA